N° d'ordre : …

Ecole Doctorale - 104 - Sciences de la Matière, du Rayonnement et de l'Environnement

UMR CNRS 8207 Unité Matériaux et Transformations

HABILITATION À DIRIGER DES RECHERCHES

Discipline : Sciences Physiques

Par

Alexandre MUSSI

Apport de la microscopie électronique en transmission quantitative à la plasticité des minéraux

Soutenue le 26 juin 2019 devant la commission d'examen formée de :

Monsieur Hosni IDRISSI (Pr) Rapporteur

Madame Florence PETTINARI-STURMEL (Pr) Rapporteur

Monsieur Christophe TROMAS (Pr) Rapporteur

Monsieur Jacques RABIER (DR) Examinateur/Président

Monsieur Edgar RAUCH (DR) Examinateur

Monsieur Patrick CORDIER (Pr) Garant

Ce n'est pas ce que tu regardes, mais ce que tu vois

Henry David Thoreau

Sommaire :

Mots-clés :
1 Plasticité
2 MET
3 Dislocations
4 Minéraux
5 Tomographie
6 ASTAR
7 Quantitatif
8 Désorientation

Keywords:
1 Plasticity
2 TEM
3 Dislocations
4 Minerals
5 Tomography
6 ASTAR
7 Quantitative
8 Misorientation

Préambule

Ce manuscrit présente mes activités au sein du laboratoire UMET (CNRS-UMR 8207) de l'Université de Lille. Mes travaux de recherche sont centrés sur la compréhension des mécanismes fondamentaux de plasticité dans les minéraux du manteau supérieur et des zones de subduction par microscopie électronique en transmission (MET). Cette thématique, entamée dans l'équipe « Physique des Minéraux », se poursuit actuellement dans l'équipe « Plasticité », sous la direction de Patrick Cordier. L'équipe « Plasticité » s'est spécialisé dans la modélisation multi-échelle de la plasticité des minéraux du manteau, associée à des essais mécaniques accompagnés de caractérisations microstructurales conduites essentiellement par MET. Mon rôle y est d'animer cette interface entre les modélisations et les observations d'échantillons déformés expérimentalement ou dans la nature.

Le volcanisme et les séismes, manifestations de la dynamique interne de la Terre, ont d'importantes répercussions sur l'humanité. Comprendre cette dynamique permettrait de prévenir plus en amont ces catastrophes naturelles. La Terre est une planète chaude, elle se refroidit par la convection du manteau constitué de roches solides. Ces mouvements convectifs profonds déforment les différentes couches du manteau terrestre et entrainent les roches situées au niveau de l'interface lithosphère-asthénosphère, par le célèbre mécanisme de tectonique des plaques qui vient de fêter ses 50 ans (Le Pichon, 1968). L'étude des mécanismes de déformation plastique des minéraux du manteau supérieur permettrait d'identifier les paramètres qui contrôlent le couplage lithosphère/asthénosphère. La subduction des plaques, conséquence de cette convection mantellique, intervient également dans la déformation plastique des minéraux du manteau et réciproquement. Dans le même état d'esprit, l'étude de la plasticité des minéraux qui constituent les plaques en subduction doit être entreprise.

Les mécanismes de déformation plastique de l'olivine, constituant majeur du manteau supérieur, ont été étudiés depuis plus de 50 ans (Raleigh, 1968). Nous sommes pourtant bien loin de disposer de données assez robustes pour être transférées à la rhéologie du manteau puisqu'une étude récente, menée sur la flexion de la croute océanique sous les volcans d'Hawaii (Zhong & Watts, 2013), a montré que le terme pre-exponentiel de la loi de fluage à basse température, proposée par Mei et ses collaborateurs (2010), est surestimée de 6 à 8 ordres de grandeur. Cet écart considérable résulte d'une hypothèse discutable qui consiste à extrapoler une loi de fluage obtenue pour des vitesses de déformation de laboratoire (10^{-5} s^{-1}), aux vitesses géologiques (10^{-14} s^{-1}). Des modifications de mécanismes de déformation plastique doivent inévitablement se produire avec de tels écarts de vitesses.

De nombreux dispositifs ont été élaborés pour reproduire les conditions de pression, de température et de taux de déformation du manteau et ainsi déterminer leurs lois rhéologiques. Avec 300 MPa de pression de confinement, Paterson (1970-1990) a mis au point un dispositif de compression et de cisaillement par torsion, en température, d'échantillons massifs, capable d'atteindre les conditions du haut de la lithosphère. Plusieurs dispositifs ont été mis au point pour suivre le géotherme dans les profondeurs de la Terre, comme le dispositif de déformation-DIA (15 GPa, Wang *et al.*, 2003), la presse rotative Drickamer (jusqu'à 27 GPa, Girard et al 2016) et la presse multi-enclume de type Kawai (25 GPa, Cordier & Rubie, 2001 ; portée récemment jusqu'à 109 GPa d'après Yamazaki *et al.*, 2014). Malheureusement, plus la pression de confinement est élevée, plus la taille des échantillons déformés se réduit (de

quelques mm^3 pour la presse Paterson à quelques μm^3 pour les presses Kawai capables d'atteindre le MBar).

Les caractérisations microstructurales *in situ* et mécaniques *in situ*, à l'échelle mésoscopique, des mécanismes de déformation plastique des matériaux, sont généralement effectuées aux grands instruments, par analyse de textures (Wenk *et al.*, 2001) et/ou par l'étude de l'évolution de l'espacement des distances inter-réticulaires (Singh *et al.*, 1998, Wang *et al.*, 2003). Pour accéder aux mécanismes fondamentaux de déformation plastique *post mortem*, la MET s'impose. Cet instrument offre des possibilités abondantes et permet d'effectuer des caractérisations :

- chimiques (cartographie EDX pour les éléments lourds (Fitzgerald *et al.*, 1968), cartographie EELS pour les éléments légers (Isaacson & Johnson, 1975 ; Colliex et *al.*, 1976)) ;
- des environnements atomiques par analyses ELNES en EELS (Taftø & Zhu, 1982) ;
- magnétiques et électriques par holographie électronique (Lichte & Lehmann, 2007) ;
- cristallographiques (clichés de diffraction en précession (Abe, 2012)) ;
- de haute résolution en mode TEM (Uyeda *et al.*, 1972) et en mode STEM (Erni *et al.*, 2009) ;
- des défauts cristallins, en ce qui nous concerne (par faisceau faible en champ sombre (Cockayne *et al.*, 1969, Cockayne 1973), par diffraction électronique en faisceau convergent à grand angle (Mornirolli, 2004)) ;
- par cartographies d'orientations (ASTAR (Rauch & Véron 2014)) ;
- tomographiques, en ajoutant une troisième dimension à ces différentes techniques par l'acquisition de série tiltées (Barnard *et al.*, 2006 ; Lepinay *et al.*, 2013 ; Yedra *et al.*, 2012) ;
- quantitative sur ces différentes aspects, suite aux avancées techniques poussées (Verbeeck & Van Aert, 2004 ; Van Aert *et al.*, 2011 ; Palatinus *et al.*, 2017 ; etc.).

Si, a priori, cet outil remarquable donne un accès global aux propriétés physico-chimiques des matériaux, il connait néanmoins quelques limitations. Les géométries des lames minces (de l'ordre de 100 nm d'épaisseur), nécessaires pour assurer la transparence aux électrons, limitent la statistique et perturbent les propriétés mécaniques des échantillons massifs (force image). Par ailleurs, les images obtenues ne sont que des projections bidimensionnelles ce qui peut, suivant certaines orientations, fausser les interprétations. Enfin, les minéraux obtenus sous hautes pressions, sont généralement sensibles aux irradiations électroniques et peuvent s'amorphiser très rapidement sous le faisceau électronique. Des compromis doivent donc être faits pour obtenir les informations souhaitées, la MET ne déroge malheureusement pas à cette règle immuable.

Je vais m'attacher, dans ce mémoire, à présenter les moyens les plus efficaces pour obtenir les données quantitatives pertinentes sur les mécanismes fondamentaux de déformation plastique des minéraux du manteau, par MET.

Lorsque les conditions expérimentales sont inaccessibles (phases de haute pression non trempables, vitesses de déformation trop lentes, etc.), des modélisations numériques peuvent être entreprises. Les cœurs de dislocations peuvent être simulés en calculant les défauts d'empilements généralisés par le modèle de Peierls-Nabarro (Peierls, 1940 ; Nabarro, 1947). Ces modélisations *ab initio* sont très couteuses en temps de calculs et se limitent à des volumes simulés de quelques paramètres de mailles. A l'échelle supérieure, l'utilisation de potentiels inter-atomiques (accessibles par calculs *ab initio*), permet d'effectuer des calculs de dynamique moléculaire (DM) sur plusieurs dizaines de millions d'atomes, mais sont plus

approximatifs. A l'échelle mésoscopique, la dynamique des dislocations (DD) permet de prendre en compte les interactions élastiques collectives entre dislocations ; elle représente le point charnière de la modélisation multi-échelle de la plasticité. Les modélisations *ab initio* et de DM sont des données d'entrée pour la DD. Si les principales propriétés des dislocations sont introduites dans le modèle de DD, alors la qualité des résultats permet de faire des analyses quantitatives et prédictives tangibles. La DD conserve néanmoins une faiblesse dans sa mise en œuvre : malgré les progrès informatiques, il est actuellement difficile de modéliser le mouvement de plusieurs centaines de dislocations, ce qui réduit la simulation de la déformation plastique à quelques %. Pour passer du monocristal au polycristal, un lien doit être effectué entre la DD et la modélisation par éléments finis (FEM), lien communément appelé modèle discret-continu (Groh *et al.*, 2003). Le principe consiste à incorporer comme lois constitutives dans les calculs FEM, non pas les lois habituelles de la cristallographie, mais les simulations par DD où les interactions à longue distance dislocations-dislocations sont prises en compte.

Il est nécessaire d'effectuer des comparaisons simulations/expériences pour des conditions accessibles au laboratoire, pour ensuite valider ces modèles numériques pour des conditions expérimentales inaccessibles (hautes pressions et/ou vitesses de déformation géologiques). En m'inspirant des travaux de Pollock et LeSar (2013), je propose de m'associer avec les modélisateurs de l'équipe pour édifier un pont entre les données expérimentales et les modélisations numériques de DD. Ce pont consiste à incorporer directement les données expérimentales en paramètre d'entrée des simulations de DD. Des informations quantitatives et prédictives de qualité pourraient ainsi être obtenues, sur les mécanismes de déformation plastique, par cette nouvelle approche.

Ce mémoire est structuré en trois parties : mes travaux de recherche effectués depuis mon arrivée au laboratoire ; mes projets à courts, moyens et longs termes ; et mon parcours scientifique. La première partie de ce document décrit, en premier lieu, les mécanismes fondamentaux de plasticité des silicates magnésiens hydratés de hautes pressions (DHMS pour Dense Hydrous Magnesium Silicates), supposés être présents dans les zones de subduction, à travers l'analyse, par caractérisations MET, des défauts résultants de déformations expérimentales. Au second chapitre de cette partie nous présentons les études axées sur le développement de la tomographie électronique en transmission des dislocations (TETD) pour l'étude de la déformation plastique de l'olivine. L'obtention, par cartographie d'orientation et de désorientation, de données semi-quantitatives sur les mécanismes de déformation plastique de minéraux hyper-déformés, est présentée dans le dernier chapitre de la première partie du mémoire. Trois projets de recherche sont ensuite décrits dans la deuxième partie de ce manuscrit. Le premier projet aborde l'analyse poussée des cartographies de désorientations pour, cette fois-ci, extraire des informations quantitatives sur les défauts cristallins. J'ambitionne également de faire évoluer la TETD pour l'analyse des minéraux sensibles aux faisceaux d'électrons, pour les années à venir. Enfin, à travers une collaboration avec le CEA à Saclay, je projette d'associer la TETD aux modélisations par DD. La dernière partie de ce document porte sur mes renseignements personnels parmi lesquels figurent mon parcours scientifique, ma liste d'articles et de communications ainsi que mes responsabilités collectives.

Références :

Abe, E. (2012): Electron microscopy of quasicrystals – where are the atoms? *Chem. Soc. Rev.*, **41**, 6787–6798.

Colliex, C., Cosslett, V.E., Leapman, R.D., Trebbia P. (1976): Contribution of electron energy loss spectroscopy to the development of analytical electron microscopy. *Ultramicroscopy*, **1**, 301-315.

Cockayne, D.J.H. (1973): The principles and practice of the weak-beam method of electron microscopy. *J. Microsc.*, **98**, 116–134.

Cockayne, D.J.H., Ray, I.L.F., Whelan, M.J. (1969): Investigations of dislocation strain fields using weak beams. *Philos. Mag.*, 20, 1265-1270.

Cordier, P. & Rubie, D.C. (2001): Plastic deformation of minerals under extreme pressure using a multianvil apparatus. *Mater. Sci. Eng., A*, **309-310**, 38-43.

Erni, R., Rossell, M.D., Kisielowski, C., Dahmen, U. (2009): Atomic-Resolution Imaging with a Sub-50-pm Electron Probe. *Phys. Rev. Lett.*, **102**, 096–101.

Fitzgerald, R., Keil, K., Heinrich, K.F.J. (1968): Solid-state energy-dispersion spectrometer for electron-microprobe x-ray analysis. *Science*, **159**, 528-530.

Girard, J., Amulele, G., Farla, R., Mohiuddin, A., Karato, S. (2016): Shear deformation of bridgmanite and magnesiowüstite aggregates at lower mantle conditions. *Science*, **351**, 144-147.

Groh, S., Devincre, B., Kubin, L.P. (2003): Dislocations and elastic anisotropy in heteroepitaxial metallic thin films. *Philos. Mag. Lett.*, **83**, 303-313.

Isaacson, M. & Johnson, D. (1975): The microanalysis of light elements using transmitted energy loss electrons. *Ultramicroscopy*, **1**, 33-52.

Le Pichon, X. (1968): Sea floor spreading and continental drift. *J. Geophys. Res.*, **73**, 3661-3697.

Lepinay, K., Lorut, F., Pantel, R., Epicier, T. (2013) Chemical 3D tomography of 28 nm high K metal gate transistor: STEM XEDS experimental method and results. *Micron*, **47**, 43-49.

Lichte, H. & Lehmann, M. (2007): Electron holography—basics and applications. *Rep. Prog. Phys.*, **71**, 016102.

Mei, S., Suzuki, A.M., Kohlstedt, D.L., Dixon, N.A., Durham, W.B. (2010): Experimental constraints on the strength of the lithospheric mantle. *J. Geophys. Res.*, **115**, B08204.

Nabarro, F.R.N. (1947): Dislocations in a simple cubic lattice. *Proc. Phys. Soc.* **59**, 256-272.

Palatinus, L., Brázda, P., Boullay, P., Perez, O., Klementová, M., Petit, S., Eigner, V., Zaarour, M., Mintova, S. (2017): Hydrogen positions in single nanocrystals revealed by electron diffraction. *Science*, **355**, 166-169.

Paterson, M.S. (1970): A high pressure, high temperature apparatus for rock deformation. *Int. J. Rock Mech. Min.*, **7**, 512-517.

Paterson, M.S. (1990): Rock deformation experimentation. In: A.G. Duba, W.B. Durham, J.W. Handin and H.F. Wang, Eds., The brittle-ductile transition in rocks: the Head volume, p. 187-194. Geophysical Monograph Series, AGU, Washington.

Peierls, R.E. (1940): The size of a dislocation. *Proc. Phys. Soc.*, **52**, 34-37.

Pollock, T.M. & LeSar, R. (2013): The feedback loop between theory, simulation and experiment for plasticity and property modeling. *Curr. Opin. Solid State Mater. Sci.*, **17**, 10-18.

Raleigh, C.B. (1968): Mechanisms of plastic deformation of olivine. *J. Geophys. Res.*, **73**, 5391-5406.

Rauch, E.F. & Véron, M. (2014): Automated crystal orientation and phase mapping in TEM. *Mater. Charact.*, **98**, 1–9.

Singh, A.K., Balasingh, C., Mao, H.K., Hemley, R.J., Shu, J. (1998): Analysis of lattice strains measured under nonhydrostatic pressure. *J. Appl. Phys.*, **83**, 7567-7575.

Taftø, J. & Zhu, J. (1982): Electron energy loss near edge structure (ELNES), a potential technique in the studies of local atomic arrangements. *Ultramicroscopy*, **9**, 349-354.

Uyeda, U., Kobayashi, T., Suito, E., Harada, Y., Watanabe, M. (1972): Molecular image resolution in electron microscopy. *J. Appl Phys.*, **43**, 5181-5189.

Van Aert, S., Batenburg, K.J., Rossell, M.D., Erni, R., Van Tendeloo, G. (2011): Three-dimensional atomic imaging of crystalline nanoparticles. *Nature*, **470**, 374-377.

Verbeeck, J. & Van Aert, S. (2004): Model based quantification of EELS spectra. *Ultramicroscopy*, 101, 207-224.

Wang, Y., Durham, W.B., Getting. I.C., Weidner, D.J. (2003): The deformation-DIA: A new apparatus for high temperature triaxial deformation to pressures up to 15 GPa. *Rev. Sci. Instrum.*, **74**, 3002-3011.

Wenk, H.R., Cont, L., Xie, Y., Lutterotti, L., Ratschbacher, L., Richardson, J. (2001): Rietveld texture analysis of Dabie Shan eclogite from TOF neutron diffraction spectra. *J. Appl. Crystallogr.*, **34**, 442-453.

Yamazaki, D., Ito, E., Yoshino, T., Tsujino, N., Yoneda, A., Guo, X., Xu, F., Higo, Y., Funakoshi, K. (2014): Over 1 Mbar generation in the Kawai-type multianvil apparatus and its application to compression of $(Mg_{0.92}Fe_{0.08})SiO_3$ perovskite and stishovite. *Phys. Earth Planet. Inter.*,**228**, 262-267.

Yedra, L., Eljarrat, A., Arenal, R., Pellicer, E., Cabo, M., Lopez-Ortega, A. Estrader, M., Sort, J., Baro, M.D., Estrade, S., Peiro, F. (2012): EEL spectroscopic tomography: Towards a new dimension in nanomaterials analysis. *Ultramicroscopy*, **122**, 12-18.

Zhong, S. & Watts, A.B. (2013): Lithospheric deformation induced by loading of the Hawaiian Islands and its implications for mantle rheology. *J. Geophys. Res.*, **118**, 6025-6048.

Première partie
Présentation des travaux réalisés

Chapitre I : Analyses des microstructures de dislocations des phases denses hydratées des zones de subduction

Collaborateurs : Patrick Cordier (UMET), Daniel James Frost (Bayerisches Geoinstitut)
Travaux réalisés entre 2010 et 2013

Introduction :

Dans les années 30, Egon Orowan, Michaël Polanyi et Geoffrey Ingram Taylor se sont servis du concept de dislocations (notion introduite par Vito Volterra en 1907) pour expliquer l'écart considérable entre l'estimation de la contrainte de cisaillement critique théorique d'un cristal parfait et les contraintes de cisaillement critiques expérimentales ($\mu/10$ vs $\mu/10^9$). L'observation de ces défauts cristallins en volume nécessite des résolutions spatiales nanométriques et des analyses en transmission. La microscopie électronique en transmission (MET), outil créé par Ernst Ruska à la même époque, est la technique la plus appropriée pour ces caractérisations. D'un point de vu général, une dislocation peut être définie par son vecteur de Burgers, son vecteur ligne et le plan qui la contient. De nombreux progrès ont été réalisés depuis les toutes premières observations des dislocations au MET (Menter *et al.*, 1956, Hirsch *et al.*, 1956). La technique du faisceau faible (WBDF) a été mise au point par Cockayne dans les années 70 (Cockayne *et al.*, 1969, Cockayne, 1973) et permet d'obtenir des micrographies de dislocations fines et contrastées avec des détails allant de 15 jusqu'à 1.5 nm d'épaisseurs (Cockayne, 1973).

L'étude de la subduction des roches hydratées invite à s'interroger sur le devenir de l'eau dans le manteau. En effet, au cours d'altérations hydrothermales, l'eau sous forme hydroxyle, s'incorpore dans les roches ultramafiques pour former notamment les serpentinites (silicates lamellaires (phyllosilicates) tels que la lizardite, l'antigorite, la chrysolite). Ces roches peuvent être entrainées par subduction et, au fur et à mesure que la pression et la température augmente, subir des décompositions et des transformations de phases tout en conservant un taux d'hydratation significatif (Schmidt & Poli, 1998). Récemment, Pearson et ses collaborateurs ont trouvé au sein d'un cristal de diamant, un cristal de ringwoodite (polymorphe de l'olivine présent dans la zone de transition) contenant 2.5 % en poids d'eau sous forme de groupement hydroxyle (Pearson *et al.*, 2014). Sachant que la zone de transition est composée d'environ 60 % de ringwoodite, elle pourrait contenir autant d'eau que tous les océans réunis. Par ailleurs, les propriétés mécaniques des roches hydratées sont fortement réduites par la présence des groupements hydroxyles. En effet, Chen *et al.* (1998) ont montré que les contraintes déviatoriques appliquées sur des polycristaux d'olivine, de wadsleyite et de ringwoodite, diminuent lorsque ces trois polymorphes sont hydratés. Cette étude a été conduite pour différentes températures, à 10 GPa pour l'olivine et la wadsleyite, et 20 GPa pour la ringwoodite. L'adoucissement est marqué pour l'olivine à 25 et 400 °C, à 600 °C pour la wadsleyite et à 1000 °C pour la ringwoodite.

La violence des séismes est considérable mais certains peuvent être d'une grande lenteur et peuvent avoir lieu sans la moindre secousse, sur des dizaines d'heures si ce n'est plusieurs mois. C'est le cas du séisme du volcan Kilauea, à Hawaï, en 2000 qui a s'est produit en 36 h (Segall *et al.*, 2006) ou bien encore le séisme de Guerrero, à Mexico, en 2001 qui a duré 6 à 7 mois (Kostoglodov *et al.*, 2003). L'initiation de la subduction et la présence des

tremblements de terre silencieux peuvent s'expliquer par la faible viscosité des phases hydratées présentes à proximité de la surface : les serpentines (Amiguet *et al.*, 2012 ; Hilairet *et al.*, 2007 ; Gasc *et al.*, 2017). Mais qu'advient-il de ces phyllosilicates au cours de la subduction ? Ulmer & Trommsdorff (1995) ont montré qu'au-delà de 200 km de profondeur, ces phases hydratées ne sont plus stables. Ringwood & Major (1967) ont caractérisé des silicates magnésiens hydratés denses (DHMS) dans le système ternaire MgO-SiO_2-H_2O, thermodynamiquement stables pour des pressions plus élevées que le domaine de stabilité des serpentines. La figure 1, tirée de l'article de Nishi *et al.* (2014), présente les différentes DHMS dans l'ordre d'apparition à profondeur croissante (phases A, B, D et H), pour les subductions rapides (l'équilibre thermodynamique n'est pas atteint au cours de leur enfouissement, ces couches de subduction sont donc plus froides que leurs milieux environnants). Il nous faut caractériser les mécanismes fondamentaux de déformation plastique des DHMS pour connaître les propriétés rhéologiques des phases hydratées au-delà de 200km de profondeur. Comme nous l'avons indiqué précédemment, la MET est l'outil le plus adapté pour caractériser les défauts cristallins engendrés par déformation plastique (les dislocations) et remonter ainsi aux mécanismes fondamentaux de plasticité.

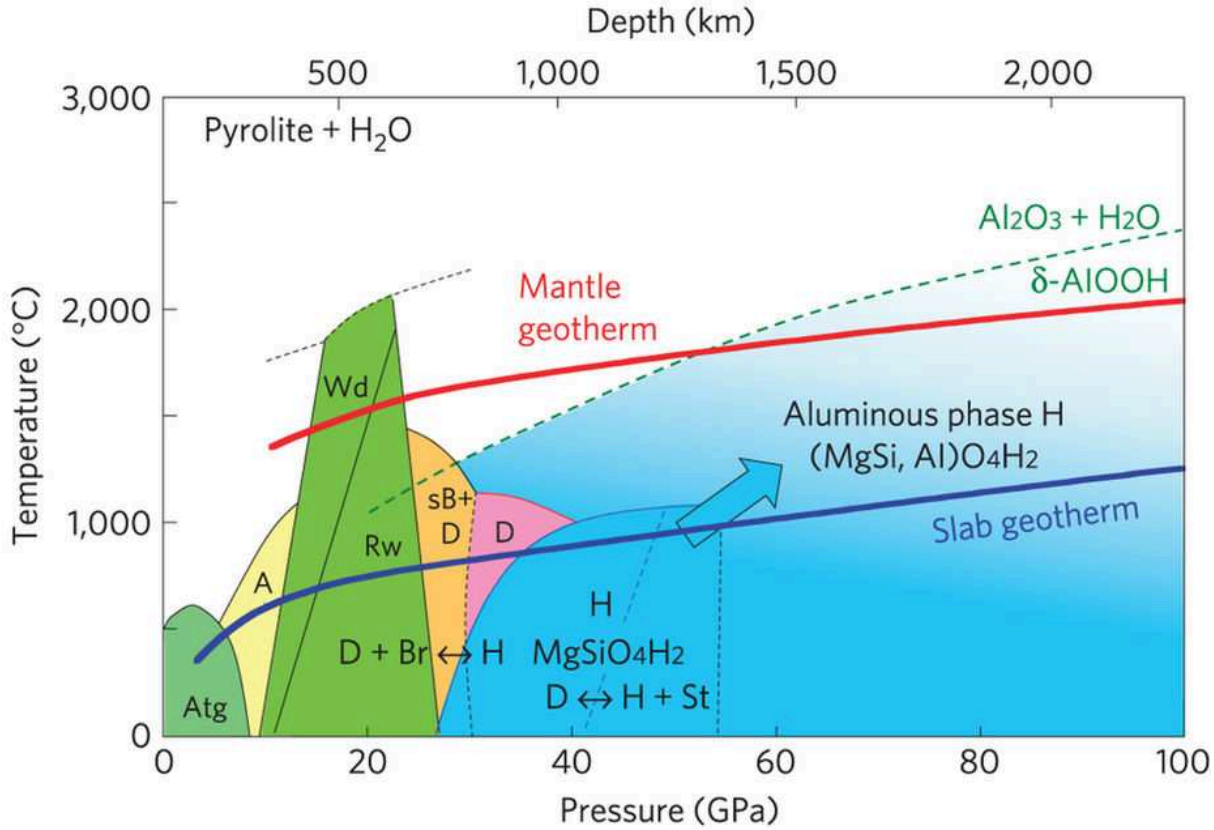

Figure 1 : *Répartition des DHMS dans les zones de subductions froides : Les domaines colorés représentent les régions où l'eau est incorporée dans les phases de hautes pressions. Le géotherme du manteau est en trait épais rouge et celui des plaques de subduction froide est en trait épais bleu. Atg. pour antigorite (serpentine) ; A pour Phase A (DHMS) ; Wd. pour wadsleyite ; Rw. pour ringwoodite ; sB pour superhydrous B (DHMS) ; Br. pour brucite ; D pour phase D (DHMS) ; et H pour phase H (DHMS). L'aluminous phase H est une solution solide entre la phase H et la phase δ-AlOOH. Figure tirée de Nishi et al. (2014).*

I-1-1 Etude de la phase A, première DHMS à apparaître dans les zones de subduction froide

Le premier article présenté dans ce mémoire porte sur l'étude des microstructures de dislocations de la première DHMS qui apparait dans les zones de subduction des plaques froides. Cette étude est également un défi technique de par l'instabilité de cette phase sous le faisceau d'électrons (dans des conditions conventionnelles d'analyses MET, 5 secondes suffisent pour amorphiser les zones d'intérêt). Avant toutes tentatives de caractérisation MET, nous avons dû trouver les meilleures conditions expérimentales pour préserver cette phase. Pour y parvenir, toutes les possibilités à notre disposition ont été mises en œuvre.

I-1-1-a Méthodes de préservation des DHMS en cours de caractérisations MET

D'un point de vue général, en MET, la présence d'un défaut (une dislocation par exemple) crée un champ de déplacement $\boldsymbol{R}$ dans la lame mince. Ce champ modifie les conditions de diffraction localement (au voisinage du cœur de la dislocation). En d'autres termes, les dislocations sont en contraste lorsque l'image est obtenue avec les électrons diffractés par les plans (hkl) affectés par le champ de déplacement (c'est-à-dire lorsque $\boldsymbol{g_{(hkl)}}.\boldsymbol{R} \neq 0$, où $\boldsymbol{g_{(hkl)}}$ est le vecteur diffractant des plans réticulaires (hkl)). En élasticité isotrope, au point M de coordonnées polaires (r,ϕ), le vecteur déplacement se met sous la forme : $\boldsymbol{R} = \frac{1}{2\pi} \cdot \left[\boldsymbol{b}\phi + \boldsymbol{b_{coin}} \frac{\sin(2\phi)}{4(1-\nu)} + \boldsymbol{b} \wedge \boldsymbol{u} \left[\frac{1-2\nu}{2(1-\nu)} ln(r) + \frac{\cos(2\phi)}{4(1-\nu)}\right]\right]$ où $\boldsymbol{b}$ est le vecteurs de Burgers, $\boldsymbol{b_{coin}}$ la composante coin du vecteur de Burgers, ν le coefficient de Poisson et $\boldsymbol{u}$ le vecteur ligne. Pour des dislocations vis, le vecteur déplacement se met sous la forme $\boldsymbol{R} = \boldsymbol{b_{vis}}\phi/2\pi$. Donc si $\boldsymbol{g_{(hkl)}}.\boldsymbol{b} = 0$, les dislocations vis sont hors contraste. Pour des dislocations coin, le vecteur déplacement se met sous une forme plus compliquée : $\boldsymbol{R} = \frac{1}{2\pi} \cdot \left[\boldsymbol{b_{coin}} \left[\phi + \frac{\sin(2\phi)}{4(1-\nu)}\right] + \boldsymbol{b_{coin}} \wedge \boldsymbol{u} \left[\frac{1-2\nu}{2(1-\nu)} ln(r) + \frac{\cos(2\phi)}{4(1-\nu)}\right]\right]$. Donc si $\boldsymbol{g_{(hkl)}}.\boldsymbol{b} = 0$ et $\boldsymbol{g_{(hkl)}}.\ \boldsymbol{b}\wedge\boldsymbol{u} = 0$, les dislocations coins sont hors contrastes (il apparaît un contraste résiduel lorsque la condition $\boldsymbol{g_{(hkl)}}.\ \boldsymbol{b}\wedge\boldsymbol{u} = 0$ n'est pas respectée). Afin que les analyses MET des dislocations soient rigoureuses, les conditions dynamiques (multiples diffractions de faisceaux d'électrons de fortes intensités) doivent être limitées au maximum. Pour y parvenir, nous devons nous mettre en conditions de deux ondes (faisceau transmis et faisceau diffracté) en sélectionnant le vecteur diffractant $\boldsymbol{g_{(hkl)}}$ souhaité, avec un grand écart à Bragg $\boldsymbol{s}$ (voir figure 2) pour réduire son intensité. Ces conditions permettent d'obtenir un contraste fin des dislocations, non parasité par le contraste d'autres faisceaux diffractés. Concrètement, seuls les plans atomiques les plus proches des cœurs des dislocations considérées sont diffractés (voir figure 2). Ces conditions sont communément appelées Weak-Beam Dark-Field (WBDF), ou en français faisceaux faibles en champ noir (Cockayne *et al.*, 1969, Cockayne, 1973). L'intensité des dislocations est alors proportionnelle au produit $\boldsymbol{g_{(hkl)}}.\boldsymbol{b}$ et aux facteurs de structure (FS) élevé au carré, du vecteur diffractant considéré.

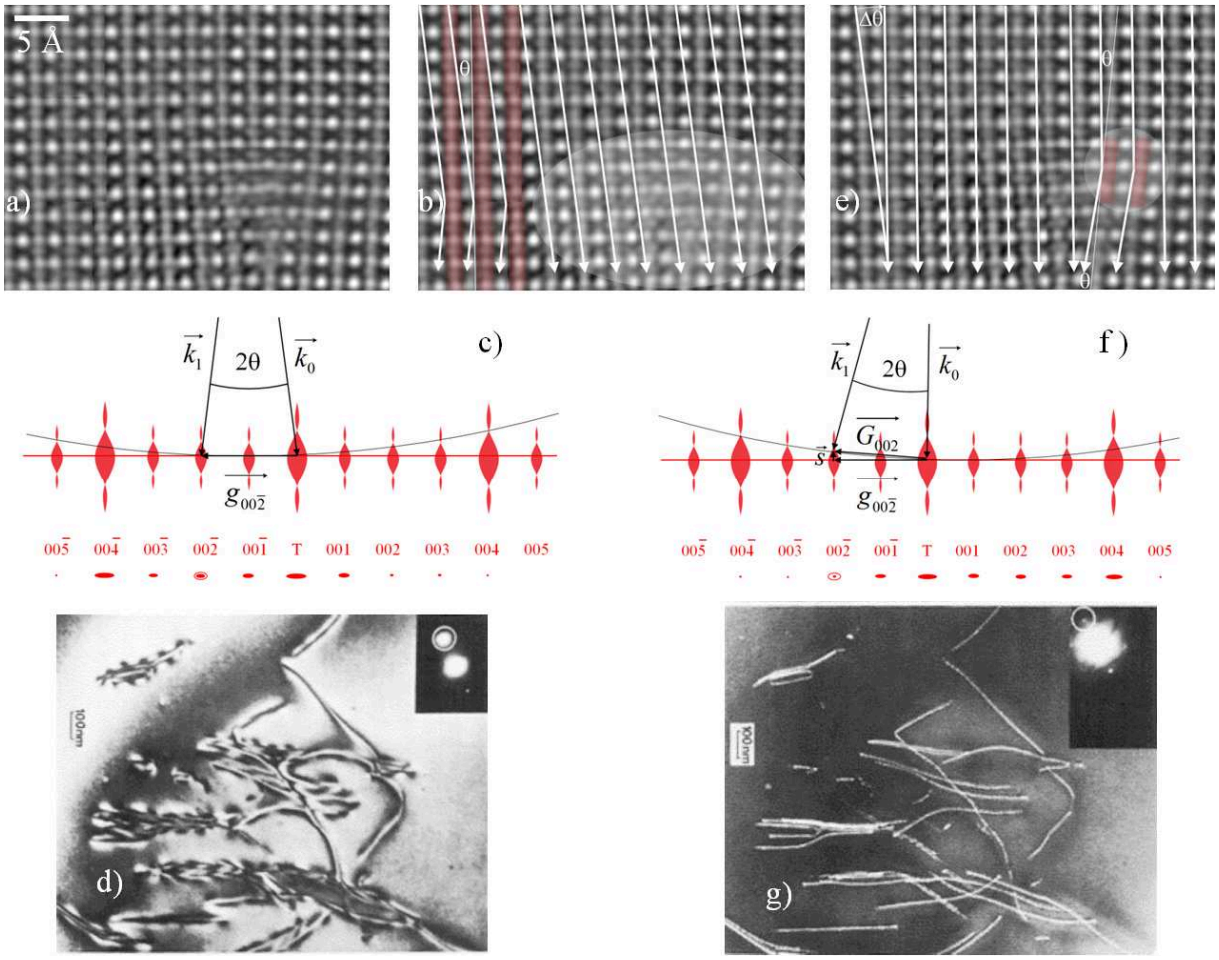

Figure 2 : *Contraste des dislocations : a) Photo haute résolution d'une dislocation coin dans $SrTiO_3$ (Jia et al., 2005). b) Faisceau d'électrons orienté suivant l'angle de Bragg θ : les électrons sont diffractés par tous les plans du cristal (en rouge sur le schéma) sauf à proximité du cœur de la dislocation (grand ovale blanc). c) Modèle d'intersection de la sphère d'Ewald avec le réseau cristallin correspondant à l'orientation décrite en b) $\overrightarrow{k_1} = \overrightarrow{k_0} + \overrightarrow{g_{00\bar{2}}}$. d) Micrographie d'une population de dislocations dans le Si (Ray & Cockayne, 1971) dans des conditions équivalentes à b) et c). Les dislocations sont épaisses (liées à la taille de l'ovale blanc en b)) et noires (le diaphragme objectif ne sélectionne pas les électrons à proximité des cœurs de dislocation). e) Faisceau d'électrons orienté avec un écart à Bragg de $\Delta\theta$: Les électrons sont diffractés uniquement par les plans les plus distordus par le cœur de la dislocation (petit disque blanc), seuls quelques plans diffractent à proximité du cœur de la dislocation (en rouge sur le schéma). f) Modèle d'intersection de la sphère d'Ewald avec le réseau cristallin correspondant à l'orientation décrite en e), l'écart à Bragg est quantifié par le vecteur **s**, avec $\overrightarrow{G_{00\bar{2}}} = \overrightarrow{g_{00\bar{2}}} + \vec{s}$. g) Micrographie d'une population de dislocations dans le Si (Ray & Cockayne, 1971) dans des conditions équivalentes à e) et f). Les dislocations sont fines (liées à la taille de petit disque blanc en e)) et blanches (le diaphragme objectif ne sélectionne que les électrons les plus proches des cœurs de dislocation).*

La précession électronique (Vincent & Midgley, 1994) a été d'une grande utilité pour optimiser la qualité des micrographies WBDF. Afin d'obtenir les meilleurs contrastes de dislocations dans le réseau direct, il est nécessaire d'identifier et d'utiliser les vecteurs diffractant dont les FS sont les plus élevés, dans le réseau réciproque. La précession à grand angle (3 ° généralement) permet d'intégrer les courbes de réflexion (ou rocking curve en anglais) des taches diffractées. Dans ces conditions, les intensités des taches sont proches des FS élevées au carré et les clichés de diffraction ainsi obtenus sont fortement liés aux clichés théoriques obtenus avec le modèle cinématique (Morniroli *et al.*, 1994). Nous avons donc

choisi, grâce à cette méthode, les vecteurs diffractant les plus à même de nous donner les micrographies de qualité tout en facilitant la détermination des vecteurs de Burgers.

L'utilisation d'un porte objet froid, d'un diaphragme condenseur de petite taille (100 µm de diamètre), d'une faible taille de sonde (300 nm de diamètre) et d'une tension d'accélération de 300 kV (pour limiter le temps de présence des électrons dans l'échantillon), nous ont permis d'augmenter le temps d'analyse de 5 secondes à 3 minutes. Néanmoins, ce temps reste insuffisant pour effectuer des caractérisations rigoureuses et en nombre satisfaisant. Contrairement aux micrographies enregistrées sur caméra CCD, les négatifs argentiques donnent accès à de larges domaines associés à une dynamique inégalable et une résolution spatiale ultime (à la molécule de chlorure d'argent près). Nous avons donc décidé ponctuellement d'avoir recours à cette technique d'acquisition qui n'est plus utilisée en routine actuellement. Néanmoins, ces conditions nous obligent la plupart du temps à travailler en aveugle. Il a donc fallu choisir les zones et les orientations les plus adaptées (régions fines proche d'axes de zone à faibles indices de Miller) et travailler le plus rapidement possible sans négliger la qualité.

Nous avons rappelé qu'en conditions WBDF, le contraste des dislocations est proportionnel au produit $\boldsymbol{g_{(hkl)}.b}$. Il faut donc suffisamment de clichés (obtenus pour différents vecteurs diffractant $\boldsymbol{g_{(hkl)}}$ indépendants) et suffisamment de conditions d'extinctions (au moins deux) pour déterminer les directions des vecteurs de Burgers $\boldsymbol{b}$. Par ailleurs, l'interaction électrons/matière engendre dans le cristal parfait des contrastes oscillants qui, en conditions WBDF (selon le vecteur diffractant $\boldsymbol{g_{(hkl)}}$), suivent la relation :

$$I_{g_{(hkl)}} = \left(\frac{\xi_{g_{(hkl)}effective}}{\xi_{g_{(hkl)}}}\right)^2 . \sin^2\left(\frac{\pi.e}{\xi_{g_{(hkl)}effective}}\right) = 1 - I_0 \qquad (1)$$

où $I_{g_{(hkl)}}$ est l'intensité du champ sombre, I_0 l'intensité du champ clair, e l'épaisseur de la lame mince, $\xi_{g_{(hkl)}}$ la distance d'extinction, $\xi_{g_{(hkl)}effective} = \xi_{g_{(hkl)}} / \sqrt{1 + \left(s.\xi_{g_{(hkl)}}\right)^2}$ la distance d'extinction effective et s l'écart à Bragg (voir figure 2). Cette expression montre que le contraste oscille avec une période de $\xi_{g_{(hkl)}effective}$ (cette période diminue lorsque l'écart à Bragg augmente). Il apparait donc, sur les clichés WBDF, des franges d'égales épaisseurs qui, comme pour les courbes de niveaux des cartes IGN, renseignent sur les épaisseurs locales des lames minces étudiées. Ishida et ses collaborateurs (1980) ont noté que ces franges s'arrêtent aux extrémités des dislocations en contraste et le nombre de franges interrompues est directement relié aux produits $\boldsymbol{g_{(hkl)}.b}$ (voir figure 3). Cette technique permet de s'affranchir du problème de contraste résiduel des dislocations non vis (si le produit $\boldsymbol{g_{(hkl)}.b}$ est nul alors aucune frange d'égale épaisseur n'est interrompue). Finalement, trois clichés WBDF de vecteurs diffractant indépendants, avec des écarts à Bragg raisonnablement grands pour observer clairement ces interruptions de franges, sont suffisants pour résoudre le système qui donnera accès aux coordonnées des vecteurs de Burgers, c'est-à-dire aux directions mais aussi aux normes des vecteurs de Burgers. L'utilisation de la technique des franges d'égales épaisseurs (Ishida *et al.*, 1980 ; Miyajima & Walte, 2009) permet donc de réduire drastiquement le nombre d'acquisitions de clichés WBDF et par conséquent la dose globale.

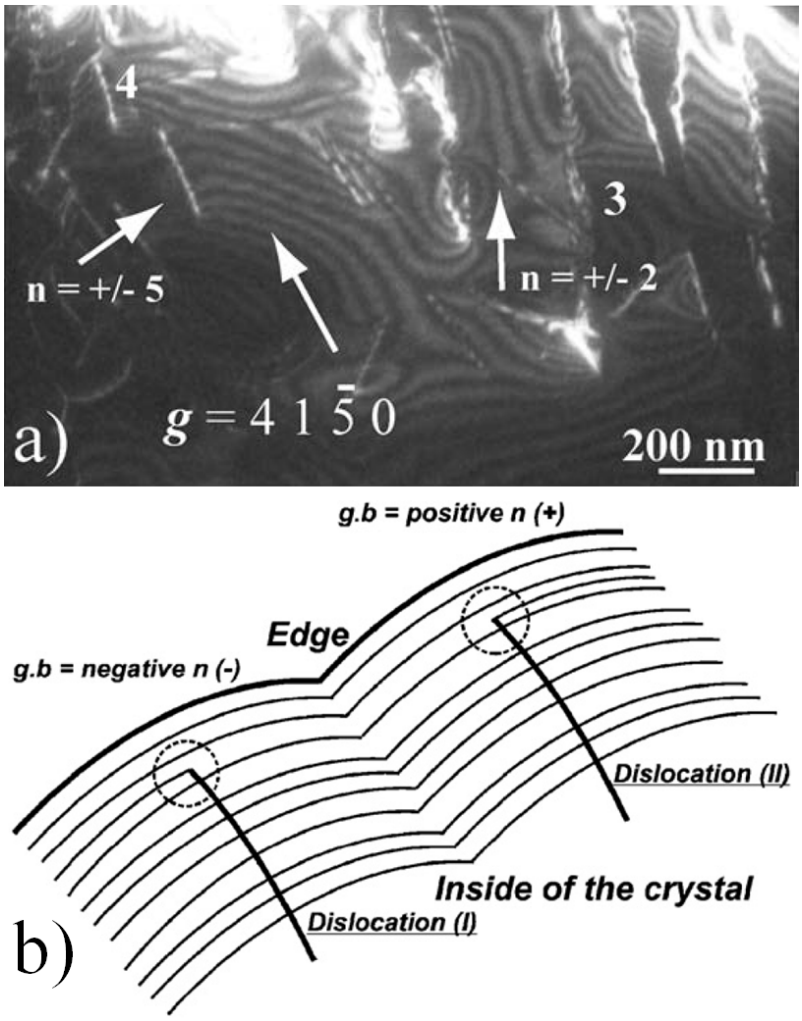

Figure 3 : *Technique des franges d'égales épaisseurs : a) Exemple de deux familles de dislocations (nommées « 3 » et « 4 » dans l'article de Mussi et al. (2012)) dont les vecteurs de Burgers vérifient* $\overrightarrow{g_{(41\bar{5}0)}}.\overrightarrow{b_3} = \pm 2$ *et* $\overrightarrow{g_{(41\bar{5}0)}}.\overrightarrow{b_4} = \pm 5$ *dans la phase A ; b) Description de la technique des franges d'égales épaisseurs d'après Miyajima et al. (2009).*

I-1-1-b Systèmes de glissement dans la phase A

Grâce à une collaboration de longue date avec le Bayrerisches GeoInstitut de Bayreuth (initiée en 1998), Patrick Cordier a pu synthétiser deux échantillons de phase A dans des presses multi-enclumes, à partir d'un mélange d'oxydes purs. Ces échantillons ont ensuite été déformés dans le domaine de stabilité de la phase A, sous contrainte déviatorique de compression, à 400 et 700 °C.

Les analyses MET ont mis en évidence des dislocations parfaites et ont permis de déterminer les systèmes de glissement mis en jeu dans la phase A à 700 °C. La phase A, de structure hexagonale, se déforme par le glissement de dislocations <a> dans le plan de base et <c+a> dans les plans pyramidaux. L'échantillon déformé à plus basse température présente des dislocations dissociées qui nous invitent à penser que les cœurs de dislocations sont étendus dans les plans de base, prismatique et pyramidaux. En effet, lorsque les températures sont faibles, les contraintes appliquées pour déformer la phase A sont suffisamment élevées pour augmenter les distances de dissociation entre dislocations partielles et ainsi mettre en

évidence leur plans de glissement par WBDF. Ce n'est plus le cas à haute température où les contraintes appliquées sont trop faibles pour séparer les dislocations partielles au-delà de la résolution spatiale en WBDF (quelques nanomètres). Néanmoins ces cœurs étendus imposent le choix des plans de glissement.

La structure cristalline des phyllosilicates, comme l'antigorite ($(Mg,Fe)_3Si_2O_5(OH)_4$), est constituée de couches de tétraèdres de SiO_4 et d'octaèdres de $(Mg,Fe)O_6$ (Wang *et al.*, 2015). La structure en feuillets des serpentines entraine un glissement fortement anisotrope principalement par le cisaillement de ces couches. Puisque les systèmes de glissement de la phase A sont bien plus complexes que ceux des phyllosilicates, les propriétés mécaniques de cette phase devraient s'éloigner de celles des serpentines.

A cet égard, Gouriet et ses collaborateurs (2015) ont déterminé les systèmes de glissement les plus probables mis en jeu dans la phase A par l'étude de défauts d'empilements généralisés associée au modèle de Peierls–Nabarro–Galerkin (Denoual, 2007) ; et par l'analyse, en parallèle, des figures de pôles obtenues après déformation D-DIA comparées à un modèle auto-cohérent viscoplastique (VPSC). Pour entreprendre des analyses de défauts d'empilements généralisés, il est nécessaire de créer des « super mailles ». Dans le cas de la phase A, ces « super mailles » sont très grandes (116 atomes pour modéliser les plans prismatiques, à titre d'exemple), or les simulations *ab initio* sont gourmandes en temps de calcul (l'étude des défauts d'empilements généralisés des plans pyramidaux n'a pu être effectuée à cet effet). Les caractérisations MET ont été d'une grande utilité pour sélectionner les plans à modéliser en *ab initio*, elles ont permis de gagner un de temps de calcul précieux. Par ailleurs, ces caractérisations expérimentales ont révélé la présence de dislocations partielles multiples et, grâce à la technique des franges d'égales épaisseurs, le vecteur de Burgers d'une dislocation partielle a pu être identifié. Ces informations ont permis de valider les calculs des cœurs de dislocations. Les systèmes de glissement caractérisés par MET ont également été retrouvés au cours des analyses VPSC ce qui, là aussi, a permis d'authentifier les résultats d'orientations cristallines préférentielles. Ces travaux ont vérifié que les propriétés d'accommodation des grandes déformations des serpentines ne se poursuivent pas au-delà de 200 km de profondeur.

L'étude des défauts cristallins produits par la déformation plastique de la phase A, en conditions de pression et de température de subduction froide, a été concluante. Puisque les presses multi-enclumes actuelles permettent de solliciter des échantillons dans la zone de transition, à la limite du manteau inférieur ; nous nous sommes intéressés à l'étude de la plasticité par MET de la première DHMS stable dans le manteau inférieur, la phase superhydrousB.

I-1-2 Etude des microstructures de dislocations dans la phase superhydrousB

Dans le prolongement de l'étude des systèmes de glissement de la phase A par MET, nous avons décidé d'analyser les défauts cristallins engendrés par la déformation plastique de la superhydrousB, DHMS de structure orthorhombique (a ≈ 5.1 Å, b ≈ 14.0 Å et c ≈ 8.7 Å), thermodynamiquement stable à la frontière de la zone de transition et du manteau inférieur.

Patrick Cordier a synthétisé la superhydrousB au Bayrerisches GeoInstitut pour des conditions de pression et température plus élevées que celles utilisées pour la phase A.

Comme précédemment, la démarche d'analyse WBDF à faible dose a été menée, mais en y associant, cette fois-ci, des analyses de faisceaux convergents diffractés à grands angles (LACBED). Cette technique donne accès au réseau réciproque par le biais des lignes de Bragg, mais également au réseau direct par l'observation de l'image défocalisée des défauts présents dans la lame mince (Tanaka *et al.*, 1980) qui se superpose au cliché de lignes. Les lignes de Bragg vont se subdiviser, en présence d'une dislocation. Comme pour la technique des franges d'égales épaisseurs (Ishida *et al.*, 1980), le nombre de subdivisions correspond au produit $\boldsymbol{g_{(hkl)}.b}$ (Cherns & Preston, 1986; Cherns & Morniroli, 1994; and Morniroli, 2004). L'obtention de clichés LACBED s'effectue en déplaçant l'échantillon loin de la position eucentrique. La grande convergence du faisceau d'électron associée à l'éloignement de l'échantillon vis-à-vis de sa position eucentrique, augmente la surface illuminée et par conséquent réduit la dose. L'échantillon est donc préservé des irradiations électroniques (Cordier *et al.*, 1995 ; Kedjar *et al.*, 2010). Même si cette technique pêche sur la localisation des dislocations (dont la visibilité est parfois assez médiocre), elle est d'une grande efficacité pour la caractérisation des vecteurs de Burgers. En effet, un unique cliché LACBED peut suffire pour caractériser de manière absolue les coordonnées du vecteur de Burgers des dislocations considérées. La figure 4 donne un exemple d'une caractérisation par LACBED d'un vecteur de Burgers $[10\bar{1}]$ d'une dislocation dans la superhydrousB.

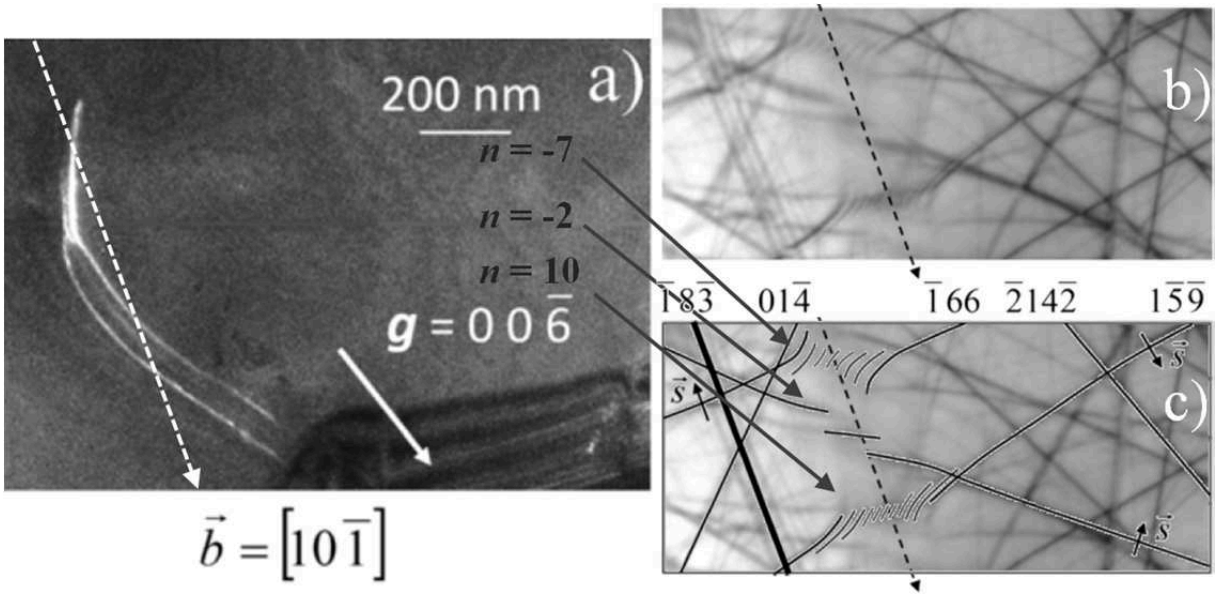

Figure 4 : *Caractérisation d'un vecteur de Burgers dans la superhydrousB par LACBED : (a) Micrographie WBDF obtenue avec le vecteur diffractant* $00\bar{6}$ *où une dislocation parfaite en cours de dissociation est en contraste ; (b) cliché LACBED correspondant, où trois subdivisions marquées de lignes de Bragg sont apparentes ; (c) Retraçage du cliché (b) où les lignes de Bragg sont indexées. Nous en déduisons le vecteur de*

Burgers $[10\bar{1}]$ *à partir de cet unique cliché. Nous pouvons noter que la résolution du LACBED n'est pas suffisante pour discerner les dislocations partielles (Mussi et al., 2013).*

Les analyses MET ont principalement révélé du glissement dans le plan (010) ainsi que certaines dislocations de norme de vecteurs de Burgers supérieure à 10 Å (voir figure 4). La présence de ces grands vecteurs de Burgers doit certainement provenir de la procédure spécifique de déformation par presse multi-enclumes (Cordier & Rubie, 2001). L'échantillon est tout d'abord pressurisé à température ambiante (avec une composante déviatorique de compression) ce qui génère de fortes contraintes ; puis il est chauffé progressivement jusqu'à la température souhaitée, ce qui permet d'atteindre un niveau de contrainte suffisamment bas pour faire circuler facilement les dislocations ; puis l'échantillon est trempé et enfin dépressurisé (Thurel *et al.*, 2003). Les systèmes de glissement qui font intervenir ces grands vecteurs de Burgers doivent probablement apparaître entre la fin de la première étape et le début de la deuxième étape, c'est-à-dire lorsque les contraintes sont les plus importantes.

Puisque le plan (010) est principalement sollicité au cours de la déformation plastique de la superhydrousB, cette phase devrait montrer une forte orientation cristallographique préférentielle. Par conséquent, au cours de la subduction des plaques froides, la superhydrousB devrait être fortement texturée et présenter une anisotropie élastique et donc sismique marquée.

Eu égard aux difficultés rencontrées pour imager les dislocations dans les DHMS, l'équipe plasticité reste actuellement la seule au monde à avoir entrepris ces caractérisations. Fort de notre expérience dans ce domaine, des études plus poussées pourront être conduites sur des minéraux plus sensibles encore comme par exemple la phase H et, en dehors des DHMS, l'akimotoite.

Références :

Amiguet, E., Reynard, B., Caracas, R., Van de Moortèle, B., Hilairet, N., Wang, Y. (2012): Creep of phyllosilicates at the onset of plate tectonics. *Earth Planet. Sci. Lett.*, **345-348**, 142-150.

Chen, J.H., Inoue, T., Weidner, D.J., Wu Y.J., Vaughan, M.T. (1998): Strength and water weakening of mantle minerals, olivine, wadsleyite and ringwoodite. *Geophys. Res. Lett.*, **25**, 575-578.

Cherns, D. & Preston, A.R. (1986): Convergent-beam diffraction of crystal defects. In Proceedings Eleventh International Congress on Electron Microscopy, Kyoto, 721.

Cherns, D. & Morniroli, J.P. (1994): Analysis of partial and Stair-Rod dislocations by large angle convergent beam electron diffraction. *Ultramicroscopy*, **53**, 2, 167-180.

Cordier, P., Morniroli, J.P., Cherns, D. (1995): Characterization of crystal defects in quartz by large-angle convergent-beam electron diffraction. *Philos. Mag. A*, **72**, 1421-1430.

Cordier, P. & Rubie, D.C. (2001): Plastic deformation of minerals under extreme pressure using a multianvil apparatus. *Mater. Sci. Eng., A*, **309-310**, 38-43.

Denoual, C. (2007): Modeling dislocation by coupling Peierls–Nabarro and element-free Galerkin methods. *Comput. Methods Appl. Mech. Engrg.*, **196**, 1915-1923.

Gasc, J., Hilairet, N., Yu, T., Ferrand, T., Schubnel, A., Wanga, Y. (2017): Faulting of natural serpentinite: Implications for intermediate-depth seismicity. *Earth Planet. Sci. Lett.*, **474**, 138-147.

Gouriet, K., Hilairet, N., Amiguet, E., Bolfan-Casanova, N., Wang, Y., Reynard, B., Cordier, P. (2015): Plasticity of the dense hydrous magnesium silicate phase A at subduction zones conditions. *Phys. Earth Planet. Inter.*, **248**, 1-11.

Hilairet, N., Reynard, B., Wang, Y.B., Daniel, I., Merkel, S., Nishiyama, N., Petitgirard, S. (2007): High-pressure creep of serpentine, interseismic deformation, and initiation of subduction. *Science*, **318**, 1910-1913.

Hirsch, P.B., Horne, R.W., Whelan, M.J. (1956): Direct observations of the arrangement and motion of dislocations in aluminium, *Philos. Mag.*, **86**, 4553-4572

Ishida, Y., Ishida, H., Kohra, K., Ichinose, H. (1980): Determination of the Burgers vector of a dislocation by weak-beam imaging in a HVEM. *Philos. Mag. A*, **42**, 453-462.

Jia, C.L., Thust, A., Urban, K. (2005): Atomic-Scale Analysis of the Oxygen Configuration at a $SrTiO_3$ Dislocation Core. *Phys. Rev. Lett.*, **95**, 225506.

Kedjar, B., Thilly, L., Demenet, J.L., Rabier, J. (2010): Plasticity of indium antimonide between -176 °C and 400 °C under hydrostatic pressure. Part II: Microscopic aspects of the deformation. *Acta Mater.*, **58**, 1426-1440.

Kostoglodov, V., Singh, S.K., Santiago, J.A., Franco, S.I., Larson, K.M., Lowry, A.R., Bilham, R. (2003): A large silent earthquake in the Guerrero seismic gap, Mexico. *Geophys. Res. Lett.*, **30**, 1807.

Menter, J.W. (1956): The direct study by electron microscopy of crystal lattices and their imperfections. *Philos. Mag.*, **86**, 4529-4552.

Miyajima, N. & Walte, N. (2009): Burgers vector determination in deformed perovskite and post-perovskite of $CaIrO_3$ using thickness fringes in weak-beam dark-field images. *Ultramicroscopy*, **109**, 683–692.

Morniroli, J.P. (2004): Large-angle convergent-beam electron diffraction applications to crystal defects, CRC Press, Boca Raton, FL, 376 p.

Morniroli, J.P., Vankieken, D., Winter, L. (1994): Electron Diffraction. Dedicated Software to Kinematicaly Simulate CBED Patterns (USTL, Lille).

Mussi, A., Cordier, P., Frost, D.J. (2012): Crystal defects in dense hydrous magnesium silicate phase A deformed at high pressure: characterization by transmission electron microscopy, *Eur. J. Mineral.*, **24**, 429-438.

Mussi, A., Cordier, P., Frost, D.J. (2013): Transmission electron microscopy characterization of the dislocations and slip systems of the dense hydrous magnesium silicate superhydrous B. *Eur. J. Mineral.*, 25, 561-568.

Nishi, M., Irifune, T., Tsuchiya, J., Tange, Y., Nishihara, Y., Fujino, K., Higo, Y. (2014): Stability of hydrous silicate at high pressures and water transport to the deep lower mantle. *Nat. Geosci.*, **7**, 224-227.

Pearson, D.G., Brenker, F.E., Nestola, F., McNeill, J., Nasdala, L., Hutchison, M.T., Matveev, S., Mather, K., Silversmit, G., Schmitz, S., Vekemans B., Vincze, L. (2014): Hydrous mantle transition zone indicated by ringwoodite included within diamond. *Nature*, **507**, 221-224.

Ray, I.L.F. & Cokayne, D.J.H. (1971): The dissociation of dislocations in silicon**.** *Proc. R. Soc. Lond. A*, **325,** 543-554.

Ringwood, A.E. & Major, A. (1967): High pressure reconnaissance investigations in system Mg_2SiO_4-MgO-H_2O. *Earth Planet. Sci. Lett.*, **2**, 130-133.

Schmidt, M.W. & Poli, S. (1998): Experimentally based water budgets for dehydrating slabs and consequences for arc magma generation. *Earth Planet. Sci. Lett.*, **163**, 361-379.

Segall, P., Desmarais, E.K., Shelly, D., Miklius, A., Cervelli, P. (2006): Earthquakes triggered by silent slip events on Kīlauea volcano, Hawaii. *Nature*, **442**, 71-74.

Tanaka, M., Ueno, K., Harada, Y. (1980): Large-angle convergent beam electron-diffraction. *J. Electron Microsc.*, **29**, 4, 408-412.

Thurel, E. & Cordier, P. (2003): Plastic deformation of wadsleyite: I. High-pressure deformation in compression. *Phys. Chem. Minerals*, **30**, 256-266.

Ulmer, P. & Trommsdorff, V. (1995): Serpentine stability to mantle depths and subduction-related magmatism. *Science*, **268**, 858-861.

Vincent, R. & Midgley, P.A. (1994): Double conical beam-rocking system for measurement of integrated electron diffraction intensities. *Ultramicroscopy*, **53**, 271-282.

Wang, A., Freemana, J.J., Jolliffa, B.L. (2015): Understanding the Raman spectral features of phyllosilicates. *J. Raman Spectrosc.*, **46**, 829-845.

Publications concernées par ces études (les travaux précédés d'un astérisque sont reproduits à la fin de ce chapitre) :

Mussi, A., Cordier, P., Mainprice, D., Frost, D.J. (2010): Transmission electron microscopy characterization of dislocations and slip systems in K-lingunite: Implications for the seismic anisotropy of subducted crust, *Phys. Earth Planet. Inter.*, **182**, 50-58.

*Mussi, A., Cordier, P., Frost, D.J. (2012): Crystal defects in dense hydrous magnesium silicate phase A deformed at high pressure: characterization by transmission electron microscopy, *Eur. J. Mineral.*, **24**, 429-438.

*Mussi, A., Cordier, P., Frost, D.J. (2013): Transmission electron microscopy characterization of the dislocations and slip systems of the dense hydrous magnesium silicate superhydrous B, *Eur. J. Mineral.*, **25**, 561-568.

Crystal defects in dense hydrous magnesium silicate phase A deformed at high pressure: characterization by transmission electron microscopy

Alexandre MUSSI[1*], Patrick CORDIER[1,2] and Daniel J. FROST[2]

[1]Unité Matériaux et Transformations, UMR 8207 CNRS-Université Lille1,
F-59655 Villeneuve d'Ascq, France
[2]Bayerisches Geoinstitut, Universität Bayreuth, Germany.

Cite as:
A. Mussi, P. Cordier & D.J. Frost (2012) Crystal defects in dense hydrous magnesium silicate phase A deformed at high pressure: characterization by transmission electron microscopy. European Journal of Mineralogy, 24, 429-438, https://doi.org/10.1127/0935-1221/2011/0024-2126

Abstract

Dense hydrous magnesium silicate (DHMS) Phase A has been deformed at 11 GPa, 700 and 400°C in the multianvil apparatus. Transmission electron microscopy (TEM) characterizations using the weak-beam dark-field (WBDF) technique, have shown that, at 700°C, two different types of perfect dislocations are activated with $\frac{1}{3}\langle 2\bar{1}\bar{1}0\rangle$ and $\frac{1}{3}\langle 2\bar{1}\bar{1}3\rangle$ Burgers vectors. The $\frac{1}{3}\langle 2\bar{1}\bar{1}0\rangle$ dislocations glide in the basal plane, but for $\frac{1}{3}\langle 2\bar{1}\bar{1}3\rangle$ dislocations, no glide plane could be identified. At 400°C, dissociation of $\frac{1}{3}\langle 2\bar{1}\bar{1}0\rangle$ dislocations is observed in the basal plane. Furthermore, prismatic and pyramidal glide planes were identified, with dissociations in pyramidal planes, at this temperature. Ultimately, a growth reticular merohedral twin has been observed. The twin law results from a rotation of 180° around the $[1\bar{5}40]$ axis.

Keywords: DHMS, phase A, TEM, dislocations, glide plane, twin, dissociation.

[*]Corresponding author: alexandre.mussi@univ-lille1.fr

Introduction

At the surface of the Earth, most activity caused by plate tectonics and mantle convection concentrates at narrow active regions called subduction zones where slabs of oceanic lithosphere sink into the mantle. Subduction zones are also the loci where water, incorporated in ultramafic rocks after hydrothermal alteration, can be injected into the mantle (Schmidt & Poli, 1998). However, serpentine minerals are not stable beyond ≈200km depth (Ulmer & Trommsdorff, 1995) and the question of potential carriers for water into the deep mantle has been raised. In 1967, Ringwood & Major have shown the existence of some dense hydrous magnesium silicate (DHMS) phases in the MgO-SiO_2-H_2O system which can be stable at high pressure. In a subducting slab, phase A is the first post-serpentine phase and the phase A + enstatite assemblage is stable up to 13 GPa (Komabayashi & Omori, 2006). At mantle transition zone pressure, water is then carried by phase E and superhydrous phase B (Komabayashi & Omori, 2006).

The importance of these hydrous phases is not restricted to water storage. Phase transitions involving hydrous phases are thought to play a significant role in the generation of intermediate and deep earthquakes (Meade & Jeanloz, 1991; Yamasaki & Seno, 2003; Komabayashi et al., 2004; Omori et al., 2004). More recently, the low viscosity of serpentine has been shown to have a strong influence on the dynamics of subduction zones at shallow and intermediate depths by accommodating large deformations (Hilairet et al., 2007, Hilairet & Reynard, 2009). At greater depths, nothing is known about the rheological properties of hydrous phases. It is the aim of the present study to shed some light on the deformation mechanisms of one of these hydrous phases, phase A, starting by the characterization of the crystal defects in this structure.

$Mg_7Si_2O_8(OH)_6$ phase A (12 wt.% H_2O) is the primary breakdown product of antigorite under the P, T conditions of cold slabs (Komabayashi et al., 2005). The structure of phase A is hexagonal, space group $P6_3$, with a = 7.8603 Å and c = 9.5730 Å (Horiuchi et al., 1979). It consists of slightly distorted close-packed layers of oxygen atoms and hydroxyl groups repeating along the *c* axis in an ABCB sequence (Horiuchi et al., 1979). In this study, iron-free $Mg_7Si_2O_8(OH)_6$ phase A has been synthesized and deformed in a multianvil apparatus. Dislocations, slip systems and

growth twins have been characterized in recovered samples by transmission electron microscopy.

Experimental details

Synthesis and deformation

Phase A was synthesized and deformed in the multianvil apparatus at the Bayerisches Geoinstitut in a standard 18/11 assembly. For synthesis, a Pt cylindrical capsule of 12 mm^3 (2 mm in diameter and 3.8 mm long) was filled with a mixture of high purity oxides (MgO, SiO_2 quartz, brucite) as a starting material. Transformation was achieved at 11 GPa (nominal pressure) and 900°C with a heating cycle duration of 240 and 210 min (runs H3006 and S4871). The resulting material is composed of a mixture of phase A and enstatite, due to an excess in MgO. The recovered samples were end-polished and placed in a second high-pressure assembly designed to induce deviatoric stresses during compression (Cordier & Rubie, 2001). In this assembly, the specimen is placed between two alumina pistons. The deformation experiments were run at 11 GPa and 700°C for a duration of 45 min (run H3008) and 400°C for a duration of 60 min (run S4873).

Transmission Electron Microscopy

The specimens recovered after deformation were cut into two halves from which two TEM foils were prepared by mechanical polishing to a thickness of 20 µm. Since phase A is very sensitive to irradiation, electron transparency was reached by ion milling (in a Gatan® DuoMill™ Model 600) at liquid nitrogen temperature in order to minimize damage. A 15° incident ion beam and 4.5 kV accelerating voltage were used for the ion sputtering conditions. A thin carbon film was finally deposited on the thin foils.

The specimens were characterized at the TEM facility of the University of Lille. A Philips® CM30 microscope operated at 300 kV was used. As already mentioned, phase A is extremely sensitive to beam damage. TEM characterization could only be performed under conditions adjusted to slow down beam damage. We used a small condenser aperture (100 µm), a small spot size (300 nm), a low magnification (M = 3900×) and a Gatan® cold stage operated with liquid nitrogen (T ≈ -160°C near the thin foil).

Weak-beam dark-field (WBDF) characterizations were conducted using the conventional invisibility criterion $\boldsymbol{g}.\boldsymbol{b} = 0$ and with the thickness-fringe method (Ishida et al., 1980, Miyajima & Walte, 2009). This latter technique gives the $\boldsymbol{g}.\boldsymbol{b}$ product by counting the number and the orientation of thickness fringes terminating on the studied dislocation. The thickness-fringe method has the following advantages:

- Three independent $\boldsymbol{g}.\boldsymbol{b}$ conditions are necessary to obtain the Burgers vector without compulsory extinction conditions.
- The extinction conditions ($\boldsymbol{g}.\boldsymbol{b} = 0$) are sometimes affected by residual contrasts (edge components, anisotropic crystals, etc). This is not the case for the thickness fringe method.

Precession electron diffraction (Vincent & Midgley, 1994) was performed with a "Spinning Star" precession module from the Nanomegas company. This technique allows easy identification of phases and selection of high structure factor reflections for dislocation imaging and characterization.

Dislocation densities have been estimated using the method of Ham (1961) based on the superimposition of a periodic square network onto the TEM images. Counting the number of intersections between the dislocation lines and the network allows estimating the local dislocation density ρ using the relation:

$$\rho = \frac{2n}{L.t}$$

where n is the number of intersections, L is the total length of the network lines and t is the average thickness of the foil in the observed area. The thickness has been estimated by the Electron Energy Loss Spectroscopy (EELS) thickness map method (Meltzman et al., 2009).

Results

Dislocation Burgers vectors and slip planes in phase A, deformed at 700°C

Dislocations are observed in most of the grains of phase A; only the smallest ones (i.e. below 2 µm) appear to be free from dislocations. The average grain size is approximately 50 ± 10 µm and the dislocation densities in all these grains are more or less equivalent (approximately 10^{13} m^{-2} as measured with the Ham method (1961)). Twelve grains have been characterized in detail in the present study.

Generally, dislocations are entangled; only few isolated dislocations have been noticed, which complicates their analyses. Some sub-grain boundaries have been seen, but their occurrence is not pervasive (Figure 1).

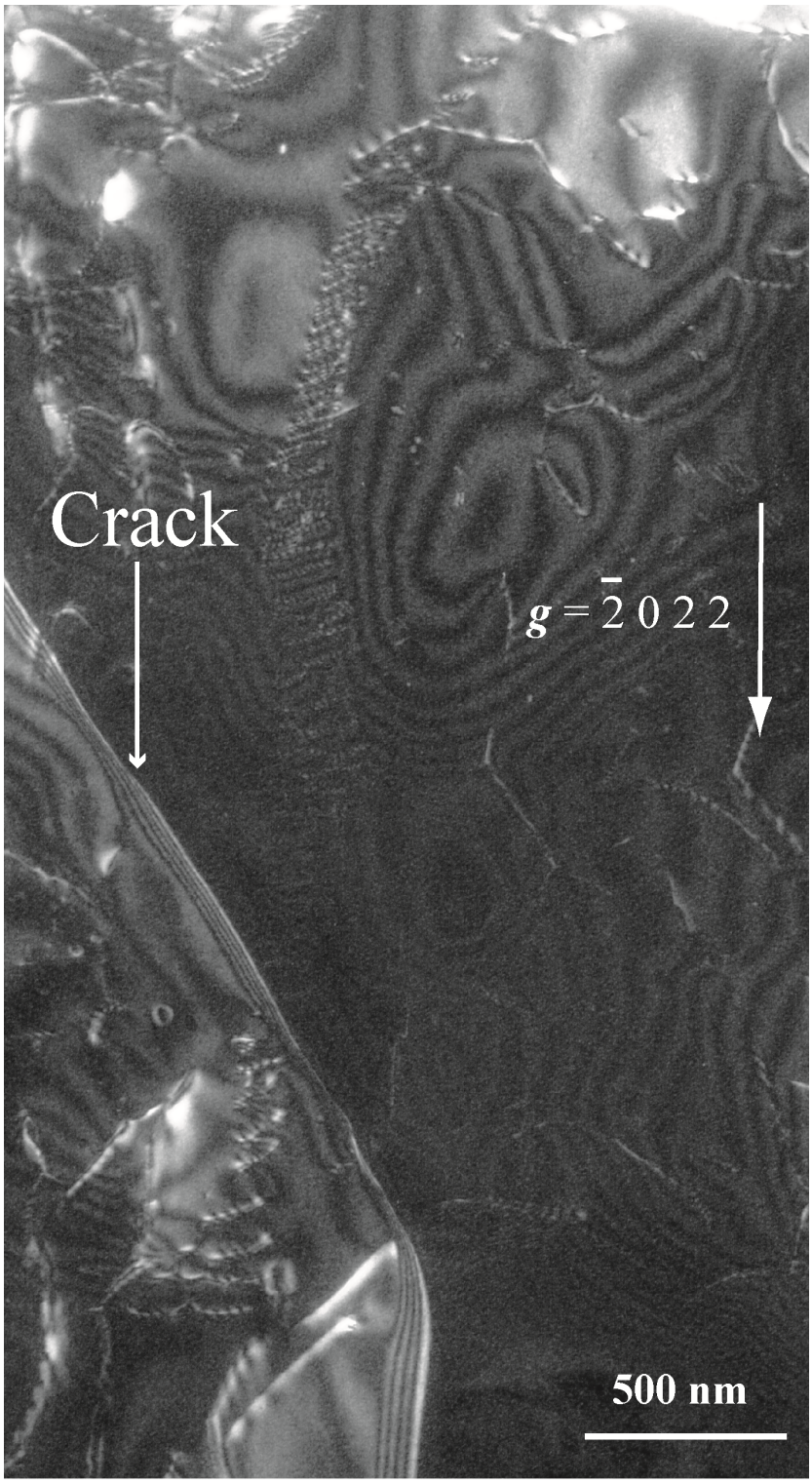

Figure 1: *WBDF images obtained along the* $[11\bar{2}3]$ *zone axis, with* ***g:*** $\bar{2}022$*, showing a sub-grain boundary crossed by a crack.*

The nature of the dislocations has been investigated using WBDF technique. Figure 2 illustrates the characterization of six dislocations observed close to the $[\bar{1}100]$ zone axis. They are in contrast with the $\bar{1}\,\bar{1}\,2\,\bar{1}$ diffraction vector (see figure 2a) and out of contrast with 0002 (see Figure 2b). They are ⅓$\langle 2\bar{1}\,\bar{1}\,0\rangle$ (also called <a>) dislocations. Figure 3 shows the characterization of two dislocation families belonging to a sub-grain. The first dislocation family is in contrast while the second one is out of contrast (figure 3a), with a diffraction vector 0004. Conversely, the second dislocation family is in contrast while the first one is out of contrast (figure 3b), with $0\bar{2}2\bar{2}$. These dislocations are perfect ones and can only be ± ⅓$[1\bar{2}13]$ or ± ⅓ $[11\bar{2}\bar{3}]$, that is to say $\langle c+a\rangle$ dislocations, for the first family, and ± ⅓$[\bar{1}2\bar{1}0]$ or ± ⅓ $[11\bar{2}0]$, i.e. $\langle a\rangle$ dislocations, for the second family. It is worth noticing that no $[0001]$ dislocation ($\langle c\rangle$) has been identified among all the analysed dislocations, but their occurrence cannot be excluded.

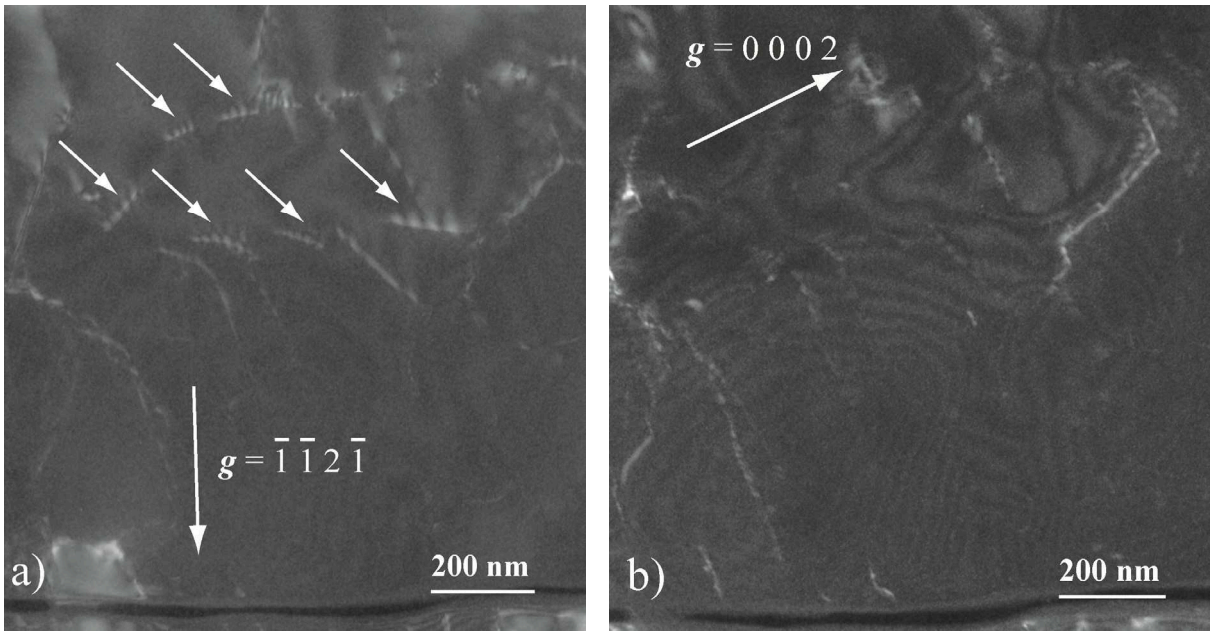

Figure 2: *Micrographs in WBDF conditions viewed along the* $[\bar{1}100]$ *zone axis. (a) Condition* ***g:*** $\bar{1}\,\bar{1}\,2\,\bar{1}$*, the six* ⅓$\langle 2\bar{1}\,\bar{1}\,0\rangle$ *dislocations (indicated by the arrows) are in contrast; (b) condition* ***g:*** 0002*, the six* ⅓$\langle 2\bar{1}\,\bar{1}\,0\rangle$ *dislocations are out of contrast.*

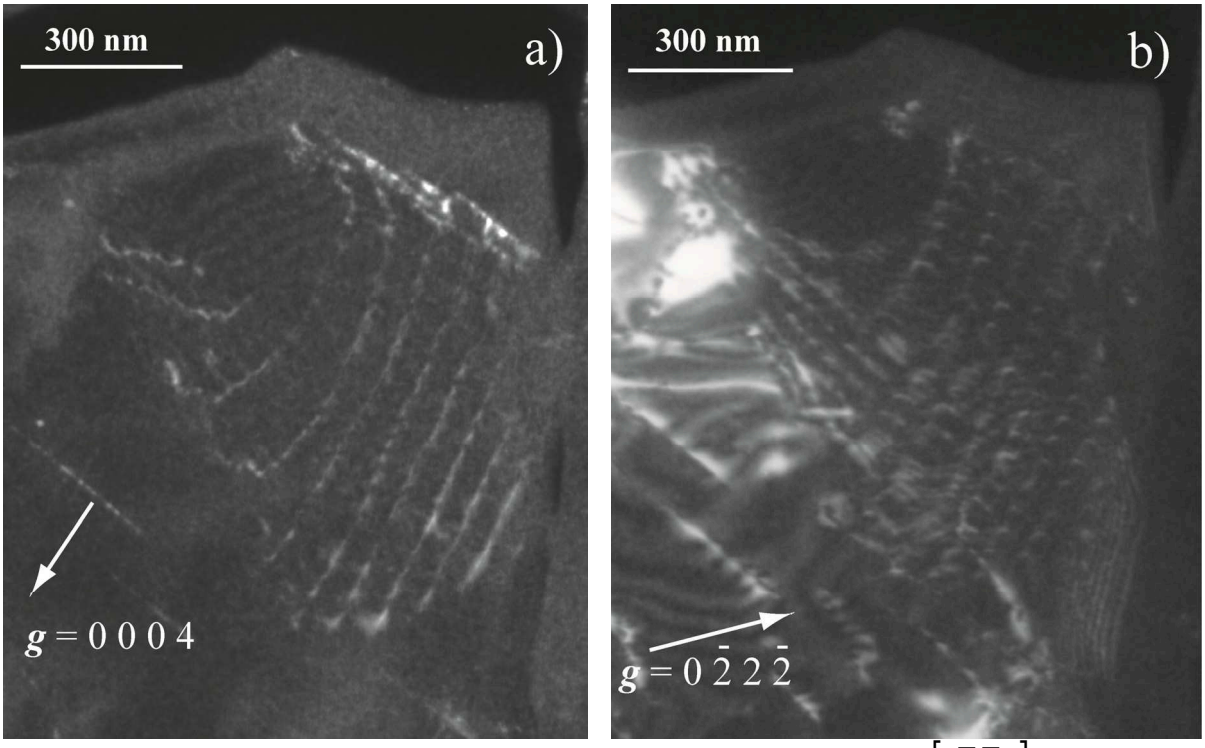

Figure 3: *Micrographs of a sub-grain, in WBDF condition, viewed along the* $[2\bar{1}\bar{1}0]$ *zone axis, (a) with* ***g:*** 0004 *and (b)* ***g:*** $0\bar{2}2\bar{2}$ *. The Burgers vector of the dislocation family in contrast with* ***g:*** 0004 *, is of the* $\langle c+a \rangle$ *type. The Burgers vector of the dislocation family in contrast with* ***g:*** $0\bar{2}2\bar{2}$ *, is of the* $\langle a \rangle$ *type.*

We have also performed slip planes characterizations. Figure 4 shows several dislocation segments which appear straight and aligned along a direction which can be interpreted as the trace of their glide plane. These dislocations are thus lying in the (0001) plane. They are in contrast with the $11\bar{2}\bar{1}$ diffraction vector, and out of contrast with 0004 showing that they are $\langle a \rangle$ dislocations gliding in (0001).

Dislocation Burgers vectors and slip planes in phase A deformed at 400°C

The specimen microstructure is composed of small grains of 8 ± 2 μm. All the analyzed grains (47 grains) contain lots of dislocations. Very few sub-grain boundaries were noted and the average dislocation density is $\rho \approx 2.10^{13}$ m^{-2}.

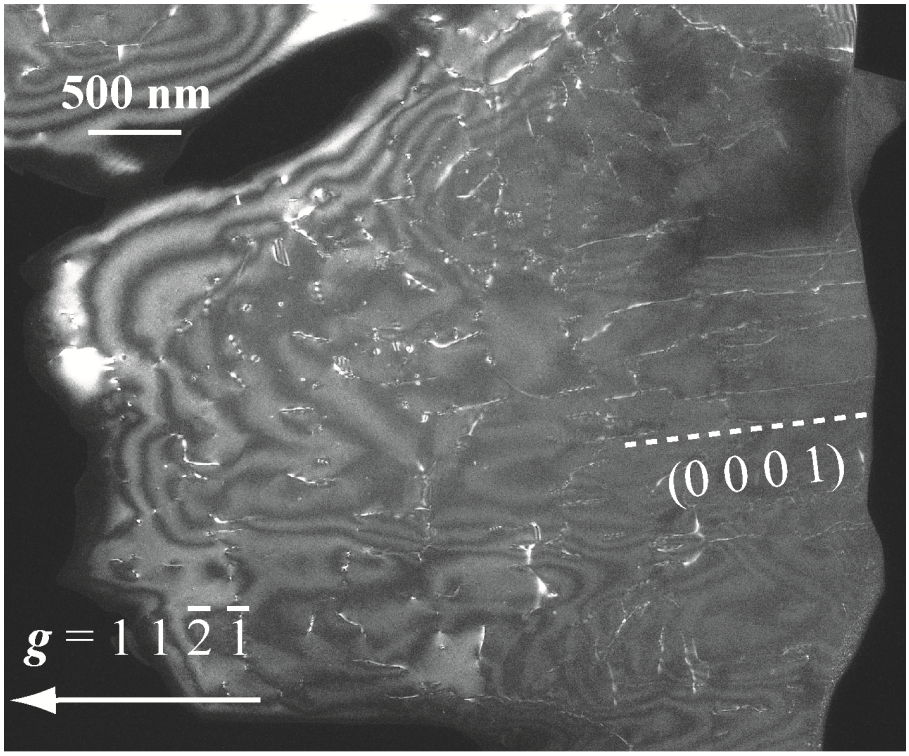

Figure 4: *WBDF picture obtained with* ***g:*** $11\bar{2}\bar{1}$, *viewed along the* $[\bar{1}100]$ *zone axis, showing several* $\langle a \rangle$ *dislocations lying in the* (0001) *plane.*

The specimen of phase A, deformed at 400°C, contains a lot of evidences for dissociated dislocations. Figure 5 shows dissociation in the basal plane. On Figure 5a (***g:*** $0\bar{2}2\bar{2}$), one partial dislocation (labelled 1) is out of contrast. The second partial dislocation (labelled 2) and the stacking fault (separation of the order of 1 μm) are in contrast. On figure 5b, the plane containing the faults and the dislocations is seen edge-on. Figure 5a shows that every third stacking faults are out of contrast when stacking faults are superimposed. Consequently, the ***g.b*** product is $n/3$. Thus, the partial dislocation 1 can only be $\pm\frac{1}{3}[01\bar{1}0]$, and the associated partial dislocation 2 is $\pm\frac{1}{3}[10\bar{1}0]$ or $\pm\frac{1}{3}[1\bar{1}00]$. Consequently, the dissociation law is:

$1/3[01\bar{1}0]+1/3[10\bar{1}0] \Leftrightarrow 1/3[11\bar{2}0]$ or $1/3[01\bar{1}0]+1/3[\bar{1}100] \Leftrightarrow 1/3[\bar{1}2\bar{1}0]$.

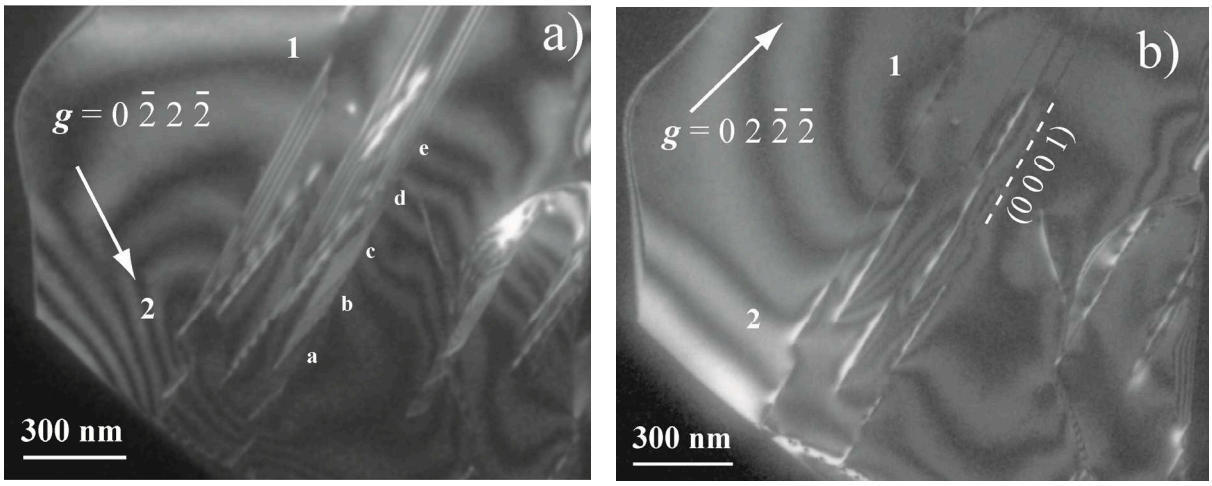

Figure 5: *WBDF micrographs of dissociated dislocations in the basal plane, viewed along the* $[2\bar{1}\,\bar{1}\,0]$ *zone axis, (a) with* ***g:*** $0\bar{2}2\bar{2}$ *, and (b)* ***g:*** $02\bar{2}\bar{2}$ *. On (a), superimposed stacking faults (noted a, b, c, d and e). "a" and "d" are out of contrast.*

Furthermore, Figure 6a shows evidence for both perfect and dissociated $\langle a \rangle$ dislocations which glide on the basal plane. With ***g*****:** $41\bar{5}0$, the thickness-fringe method shows that the ***g.b*** product is $\pm$ 2 for the dislocation labelled 3 which is compatible with the Burgers vector of a partial dislocation: $\pm 1/3[01\bar{1}0]$. Moreover, with the same diffraction vector and next to the previous dislocation, the thickness-fringe method shows a dislocation (labelled 4) with a ***g.b*** product of $\pm$ 5. This corresponds to a perfect $\pm 1/3[1\bar{1}20]$ dislocation.

We found in the specimen deformed at 400°C evidences for prismatic and pyramidal glide. Figure 6b shows evidences for glide in $(1\bar{2}10)$ and $(\bar{2}110)$ (seen edge on). Similarly, figure 7a shows pyramidal planes $(11\bar{2}1)$ and $(11\bar{2}\,\bar{1})$ edge-on containing evidences of glide. In the same area (Figure 7b), we found dislocations with dissociation out of the basal plane. The angle between the stacking fault and the basal plane suggest that dissociation occurs in a pyramidal plane. This defect must be related to $\frac{1}{3}\langle 2\bar{1}\,\bar{1}\,3\rangle$ glide. Several observations show that the two related partial dislocations exhibit the same contrast suggesting a symmetrical dissociation law, possibly: $1/6\langle 2\bar{1}\,\bar{1}\,3\rangle + 1/6\langle 2\bar{1}\,\bar{1}\,3\rangle \Leftrightarrow 1/3\langle 2\bar{1}\,\bar{1}\,3\rangle$**.**

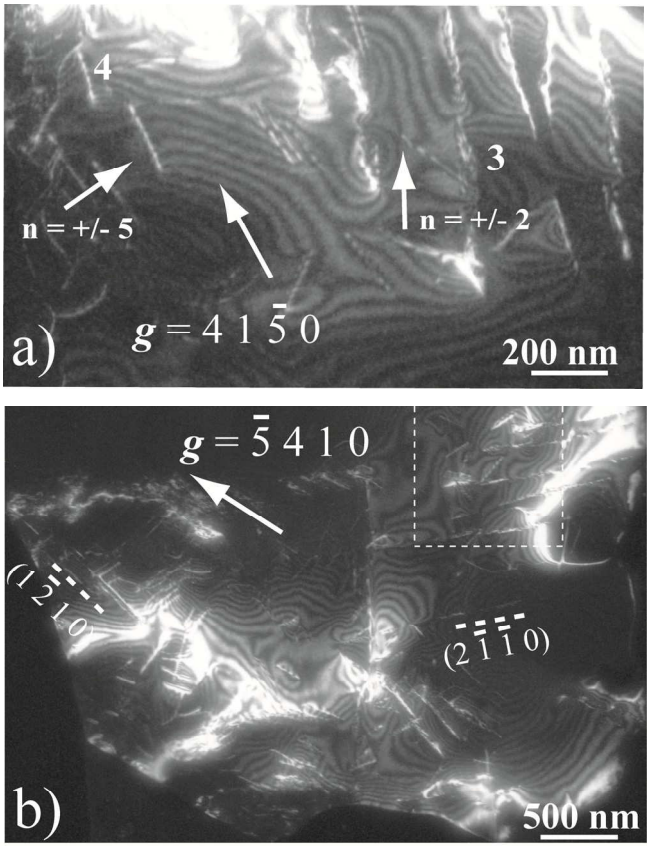

Figure 6: *(a) Micrograph (close to* $[0001]$ *zone axis and with* ***g:*** $41\bar{5}0$*), with* $\pm 1/3[11\bar{2}0]$ *and* $\pm 1/3[01\bar{1}0]$ *dislocations showing fringe contrast characteristic of* ***g.b*** *products ± 5 and ± 2 respectively; (b) The dashed rectangle indicates the area magnified in (a):* $(1\bar{2}10)$ *and* $(2\bar{1}\bar{1}0)$ *glide planes are highlighted (dashed white straight lines), with* ***g:*** $\bar{5}410$ *.*

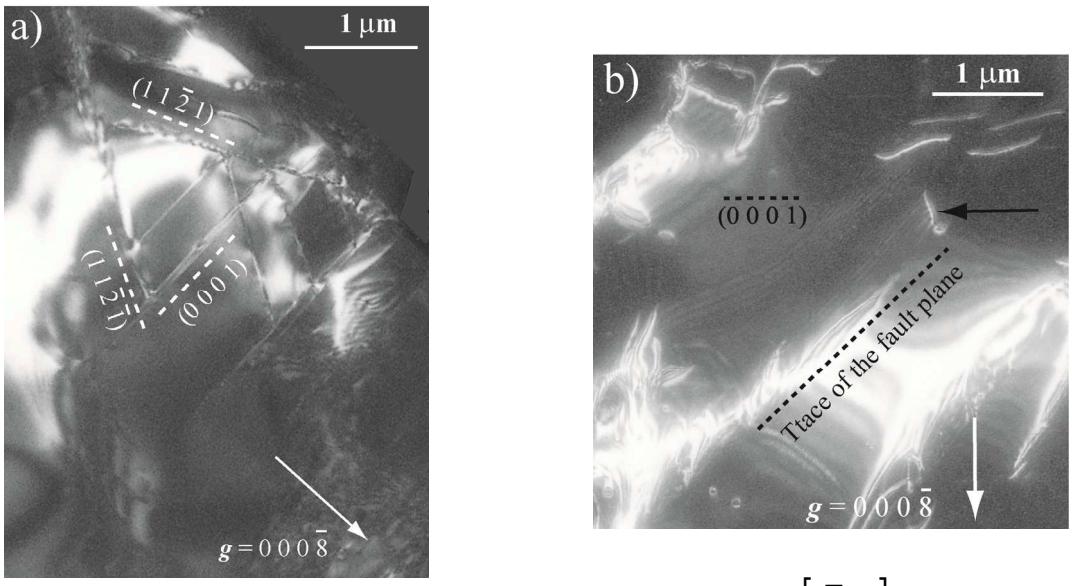

Figure 7: *Micrographs in WBDF conditions with* ***g:*** $000\bar{8}$*, along the* $[1\bar{1}00]$ *zone axis. (a) The* (0001)*,* $(11\bar{2}1)$ *and* $(11\bar{2}\bar{1})$ *planes are edge one (dashed white straight lines); (b) highly dissociated dislocations in a pyramidal plane are indicated by a black arrow.*

Twinning

In addition to these slip systems, we have found some evidence for twinning in phase A. Figures 8a and 8b show a straight boundary parallel to (0001) which separates two domains with markedly different orientations as shown by their diffraction contrasts. The micrograph has been obtained near the $[2\bar{1}\bar{1}0]$ zone axis. However, when a WBDF image is formed with the 0004 diffraction vector, the boundary vanishes and the diffraction contrast appears perfectly continuous across the boundary (figure 8c). Both sides of this boundary share the same $[0001]$ direction, either positive or negative, suggesting a twinning relationship. Here, the twin plane is (0001). We have performed selected area precession electron diffraction on both sides of the twin boundary seen on figure 8. A symmetry relationship is clearly visible on these diffraction patterns (Figure 10), confirming twinning.

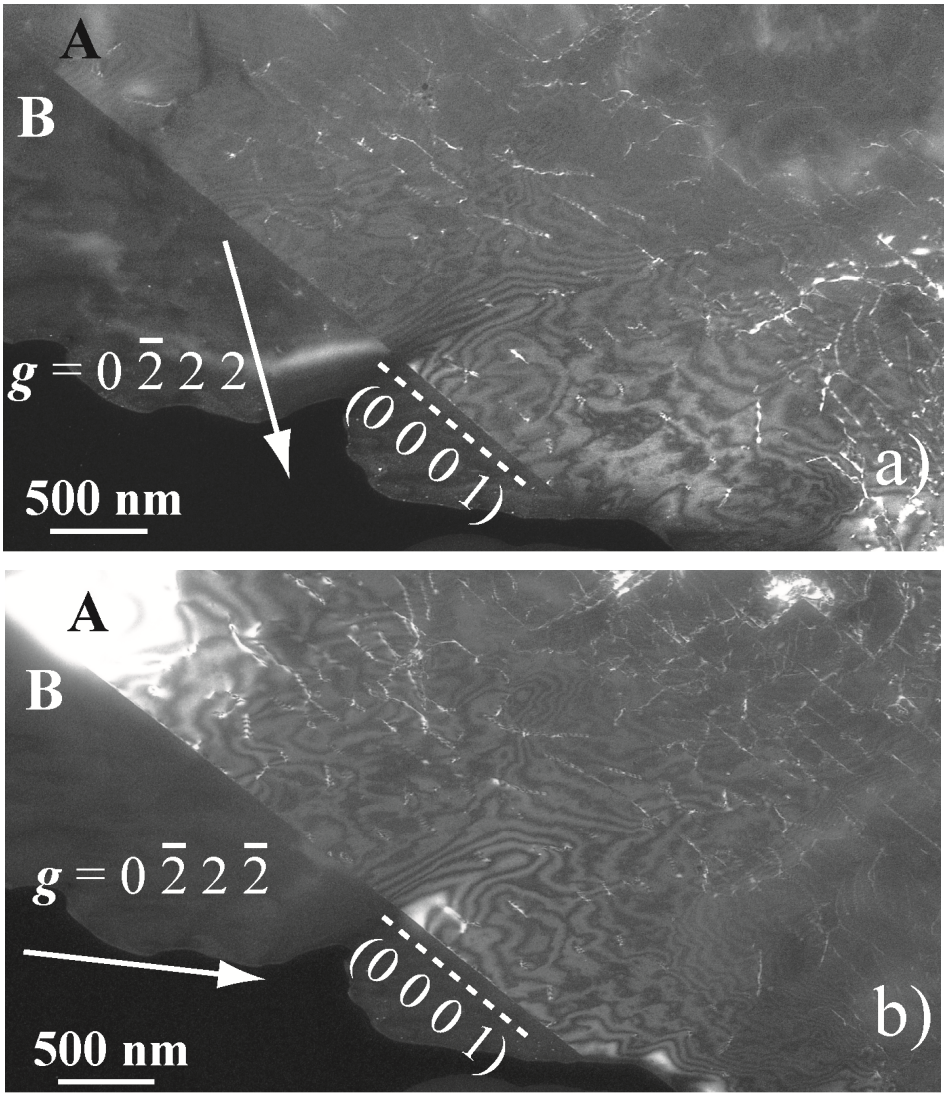

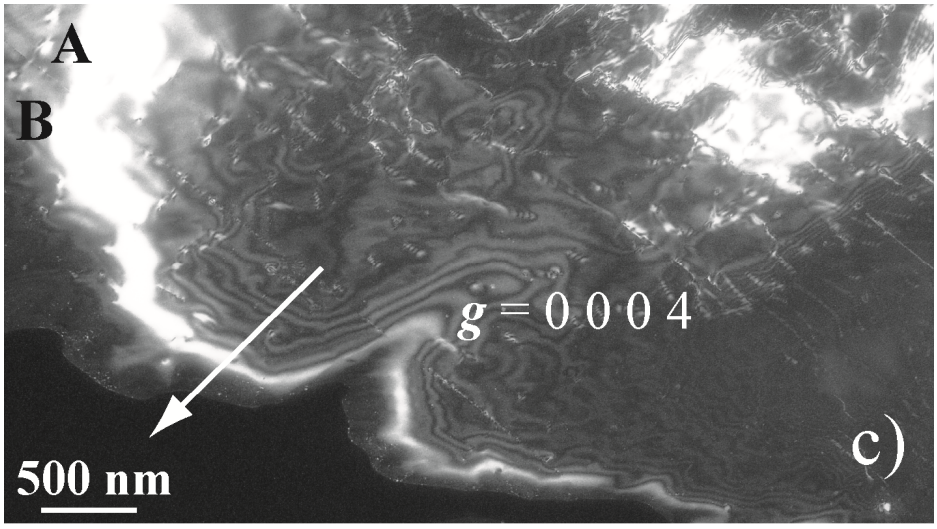

Figure 8: *WBDF images obtained along the* $[2\bar{1}\bar{1}0]$ *zone axis, (a) with* ***g:*** $0\bar{2}2\bar{2}$ *, (b)* ***g:*** $0\bar{2}22$ *and (c)* ***g:*** 0004 *. A twin, along the* (0001) *plan, is noticeable. The* $[0004]$ *direction seems to be invariant; otherwise the* $[0004]$ *direction is changed into the* $[000\bar{4}]$ *direction.*

Discussion

Plastic deformation experiments in the multianvil apparatus represent complex tests as discussed by Cordier & Rubie (2001) and Thurel & Cordier (2003). Large, non-hydrostatic, stresses are applied during cold compression. When the specimen is heated, and if temperature is high enough, plasticity is induced by relaxation. Recovery of cold deformation (if present) starts and new dislocation sources can operate. After a given time, stresses are relaxed, plastic deformation stops, but recovery processes can still be active if temperature is high enough. These experiments are poorly adapted to quantitative rheological studies, however, they represent a very efficient way to introduce dislocations. Since strains are small, and since recovery can be enhanced (depending on temperature and time duration), the dislocation densities are usually well adapted for TEM characterization of dislocation Burgers vectors and slip plane. This is the case in the present study where the sample, made of a mixture of phase A and enstatite, shows pervasive evidence of dislocation activity with a dislocation density of the order of 10^{13} m^{-2}.

Dislocations are very energetic defects. The elastic energy stored in the crystal surrounding the dislocation line roughly scales as μb^2 where μ is the shear modulus and b the modulus of the Burgers vector. For this reason, dislocation Burgers vectors are usually in the direction of the smallest lattice repeats of the unit cell. Phase A is

hexagonal with a c/a ratio of 1.22. The modulus of the Burgers vectors of $\langle a \rangle$ dislocations (the smallest lattice dimension) is already quite large: 7.86 Å. Perfect $\langle a \rangle$ dislocations represent an important fraction of the observed defects establishing their role in the plasticity of phase A. We did not find any evidence for $\langle c \rangle$ dislocations. Although it is difficult to definitely rule out the possibility of $\langle c \rangle$ glide. Alternatively, we have found pervasive evidence for activation of $\langle c + a \rangle$ dislocations. Their Burgers vector's length is 12.39 Å, corresponding to an elastic energy 2.5 times larger than that of $\langle a \rangle$ dislocations. Such large Burgers vectors are unusual in materials science (with the exception of recently discovered complex metallic alloys (Heggen et al., 2010)) but there exist other cases in mineral physics, in olivine, wadsleyite or garnets for instance. In olivine, the absence of [010] dislocations has been generally attributed to the magnitude of its Burgers vector (10.2 Å). Generalized stacking fault calculations have shown recently, however, that the absence of [010] dislocations is due in fact to the difficulty of shearing the olivine structure along this direction (Durinck et al., 2005). In wadsleyite, [010] dislocations exhibit very large Burgers vectors (11.44 Å), however, the core energy is relaxed by complex dissociation schemes (Thurel & Cordier, 2003, Metsue et al., 2010). Garnets, for which the Burgers vectors of ½<111> dislocations is ca. 10 Å is more comparable to phase A deformed at 700°C, since in both cases WBDF shows no visible dissociation. Given the resolution of WBDF, this means that if some core spreading exists, it must be less than 15 nm wide.

However, dissociated dislocations in basal and pyramidal planes are present in the specimen deformed at 400°C. These partial dislocations result from the dissociation of $\langle a \rangle$ and $\langle c + a \rangle$ dislocations, respectively.

This leads us to the issue of slip planes. The crystal structure of phase A differs strongly from those of phyllosilicates which carry water at lower pressures. It consists of slightly distorted close-packed layers of oxygen atoms and hydroxyl groups with magnesium in octahedral sites and silicon in tetrahedral sites. The usual requirement that slip planes avoid cutting the strong Si-O bonds is easily met (Figures 9a and 9b) and does not strongly constrain the choice of slip planes.

Perfects and dissociated $\langle a \rangle$ dislocations are found in the basal plane (at 700 and 400°C, respectively). Dissociated $\langle c+a \rangle$ dislocations are observed in pyramidal planes at 400°C, and prismatic glide is found at 400°C. All these observations are compatible with the crystal structure (no Si-O bonds cut). We can raise the hypothesis that the core dislocations in phase A is spread (in the basal plane for $\langle a \rangle$ dislocations and in pyramidal planes for $\langle c+a \rangle$ dislocations). At 700°C, this core spreading is too small to be observed by WBDF, but it strongly constrains the choice of the glide planes and slip systems. Larger stresses related to deformation at 400°C allow wide separation of the partial dislocations and reveal this core structure.

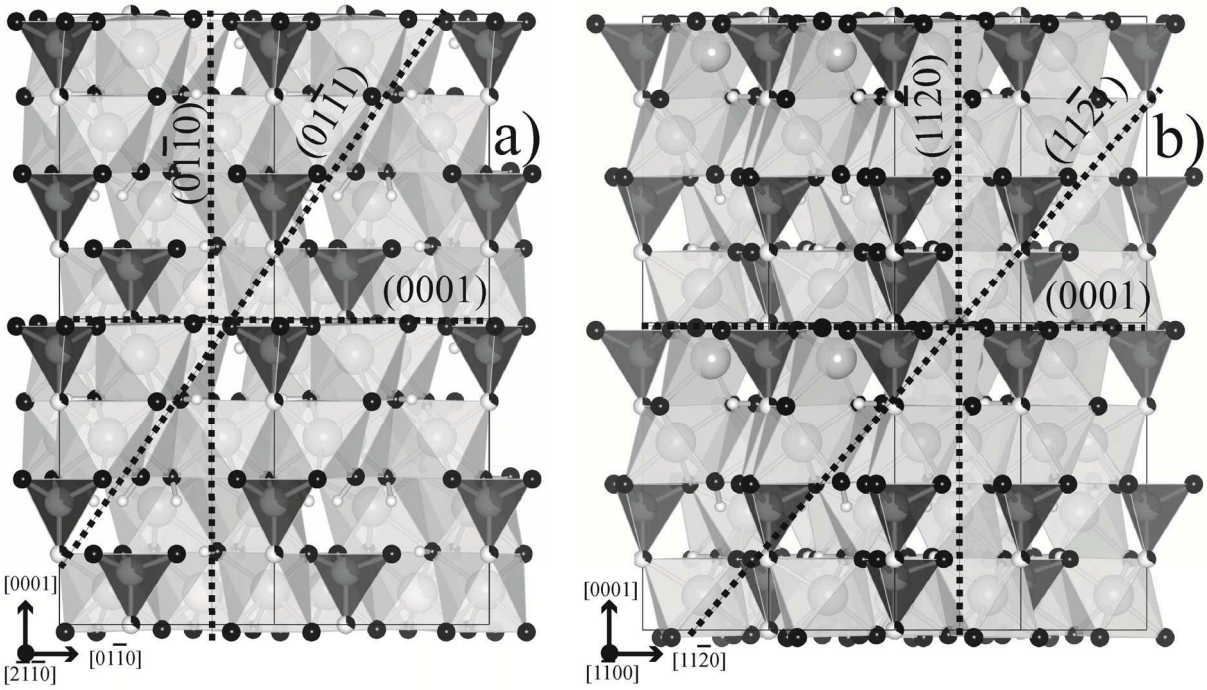

Figure 9: *Projection of the SiO_4 tetrahedrons (a) along the $[2\bar{1}\bar{1}0]$ zone axis, and (b) along $[1\bar{1}00]$. The trace of the (0001), $(01\bar{1}0)$, $(11\bar{2}0)$, $(01\bar{1}1)$ and $(11\bar{2}1)$ planes, are indicated by dashed black straight lines.*

Furthermore, twinning in phase A has been evidenced. Figure 10 shows zone axis patterns of zone A and zone B (see figure 8). When we compare the experimental and simulated precession diffraction patterns in zone A (fig. 10a and 10b), and proceed similarly in zone B (fig. 10c and 10d), as well as in zone A/B (fig.

10e and 10f), we notice that some reticular planes are in common both in zone A and B (see table I).

***Table 1**: List of the superimposed reciprocal directions in zone A and B.*

g in zone A	Corresponding **g** in zone B
$1\bar{5}40$	$1\bar{5}40$
$\bar{1}\bar{2}36$	$2\bar{3}1\bar{6}$
$\bar{2}3\bar{1}6$	$12\bar{3}\bar{6}$
$07\bar{7}\bar{6}$	$\bar{3}8\bar{5}6$
$38\bar{5}\bar{6}$	$0\bar{7}76$
$3\bar{1}\bar{2}\bar{1}2$	$\bar{3}1212$

The twin law is obtained using the stereographic projections. We have superimposed the stereographic projections along the pole directions $\left[3\bar{1}\bar{2}1\right]_A$ and $\left[\bar{3}12\bar{1}\right]_B$. These projections are then rotated along the similar poles in order to have $\left(1\bar{5}40\right)_A$ // $\left(1\bar{5}40\right)_B$. By analyzing the stereographic projection along the $\left[1\bar{5}40\right]$ invariant direction, we can note that the rotation angle which verifies the previous relations, is 180° (see fig. 11). Consequently, the twin law corresponds to a rotation of 180° around the $\left[1\bar{5}40\right]$ axis.

Moreover, the twin index Σ is given by the following formula (Friedel, 1964):

$\Sigma = X/2$ with $X = \left|uh + vk + wl\right|$ if *X* is pair, otherwise $\Sigma = X$

where *u*, *v* and *w* are the indices of the twin axis (with three indices notation), and *h*, *k* and *l* are the indices of the plane perpendicular to the twin axis (three indices notation). Here, *u* = -1, *v* = -3, *w* = 0, *h* = 1, *k* = -5 and *l* = 0, consequently we can deduce that Σ = 7. Furthermore, the number of spots which match with zone A and B (see fig. 10f), corresponds to Σ - 1. Here, we find 6 of them; so we obtain Σ = 7 again. The twin observed in figure 7 is consequently a reticular merohedral twin with an index of 7 obtained with a 180° rotation around the $\left[1\bar{5}40\right]$ axis. It is unusual to observe index twins higher than 5. However, some examples are available as, for example, for chalcocite where the $\left[7413\right]$ twin axis creates a twin index of Σ = 19 (Nespolo et al., 2006). Furthermore, a twin index of 7, for a hexagonal structure with a c/a ratio of 1.22, has already been mentioned by Grimmer & Kunze (2004).

Moreover, the microstructure of those twins (large domains, no dislocation involved) suggests that they result from growth rather than from plastic deformation.

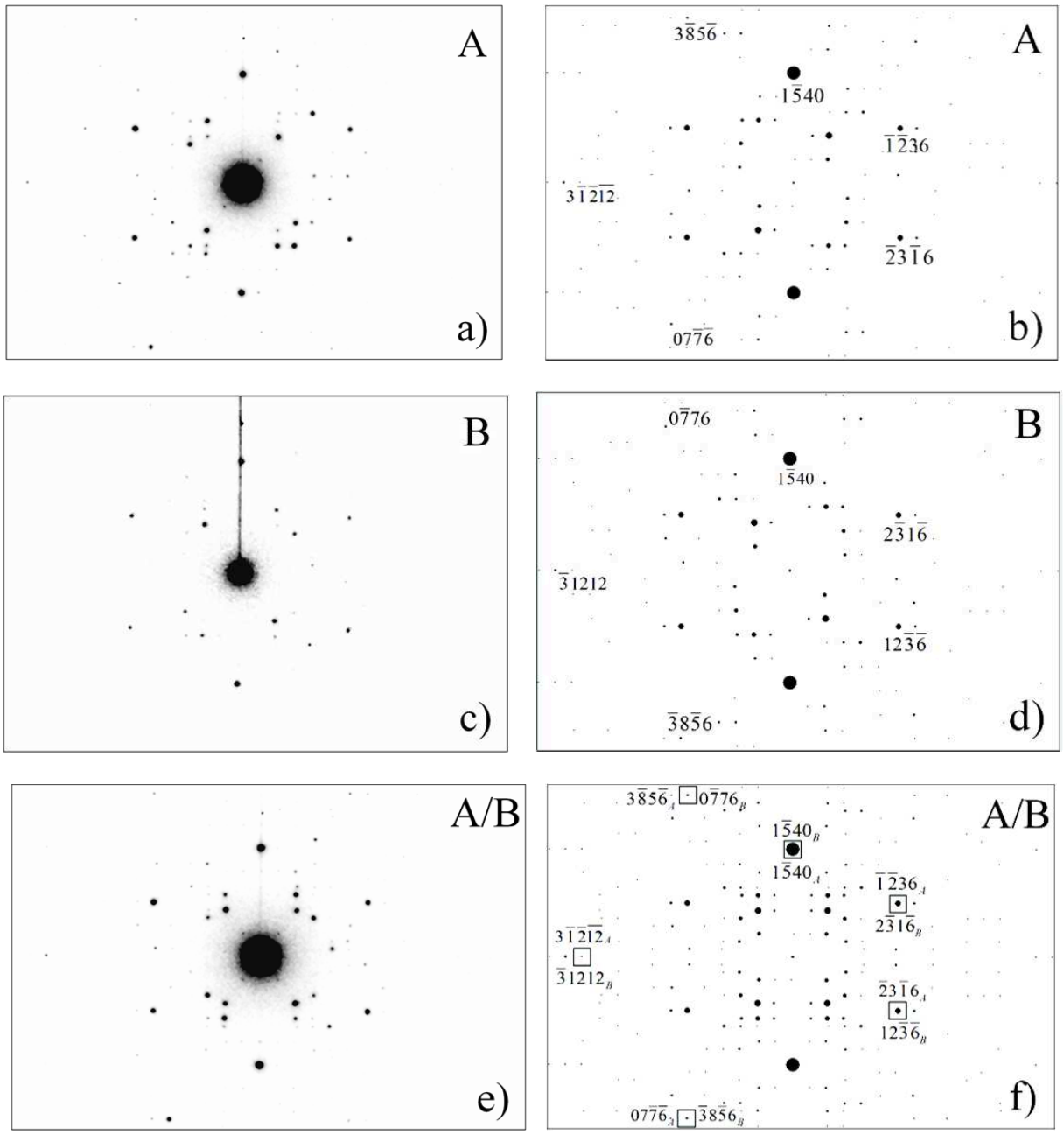

Figure 10: *Precession Electron diffraction patterns: (a) experimental pattern in zone A; (b) simulated pattern in zone A (zone axis =* $[3\bar{1}\bar{2}1]$*); (c) experimental pattern in zone B; (d) simulated pattern in zone B (zone axis =* $[\bar{3}12\bar{1}]$*); (e) experimental pattern in zone A/B; (f) simulated pattern in zone A/B with coincidence spots annotated by black empty squares.*

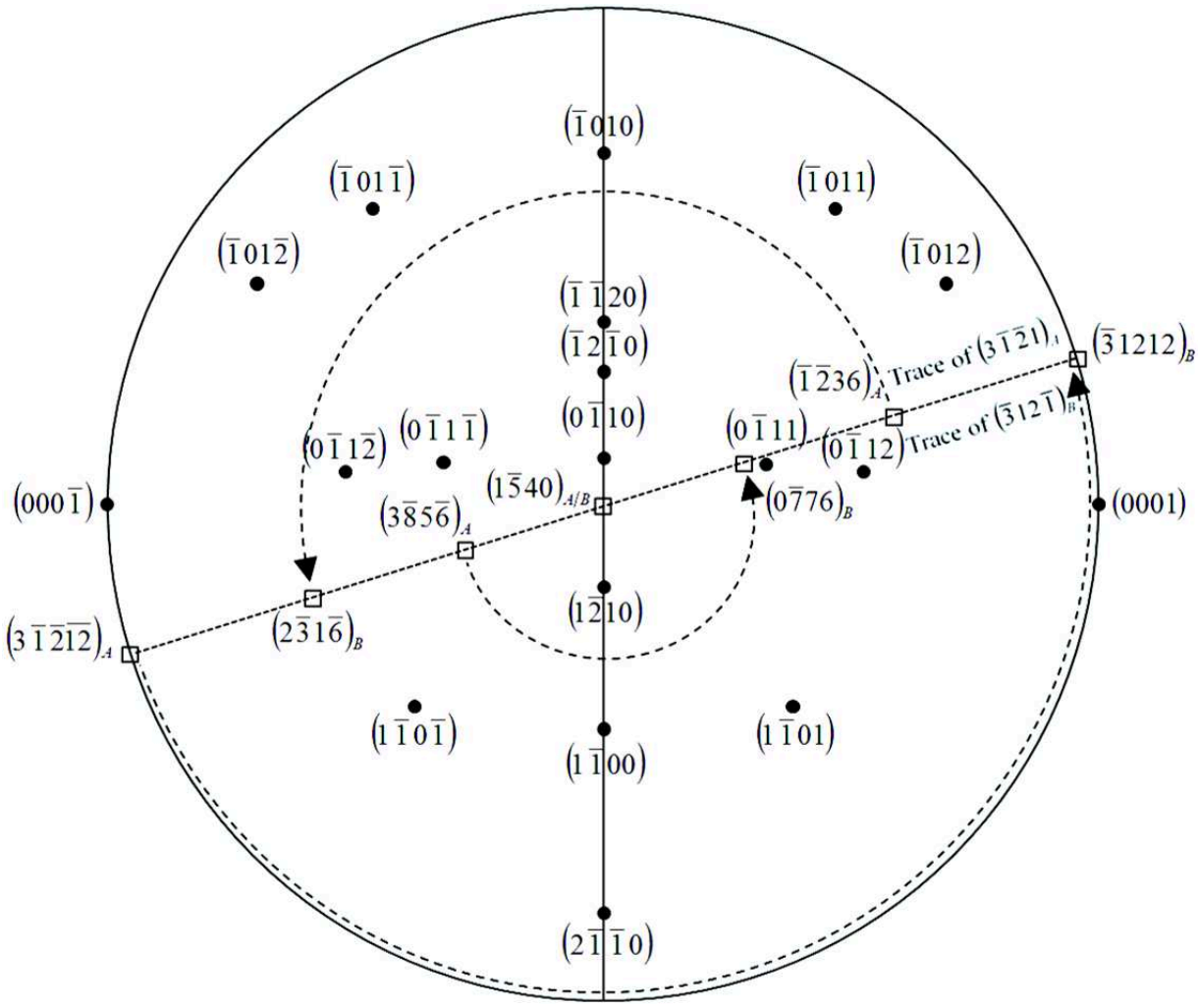

Figure 11: *Stereographic projection along the* $[1\bar{5}40]$ *invariant pole. The trace of the perpendicular planes to the zone axes of figure 10, for zone A (i.e.* $(3\bar{1}\bar{2}1)_A$*) and zone B (i.e.* $(\bar{3}12\bar{1})_B$*), are indicated by a dashed straight line. The reticular planes which coincide with zone A and zone B are appointed by empty black squares. The rotations along the* $[1\bar{5}40]$ *invariant pole verify that the* $(3\bar{1}\bar{2}\bar{1}\bar{2})_A$ *reticular plane coincides with the* $(\bar{3}1212)_B$ *one; the* $(\bar{1}\bar{2}36)_A$ *reticular plane coincides with the* $(2\bar{3}1\bar{6})_B$ *one; and the* $(3\bar{8}5\bar{6})_A$ *reticular plane coincides with the* $(0\bar{7}76)_B$ *one. The twin law is consequently a rotation of 180° along the* $[1\bar{5}40]$ *direction.*

To recapitulate, two specimens of phase A, from an assemblage containing enstatite, were synthesized using a multianvil press at 900°C and 11 GPa. Then, a sample is deformed at the same pressure at 700°C, and another sample is deformed at the same pressure, at 400°C. Under these conditions, both phases are significantly deformed by dislocations. Dislocations with $\langle a \rangle$ and $\langle c+a \rangle$ Burgers vectors have been identified. No $\langle c \rangle$ type dislocations could be characterized

precisely, but we cannot exclude their occurrence. The $\langle a \rangle$ dislocations glide in the basal plane where they can be observed widely dissociated at 400°C. The same kind of conclusion holds for $\langle c+a \rangle$ dislocations in pyramidal planes. Dislocations gliding in $\{1\bar{1}20\}$ prismatic planes have not been identified.

Furthermore, we have characterized a reticular merohedral twin with a twin index of 7, defined by a rotation of 180° around the $[1\bar{5}40]$ direction.

Acknowledgements:

This study was supported by the ANR project SUBDEF grant n° ANR-08-BLAN-0192. The TEM national facility in Lille is supported by the CNRS (INSU) and the Conseil Régional du Nord – Pas de Calais, France.

References

Cordier, P. & Rubie, D.C. (2001): Plastic deformation of minerals under extreme pressure using a multianvil apparatus. *Mater. Sci. Eng. A*, **309-310**, 38-43.

Durinck, J., Legris, A., Cordier, P. (2005): Pressure sensitivity of olivine slip systems: first-principle calculations of generalised stacking faults. *Phys. Chem. Minerals*, **32**, 646–654.

Friedel, G. (1964): Leçon de cristallographie. A. Blanchard éd., Paris, 250 p.

Grimmer, H. & Kunze, K. (2004): Twinning by reticular pseudo-merohedry in trigonal, tetragonal and hexagonal crystals. *Acta Cryst. A*, **60**, 220-232.

Ham, R.K. (1961): The determination of dislocation densities in thin films. *Phil. Mag.*, **6**, 1183-1184.

Heggen, M., Houben, L., Feuerbacher, F. (2010): Plastic-deformation mechanism in complex solids, *Nature Materials*, **9**, 332-336.

Hilairet, N. & Reynard, B. (2009): Stability and dynamics of serpentinite layer in subduction zone. *Tectonophysics*, **465**, 24-29.

Hilairet, N., Reynard, B., Wang, Y.B., Daniel, I., Merkel, S., Nishiyama, N., Petitgirard, S. (2007): High-pressure creep of serpentine, interseismic deformation, and initiation of subduction. *Science*, **318**, 1910-1913.

Horiuchi, H., Morimoto, N., Yamamoto, K., Akimoto, S.I. (1979): Crystal-structure of $2Mg_2SiO_4.3Mg(OH)_2$, a new high-pressure structure type. *Am. Miner.*, **64**, 593-598.

Ishida, Y., Ishida, H., Kohra, K., Ichinose, H. (1980): Determination of the Burgers vector of a dislocation by weak-beam imaging in a HVEM. *Phil. Mag. A*, **42**, 453-462.

Komabayashi, T. & Omori, S. (2006): Internally consistent thermodynamic data set for dense hydrous magnesium silicates up to 35 GPa, 1600 degrees C: Implications for water circulation in the Earth's deep mantle. *Phys. Earth Planet. Inter.*, **156**, 89-107.

Komabayashi, T., Omori, S., Maruyama, S. (2004): Petrogenetic grid in the system $MgO-SiO_2-H_2O$ up to 30 GPa, 1600 degrees C: Applications to hydrous peridotite subducting into the Earth's deep interior. *J. Geophys. Re*s., **109**, B03206.

Komabayashi, T., Omori, S., Maruyama, S. (2005): Experimental and theoretical study of stability of dense hydrous magnesium silicates in the deep upper mantle. *Phys. Earth Planet. Inter.*, **153**, 191-209.

Meade, C. & Jeanloz, R. (1991): Deep-focus earthquakes and recycling of water into the earth's mantle. *Science*, **252**, 68-72.

Meltzman, H., Kauffman, Y., Tangadurai, P., Drozdov, M., Baram, M., Brandon, D., Kaplan, W.D. (2009): An experimental method for calibration of the plasmon mean free path. *J. Microsc.*, **236**, 165-173.

Metsue, A., Carrez, P., Denoual, C., Mainprice, D., Cordier, P. (2010): Plastic deformation of wadsleyite: IV Dislocation core modelling based on the Peierls–Nabarro–Galerkin model. *Acta Mater.*, **58**, 1467–1478.

Miyajima, N. & Walte, N. (2009): Burgers vector determination in deformed perovskite and post-perovskite of $CaIrO_3$ using thickness fringes in weak-beam dark-field images, *Ultramicroscopy*, **109**, 683–692.

Nespolo, M. & Ferraris, G. (2006): The derivation of twin laws in non-merohedric twins. Application to the analysis of hybrid twins. *Acta Cryst. A*, **62**, 336-349.

Omori, S., Komabayashi, T., Maruyama, S. (2004): Dehydration and earthquakes in the subducting slab: empirical link in intermediate and deep seismic zones. *Phys. Earth Planet. Inter.*, **146**, 297-311.

Ringwood, A.E. & Major, A. (1967): High pressure reconnaissance investigations in system Mg_2SiO_4-MgO-H_2O. *Earth Planet. Sci. Lett.*, **2**, 130-133.

Schmidt, M.W. & Poli, S. (1998): Experimentally based water budgets for dehydrating slabs and consequences for arc magma generation. *Earth Planet. Sci. Lett.*, **163**, 361-379.

Thurel, E. & Cordier, P. (2003): Plastic deformation of wadsleyite: I. High-pressure deformation in compression. *Phys. Chem. Minerals*, **30**, 256-266.

Ulmer, P. & Trommsdorff, V. (1995): Serpentine stability to mantle depths and subduction-related magmatism. *Science*, **268**, 858-861.

Vincent, R. & Midgley, P.A. (1994): Double conical beam-rocking system for measurement of integrated electron diffraction intensities. *Ultramicroscopy*, **53**, 271-282.

Yamasaki, T. & Seno, T. (2003): Double seismic zone and dehydration embrittlement of the subducting slab. *J. Geophys. Res.*, **108**, 2212.

Transmission electron microscopy characterization of the dislocations and slip systems of superhydrous B

Alexandre MUSSI[1*], Patrick CORDIER[1,2] and Daniel J. FROST[2]

[1]Unité Matériaux et Transformations, UMR 8207 CNRS-Université Lille1,
F-59655 Villeneuve d'Ascq, France
[2]Bayerisches Geoinstitut, Universität Bayreuth, Germany.

Cite as:
A. Mussi, P. Cordier & D.J. Frost (2013) Transmission electron microscopy characterization of the dislocations and slip systems of superhydrous B. European Journal of Mineralogy, 25, 561-568, https://doi.org/10.1127/0935-1221/2013/0025-2308

Abstract

Superhydrous B (shy B), is a dense hydrous magnesium silicate (DHMS) which exhibits a large stability field in cold slab conditions. It was deformed at 20GPa and at temperatures 1000-1100°C. The resulting dislocations have been characterized by transmission electron microscopy (TEM) with the weak beam dark field (WBDF) and the large angle convergent beam electron diffraction (LACBED) techniques. We emphasize the role of (010) plane in the plasticity of phase Shy B. We report that $[100]$ and $[001]$ glide in (010), and also climb of $[100]$. We also observe $\langle 101 \rangle$ glide in (010) and $\{111\}$ planes under high stress conditions.

Keywords: DHMS, superhydrous B, TEM, LACBED, dislocations, glide plane, climb.

[*]Corresponding author: alexandre.mussi@univ-lille1.fr

Introduction

The dynamics of the mantle is evidenced at the surface of the Earth by plate tectonics and associated phenomenons like volcanism, earthquakes and mountain building. Subduction zones are of utmost importance since they represent the cold downwelling boundary of convection and can be considered as the driving force for plate tectonic. Concerning the water budget of the mantle, the subduction zones play a key role since they are the place where water can be incorporated into the mantle through hydrous phases (Schmidt & Poli, 1998). Water, or hydrogen, considerably modifies the mechanical properties of the mantle, reducing the solidus temperature of the mantle rocks. Furthermore, water or water-bearing phases may be responsible for intermediate and deep earthquakes by phase transitions (Meade & Jeanloz, 1991; Yamasaki & Seno, 2003; Komabayashi *et al.*, 2004; Omori *et al.*, 2004). For instance, antigorite destabilizes at a depth exceeding 200km (Ulmer & Trommsdorff, 1995) and transforms into dense hydrous magnesium silicates (DHMS, see Ringwood & Major (1967) for synthesis and characterization in the Mg_2SiO_4 - MgO - H_2O system). Under cold slabs conditions, phase A ($Mg_7Si_2O_{14}H_6$), is the first DHMS to form (Komabayashi & Omori, 2006), followed by phase E ($Mg_{2.27}Si_{1.26}O_{2.4}H_6$), superhydrous B (shy B) ($Mg_{10}Si_3O_{18}H_4$) and then phase D ($MgSi_2O_2H_6$) which is stable under lower mantle conditions.

Up to now, very few studies have been conducted on the rheology of hydrous phases under pressure and temperature conditions relevant for subduction. Hilairet *et al.* (2007, 2009) have established that the viscosity of antigorite is very low, which may enable silent earthquakes through large deformation accommodations. Furthermore, Amiguet *et al.* (2012) have shown that lizardite is also very weak (flow stresses between 20 and 200 MPa). This phase which deforms easily by basal glide and kinking, could have played a role in initiating subduction. Recently, we have performed, by transmission electron microscopy (TEM), a first study on the plastic deformation mechanisms of phase A at 11 GPa, 700 and 400 °C (Mussi *et al.*, 2012). We have shown that phase A deforms primarily by basal glide of $1/3\langle 2\bar{1}\bar{1}0\rangle$ dislocations, and by pyramidal glide of $1/3\langle 2\bar{1}\bar{1}3\rangle$ dislocations (Mussi *et al.*, 2012).

In this study, we focus on the plastic deformation mechanisms of shy B. This phase is stable over a large domain (*ca.* 300 km in depths) which coincides approximately with the mantle transition zone (Komabayashi & Omori, 2006). We have synthetized and deformed a specimen of shy B under cold slab P, T conditions in the multianvil apparatus. The deformation microstructures have then been characterized by TEM to identify the dislocations and slip systems.

Experimental details

Crystal structure

Pacalo & Parise (1992) have characterized an orthorhombic crystal structure ($a_{PP} \approx 5.09$Å, $b_{PP} \approx 13.97$Å and $c_{PP} \approx 8.70$Å), with a *Pnnm* space group, for a shy B polycrystal of composition $Mg_{10}Si_3O_{14}(OH)_4$ synthesized at 1400 °C and 20 GPa. In this structure, double layers, which contain both magnesium in octahedral sites and silicon in tetrahedral sites (O-T layers), alternate along the *b* axis with single layers (O layers) which contain both magnesium and silicon in octahedral sites (Pacalo *et al.*, 1992). Hydrogen atoms are located between the O-T layers and are linked to the oxygen atoms associated with magnesium. However, Koch-Müller *et al.* (2005) proposed a lower symmetry space group (*Pnn*2) for a polycrystal synthesized at 1200°C and 22GPa, with $a_{KM} \approx 5.11$Å, $b_{KM} \approx 14.02$Å and $c_{KM} \approx 8.73$Å, using the (a, b, c) $\Rightarrow$ (b, a, -c) rotation law as the structure setting.

High pressure synthesis and deformation

The sample of shy B used in this study was synthesized and deformed at the Bayerisches Geoinstitut in a Kawai multianvil apparatus. For synthesis, a mixture of high purity oxides (MgO, SiO_2 quartz, brucite), was compressed under quasi-hydrostatic conditions, and annealed 3 hours at 20GPa and 1100°C (run S5128). Then, the resulting phase was recovered, end-polished and positioned in another high-pressure cell designed to induce deviatoric stresses (Cordier & Rubie, 2001), at the same pressure and at temperatures 1000-1100°C, during 30min (run S5131).

Transmission electron microscopy

Two thin foils were ion milled down to electron transparency, at liquid nitrogen temperature (in a Gatan® DuoMill™ Model 600), to reduce ion damage since shy B is sensitive to ion irradiation. For the same reasons, TEM analyses were conducted at

the university of Lille with a Philips® CM30 microscope operated at 300kV and associated with a Gatan® cold stage (liquid nitrogen temperature) in order to minimize electron damage.

Precession electron diffraction (PED) has been used to set diffraction conditions appropriate for dislocation imaging and characterization. This technique strongly reduces multiple diffractions and leads to intensities of diffraction spots closely related to the structure factors (Vincent & Midgley, 1994). Hence, it facilitates structure identification. PED is achieved with a “Spinning Star” precession module from the Nanomegas company.

The dislocation Burgers vector identifications are performed using the conventional invisibility criterion $\boldsymbol{g}.\boldsymbol{b} = 0$ with the weak-beam dark-field (WBDF) technique, the Ishida’s thickness fringe method (Ishida *et al.*, 1980; and Miyajima & Walte, 2009) and the LACBED technique (Tanaka *et al.*, 1980; Cherns & Preston, 1986; Cherns & Morniroli, 1994; and Morniroli, 2004). These last two methods are useful to characterize electron sensitive materials. Indeed, they give access to the $\boldsymbol{g}.\boldsymbol{b}$ product, considering the orientation and the number of thickness fringes terminating on the analyzed dislocation (Ishida’s method), or considering the orientation and the number of Bragg line splittings on the investigated dislocation (LACBED technique). Consequently, only three diffraction conditions are necessary to index a dislocation. When the dislocation segment analyzed is long enough, a single LACBED pattern may be sufficient to gather these three diffraction conditions.

Results

The sample average grain size is $30 \pm 5\mu m$. In some grains, we have observed boundaries which are crystallographically controlled (figure 1). Further analyses of electron diffraction patterns performed with the PED technique suggests that both *Pnnm* and *Pnn*2 may coexist in our sample. Since these two phases exhibit only slight structural differences that are not likely to affect dislocation structure, we will, in a first approach ignore the influence of space group differences in our characterization. We further note that the absence of evidence between dislocations and boundaries is a further evidence that plasticity is not significantly affected by these structural details. Most grains contain dislocations. Seven grains have been

investigated in details. In all these grains, the dislocation densities, obtained with the Ham method (1961), are approximately the same (around 2.10^{12} m^{-2}). Abundant low-angle sub-grain boundaries have been observed (Figure 2).

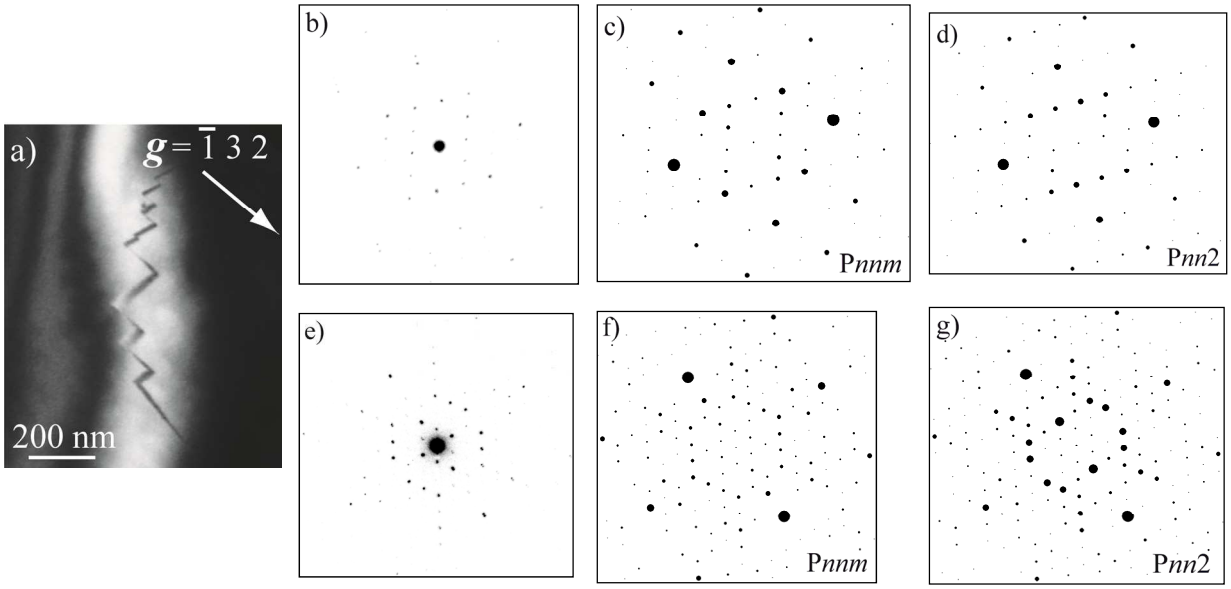

Figure 1: *Antiphase boundary (APB), Pnnm and Pnn2 phase occurrences. (a) WBDF picture obtained along the* $[11\bar{1}]$ *zone axis, with* ***g:*** $\bar{1}32$*, showing a faceted APB in contrast; (b) PED experimental pattern of a grain along the* $[212]$ *zone axis; (c) corresponding PED simulated pattern with the Pnnm space group, achieved with the Electron Diffraction software (Morniroli et al., 1994), with kinematic simulation, close to the experimental pattern; (d) corresponding PED simulated pattern with the Pnn2 space group, far from the experimental pattern; (e) PED experimental pattern of a grain along the* $[100]$ *zone axis; (f) corresponding PED simulated pattern with the Pnnm space group, far from the experimental pattern; (g) corresponding PED simulated pattern with the Pnn2 space group, close to the experimental pattern.*

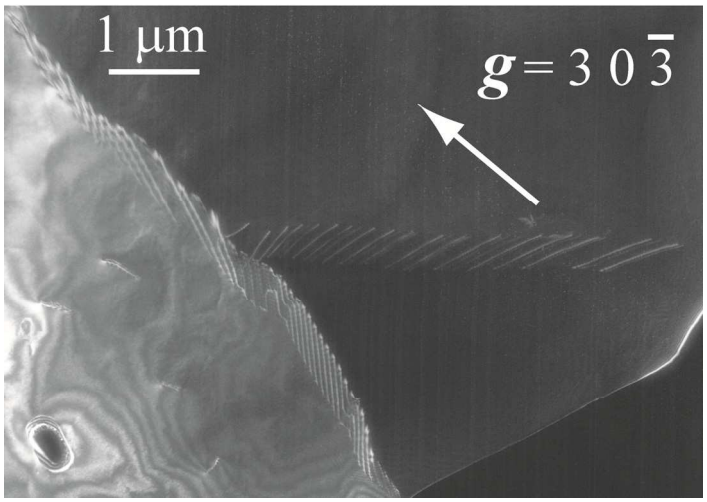

Figure 2: *Micrographs of two sub-grains, viewed along the* $[111]$ *zone axis, in WBDF condition, with* ***g:*** $30\bar{3}$.

Dislocation Burgers vectors

Figures 3a and 3b show a grain containing four dislocation families labeled *"1"*, *"2"*, *"3"* and *"4"*. Figures 3c is an enlargement of a dislocation from figure 3a which is shown in figure 3d with a different diffraction vector. From figure 3c, imaged with the $\bar{3}0\bar{3}$ diffraction vector, the ***g.b*** product value of the considered dislocation is $n = \pm 3$, as determined from the Ishida's method (Ishida *et al.* 1980). This dislocation is out of contrast with g: $00\bar{6}$, and exhibits $n = \pm 1$ with g: $\bar{1}23$ (figure 3d). The Burgers vector of this dislocation is thus $\pm[100]$.

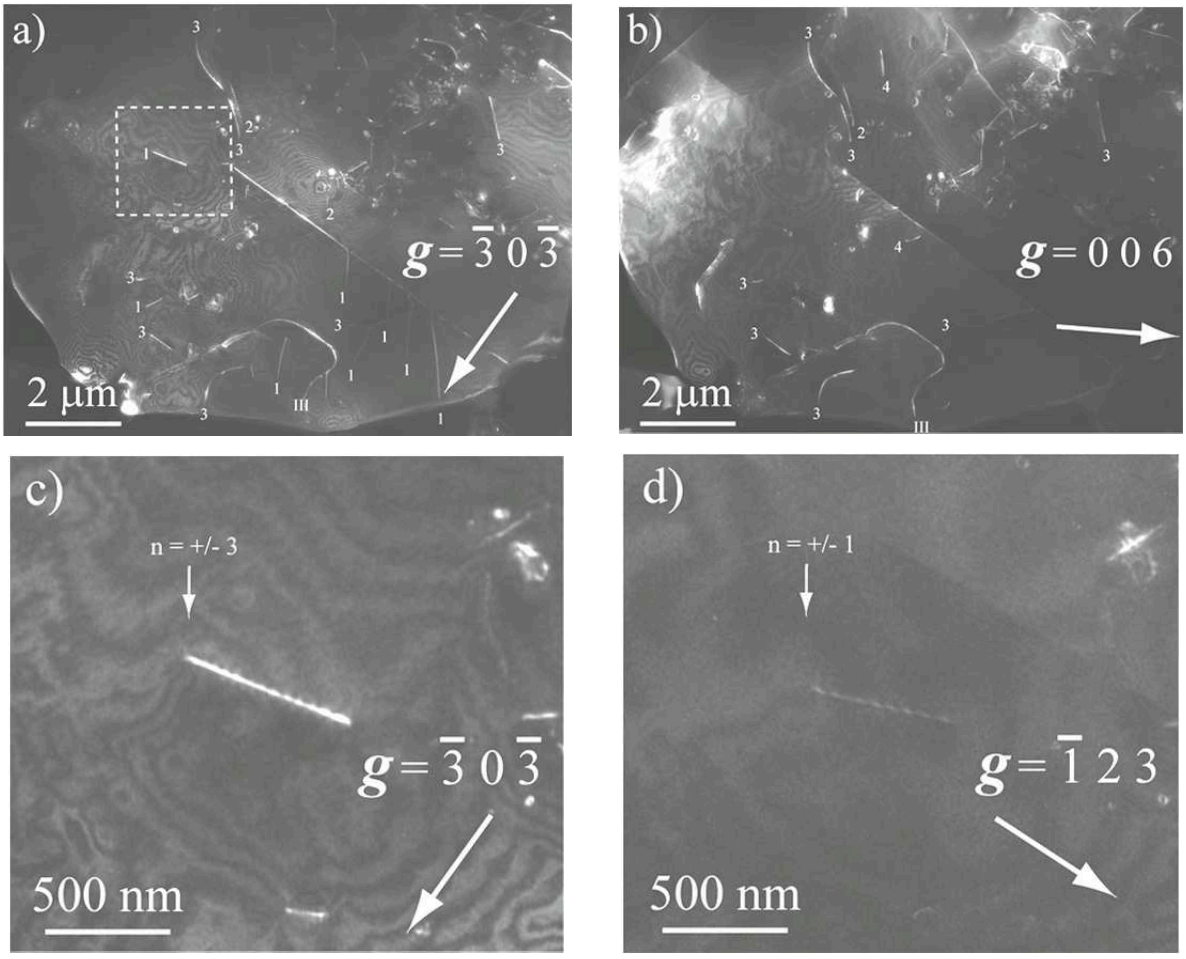

Figure 3: *WBDF micrographs obtained along the* $[010]$ *zone axis. (a) Diffraction vector* ***g:*** $\bar{3}0\bar{3}$, *eight dislocations labeled "1", two dislocations labeled "2", and eight dislocations labeled "3" are in contrast, whose a long and curved dislocation labeled "III"; the dashed white lines rectangle designates the region magnified in (c) and (d); (b) diffraction vector* ***g:*** 006, *dislocations "2", dislocations labeled "3", and two dislocations labeled "4" are in contrast; (c) zone magnified from (a) with* ***g:*** $\bar{3}0\bar{3}$ *showing a dislocation with fringe contrast characteristic of* ***g.b***$=\pm 3$*; (d) same zone than (c) with* ***g:*** $\bar{1}23$ *showing a dislocation with fringe contrast characteristic of a* ***g.b***$=\pm 1$.

Figure 4a shows a grain containing three dislocation families. The dislocation (labeled *"2"*) shown in figure 4b exhibits a ***g.b*** product $n = \pm 6$ when imaged with g: 006 diffraction vector and is out of contrast with g: 600 (figure 4c). Furthermore, it appears, from other diffraction analyzes, that there is no $[0v0]$ component in the dislocation Burgers vector. Consequently, the Burgers vector of this dislocation is $\pm[001]$.

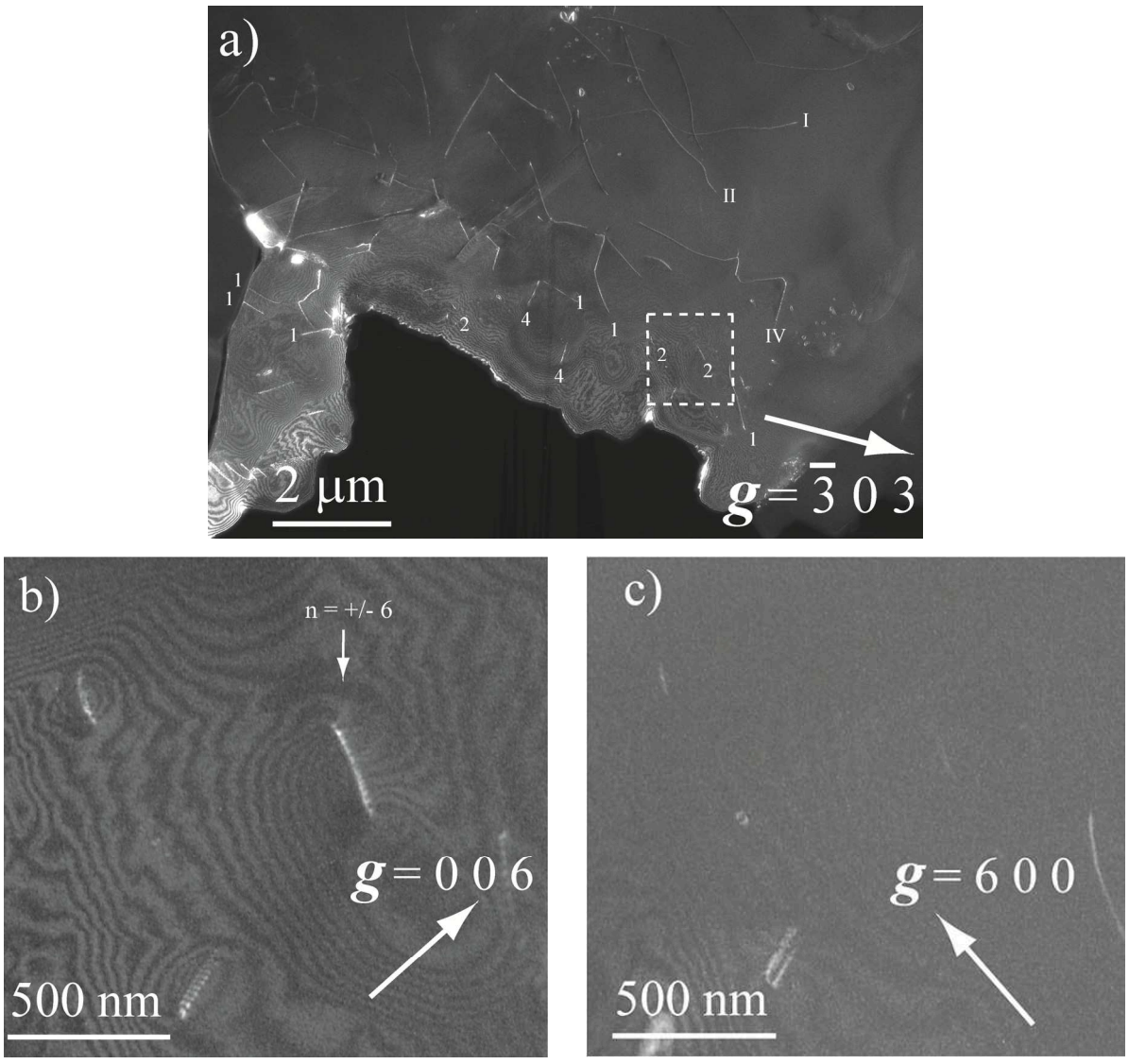

Figure 4: *WBDF images achieved along the* $[010]$ *zone axis. (a) Condition* ***g:*** $\bar{3}03$*, seven dislocations labeled "1", whose a long and curved dislocation labeled "I", four dislocations labeled "2", whose a long and curved dislocation labeled "II", three dislocations labeled "4", whose a long and curved dislocation labeled "IV"; the dashed white straight lines rectangle designates the region zoomed in (b) and (c); (b) zone extracted from (a) with* ***g:*** 006 *showing a dislocation with fringe contrast characteristic of a* ***g.b*** *product of* ± 6*; (c) same zone than (b) with* ***g:*** 600*, the dislocation designated by an arrow in (b) is out of contrast.*

An example of a Burgers vector characterization, obtained exploiting the LACBED technique, is illustrated in figure 5. Three independent Bragg lines, indexed using the ‘‘Electron Diffraction’’ software from J.P. Morniroli *et al.* (1994), are superimposed over the studied dislocation. The Cherns and Preston rules (Cherns & Preston, 1986), enable us to identify $n=-7$ with the $\bar{1}66$ diffraction vector, $n=-2$ with $\bar{1}71$, and $n=10$ with $15\bar{9}$, looking at the splittings generated by the dislocation / Bragg line interactions. The resolution of the system of three equations gives the $[10\bar{1}]$Burgers vector. It can be noted, from the WBDF micrograph of the dislocation observed on figure 5, that this dislocation is partially dissociated. The dissociation distance is too small to affect the LACBED patterns. The dissociation law should be symmetrical as various micrographs, obtained with three different diffraction conditions, reveal that both of the connected partial dislocations show the same contrast. We tentatively propose the following dissociation scheme: $[10\bar{1}] \Leftrightarrow 1/2[10\bar{1}]+1/2[10\bar{1}]$.

Using the same methodology, all dislocation families labeled *“1”*, *“2”*, *“3”* and *“4”*, observed on figures 3a, 3b and 4a, can be attributed the following Burgers vectors: $\pm[100]$, $\pm[001]$, $\pm[101]$ and $\pm[10\bar{1}]$, respectively. It is worth noticing that all the $\langle 101\rangle$ dislocations, observed in these figures, are dissociated very probably with a symmetrical dissociation law: $\langle 101\rangle \Leftrightarrow 1/2\langle 101\rangle + 1/2\langle 101\rangle$.

The diffraction vectors used for this characterization (006, 600, 303, $30\bar{3}$, 0120 …) have been selected for their high structure factor values (Table 1) which lead to a high contrast whenever the invisibility contrast is not satisfied.

During this study, 23 $[100]$ dislocations, 12 $[001]$ dislocations and 17 $\langle 101\rangle$ and $1/2\langle 101\rangle$ dislocations were found.

Table 1: Structure factors *F* for several diffraction vectors *g* calculated for *Pnn*2 and *Pnnm* respectively

g	F	g	F	g	F	g	F
101	179/155	002	2287/222	200	442/169	020	57/136
202	57/0	004	259/606	400	221/0	040	0/2
303	4048/4606	006	3783/4107	600	651/771	060	108/444
404	55/99	008	254/31	800	14/15	080	56/70
505	21/4	0010	10/42	1000	19/1	0100	85/36
						0120	1095/1654
						0140	0/12
						0160	173/193

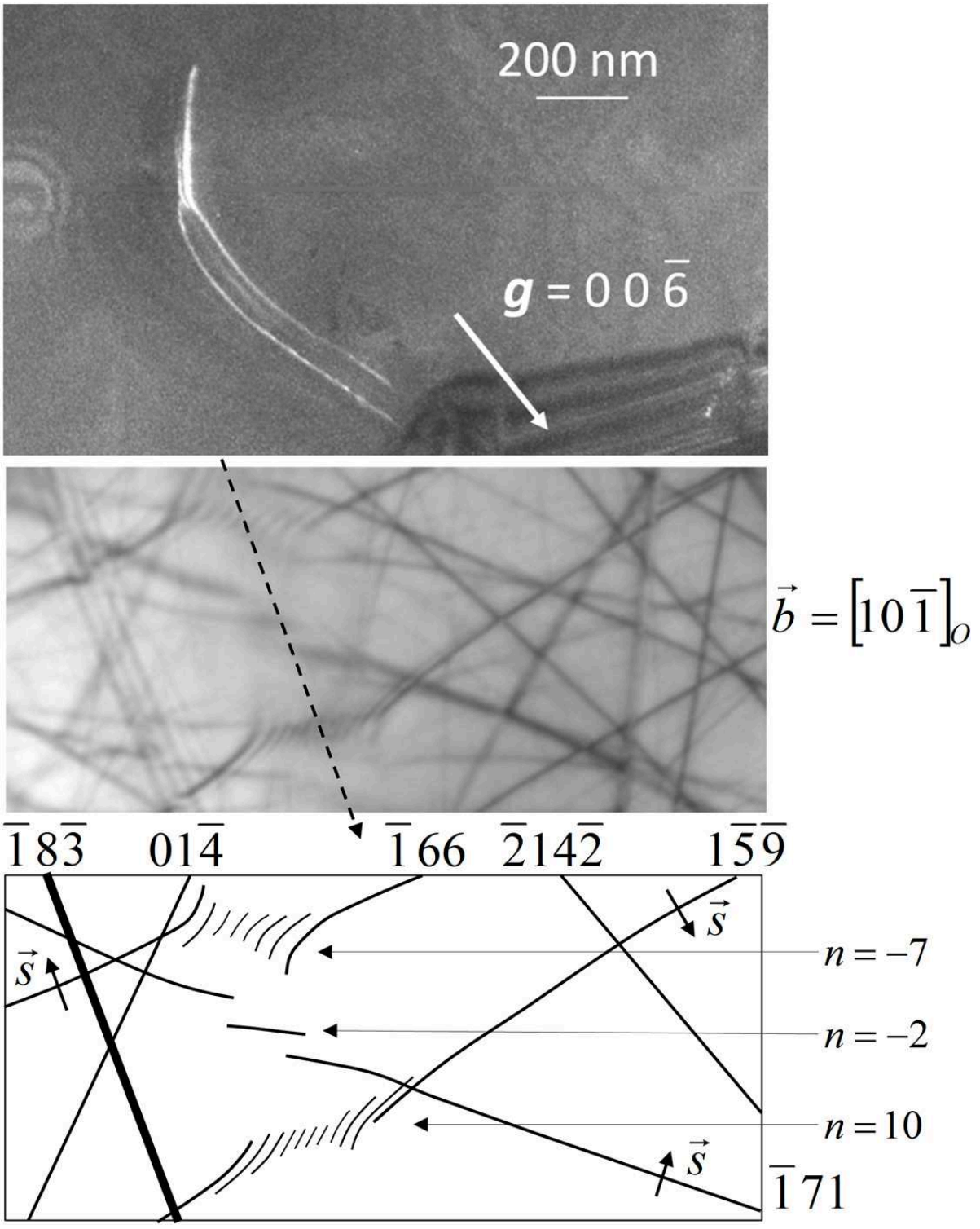

Figure 5: *Indexation of a dislocation with the LACBED technique: (a) Micrograph of the studied dislocation viewed along the* $[100]$ *zone axis, with* ***g:*** $00\bar{6}$*; (b) experimental LACBED pattern where the black dashed arrow designates the shadow image of the dislocation (on the left of the pattern) and the orientation of the line vector; (c) kinematical simulation of the Bragg lines and kinematical simulation of the sign of the s deviation parameter, achieved with the Electron Diffraction software (Morniroli et al., 1994), corresponding to the experimental pattern (the Bragg line splittings are indicated).*

Slip planes and climb mechanisms

Very long dislocations (several μm long), observed along two zone axes ($[100]$ and $[111]$), are in contrast with the $\bar{3}03$ and the $\bar{1}4\bar{3}$ diffraction vectors (figures 6a-6b), with $n=\pm 3$ and $n=\pm 1$ respectively, and out of contrast with the $00\bar{6}$ and the 0120 diffraction vectors (figures 6c-6d). Consequently, the Burgers vector of these dislocations is $\pm[100]$. As they are aligned along the $[001]$ direction, they have an edge nature. This explains why a residual contrast is observed under conditions where ***g.b***=0 (figures 6c-6d). This residual contrast enables us to note that, along the $[100]$ zone axis, the plane which contains the considered dislocations is edge-on (dashed line on figure 6d highlighting the trace of the (010) plane). Consequently, this dislocation belongs to the $[100](010)$ slip system. Furthermore, a curved and long $[100]$ dislocation (labeled "l") has been observed along the $[010]$ zone axis in figure 4a. This confirms that $[100]$ dislocations glide on the (010) plane. Most of the analyzed sub-grain boundaries are composed of $[100]$ dislocations, as in figure 2 for example, which increases the proportion of $[100]$ in relation to $[001]$, $\langle 101\rangle$ and $1/2\cdot\langle 101\rangle$ dislocations. Thus, $[100]$ dislocations are also moving by climb, which is required to form equilibrated sub-grain boundaries.

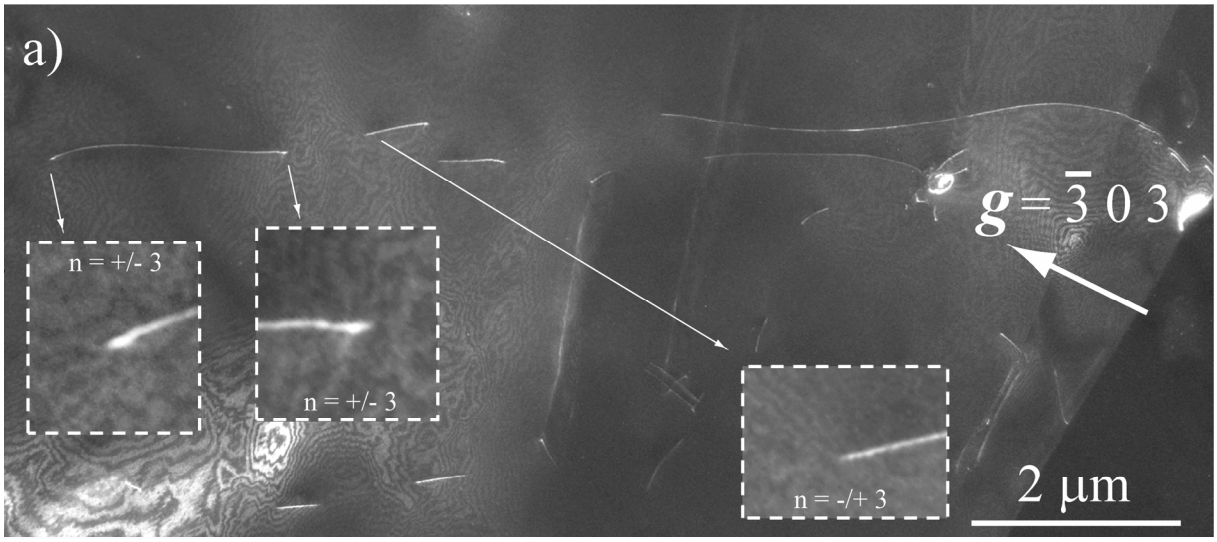

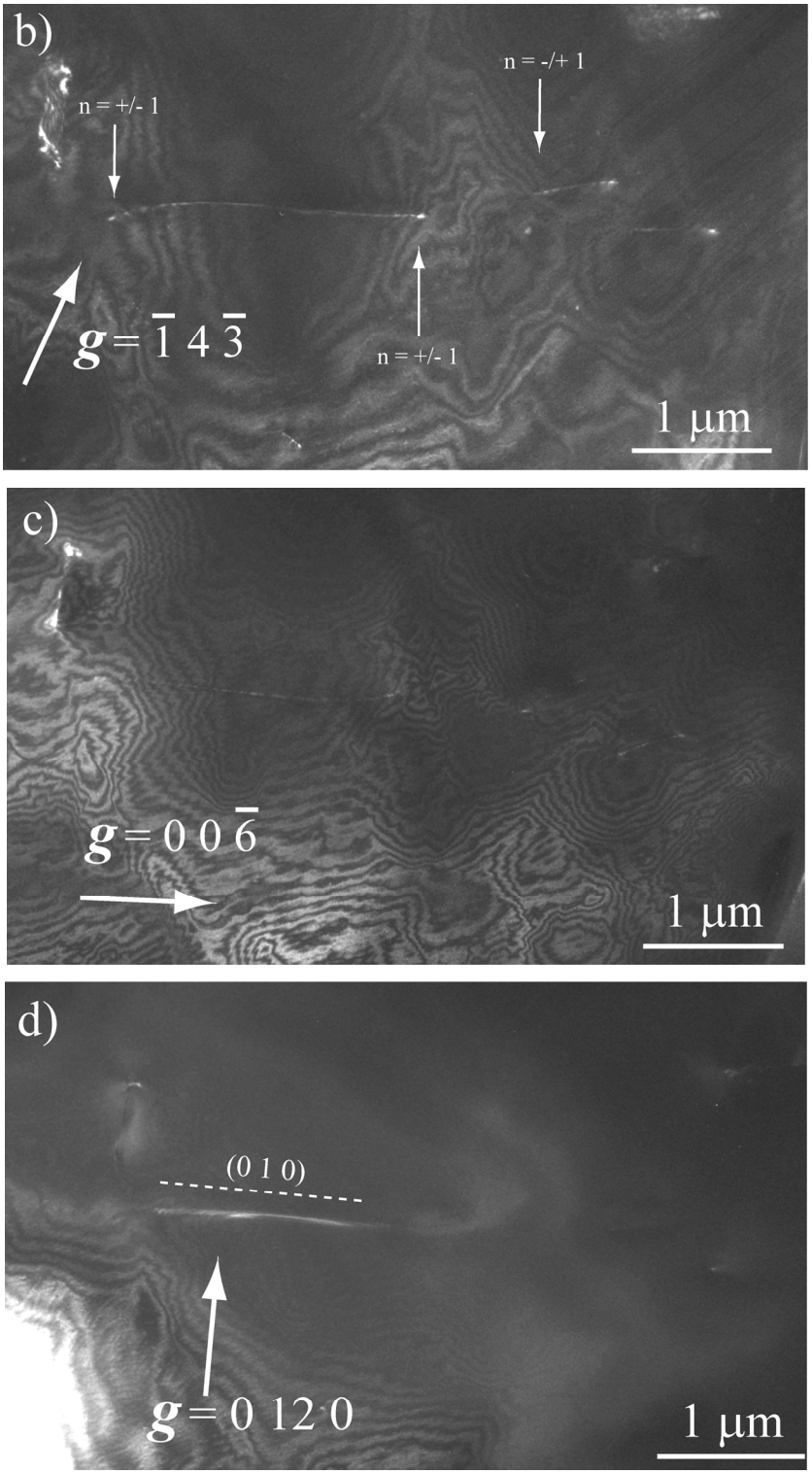

Figure 6: *WBDF pictures achieved along the* $[100]$ *zone axis. (a) Condition* ***g:*** $\bar{3}03$*, showing long dislocations (the size of the longest one is 3.5*μ*m) with fringe contrast characteristic of a* ***g.b*** *product of* ± 3 *(three zooms are done in order to see the fringe contrasts); (b) condition* ***g:*** $\bar{1}4\bar{3}$ *(left part of (a)), showing dislocations with fringe contrast characteristic of a* ***g.b*** *product of* ± 1*; (c) same zone than (b) with* ***g:*** $00\bar{6}$*, the long dislocations are out of contrast; (d) same zone than (b) with* ***g:*** 0120*, the long dislocations have a residual contrast, which enables us to notice that the* (010) *plane is edge-on.*

From figures 3a and 4a, long and curved dislocations, labeled “II”, “III”, and “IV”, are observed along the $[010]$ zone axis. As established previously, the Burgers vector of these dislocations are $\pm[001]$, $\pm[101]$ and $\pm[10\bar{1}]$ respectively. This suggests (010) as a likely glide plane for this dislocations, which leads to the slip systems: $[001](010)$, $[101](010)$, and $[10\bar{1}](010)$.

Figures 7a and 7b show several dissociated dislocations; a perfect one which begins to dissociate into two partial ones, labeled “single”; and dislocations dissociated into two, three and four partials, labeled “double”, “triple” and “quadruple”, respectively. They all exhibit the same line orientation: $[0\bar{1}1]$. We propose as a working hypothesis that they belong to the same dislocation family. From figure 7c, the ***g.b*** product value of the dislocation labeled “double” is found to be $n = \pm 3$ with the $00\bar{6}$ diffraction vector (figure 7c). Furthermore, this dislocation is out of contrast with the $\bar{3}0\bar{3}$ diffraction vector (figure 7d), and the stacking fault is in contrast with the $\bar{1}32$ diffraction vector (figure 7a). This suggests that the Burgers vectors of each partial dislocation are $\pm 1/2[10\bar{1}]$, as already suggested. Taking into account the line direction of this dislocation, $[0\bar{1}1]$, the glide plane is (111), and so the slip system is $[10\bar{1}](111)$. Moreover, the studied dissociated dislocation belongs to the $(10\bar{1})$ plane, as this plane is seen edge-on, in figure 7b. Consequently, this dislocation glide on the (111) plane and climb dissociates on the $(10\bar{1})$ plane with a large dissociation width (approximately 130 nm).

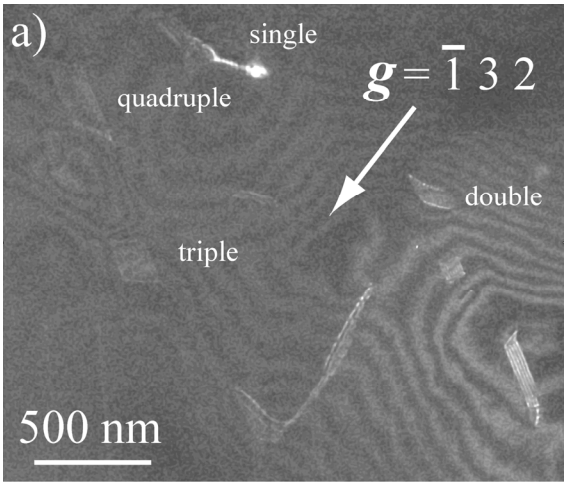

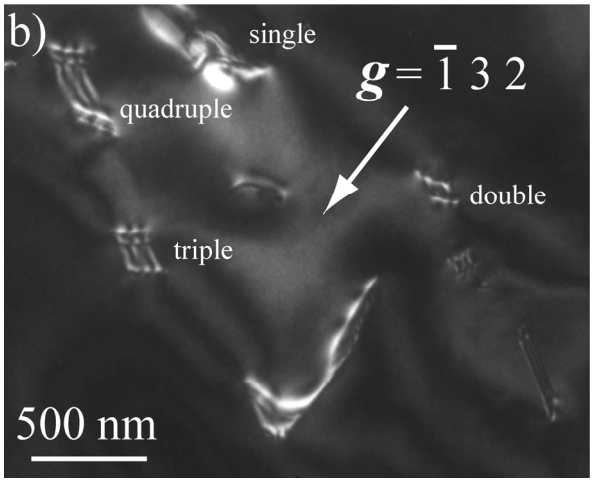

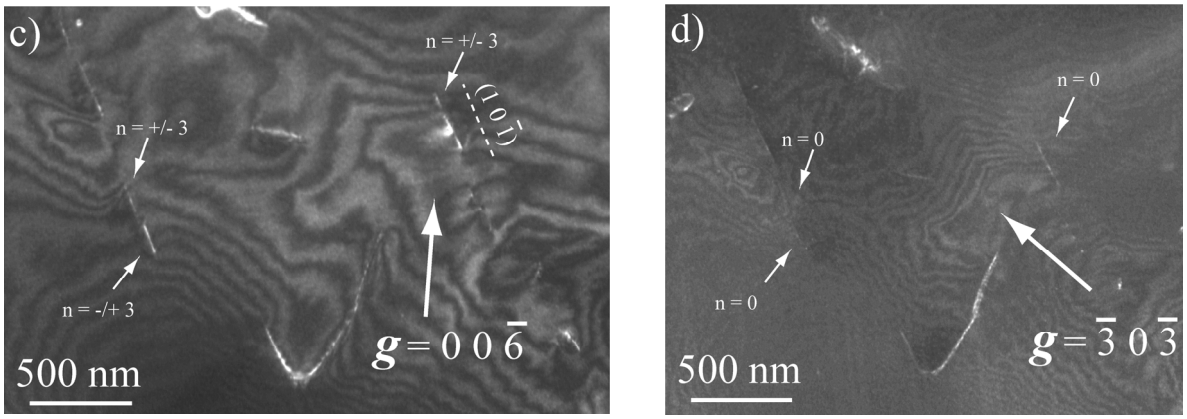

Figure 7: *Micrographs in WBDF conditions. (a) Condition* ***g:*** $\bar{1}32$*, along the* $[11\bar{1}]$ *zone axis, dissociated dislocations labeled "single", "double", "triple" and "quadruple" are obtained with an high deviation parameter (the stacking faults are in contrast); (b) same zone, with the same condition, but with a smaller deviation parameter than in (a); (c) same zone, condition* ***g:*** $00\bar{6}$*, along the* $[010]$ *zone axis, showing three dislocations with fringe contrast characteristic of a* ***g.b*** *product of* ± 3*; (d) same zone, condition* ***g:*** $\bar{3}0\bar{3}$*, along the* $[010]$ *zone axis, the three dislocations designated by arrows in (c) are out of contrast.*

Discussion

The elastic energy associated with a dislocation is proportional to μb^2 (per unit length of dislocation line), where μ is the shear modulus of the considered dislocation glide plane. From a simple energetic point of view, one expects that dislocations involve preferentially the shortest Burgers vector allowed by the crystal structure (in fact, the Bravais lattice). Indeed, in this study, we have shown the predominance of $[100]$ dislocations (b ≈ 5.1Å), followed by $[001]$ dislocations (b ≈ 8.7Å). Dislocations with the longest Burgers vector, $\langle 101 \rangle$ (b ≈ 10.1Å), are frequently dissociated into two $1/2\langle 101 \rangle$ partial dislocations (b ≈ 5.0Å).

The occurrence of dislocations with Burgers vectors larger than 10Å raises the question of their stability. Frank (1951) has suggested that eventually, the elastic energy of a dislocation might exceed the surface energy leading to the formation of a hollow core. Nevertheless, such Burgers vectors have been recently discovered in anhydrous minerals like garnet and wadsleyite, and hydrous minerals as phase A. In phase A, we have reported $1/3\langle 11\bar{2}3 \rangle$ dislocations with very large Burgers vectors (12.4Å) (Mussi *et al.*, 2012). In garnets, Voegelé *et al.* (1998) have characterized $1/2\langle 111 \rangle$ (b ≈ 10.0Å), $\langle 100 \rangle$ (b ≈ 11.5Å) and (less frequently) $\langle 110 \rangle$ dislocations (b ≈

16.3Å). The latter is however restricted to the lowest temperatures where garnets approaches the brittle-ductile transition. In case of wadsleyite deformed experimentally, the observation of $[010]$ dislocations (11.4 Å) has been interpreted as the result of large stresses generated during cold compression of the sample in the multianvil apparatus (Thurel *et al.*, 2003). It is likely that the observation in our specimen of $\langle 101 \rangle$ dislocations with a large Burgers vector result from the same mechanism. Those dislocation are thus not regarded as the result of the deformation of shy B at high-P, high-T.

The $[100](010)$ and $[001](010)$ slip systems have been identified in this study. Moreover, climb dissociation of $\langle 101 \rangle$ perfect dislocations into $1/2\langle 101 \rangle$ partial dislocations, in the $\{101\}$ planes, have been characterized in this specimen. The plastic anisotropy of shy B is strongly constrained geometrical by the predominant role of the (010) plane in plastic glide. The observation of climb dissociation in some $\{101\}$ planes suggests that secondary glide or climb may take place in those planes. Glide in $\{111\}$ planes is observed, but only for dislocations with Burgers vectors of the $\langle 101 \rangle$ type, generated at low temperatures under high stresses.

Conclusion

Our study suggests that under cold subduction conditions, plastic deformation of shy B could be accommodated by dislocations with plastic shear strongly localized in the (010) plane. Several shear directions along the $[100]$, $[001]$ (and possibly $\langle 101 \rangle$ Burgers vectors under high stress) could be activated in this plane. This strongly anisotropic plastic behavior suggests that during subduction, shy B, if present, may develop strong crystal preferred orientation leading to markedly anisotropic elastic properties.

Acknowledgements:

The TEM national facility in Lille is supported by the CNRS (INSU) and the Conseil Régional du Nord – Pas de Calais, France. This study was supported by the ANR project SUBDEF grant n° ANR-08-BLAN-0192 to Bruno Reynard.

References

Amiguet, E., Reynard, B., Caracas, R., Van de Moortèle, B., Hilairet, N., Wang, Y. (2012): Creep of phyllosilicates at the onset of plate tectonics. *Earth Planet. Sci. Lett.*, **345-348**, 142-150.

Bell, I.A., Wilson, C.J.L., McLaren, A.C., Etheridge, M.A. (1986): Kinks in mica: Role of dislocations and (001) cleavage. *Tectonophysics*, **127**, 49-65.

Cherns, D. & Morniroli, J.P. (1994): Analysis of partial and Stair-Rod dislocations by large angle convergent beam electron diffraction. *Ultramicroscopy*, **53**, 2, 167-180.

Cherns, D. & Preston, A.R. (1986): Convergent-beam diffraction of crystal defects. In Proceedings Eleventh International Congress on Electron Microscopy, Kyoto, 721.

Christoffersen, R. & Kronenberg, A.K. (1993): Dislocation interactions in experimentally deformed biotite. *J. Struc. Geolg.*, **15**, 1077-1095.

Cordier, P. & Rubie, D.C. (2001): Plastic deformation of minerals under extreme pressure using a multianvil apparatus. *Mater. Sci. Eng. A*, **309-310**, 38-43.

F. C. Frank, Acta Cryst. 4, 497 (1951).

Ham, R.K. (1961): The determination of dislocation densities in thin films. *Phil. Mag.*, **6**, 1183-1184.

Heggen, M., Houben, L., Feuerbacher, F. (2010): Plastic-deformation mechanism in complex solids, *Nature Materials*, **9**, 332-336.

Hilairet, N. & Reynard, B. (2009): Stability and dynamics of serpentinite layer in subduction zone. *Tectonophysics*, **465**, 24-29.

Hilairet, N., Reynard, B., Wang, Y.B., Daniel, I., Merkel, S., Nishiyama, N., Petitgirard, S. (2007): High-pressure creep of serpentine, interseismic deformation, and initiation of subduction. *Science*, **318**, 1910-1913.

Ishida, Y., Ishida, H., Kohra, K., Ichinose, H. (1980): Determination of the Burgers vector of a dislocation by weak-beam imaging in a HVEM. *Phil. Mag. A*, **42**, 453-462.

Koch-Müller, M., Dera, P., Fei, Y., Hellwig, H., Liu, Z., Van Orman, J., Wirthe, R. (2005): Polymorphic phase transition in superhydrous phase B. *Phys. Chem. Minerals*, **32**, 349-361.

Komabayashi, T. & Omori, S. (2006): Internally consistent thermodynamic data set for dense hydrous magnesium silicates up to 35GPa, 1600°C: implications for water circulation in the Earth's deep mantle. *Phys. Earth Planet. Inter.*, **156**, 89–107.

Meade, C. & Jeanloz, R. (1991): Deep-focus earthquakes and recycling of water into the earth's mantle. *Science*, **252**, 68-72.

Metsue, A., Carrez, P., Denoual, C., Mainprice, D., Cordier, P. (2010): Plastic deformation of wadsleyite: IV Dislocation core modelling based on the Peierls–Nabarro–Galerkin model. *Acta Mater.*, **58**, 1467–1478.

Miyajima, N. & Walte, N. (2009): Burgers vector determination in deformed perovskite and post-perovskite of $CaIrO_3$ using thickness fringes in weak-beam dark-field images, *Ultramicroscopy*, **109**, 683–692.

Morniroli, J.P. (2004): Large-angle convergent-beam electron diffraction applications to crystal defects, CRC Press, Boca Raton, FL, 376 p.

Morniroli, J.P., Vankieken, D., Winter, L. (1994): Electron Diffraction. Dedicated Software to Kinematicaly Simulate CBED Patterns (USTL, Lille).

Mussi, A., Cordier, P., Frost, D.J. (2012): Crystal defects in dense hydrous magnesium silicate phase A deformed at high pressure: characterization by transmission electron microscopy, *Eur. J. Mineral.*, **24**, 429-438.

Omori, S., Komabayashi, T., Maruyama, S. (2004): Dehydration and earthquakes in the subducting slab: empirical link in intermediate and deep seismic zones. *Phys. Earth Planet. Inter.*, **146**, 297-311.

Pacalo, R.E.G. & Parise, J.B. (1992): Crystals structure of superhydrous B, a hydrous magnesium silicate synthesized at 1400°C and 20GPa. *Am. Miner.*, **77**, 681-684.

Ringwood, A.E. & Major, A. (1967): High pressure reconnaissance investigations in system Mg_2SiO_4-MgO-H_2O. *Earth Planet. Sci. Lett.*, **2**, 130-133.

Schmidt, M.W. & Poli, S. (1998): Experimentally based water budgets for dehydrating slabs and consequences for arc magma generation. *Earth Planet. Sci. Lett.*, **163**, 361-379.

Tanaka, M., Ueno, K., Harada, Y. (1980): Large-angle convergent beam electron-diffraction. *J. Electron Microsc.*, **29**, 4, 408-412.

Thurel, E. & Cordier, P. (2003): Plastic deformation of wadsleyite: I. High-pressure deformation in compression. *Phys. Chem. Minerals*, **30**, 256-266.

Ulmer, P. & Trommsdorff, V. (1995): Serpentine stability to mantle depths and subduction-related magmatism. *Science*, **268**, 858-861.

Vincent, R. & Midgley, P.A. (1994): Double conical beam-rocking system for measurement of integrated electron diffraction intensities. *Ultramicroscopy*, **53**, 271-282.

Voegele, V., Cordier, P., Sautter, V., Sharp, T.G., Lardeaux, J.M., Marques, F.O. (1998): Plastic deformation of silicate garnets II. Deformation microstructures in natural samples. *Phys. Earth Planet. Inter.*, **108**, 319-338.

Yamasaki, T. & Seno, T. (2003): Double seismic zone and dehydration embrittlement of the subducting slab. *J. Geophys. Res.*, **108**, 2212.

Chapitre II : Développement de la tomographie des dislocations pour l'étude de la plasticité de l'olivine

Collaborateurs : Patrick Cordier (UMET), Sylvie Demouchy (GeoSciences Montpellier), Laurent Dupuy (CEA DEN/DMN/SRMA), Fabien Onimus (CEA DEN/DMN/SRMA)
Travaux réalisés depuis 2013

Introduction :

Comme nous l'avons vu précédemment, la détermination des vecteurs de Burgers $\boldsymbol{b}$ peut s'effectuer en WBDF par l'utilisation de plusieurs vecteurs diffractant $\boldsymbol{g}$ indépendants (généralement plusieurs $\boldsymbol{g}$ dont deux conditions d'extinction sont nécessaires). Il ne faut néanmoins pas négliger les problèmes liés aux contrastes résiduels. En effet, les conditions d'extinction *stricto sensu* doivent vérifier à la fois le produit $\boldsymbol{g}.\boldsymbol{b} = 0$, mais également le produit $\boldsymbol{g}.(\boldsymbol{b}\wedge\boldsymbol{u}) = 0$ où $\boldsymbol{u}$ est le vecteur ligne. Ces deux conditions sont rarement vérifiées simultanément. L'utilisation de la technique des franges d'égales épaisseurs (Ishida *et al.*, 1980) réduit le nombre de $\boldsymbol{g}$ indépendants à trois et permet de passer outre ce problème de contraste résiduel. Enfin, la caractérisation du vecteur de Burgers d'une dislocation est réalisable par LACBED en un cliché unique (voir exemple figure 4) et ce avec une dose limitée (Cordier & Heidelbach, 2013). La caractérisation des vecteurs de Burgers par MET est donc actuellement parfaitement maitrisée et optimisée.

Ce n'est pas encore le cas pour l'obtention des plans de glissement/montée des dislocations. D'un point de vue pratique, le porte-objet (PO) doit être pivoté pour mettre les plans à caractériser debout. Dans ces conditions d'orientation, les projections des lignes de dislocation vont se retrouver parfaitement rectilignes. Les indices de Miller des plans peuvent donc être indexés connaissant l'orientation de l'échantillon (voir par exemple figures 10 et 13, Thurel & Cordier 2003). Néanmoins, les gammes angulaires des PO sont limitées par leurs géométries et par l'espacement des pièces polaires des microscopes utilisés (ces gammes varient de +/- 30 ° à +/- 60 ° pour des PO conventionnels). Du fait de ces limitations techniques, il arrive que nous nous retrouvions dans l'impossibilité de mettre les plans recherchés debout. L'utilisation des projections stéréographiques (Tahara *et al.*, 2017) permet de sortir de cette impasse. Mais cette technique est fastidieuse et peu précise, elle ne peut être appliquée que pour quelques dislocations. Nous nous sommes donc dirigés vers la tomographie électronique en transmission des dislocations (TETD) pour lever ce verrou technique. L'optimisation de cet outil est détaillée dans le premier article présenté dans ce chapitre.

Les mécanismes fondamentaux de déformation plastique de l'olivine sont étudiés depuis plus de 50 ans sur toute la gamme de température du manteau supérieur (Raleigh, 1968) ; et pourtant de nombreuses questions subsistent … Dans la partie haute du manteau supérieur, l'olivine est sollicitée à des températures inférieures à 900 °C. Dans ces conditions de température, du fait de la forte friction de réseau, les dislocations sont en grande majorité vis et rectilignes ; leurs plans de glissement sont de ce fait difficiles à déterminer. A plus haute température, les microstructures des dislocations sont en revanche beaucoup plus complexes et en trois dimensions. En conclusion, la détermination des plans de glissement des dislocations dans l'olivine est souvent délicate. Nous avons donc développé la TETD pour que la troisième dimension nous permette de voir les microstructures d'un nouveau point de

vue et de révéler des mécanismes de déformation plastique originaux. Trois articles sur l'utilisation de la TETD sont présentés dans ce chapitre dans le but de comprendre les mécanismes de déformation de l'olivine.

I-2-1 Optimisation de la tomographie électronique des dislocations

Les premières études de tomographie datent des années 70 (Hounsfield, 1973). Ces recherches, à visées médicales, avaient pour objectifs de cartographier des organes par rayons X. Cependant, la résolution spatiale de cette technique ne permet pas d'observer des détails sub-microniques. Pour améliorer la résolution spatiale des volumes reconstruits de plusieurs ordres de grandeur, les études se sont dirigées vers la tomographie électronique en transmission (TET). Une des premières TET a permis d'obtenir des détails de 4 nm (Landis *et al.*, 1993) et il est actuellement possible d'atteindre des résolutions atomiques (Scott *et al.*, 2012 ; Chen *et al.*, 2013 ; Miao *et al.*, 2016).

Classiquement, la procédure expérimentale consiste à faire l'acquisition d'une série d'images projetées tous les 1 ou 2 degrés (série tiltée), qu'il faut ensuite aligner. La série tiltée alignée est transformée en empilement à l'aide d'algorithmes de reconstruction. L'algorithme le plus communément utilisé est la rétroprojection filtrée (WBP pour Weighted Back Projection, Herman *et al.*, 1976) qui comme son nom l'indique projette en sens inverse l'image sur l'objet à reconstruire (le filtre permet de réduire l'intensité des informations parasites). Une description de la méthode est détaillée sur la figure 5. La rétroprojection s'appuie sur la transformée de Radon, transformée qui consiste à intégrer une fonction le long de droites pour différentes orientations. Ces droites représentent les projections et sont exprimées en coordonnées polaires, et la fonction représente l'objet. L'algorithme WBP est principalement utilisé pour reconstruire des volumes fortement contrastés (idéalement en noir et blanc). D'autres algorithmes, comme l'ART (Algebric Reconstruction Technique) et le SIRT (Simultaneous Iterative Reconstruction Technique), peuvent être employés pour reconstruire des volumes faiblement contrastés. Ces algorithmes sont construits sur des méthodes itératives (Gordon *et al.*, 1970 ; Penczek *et al.*, 1992).

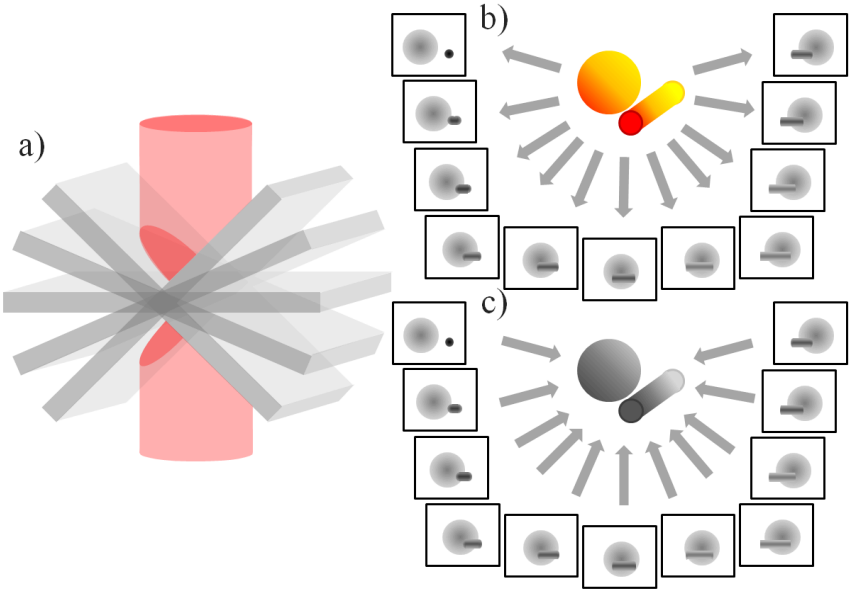

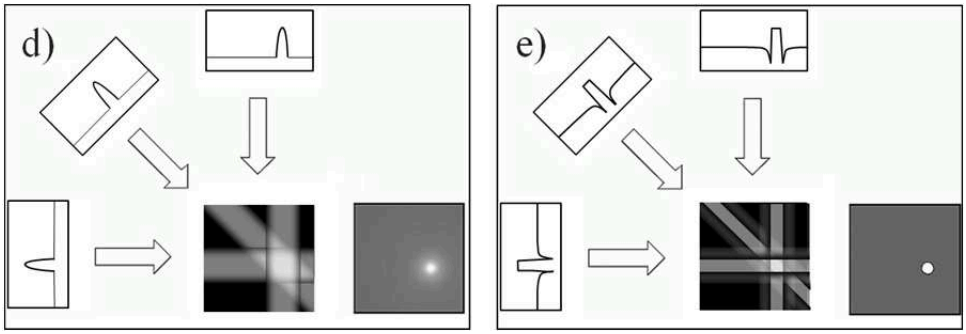

Figure 5 : *Technique de tomographie électronique : a) Le faisceau d'électrons traverse la lame mince pour chaque angle de pivotement et forme des images projetées (la gamme angulaire du PO est limitée et laisse derrière elle un volume manquant ou « missing-wedge » en anglais) ; b) l'ensemble des images projetées forme une série-tiltée ; c) l'algorithme de retro-projection, projette en sens inverse les images projetées et reconstruit le volume d'origine ; d) le volume reconstruit est flou lorsque l'algorithme de retro-projection n'est pas filtré; e) le volume est net lorsque l'algorithme de retro-projection est filtré.*

Contrairement à la TET conventionnelle qui s'appuie sur le contraste d'absorption, la TETD repose sur le contraste de diffraction. Comme indiqué précédemment (voir figure 2e), le contraste des dislocations est intimement lié à l'écart à Bragg ***s***. Pour garder le même contraste de dislocations sur toute la série tiltée, il faut donc s'assurer que ***s*** reste le même quel que soit l'angle de pivotement du PO. A cet égard, le vecteur diffractant ***g*** approprié (FS élevé et produit ***g***.***b*** différent de 0) doit être parfaitement aligné avec l'axe principal du PO (de préférence avec un écart angulaire inférieur à 0.1 °). Pour faciliter l'orientation des vecteurs diffractant, nous avons fait l'acquisition d'un PO à six degrés de liberté (déplacements en x, y et z ; et rotation en $\alpha = \pm 80$ °, $\beta = \pm 7.5$ ° et azimutal = ±5 ° à ±0.01 °). Il s'agit du PO HATA (High angle Triple Axes) obtenu à l'aide d'un financement BQR, d'un apport financier du Centre Commun de Microscopie (CCM) et de l'ERC RheoMan de Patrick Cordier (voir figure 6).

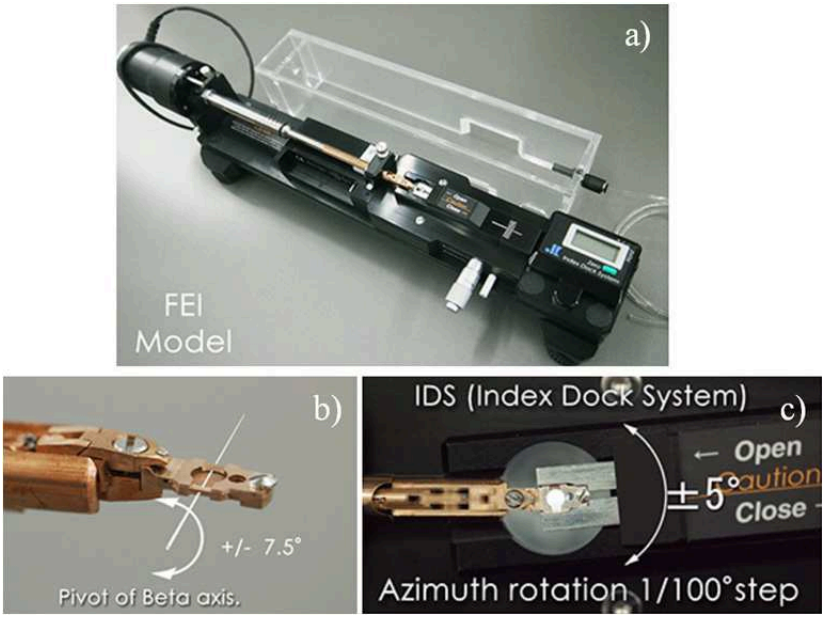

Figure 6 : *PO HATA : a) Visualisation globale : le PO a une gamme angulaire en α de ± 80 ° ; b) une gamme angulaire en β de ± 7.5 ° ; c) et une gamme angulaire en rotation azimutale de ± 5 ° avec une précision de 0.01 °. Photos extraites du site internet http://www.melbuild.com/newprouct_HATA_G2.html le 3 août 2018 (Hata et al., 2011).*

I-2-1-a Tomographie électronique en transmission des dislocations en mode WBDF

Cette section traite de la première TETD entreprise sur un minéral au travers d'un article disponible à la fin de ce chapitre. Ce travail de recherche, mené activement avec la collaboration de Patrick Cordier, décrit la méthode d'optimisation de la TETD en mode WBDF à partir d'un polycristal d'olivine élaboré et déformé par Sylvie Demouchy à 900 °C (collaboration avec le laboratoire GeoSciences à Montpellier). Nous avons utilisé un MET FEI® Tecnaï qui fonctionne à 200kV avec un filament LaB_6. Ce microscope, disponible au CCM, offre une grande gamme angulaire pour des PO double tilt (+/- 60 °).

La TETD peut être effectuée en mode WBDF (Barnard *et al.*, 2006), mais également en mode Scanning Transmission Electron Microscopy (STEM) (Tanaka *et al.*, 2008a-b ; Liu *et al.*, 2014 ; Oveisi *et al.*, 2017). En effet, il est possible, en principe, d'obtenir un contraste de dislocation de qualité en faisceau faible en mode STEM, en suivant le principe de réciprocité (Phillips *et al.*, 2011a-b). Nous avons exploré les deux possibilités. La MET conventionnelle (WBDF) donne un bon rapport signal sur bruit, mais les franges d'égales épaisseurs et le contraste oscillant des dislocations qui traversent l'épaisseur de la lame mince, créent un contraste trop hétérogène pour obtenir des volumes reconstruits interprétables. À l'inverse, le faisceau faible en mode STEM permet d'avoir un contraste homogène des dislocations et du fond, mais le rapport signal sur bruit est trop faible à cause de l'émission restreinte du filament LaB_6. La première difficulté a donc été de trouver des conditions d'observation des dislocations qui présentent un contraste homogène associé à un bon rapport signal sur bruit. En m'inspirant des travaux de Rebled et ses collaborateurs (2011), nous avons utilisé la précession électronique pour moyenner le contraste des micrographies. La figure 7 montre l'effet d'une précession de 0.1 ° sur une micrographie de dislocations dans d'olivine. Nous avons donc décidé de travailler en mode WBDF avec une légère précession pour obtenir des images contrastées et homogènes. Cette méthodologie est originale et particulièrement attrayante : elle permet de réaliser des reconstructions de dislocations 3D remarquables sans nécessairement être obligé d'utiliser un microscope onéreux. L'association de la précession à un MET qui fonctionne avec un canon à électrons d'émission thermoïonique (tungstène ou LaB_6), suffit amplement.

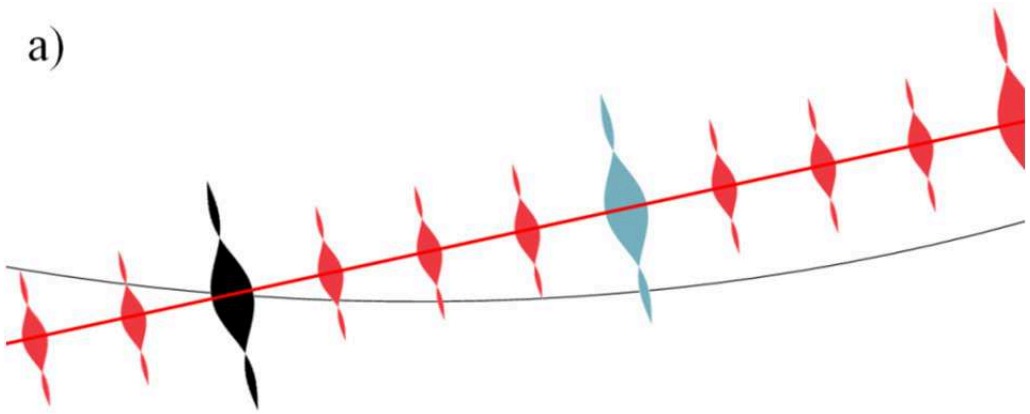

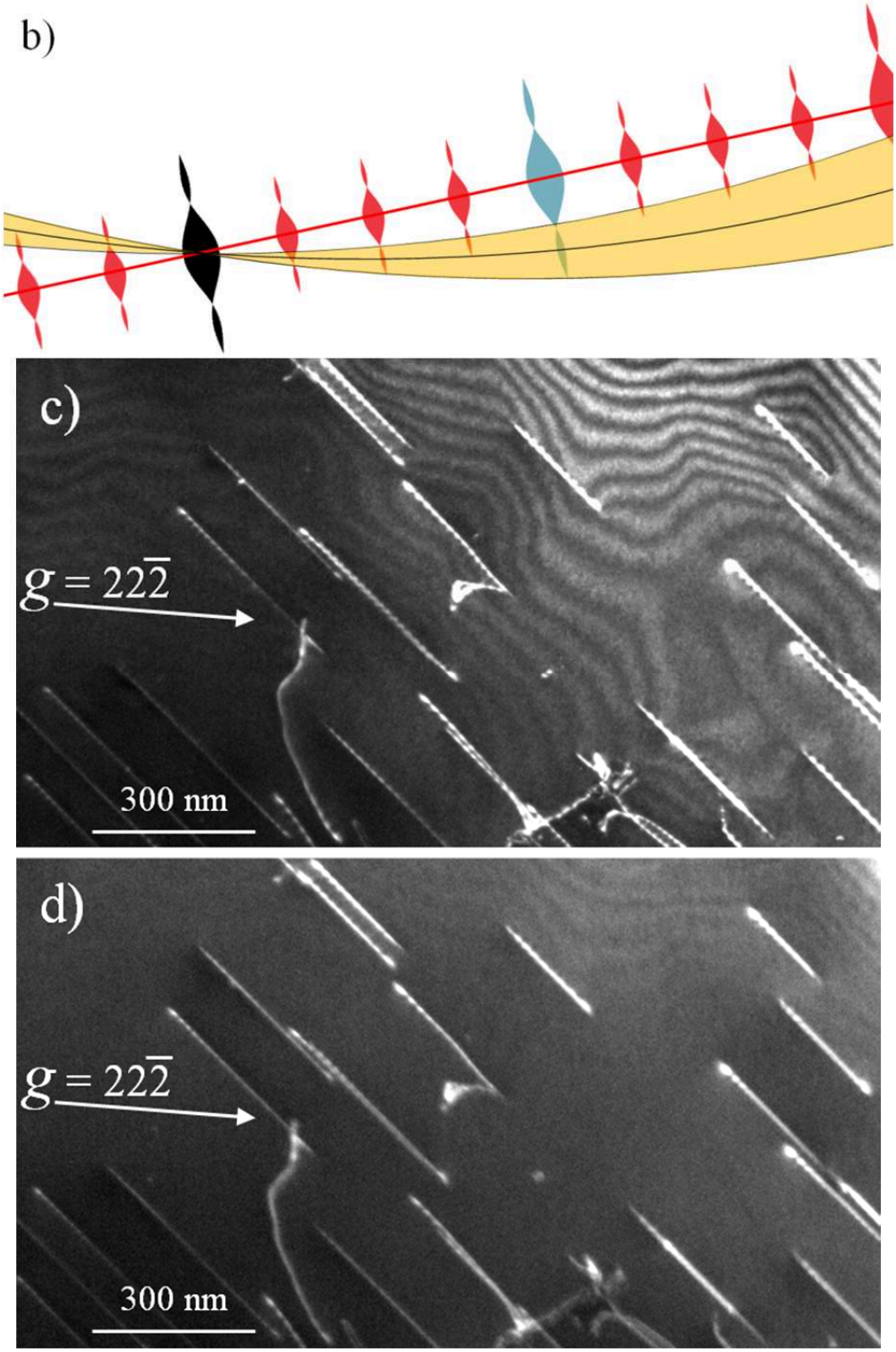

Figure 7 : *Effets de la précession sur la microstructure des dislocations : (a) Modèle d'intersection de la sphère d'Ewald, avec un réseau cristallin quelconque, dans le réseau réciproque, en WBDF, sans précession (la tache transmise est en noire et le tache diffractée, sélectionnée pour faire la micrographie WBDF, est en bleue) ; (b) Modèle d'intersection de la sphère d'Ewald, avec un réseau cristallin quelconque (en lien avec a)), dans le réseau réciproque, en WBDF, avec précession (la courbe de réflexion de la tache diffractée sélectionnée pour faire la micrographie WBDF, est en partie intégrée) ; (c) Micrographie WBDF obtenue avec le vecteur diffractant* $22\bar{2}$ *sans précession d'un monocristal d'olivine déformé à 806 °C; (d) Même image obtenue avec 0.1 ° de précession.*

Les post-traitements ont également toutes leurs importances. Les contrastes en mode WBDF restent faibles et rendent difficiles les alignements en mode automatique. Pour faciliter la réalisation de cette étape, nous avons fait en sorte, en cours d'acquisitions, de mettre des détails fins (par exemple des boucles de dislocation de quelques nm de diamètre) au centre des micrographies (au plus proche de l'axe de pivotement). Ces détails servent de repères pour l'étape d'alignement manuel. La figure 8 présente une sommation d'images alignées d'une série tiltée. Le détail qui a servi de repère, entouré en rouge sur la figure 8, est sommé à chaque image, puisqu'immobile après alignement, il est donc très contrasté. Les terminaisons de dislocations sur les faces supérieure et inférieure de la lame mince vont suivre une trajectoire perpendiculaire à l'axe de pivotement de la lame. Ces trajectoires sont très utiles pour déterminer l'orientation de l'axe de pivotement de la lame (voir figure 8). Par ailleurs, pour optimiser l'information, les images ont été filtrées numériquement (contraste de fond homogène et très sombre ; contraste des dislocations homogène et très clair). Nous avons choisi d'utiliser l'algorithme WBP, plus approprié pour reconstruire des objets contrastés.

Les microstructures 3D nous ont permis de retrouver les systèmes de glissement déjà observés dans la littérature (Raleigh, 1968 ; Gaboriaud *et al.*, 1981), mais également de révéler la présence de nouveaux systèmes. Cette étude a vérifié que le système de glissement [001]{110} est facile et donne une première vision statistique de la TETD (environ soixante plans de glissement ont été indexés). La tomographie nous a permis également de caractériser formellement le mécanisme de glissement dévié. Ces résultats auraient été difficilement obtenus par la technique stéréographique.

Des détails complémentaires, en liens avec cette étude, sont disponibles dans l'article sus-cité, accessible à la fin de ce chapitre (Mussi *et al.*, 2014).

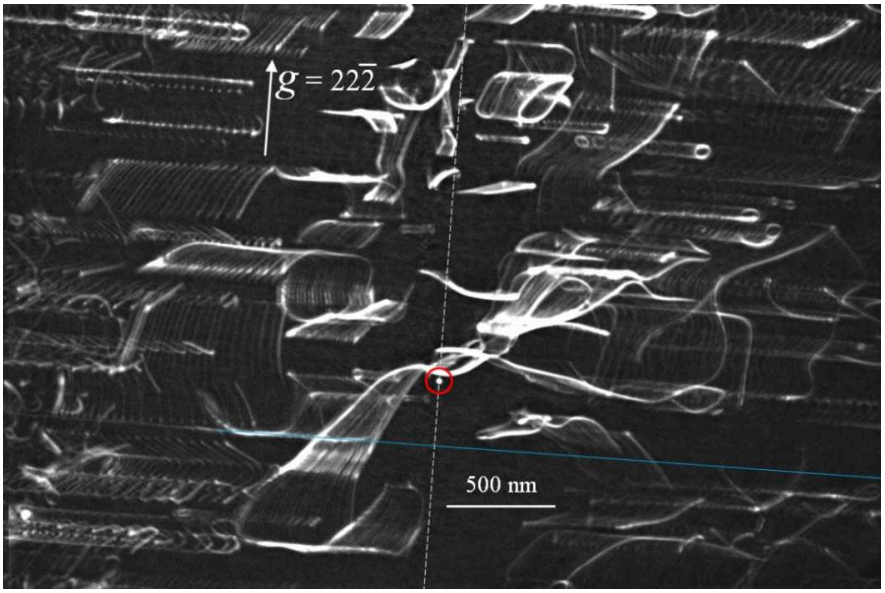

Figure 8 : *Détermination précise de l'axe de pivotement d'une série tiltée : La sommation des images projetées de la série tiltée (centrée et filtrée numériquement) fait ressortir un détail immobile (entouré en rouge sur la figure). L'axe de pivotement passe par ce détail. Les éléments contrastés, éloignés de l'axe de pivotement, se déplacent perpendiculairement à cet axe (exemple de chemin indiqué par la ligne bleue sur la figure). L'axe de pivotement peut donc être obtenu facilement par cette méthode (ligne blanche hachurée).*

I-2-1-b Tomographie électronique en transmission des dislocations en mode STEM

Ce travail de recherche est mené en collaboration avec Laurent Dupuy et Fabien Onimus à l'institut national des sciences et techniques nucléaire au service de recherches

métallurgiques appliquées du CEA, ainsi que Patrick Cordier du laboratoire UMET à Lille. L'objectif de cette première collaboration est de comprendre comment se sont formées les microstructures de dislocations du Zr déformé puis irradié aux ions en température. Les interactions de boucles de dislocations nanométriques avec les dislocations forment des configurations de dislocations complexes et très fines. Nous avons eu la chance de débuter cette collaboration en simultané avec l'installation d'un MET FEI® Titan Themis à l'Université de Lille (inauguré le 9 novembre 2017). Ce microscope de dernière génération, dédié au mode STEM, est équipé d'un filament X-FEG intense et cohérent, associé à un monochromateur. Ce microscope qui fonctionne à 300 kV, est parfaitement adapté à l'étude que nous voulons mener. L'intensité du faisceau est suffisamment élevée pour aller chercher des écarts à Bragg conséquents et ainsi obtenir des images de dislocations de finesses ultimes (résolutions proches de la taille des vecteurs de Burgers). La tension de 300 kV permet d'analyser des zones épaisses (plusieurs centaines de nm) et le monochromateur qui n'est jamais complètement éteint, permet de contrôler la dose électronique. L'acquisition récente d'un PO HATA (voir figure 6) nous permet également de faciliter le positionnement des échantillons pour faire de la TETD.

Nous avons suivi le principe de réciprocité pour optimiser les conditions d'observation des dislocations en mode STEM : les angles d'incidence et de collection en MET conventionnelle sont respectivement égaux aux angles de collection et d'incidence en STEM (Phillips *et al.*, 2011a-b). En d'autres termes, sachant qu'il faut des angles d'incidence parallèles pour réaliser des clichés WBDF de qualité, il faudra de faibles angles de collection et donc utiliser de grandes longueurs de caméra en mode STEM. Il a bien sûr fallu trouver le meilleur compromis entre une grande longueur de caméra qui fait ressortir des contrastes de Bragg parasites et une petite longueur de caméra qui efface le contraste des dislocations. Par ailleurs, en mode STEM, l'augmentation de l'angle de convergence entraine un agrandissement des zones d'observation des dislocations (voir figure 9). Nous avons donc choisi l'angle de convergence à partir duquel les disques de diffraction commencent à se recouvrir.

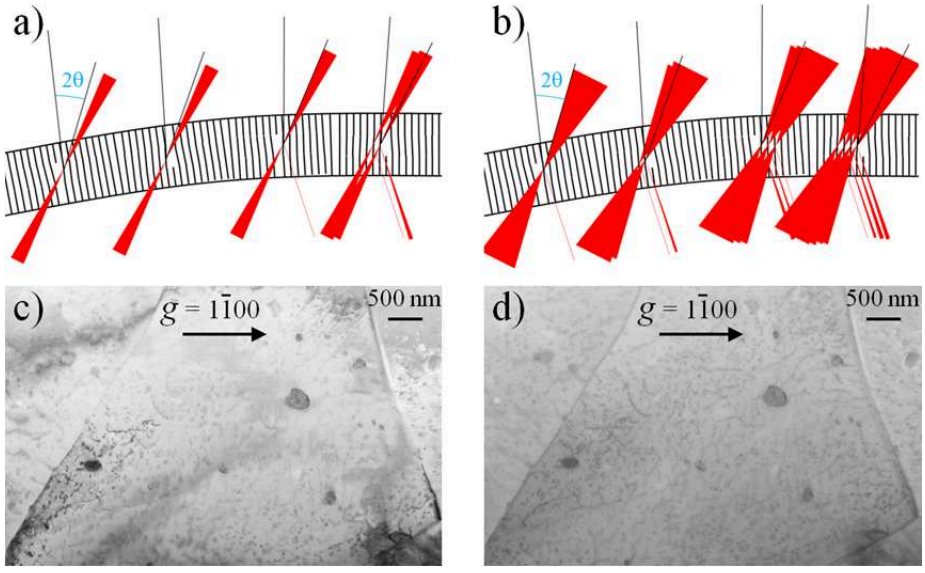

Figure 9 : *Effet de l'angle de convergence sur les microstructures de dislocations en mode STEM : a) Schéma de l'interaction de faisceaux faiblement convergents avec une lame mince qui contient quelques dislocations ; b) même schéma qu'en a) mais avec un faisceau fortement convergent ; c) micrographie de dislocations dans le Zr irradié aux ions observé en mode STEM avec un angle de convergence de 0.5 mrad ; d) même micrographie qu'en c) mais avec un angle de convergence de 4 mrad. Le contraste des dislocations est plus homogène et plus étendu avec un angle de convergence de 4 mrad qu'avec un angle de 0.5 mrad.*

Pour faire ressortir au mieux le contraste des dislocations, les micrographies ont été prises en champ sombre. Cependant, les détecteurs STEM champ sombre sont annulaires et collectent les électrons des autres taches diffractées. L'originalité de cette étude a consisté à déplacer la tache de diffraction du vecteur diffractant approprié sur le détecteur circulaire champ clair. Suite à cette démarche d'optimisation, nous avons obtenu des micrographies étendues de dislocations homogènes, avec une finesse pratiquement ultime (résolution des dislocations de 6.3 Å alors que les normes des vecteurs de Burgers font 3.2 Å, voir figure 10). Par ailleurs, dans la gamme angulaire d'acquisition, les algorithmes de reconstruction calculent les intensités des dislocations par interpolation. En dehors de cette gamme, c'est-à-dire dans le volume manquant (ou missing wedge en anglais), le calcul des intensités est extrapolé, ce qui crée plus d'incertitudes. Par conséquent, les largeurs des dislocations reconstruites sont les plus élevées pour des angles de projection de 90 ° (les intensités sont réparties sur de larges gaussiennes liées aux probabilités de présence étalées des dislocations) et les plus fines pour des angles de projection de 0 °. Après reconstructions, les dislocations n'apparaissent pas comme des cylindres mais plutôt comme des rubans. Nous nous sommes servis du logiciel Chimera (Pettersen *et al.*, 2004) pour retracer et retrouver l'allure réelle des dislocations. La figure 11 montre une série de plusieurs micrographies de dislocations filtrées numériquement, tirée de la série tiltée, et associées à leurs reconstructions retracées respectives. Ces volumes reconstruits nous ont permis de trouver les plans d'habitat de nombreuses boucles de dislocation et d'effectuer une étude approfondie de la montée dans le Zr. Ce travail, est en cours de publication.

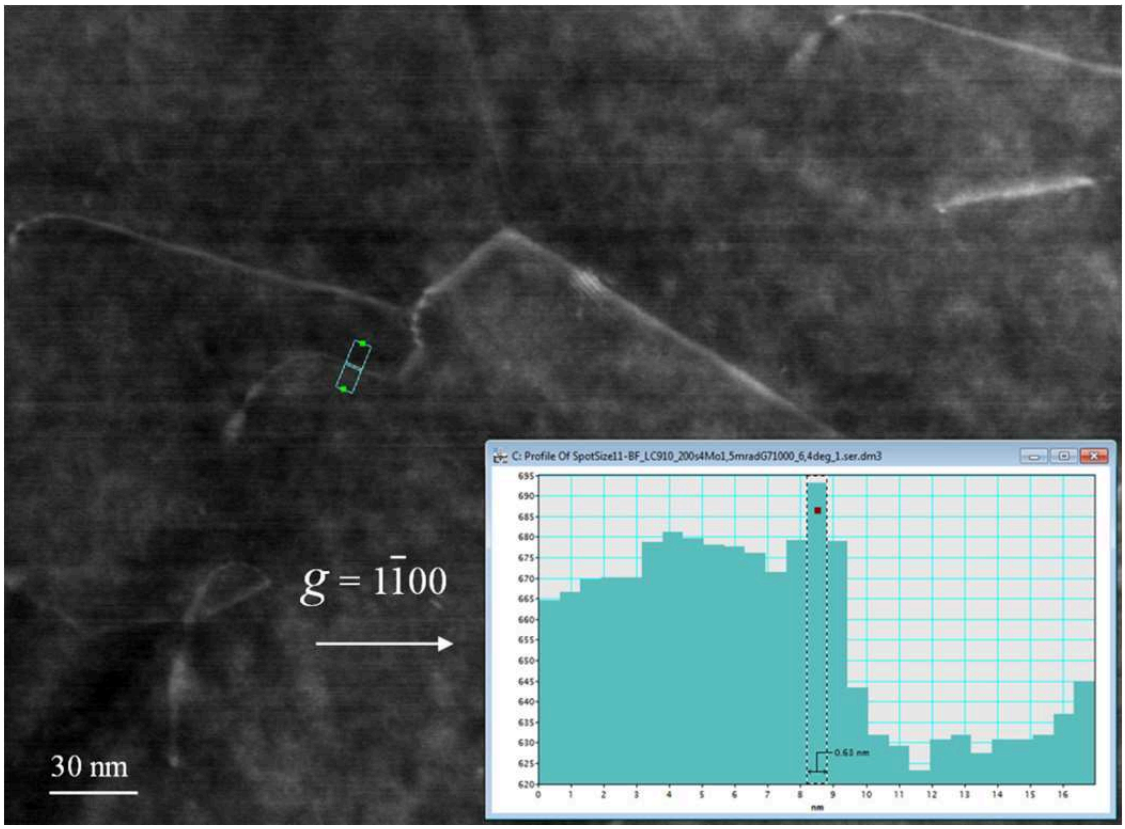

Figure 10 : *Micrographie de dislocations dans le Zr irradié aux ions, en température, en conditions ultime de champ faible. Le profil (en vert sur la figure) montre une dislocation de 6.3 Å d'épaisseur, soit deux fois la norme du vecteur de Burgers* $\frac{1}{3}\langle 11\bar{2}0\rangle$.

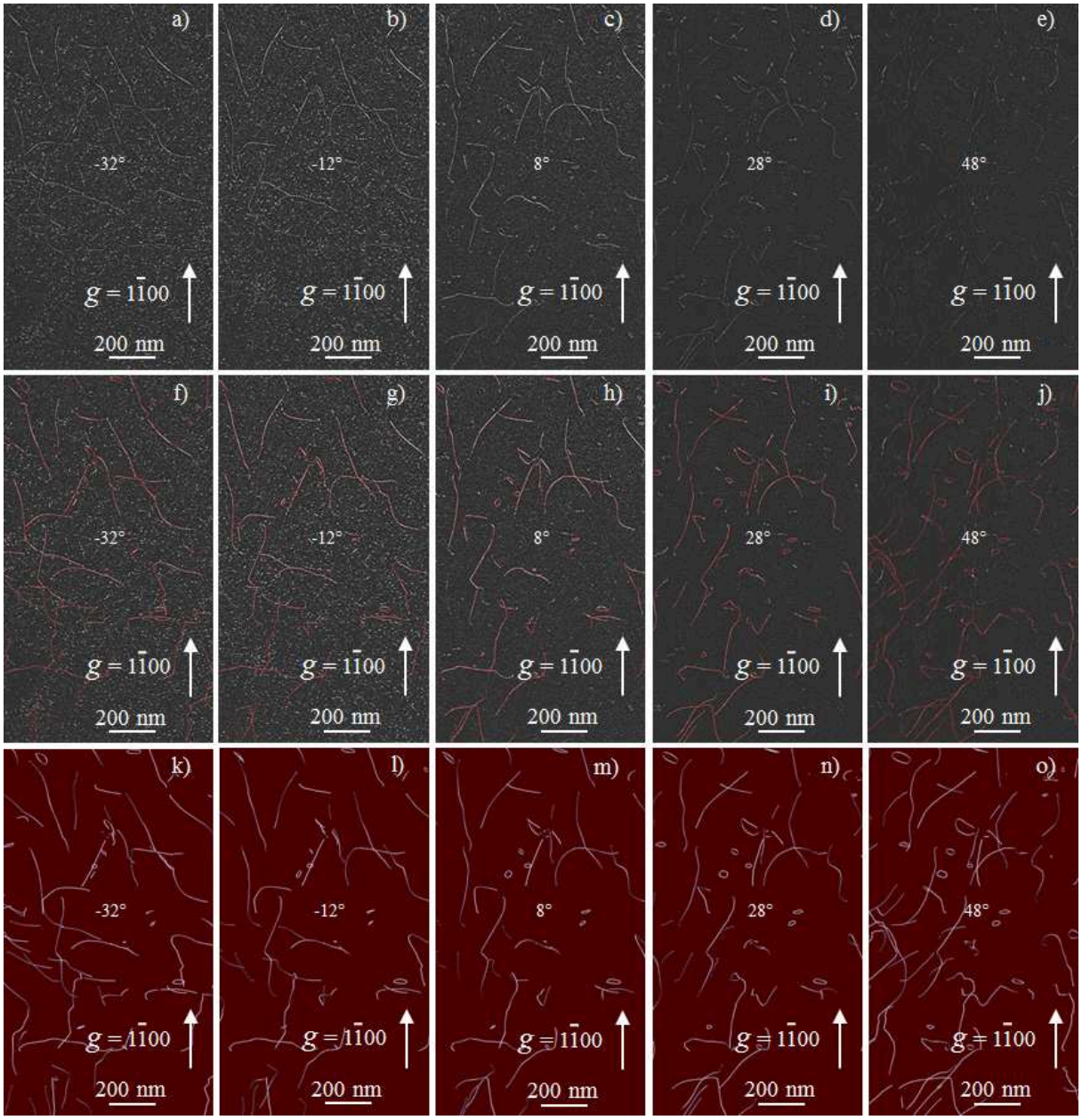

Figure 11 : *Série tiltée de dislocations présentes dans le Zr irradié aux ions, suivant le vecteur diffractant* $1\bar{1}00$ *: a)-e) Micrographies filtrées numériquement pour faire ressortir les dislocations, pour des angles de projection de respectivement -32 °, -12 °, 8 °, 28 ° et 48 ° ; f)-j) même micrographies qu'en a)-e) mais superposées avec le retraçage des dislocations (en rouge), effectué avec le logiciel Chimera (Pettersen et al., 2004) ; k)-o) retraçage des dislocations avec l'aide du logiciel Chimera, pour les angles de projections -32 °, -12 °, 8 °, 28 ° et 48 °.*

I-2-2 Interactions de dislocations dans l'olivine déformée sous 900 °C

La déformation plastique de l'olivine (minéral de structure orthorhombique, a ≈ 4.8 Å, b ≈ 10.2 Å et c ≈ 6.0 Å, dans la représentation *Pbnm*) s'effectue principalement par le mouvement de dislocations rectilignes de nature vis et de vecteur de Burgers [001], pour des températures inférieures à 900 °C. Malgré cette simplicité apparente, les microstructures de dislocations sont complexes avec la présence de nombreuses zones d'enchevêtrement. Une première explication de l'origine de la formation d'enchevêtrements peut être interprétée par

des mécanismes d'interactions de dislocations. Le deuxième article présenté dans de ce chapitre décrit les différentes interactions observées dans l'olivine déformée pour des températures inférieures à 900 °C.

La maîtrise de la TETD s'est vue très utile pour caractériser les interactions de dislocations dans l'olivine. La rotation des volumes reconstruits permet de révéler des mécanismes d'interactions qui étaient jusqu'alors passés inaperçu. Quelques jonctions $\langle 101 \rangle$ ont été caractérisées en nombre restreint. D'après la règle de Frank, l'interaction entre deux dislocations de vecteur de Burgers $\boldsymbol{b}_1$ et $\boldsymbol{b}_2$ est attractive si l'énergie de la jonction est inférieure à la somme des énergies de chaque dislocation, soit $\boldsymbol{b}_1.\boldsymbol{b}_2 < 0$. Les jonctions $\langle 101 \rangle$ avaient uniquement été anticipées en DD (Durinck *et al.*, 2007) mais n'avaient pas été prises en compte comme mécanisme de durcissement puisque les dislocations [100] et [001] sont perpendiculaires entre elles (ici $\boldsymbol{b}_1.\boldsymbol{b}_2 = 0$). Des interactions colinéaires ont également été mises en évidence. La figure 12 montre une dislocation [001] dans le plan de glissement $(1\bar{1}0)$ qui interagit avec une dislocation $[00\bar{1}]$ dans le plan (140) et une seconde dislocation $[00\bar{1}]$ dans le plan (010). Très peu d'interactions colinéaires ont été caractérisées directement par MET (Stach *et al.*, 2000 ; Madec *et al.*, 2003). En approfondissant nos analyses, nous avons trouvé un nouveau mécanisme de double interaction colinéaire avec une boucle sessile. Les détails de ce mécanisme sont disponibles à la fin de ce chapitre, dans l'article correspondant (Mussi *et al.*, 2015a). Sans l'aide de la tomographie, un tel mécanisme aurait été difficilement déterminé.

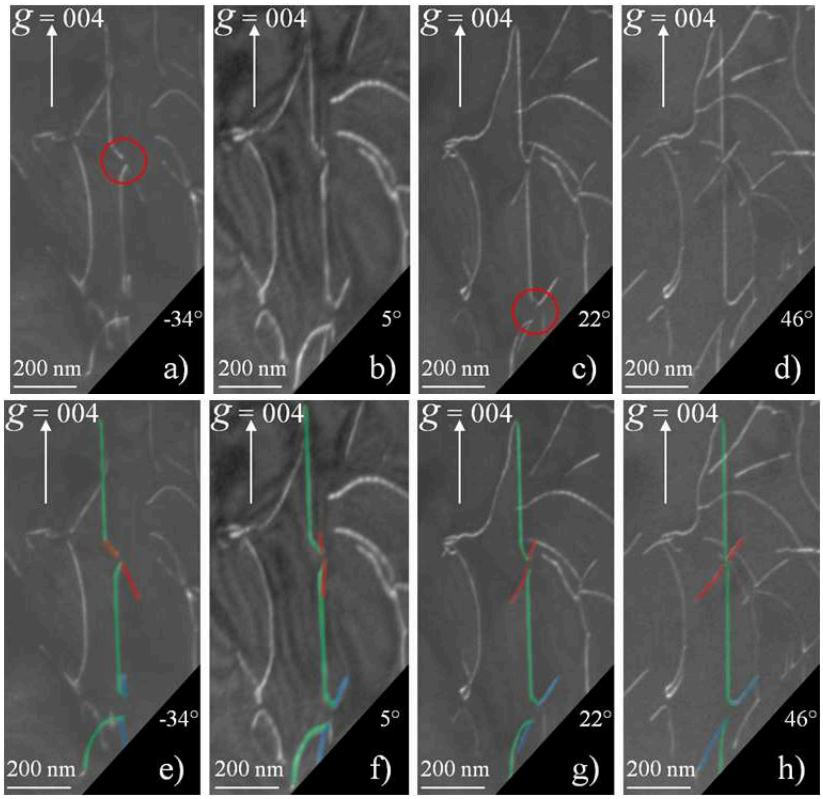

Figure 12 : *Interactions colinéaires : a) Cliché WBDF obtenu avec le vecteur diffractant* 004 *pour un angle de projection de -34 ° ; b) idem à 5 ° ; c) idem à 22 ° ; d) idem à 46 ° ; e) même cliché qu'en a) avec, indiqué en vert, le système de glissement* $[001](1\bar{1}0)$*, indiqué en rouge le système de glissement* $[00\bar{1}](010)$ *et indiqué en bleu le système de glissement* $[00\bar{1}](140)$*, le plan* (140) *est pratiquement debout ; f) idem à 5 °, le plan* (010) *est pratiquement debout ; g) idem à 22 ° ; h) idem à 46 °. Ces micrographies mettent en évidence deux interactions colinéaires entouré en rouge en a) et c).*

I-2-3 Mécanismes de déformation plastique de l'olivine dans les conditions de température du manteau supérieur

I-2-3-a Déformation plastique de l'olivine au niveau de la zone supérieure de la lithosphère

Comme nous l'avions évoqué précédemment, les microstructures de dislocations de l'olivine déformée sous 900 °C permettent difficilement d'obtenir les systèmes de glissement du fait des configurations rectilignes des dislocations. Nous avons entrepris de la TETD sur deux monocristaux d'olivine élaborés par Sylvie Demouchy (GéoScience Montpellier), afin de démêler les microstructures de dislocations pour, par la suite, mieux appréhender les mécanismes fondamentaux de déformation plastique dans ces conditions de température. Les mécanismes d'écrouissage de l'olivine, pour des températures inférieures à 900 °C, sont présentés dans le troisième article décrit dans cette section.

L'étude approfondie de la déformation de deux monocristaux d'olivine pour deux orientations de sollicitations distinctes ont montré que les systèmes de glissement $[001]\{110\}$ et $[001](100)$ sont faciles, et le système $[001](010)$ est très difficile. Nous avons noté, par ailleurs, du glissement dévié simple et multiple, la présence de plans non glissiles et de boucles de dislocations de différentes tailles (Mussi *et al.*, 2015b).

Pour déchiffrer ces microstructures, nous nous sommes penchés sur les familles de boucles de dislocations. L'annihilation progressive de dipôles de dislocations par montée (Lagerlöf *et al.*, 1989), surprenant pour des températures aussi basses, est à l'origine d'une première famille de boucles de dislocation de petites tailles (<10 nm de diamètre, voir figure 13). Nous avons également relevé une deuxième famille de boucles de dislocations, de plus grandes tailles (entre 10 et 30 nm de diamètre), contenues dans des plans plus ou moins parallèles entre eux, qui semblent provenir du mécanisme de double glissement dévié. Ces familles d'obstacles bloquent le mouvement des dislocations par annihilations colinéaires, provoquent un écrouissage conséquent et aboutissent à la rupture du matériau avant d'atteindre le plateau de déformation. La description détaillée des mécanismes de durcissement est disponible à la fin de ce chapitre dans l'article correspondant.

Néanmoins, il faut garder à l'esprit que les conditions de déformation expérimentales de l'olivine ne sont pas celles exercées dans la lithosphère. Les vitesses de déformation géologiques sont beaucoup plus lentes. En conditions naturelles, la diffusion a plus de temps pour finaliser les annihilations dipolaires par montée. La densité d'obstacles devrait donc être réduite ce qui limiterait l'écrouissage et permettrait d'atteindre le plateau de déformation. Des caractérisations de déformations post-séismiques (Freed *et al.*, 2010), de rebonds post-glaciaires (Paulson *et al.*, 2007) et de vitesses géodésiques des plaques, par analyses GPS (Kreemer *et al.*, 2014), permettent d'accéder aux conditions de déformations géologiques réelles. Dans cet état d'esprit, une étude récente de Zhong & Watts (2013) a montré que le terme pré-exponentiel de la loi de fluage de Mei et ses collaborateurs (2010), doit être diminué de 6 à 8 ordres de grandeurs pour satisfaire leur modèle amélioré à trois dimensions en éléments finis (ce modèle simule les déformations en surfaces induites par les contraintes créées par les volcans des îles Hawaiiennes). Une étude de simulation par DD, tirée de nos résultats expérimentaux de TETD (Mussi *et al.*, 2015b), en associant de ce fait le glissement et la montée de dislocations (Boioli *et al.*, 2015), a permis d'obtenir des contraintes d'écoulement voisines de celles de Zhong & Watts (2013), c'est-à-dire bien plus proches des conditions naturelles.

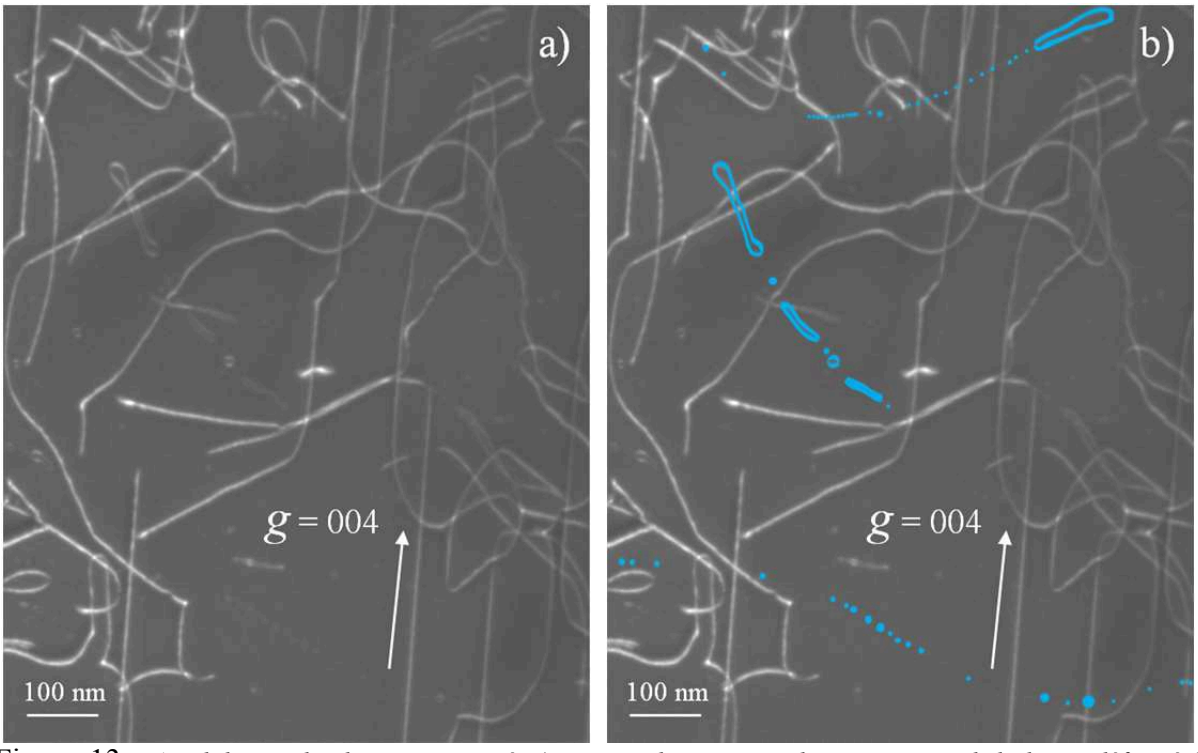

Figure 13 : *Annihilation dipolaire par montée (micrographie extraite d'un monocristal d'olivine déformé à 850 °C) : a) Micrographie WBDF obtenue avec le vecteur diffractant* 004*, de nombreuse boucles de petites tailles (<10 nm) sont visibles ; b) les petites boucles sont retracées en bleu pour les faire ressortir. La disposition des boucles montre qu'il s'agit d'annihilation dipolaire par montée.*

I-2-3-b Déformation plastique de l'olivine à la frontière lithosphère/asthénosphère

Cet article est l'aboutissement d'un travail de longue haleine. Les mécanismes de déformation plastique de l'olivine à la frontière lithosphère/asthénosphère auraient difficilement été décryptés sans l'association de la TETD avec les premières études effectuées pour des températures inférieures à 900 °C.

Dans ces conditions de température, la présence des dislocations [100] n'est plus négligeable et les mécanismes de diffusion sont amplifiés. De par la multitude des interactions (jonctions ⟨101⟩, interactions colinéaires des dislocations [001] et des dislocations [100]) et les nombreux mécanismes mis en jeu (montée, glissement et glissement dévié simple et multiples), les microstructures de dislocations résultantes sont hautement complexes (voir figure 14). Avec l'indexation de plus de 1000 plans où sont inclus les segments de dislocation, la TETD nous a permis d'obtenir une statistique fiable de glissement et de montée de dislocations. Le mécanisme de montée n'est plus employé principalement pour l'annihilation dipolaire, mais également pour libérer les configurations de dislocations bloquées par les jonctions et interactions colinéaires. Le principe du glissement dévié a d'ailleurs le même effet que la montée, c'est-à-dire libérer les dislocations immobilisées. Cependant, ces deux mécanismes créent des configurations de dislocations 3D qui vont à l'inverse de la libération du mouvement des dislocations. Un exemple de multiples interactions et de mécanisme de double glissement dévié est décrit sur la figure 15 (Mussi *et al.*, 2017). D'après la figure 3 de l'article de Demouchy et ses collaborateurs (2013), la limite d'élasticité du monocristal est d'environ 20 MPa, suivi d'un fort écrouissage jusqu'à environ 500 MPa, juste avant rupture.

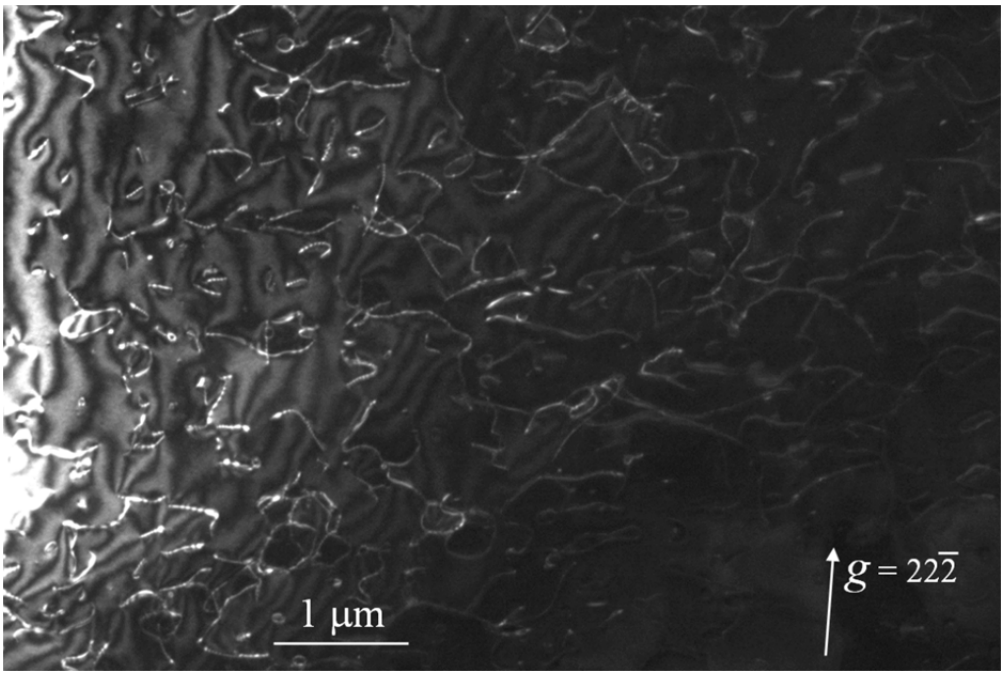

Figure 14 : *Micrographie WBDF, obtenue avec le vecteur diffractant* $22\bar{2}$*, extraite d'un monocristal d'olivine déformé à 1090 °C, qui met en relief une microstructure de dislocations extrêmement complexe.*

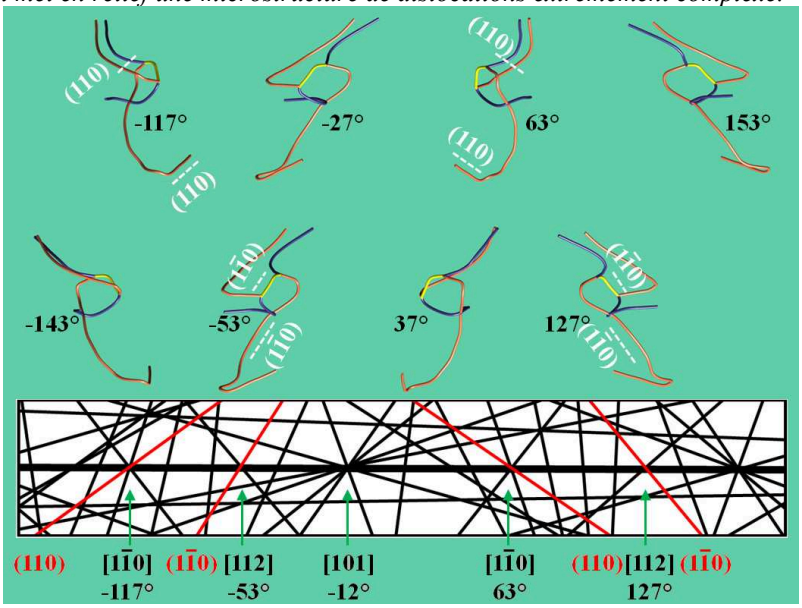

Figure 15 : *Volume reconstruit obtenu avec le vecteur diffractant* $g = 22\bar{2}$*, imagé suivant les angles de projection de -143 °, -117 °, -53 °, -27 °, 37 °, 63 °, 127 ° et 153 °. Le plan* (110) *est debout pour les angles de projection de -117 ° et 63 ° et le plan* $(1\bar{1}0)$ *est debout pour les angles de projection de -53 ° et 127 °. La configuration de dislocation complexe est composée d'une dislocation* $[100]$ *(segment bleu), d'une dislocation* $[001]$ *(segment orange), d'une jonction* $[10\bar{1}]$ *(segment jaune) et d'un état croisé* $[100]/[001]$*. Nous pouvons noter un mécanisme de double glissement dévié* $[001](110)/[001](1\bar{1}0)$*.*

Dans la même optique que l'étude précédente, pour des vitesses de déformation géologiques, les mécanismes de montée de dislocations devraient être à même de jouer un rôle plus significatif et par conséquent de réduire l'écrouissage, pour atteindre le plateau de déformation pour de faibles contraintes d'écoulement. Une toute nouvelle loi rhéologique a été modélisée par DD, à partir d'un monocristal orienté de manière à maximiser le facteur de

Schmid du système de glissement [001](010), sur toute l'étendue de température de la lithosphère (Gouriet *et al.*, 2019) :

$$\dot{\varepsilon} = 1{,}7.10^{16}\left(\frac{\sigma}{\mu}\right)^{2.95}\exp\left(-\frac{460.10^3}{RT}\left(1-\left(\frac{\sigma}{\Sigma}\right)^{1.52}\right)^2\right) \qquad (2)$$

où, μ représente le module de cisaillement (80 GPa dans les conditions de l'article) et Σ une contrainte d'ajustement. Nous obtenons, pour une vitesse de déformation de 10^{-14} s^{-1} et une température de 1090 °C, une contrainte d'écoulement de seulement 5 MPa.
Le mécanisme de montée permet d'atteindre un régime stationnaire de création et d'annihilation de dislocations. Dans ces conditions, le durcissement peut être stoppé pour atteindre une contrainte d'écoulement. Puisque la vitesse de déformation est plus faible de neuf ordres de grandeur par rapport aux conditions de laboratoire, nous nous attendons à obtenir une contrainte d'écoulement bien en deçà des 20 MPa (limite d'élasticité du monocristal déformé en condition de laboratoire). Elle est, ici, quatre fois plus faible. Précisons que le système de glissement [001](010), utilisé pour la simulation, est moins facile que [001](100), système de glissement qui maximise le facteur de Schmid du monocristal déformé en condition de laboratoire. Par conséquent, dans les mêmes conditions d'orientation, la contrainte d'écoulement du monocristal devrait être strictement inférieure à 5 MPa pour des vitesses de déformation géologiques.

I-2-4 Apport de la tomographie électronique des dislocations

Comme la technique des franges d'Ishida (Ishida *et al.*, 1980) ou, mieux encore, la technique LACBED (Tanaka *et al.*, 1980 ; Cherns & Preston, 1986 ; Cordier *et al.*, 1995), ont permis d'améliorer la détermination des vecteurs de Burgers ; la TETD se destine à faciliter la détermination des plans de glissement et donc des systèmes de glissement. Depuis l'émergence de la TETD, plusieurs champs d'étude s'ouvrent à nous. Plutôt que de se limiter à l'obtention des systèmes de glissement, la TETD nous permet de voir sur un angle nouveau des mécanismes peu caractérisés, tels que les interactions entre dislocations, le glissement dévié et la montée de dislocations.

Même si les toutes premières TETD ont été réalisées voilà plus de 10 ans (Barnard *et al.*, 2006), actuellement moins de dix équipes dans le monde se sont intéressées à cette technique (Barnard *et al.*, 2006 ; Tanaka *et al.*, 2008a-b ; Ramar *et al.*, 2010 ; Schryvers *et al.*, 2013 ; Liu *et al.*, 2014 ; Mussi *et al.*, 2014 ; Niehle *et al.*, 2017 ; Oveisi *et al.*, 2017 ; Feng *et al.*, 2017). Nous restons encore les pionniers à pratiquer cette technique sur les minéraux à travers le monde. La nécessité d'orienter parfaitement les échantillons a été le principal frein à son développement. Les premières études n'ont pas rencontré cette difficulté puisque les échantillons avaient des orientations prédéfinies précises (couches épitaxiées de GaN (Barnard *et al.*, 2006) ou wafer de Si (Tanaka *et al.*, 2008a-b)). Grace à la récente commercialisation d'un PO capable de faciliter l'installation optimisée des échantillons pour faire de la TETD (Hata *et al.*, 2011), cette technique va sans nul doute se développer rapidement.

Références :

Barnard, J.S., Sharp, J., Tong, J.R., Midgley, PA (2006): High-resolution three-dimensional imaging of dislocations. *Science*, **313**, 319.

Boioli, F., Tommasi, A., Cordier, P., Demouchy, S., Mussi, A. (2015): Low steady-state stresses in the cold lithospheric mantle inferred from dislocation dynamics models of dislocation creep in olivine *Earth Planet*. Sci. Lett., **432**, 232-242.

Chen, C.C., Zhu, C., White, E.R., Chiu, C.Y., Scott, M.C., Regan, B.C., Marks, L.D., Huang, Y., Miao, J. (2013): Three-dimensional imaging of dislocations in a nanoparticle at atomic resolution. *Nature*, **496**, 74-77.

Cherns, D. & Preston, A.R. (1986): Convergent-beam diffraction of crystal defects. In Proceedings Eleventh International Congress on Electron Microscopy, Kyoto, 721.

Cordier, P. & Heidelbach, F. (2013): Origin of twist in 'gwindel' quartz crystals from the Alps: a transmission electron microscopy study. *Eur. J. Mineral.*, **25**, 145-153.

Cordier, P., Morniroli, J.P., Cherns, D. (1995): Characterization of crystal defects in quartz by large-angle convergent-beam electron diffraction. *Philos. Mag. A*, **72**, 1421-1430.

Demouchy, S., Tommasi, A., Ballaran, T.B., Cordier, P. (2013): Low strength of Earth's uppermost mantle inferred from tri-axial deformation experiments on dry olivine crystals. *Phys. Earth Planet. Inter.*, **220**, 37-49.

Durinck, J., Devincre, B., Kubin, L., Cordier, P. (2007): Modeling the plastic deformation of olivine by dislocation dynamics simulations**.** *Am. Mineral.*, **92**, 1346-1357.

Feng, Z.Q., Lin, C.W., Li, T.T., Luo, X., Wu, G.L., Huang, X.X. (2017): Electron tomography of dislocations in an Al-Cu-Mg alloy. *IOP Conf. Ser.: Mater. Sci. Eng.*, **219,** 012018.

Freed, A.M., Herring, T., Bürgmann, R. (2010): Steady-state laboratory flow laws alone fail to explain post-seismic observations, *Earth Planet. Sci. Lett.*, **300**, 1–10.

Gaboriaud, R.J., Darot, M., Gueguen, Y., Woirgard, J. (1981): Dislocations in olivine indented at low-temperatures. *Phys. Chem. Miner.*, **7**, 100-104.

Gordon, R., Bender, R., Herman, G.T. (1970): Algebraic reconstruction techniques (ART) for three-dimensional electron microscopy and x-ray photography. *J. Theor. Biol.*, **29**, 471-481.

Gouriet, K., Cordier, P., Garel, F., Thoraval, C., Demouchy, S., Tommasi, A., Carrez, P. (2019): Dislocation Dynamics modelling of the power-law breakdown in olivine single crystals: toward a unified creep law for the upper mantle. *Earth Planet. Sci. Lett.*, **506**, 282-291.

Hata, S., Miyazaki, H., Miyazaki, S., Mitsuhara, M., Tanaka, M., Kaneko, K., Higashida, K., Ikeda, K., Nakashima, H., Matsumara, S., Barnard, J.S., Sharp, J.H., Midgley, P.A. (2011): High-angle triple-axis specimen holder for three-dimensional diffraction contrast imaging in transmission electron microscopy. *Ultramicroscopy*, **111**, 1168-1175.

Herman, G.T., Lakshminarayanan, A.V., Naparstek, A. (1976): Convolution reconstruction techniques for divergent beams. *Comput. Biol. Med.*, **6**, 259-271.

Hounsfield, G.N. (1973): Computerized transverse axial scanning (tomography): Part I. Description of system. *Br.* J. Radiol.*,* **46***,* 1016-1022.

Ishida, Y., Ishida, H., Kohra, K., Ichinose, H. (1980): Determination of the Burgers vector of a dislocation by weak-beam imaging in a HVEM. *Philos. Mag. A*, **42**, 453-462.

Kreemer, C., Blewitt, G., Klein, E.C. (2014): A geodetic plate motion and Global Strain Rate Model. *Geochem. Geophys. Geosyst.*, **15**, 3849-3889.

Lagerlöf, K.P.D., Mitchell, T.E. Heuer, A.H. (1989): Energetics of the break-up of dislocation dipoles into prismatic loops. *Acta Metall. Mater.*, **37**, 3315-3325.

Landis, W.J., Song, M.J., Leith, A., McEwen, L., McEwen, B.F. (1993): Mineral and Organic Matrix Interaction in Normally Calcifying Tendon Visualized in Three Dimensions by High-Voltage Electron Microscopic Tomography and Graphic Image Reconstruction. J. Struct. Biol., **110**, 39-54.

Liu, G.S., House, S.D., Kacher, J., Tanaka, M., Higashida, K., Robertson, I.M. (2014): Electron tomography of dislocation structures. *Mater. Charact.*, **87**, 1-11.

Madec, R., Devincre, B., Kubin, L., Hoc, T., Rodney, D. (2003): The Role of Collinear Interaction in Dislocation-Induced Hardening. *Science*, **301**, 1879-1882.

Mei, S., Suzuki, A.M., Kohlstedt, D.L., Dixon, N.A., Durham, W.B. (2010): Experimental constraints on the strength of the lithospheric mantle. *J. Geophys. Res.*, **115**, B08204.

Miao, J., Ercius, P., Billinge, S.J. (2016): Atomic electron tomography: 3D structures without crystals. *Science*, **353**, aaf2157.

Mussi, A., Cordier, P., Demouchy, S. (2015a): Characterization of dislocation interactions in olivine using electron tomography, *Philos. Mag.*, **95**, 335-345.

Mussi, A., Cordier, P., Demouchy, S., Hue, B. (2017): Hardening mechanisms in olivine single crystal deformed at 1090 °C: an electron tomography study, *Philos. Mag.*, **97**, 3172-3185.

Mussi, A., Cordier, P., Demouchy, S., Vanmansart C. (2014): Characterization of the glide planes of the [001] screw dislocations in olivine using electron tomography. *Phys. Chem. Miner.*, **41**, 537-545.

Mussi, A., Nafi, M., Demouchy, S., Cordier, P. (2015b): On the deformation mechanism of olivine single crystals at lithospheric temperatures: an electron tomography study, *Eur. J. Mineral.*, **27**, 707-715.

Niehle, M., Trampert, A., Rodriguez, J.B., Cerutti, L., Tournié, E. (2017): Electron tomography on III-Sb heterostructures on vicinal Si(001) substrates: Anti-phase boundaries as a sink for threading dislocations. *Scripta Mater.*, **132**, 5-8.

Oveisi, E., Letouzey, A., Alexander, D.T.L., Jeangros, Q., Schäublin, R., Lucas, G., Fua, P., Hébert, C. (2017): Tilt-less 3-D electron imaging and reconstruction of complex curvilinear structures. *Sci. Rep.*, **7**, 10630.

Paulson, A., Zhong, S.J., Wahr, J. (2007): Inference of mantle viscosity from GRACE and relative sea level data, *Geophys. J. Int.*, **171**, 497–508.

Penczek, P., Radermacher, M., Frank, J. (1992): Three-dimensional reconstruction of single particles embedded in ice. *Ultramicroscopy*, **40**, 33–53.

Pettersen, E.F., Goddard, T.D., Huang, C.C., Couch, G.S., Greenblatt, D.M., Meng, E.C., Ferrin, T.E. (2004): UCSF Chimera: A visualization system for exploratory research and analysis. *J. Comput. Chem.*, **25**, 1605–1612.

Phillips, P.J., Brandes, M.C., Mills, M.J., De Graef, M. (2011a): Diffraction contrast STEM of dislocations: Imaging and simulations. *Ultramicroscopy*, **111**, 1483-1487.

Phillips, P.J., Mills, M.J., De Graef, M. (2011b): Systematic row and zone axis STEM defect image simulations. *Philos. Mag.*, **91**, 2081-2101.

Raleigh, C.B. (1968): Mechanisms of plastic deformation of olivine. *J. Geophys. Res.*, **73**, 5391-5406.

Ramar, A., Hata, S., Huang, X., Dunin-Borkowski, R. E.. Winther, G. (2010): Dislocation electron tomography of boundaries in deformed aluminium. In Proceedings Challenges in materials science and possibilities in 3D and 4D characterization techniques (Riso

International Symposium on Materials Science). Editor: Hansen, N., Juul Jensen, D., Nielsen, S,F., Poulsen, H.F., Ralph, B., Riso (DK), 397-404.
Rebled, J.M., Yedra, L., Estrade, S., Portillo, J., Peiro, F. (2011): A new approach for 3D reconstruction from bright field TEM imaging: Beam Precession Assisted Electron Tomography. *Ultramicroscopy*, **111**, 1504-1511.
Schryvers, D., Cao, S., Tirry, W., Idrissi H., Van Aert, S. (2013): Advanced three-dimensional electron microscopy techniques in the quest for better structural and functional materials. *Sci. Technol. Adv. Mater.*, **14**, 014206.
Scott, M.C., Chen, C.C., Mecklenburg, M., Zhu, C., Xu, R., Ercius, P., Dahmen, U., Regan, B.C., Miao, J. (2012): Electron tomography at 2.4-angstrom resolution. *Nature*, **486**, 444-447.
Stach, E.A., Hull, R., Tromp, R.M., Ross, F.M., Reuter, M.C., Bean, J.C. (2000): In-situ transmission electron microscopy studies of the interaction between dislocations in strained SiGe/Si(001) heterostructures. *Philos. Mag. A*, **80**, 2159-2200.
Tahar, M., Okano, N., Inamura, T., Hosoda, H. (2017): Plastic deformation behaviour of single-crystalline martensite of Ti-Nb shape memory alloy. *Sci. Rep.*, **7**, 15715.
Tanaka, M., Higashida, K., Kaneko, K., Hata, S., Mitsuhara, M. (2008a): Crack tip dislocations revealed by electron tomography in silicon single crystal. *Scripta Mater.*, **59**, 901-904.
Tanaka, M., Honda, M., Mitsuhara, M., Hata, S., Kaneko, K., Higashida, K. (2008b): Three-dimensional observation of dislocations by electron tomography in a silicon crystal. *Mater. Trans.*, **49**, 1953-1956.
Tanaka, M., Saito, R., Ueno, K., Harada, Y. (1980): Large-angle convergent-beam electron diffraction. *J. Electron. Microsc.*, **29**, 408-412.
Thurel, E. & Cordier, P. (2003): Plastic deformation of wadsleyite: I. High-pressure deformation in compression. *Phys. Chem. Minerals*, **30**, 256-266.
Volterra, V. (1907): Sur l'équilibre des corps élastiques multiplement connexes. *Annal. Sci. de l'ENS*, **24**, 401–517.
Zhong, S. & Watts, A.B. (2013): Lithospheric deformation induced by loading of the Hawaiian Islands and its implications for mantle rheology. *J. Geophys. Res.*, **118**, 6025-6048.

Publications concernées par ces études (les travaux précédés d'un astérisque sont reproduits à la fin de ce mémoire) :

Demouchy, S., Mussi, A., Barou, F., Tommasi, A., Cordier, P. (2014): Viscoplasticity of polycrystalline olivine experimentally deformed at high pressure and 900°C, *Tectonophysics*, **623**, 123-135.
*Mussi, A., Cordier, P., Demouchy, S., Vanmansart, C. (2014): Characterization of the glide planes of the [001] screw dislocations in olivine using electron tomography, *Phys. Chem. Minerals*, **41**, 537-545.
*Mussi, A., Cordier, P., Demouchy, S. (2015a): Characterization of dislocation interactions in olivine using electron tomography, *Philos. Mag.*, **95**, 335-345.
Boioli, F., Tommasi, A., Cordier, P., Demouchy, S., Mussi, A. (2015): Low steady-state stresses in the cold lithospheric mantle inferred from dislocation dynamics models of dislocation creep in olivine, *Earth Planet. Sci. Lett.*, **432**, 232-242.
*Mussi, A., Nafi, M., Demouchy, S., Cordier, P. (2015b): On the deformation mechanism of olivine single crystals at lithospheric temperatures: an electron tomography study, *Eur. J. Mineral.*, **27**, 707-715.

Mussi, A., Cordier, P., Ghosh, S., Garvik, N., Nzogang, B.C., Carrez, P., Garruchet, S. (2016): Transmission electron microscopy of dislocations in cementite deformed at high pressure and high temperature, *Philos. Mag.*, **96**, 1773-1789.

*Mussi, A., Cordier, P., Demouchy, S., Hue, B. (2017): Hardening mechanisms in olivine single crystal deformed at 1090 °C: an electron tomography study, *Philos. Mag.*, **97**, 3172-3185.

Phys Chem Minerals (2014) 41:537–545
DOI 10.1007/s00269-014-0665-1

ORIGINAL PAPER

Characterization of the glide planes of the [001] screw dislocations in olivine using electron tomography

Alexandre Mussi · Patrick Cordier · Sylvie Demouchy · Claude Vanmansart

Received: 28 November 2013 / Accepted: 26 February 2014 / Published online: 11 March 2014

Abstract A San Carlos olivine polycrystal has been deformed under uppermost mantle conditions, by compression at 900 °C, at a strain rate of 1.1×10^{-5} s^{-1}, under a confining pressure of 300 MPa, using the Paterson press. Transmission electron tomography of dislocations has been performed by scanning transmission electron microscopy, by conventional transmission electron microscopy using the weak-beam dark-field technique, associated with precession or not, in order to determine the glide planes of [001] screw dislocations. This recent technique is the most suitable one since most [001] dislocations exhibit straight screw segments due to the high lattice friction on this character at low temperature. We find that [001] dislocations glide in (100), (010) and {110} as already reported, but also more unexpectedly in {120} and {130}. We show that at 900 °C, [001] {110} glide is dominant in polycrystals. We have, however, noted and characterized numerous cross-slip events in the specimen.

Keywords Olivine · Tomography · Precession · TEM · Dislocation · Glide plane

Introduction

Being the most abundant and the weakest phase of the Earth's upper mantle, olivine [$(Mg, Fe)_2SiO_4$] is the key mineral which controls the rheology of the upper mantle. The crystal structure of olivine is orthorhombic ($a \approx 4.752$ Å, $b \approx 10.193$ Å and $c \approx 5.977$ Å), with a *Pbnm* space group (Hazen 1976). Plastic deformation of olivine has been the subject of many experimental studies. The dominant slip systems in olivine involve [100] glide at high temperature (i.e. above ca. 1,000 °C) and low differential stresses, whereas [001] glide plays a greater role at lower temperature and high differential stresses (Barber et al. 2010). Most studies have addressed the rheology of olivine (or forsterite, the iron-free end member) at temperatures above 1,400 °C (Bai and Kohlstedt 1992; Darot and Gueguen 1981; Durham and Goetze 1977; Durham et al. 1977; Gueguen 1979; Gueguen and Darot 1982; Jaoul et al. 1979 and Kohlstedt and Goetze 1974), and hence, the deformation mechanisms are reasonably well known in this temperature range. In comparison, less attention has been given to the rheology of olivine in the temperature condition of the uppermost lithospheric mantle (Raleigh 1968; Phakey et al. 1972; Evans and Goetze 1979; Gaboriaud et al. 1981; Raterron et al. 2004; Demouchy et al. 2009; Demouchy et al. 2013a, b), and the deformation mechanisms need to be better constrained in these conditions to support flow laws measured in laboratory conditions (see recent discussion in Demouchy et al. 2013a, b).

From analyses of the slip bands on the surfaces of deformed olivine single crystals, Raleigh (1968) has proposed that glide of [001] dislocations occurs in the {110} and (100) planes for temperatures below 1,000 °C. Furthermore, Phakey et al. (1972) have conducted an extensive study by transmission electron microscopy (TEM), of the deformation microstructures of single crystals deformed in the low-temperature regime. At 800 °C, the activation of [001] {110} was established with some

A. Mussi (✉) · P. Cordier · C. Vanmansart
Unité Matériaux et Transformations, UMR 8207 CNRS, Université Lille1, 59655 Villeneuve d'Ascq, France
e-mail: alexandre.mussi@univ-lille1.fr

S. Demouchy
Géoscience Montpellier, UMR 5342 CNRS, Université Montpellier 2, 34095 Montpellier, France

suggestions of [001] glide in (100) and (010). Combining the decoration technique (Kohlstedt et al. 1976), with TEM analyses, Gaboriaud et al. (1981) have confirmed that, below 900 °C (and down to 20 °C), the microstructure is essentially composed of straight [001] screw dislocations. Information on the slip planes was inferred from observations on decorated samples suggesting glide of [001] dislocations in (100) and, to a lesser extent, in {110} for temperatures higher than 600 °C. So far, TEM-detailed characterizations of slip planes in olivine are very scarce and unfortunately all restricted to characterization of experimentally deformed single crystals of olivine (Fo_{90}) or forsterite (Fo_{100}). In our study, we provide the characterization of glide planes for the [001] screw dislocation in a deformed olivine aggregate using electron tomography.

For characterization of [001] glide, there is a specific difficulty associated with the fact that, at low temperature, [001] dislocations bear a high lattice friction on screw characters. Then, most of the dislocations are straight screw segments with relatively few non-screw segments, which could allow slip plane determination. To identify the slip plane, one must tilt the specimen to put the plane edge-on. Depending on the orientation, this may require tilt angles that can be high or even not accessible. Alternatively, the stereographic projection originally proposed 175 years ago by Miller (1839) and applied to TEM analyses 40 years ago by Head et al. (1973) can be applied. This method is, however, very time-consuming and very often of very poor accuracy. However, today transmission electron tomography enables the reconstruction of a volume from a series of projected images (called a tilted series). Most often, the reconstructed volumes are obtained using images based on an absorption contrast (Buseck et al. 2001; Arslan et al. 2006; Midgley and Dunin-Borkowski 2009). The more the angular range increases, the more the omitted volume (missing wedge) decreases, and the more the reconstruction volume quality rises. The first successful transmission electron tomography of dislocations has been performed in a semiconductor (GaN) by Barnard et al. (2006a, b, 2010). The reconstruction has been performed based on images obtained in conventional TEM (diffraction contrast mode) using the weak-beam dark-field (WBDF) technique. Under these imaging conditions, the contrast is extremely sensitive to the specimen orientation with respect to the electron beam. The deviation from exact Bragg conditions (s_g) has to be kept strictly constant for the entire tilted series. To reach these conditions, the tilt axis has to be perfectly aligned, with a precision of the order of a tenth of a degree, with the diffraction vector used to image the dislocations. However, the contrast of dislocation is usually oscillating in WBDF (i.e. when dislocation lines are inclined within the thin foil), and the background is always inhomogeneous due to the occurrence of thickness fringes and bend contours. Consequently, despite a good signal-to-noise ratio, it is necessary to carefully filter each image to succeed in correctly reconstructing the dislocations. Unfortunately, this image processing results in a loss of information. Scanning transmission electron microscopy (STEM) has also been used to image crystal defects (Phillips et al. 2011a, b) and to perform electron tomography (Sharp et al. 2008; Tanaka et al. 2008a, b). The STEM mode allows to obtain a homogeneous background, but, except for field emission guns (FEG), the signal-to-noise ratio is weak. A recent study from Rebled et al. (2011) associates tomography with precession. The precession technique reduces bend contours, dislocation oscillating contrasts and thickness fringes while keeping a good signal-to-noise ratio.

In the present study, we show that dislocation transmission electron tomography associated with precession significantly expands the possibility to characterize glide planes in deformed minerals. We present an application on the characterization of glide planes of [001] dislocations in a polycrystal of olivine deformed at 900 °C, 300 MPa (Demouchy et al. 2013a, b, 2014).

Experimental details

Sample and deformation experiment

A polycrystal of San Carlos olivine has been deformed at 900 °C under a confining pressure of 300 MPa, at a 1.1×10^{-5} s^{-1} strain rate using a gas medium high pressure and high temperature deformation apparatus (Paterson 1970, 1990). The fine-grained olivine powder was first cold pressed at room pressure then sintered at high temperature (1,250 °C) and high pressure (300 MPa) for 3 h before temperature was cooled down, and stabilized to 900 °C prior to tri-axial deformation. The starting polycrystal olivine has cylindrical geometry of ca. 1 cm^3 (the starting Ni sleeve is 9.45 mm in diameter and 20.03 mm long). The details of the geometry of the experimental set-up can be found in previous studies (Paterson 1990; Chen et al. 2006; Demouchy 2010; Demouchy et al. 2012, 2013a, b). At high temperature, to buffer oxygen fugacity to values relevant of the upper most mantle (McCammon 2005), a pure nickel film has been integrated between the polycrystal olivine and the outer iron jacket. A hydrostatic pressure of 300 MPa of argon gas (inert gas) and a compressive deviatoric stress is applied to deform the sample at a constant displacement rate.

Transmission electron tomography

To prepare the TEM thin foils, a slice containing the compression axis was cut and mechanically polished to a thickness of ca. 30 μm. Electron transparency was further obtained by

ion milling (in a Gatan® DuoMillTM Model 600). To insure electron conduction, a thin carbon film has been coated on the thin foil. A FEI® Tecnaï $G^2$20Twin microscope, operating at 200 kV with a LaB_6 filament, was used at the TEM facility of the University of Lille. Six tilted series were acquired every 2°, in a double tilt sample holder (the acquisition conditions are summarized in Table 1). During this study, we have used different acquisition methods: WBDF, STEM and WBDF associated with precession. As the contrast is very weak in WBDF, automatic focus and alignment are inefficient. Consequently, the tilted series are acquired and aligned manually to achieve pixel precision. To improve the background homogeneity, each image is filtered using the ImageJ software, with a polynomial fit. Then, a convolution of each image with a Kernel matrix is performed to increase the dislocation contrast (Barnard et al. 2010). Finally, the reconstructed volumes are obtained using the Gatan® 3D reconstruction software with the simultaneous iterative reconstruction technique (SIRT) algorithm (Penczek et al. 1992).

Results

The size of the studied grains ranges between 5 and 13 μm with analysed zones being slightly smaller (2–4 μm).

Table 1 Acquisition conditions for each grain

	Microscope modes	Diffraction vector	Tilted series ranges
Grain I	STEM	004	−56° to 58° every 2°
Grain II	WBDF	004	−60° to 50° every 2°
Grain III	WBDF	004	−56° to 50° every 2°
Grain IV	WBDF + precession	222	−56° to 50° every 2°
Grain V	WBDF + precession	222	−56° to 46° every 2°
Grain VI	WBDF + precession	222	−54° to 52° every 2°

Considering the tomographic reconstructed volumes, a typical dislocation density of 10^{13} m^{-2} was measured.

After the reconstructions of the centred filtered tilted series, the tomographic volumes are precisely oriented in order to place specific planes [e.g. (100), (010), {110}, {120}, {130}, {140}, {210}, {310} and {410}] edge-on. An example of slip plane determination of a [001] dislocation (labelled "I") is shown on Fig. 1. A marked curvature is observed when the dislocation is viewed along the [410] zone axis (Fig. 1a). When the same dislocation "I" is viewed along the $[\bar{1}10]$ zone axis, it appears as a

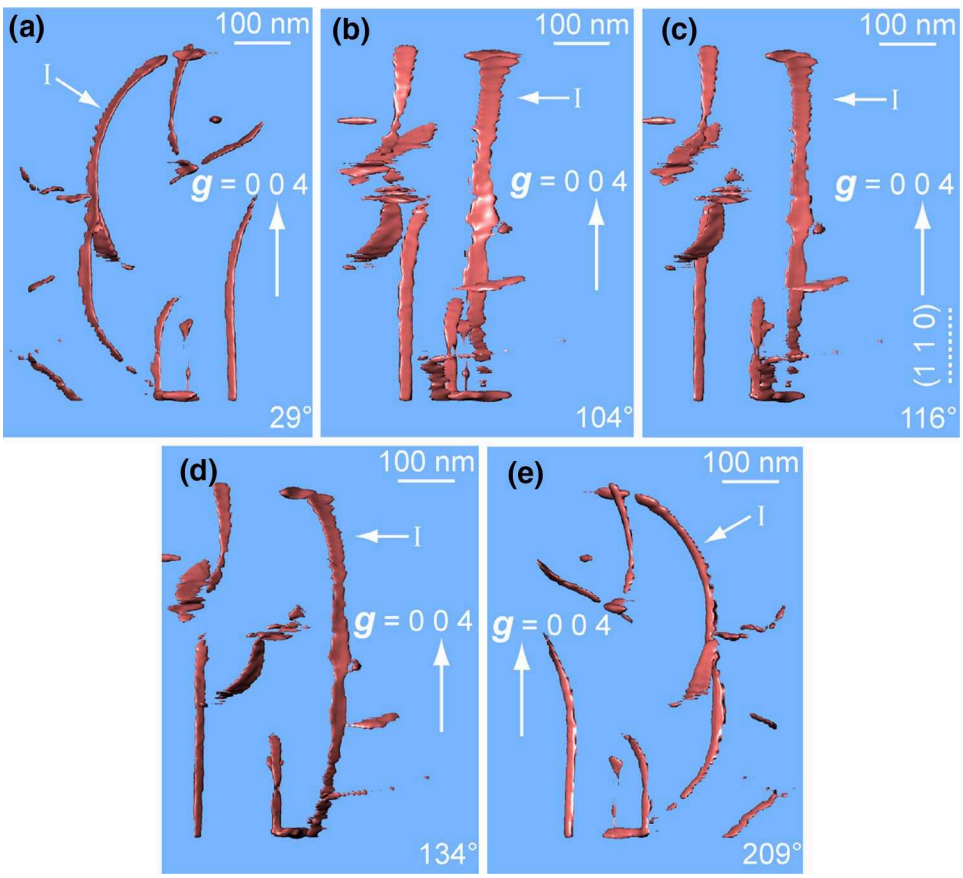

Fig. 1 [001] dislocation in (110). Reconstructed volume of a part of grain III (see the acquisition conditions in Table 1 and the method in the main text). **a** The [001] dislocation labelled "I" (indicated by a *white arrow*) is strongly curved when seen along the [410] zone axis; **b** the glide plane of "I" is nearly edge-on along the $[\bar{1}20]$ zone axis, since this dislocation exhibits only a slight curvature along this orientation; **c** seen along the $[\bar{1}10]$ zone axis, dislocation "I" appears as a *straight line*, showing that it is contained in the (110) plane which is edge-on (here for a tilt angle of 116°); **d** dislocation "I" seen along the $[\bar{2}10]$ zone axis; **e** dislocation "I" is strongly curved, in the opposite direction to (**a**), along the $[\bar{4}\bar{1}0]$ zone axis

straight line parallel to the (110) plane (Fig. 1c). Further rotation of the reconstructed volume along the tilt axis shows the same curvature with another maximum when the $[4\bar{1}0]$ zone axis is reached (Fig. 1e). The glide plane of dislocation "I" is almost in the plane of the micrograph.

Several dislocations exhibit lines made of segments which belong to several planes. Figure 2 illustrates such a case with a [001] dislocation constituted of two segments (labelled "1" and "2"). The reconstructed tomographic volume has been obtained from images taken with the 004 diffraction vector. The segment "1" appears straight when the reconstructed volume is tilted in such a way that the $(1\bar{1}0)$ plane is edge-on, i.e. for a tilt angle of approximately 121° (Fig. 2e). For the segment "2" to appear linear, the reconstructed volume has to be tilted to ca. 71° in order to put the (110) plane edge-on (Fig. 2c). The line of this dislocation belongs to the $(1\bar{1}0)$ and to the (110) planes. This determination would have been beyond reach by a standard tilting experiment.

Beyond the usual (100), (010) and {110} glide planes that were expected from the literature, we have characterized several other planes containing [001] dislocations. Dislocation labelled "II" on Fig. 3a is highly curved when the reconstructed volume is observed along the $[\bar{2}10]$ zone axis, but it is seen as a straight line when the $(1\bar{2}0)$ plane is edge-on (Fig. 3b). Similarly, Fig. 4 shows that the dislocation labelled "III" glides on the (130) plane.

The number of dislocation segments observed in each glide plane characterized in this study is summarized in Table 2. It is worth noticing that a majority of {110} glide planes are characterized in each grain. Furthermore, Table 3 recapitulates all the observations of dislocations lines belonging to more than one single glide plane.

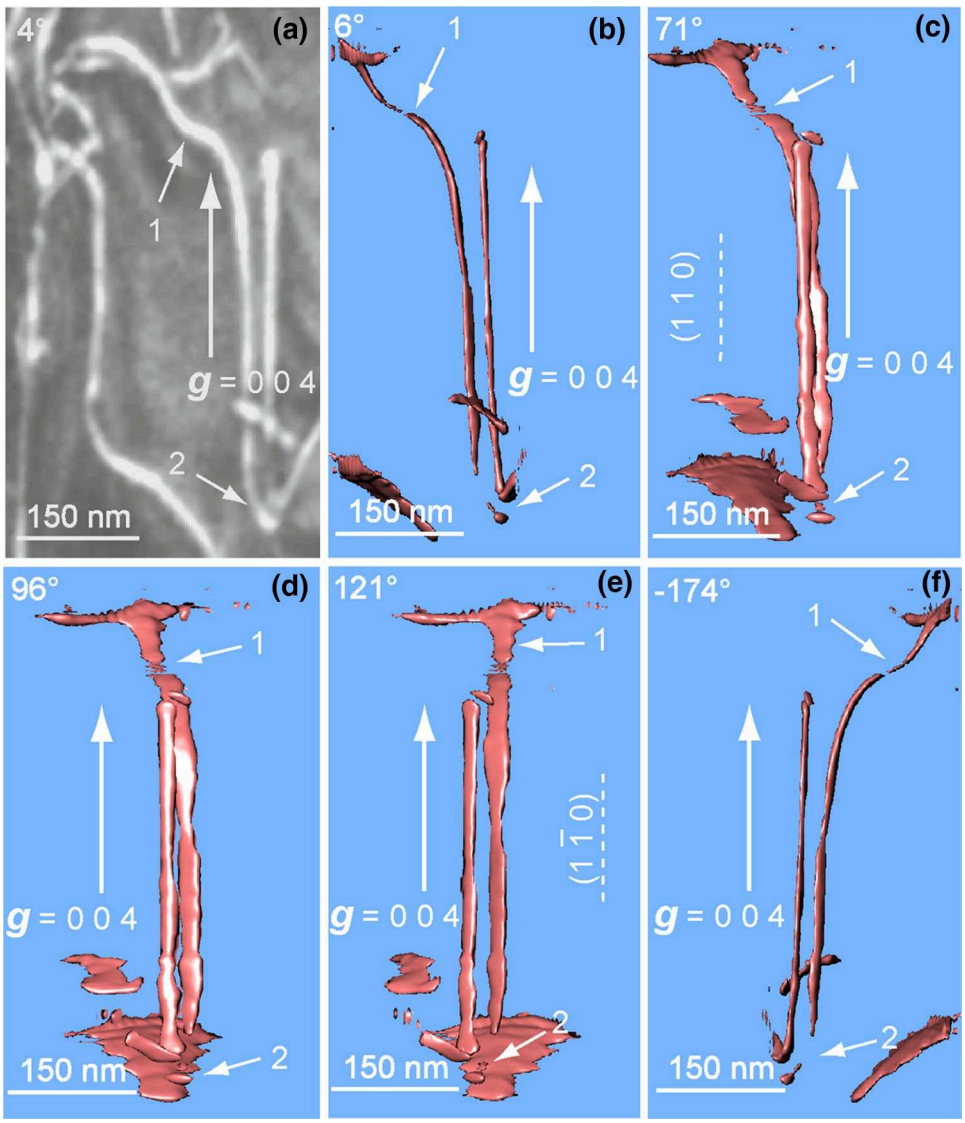

Fig. 2 Cross-slip of a [001] dislocation: **a** micrograph of grain III, with the conditions indicated in Table 1 (the grain is imaged along the [100] zone axis); **b** corresponding reconstructed volume seen along the same direction; it is successively tilted to be viewed along the $[1\bar{1}0]$ zone axis (tilt of 71° in **c**); along the $[0\bar{1}0]$ zone axis (tilt of 96° in **d**); along the $[\bar{1}\bar{1}0]$ zone axis (tilt of 121° in **e**); and along the $[\bar{1}00]$ zone axis (tilt of −174° in **f**). One segment of the dislocation labelled "1" lies in the $(1\bar{1}0)$ plane (see **e**), whereas the other segment of the dislocation labelled "2" lies in (110) (see **c**)

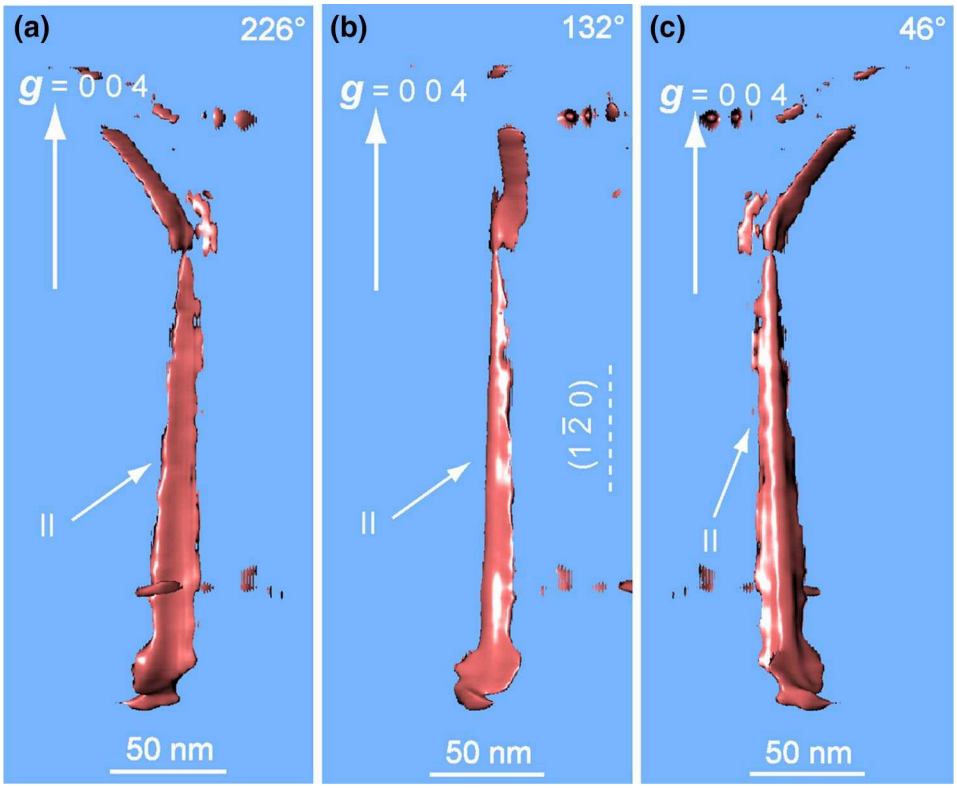

Fig. 3 [001] dislocation lying in $(1\bar{2}0)$ (3D reconstruction volume of a part of grain III and acquisition conditions in Table 1): The [001] dislocation (labelled "II" and indicated by a *white arrow*) is seen along the $[2\bar{1}0]$ zone axis (**a**); along the [210] zone axis (tilt angle 132°), where it appears as a straight line parallel to $(1\bar{2}0)$ (**b**); and along the $[\bar{2}10]$ zone axis (tilt of 42° in **c**)

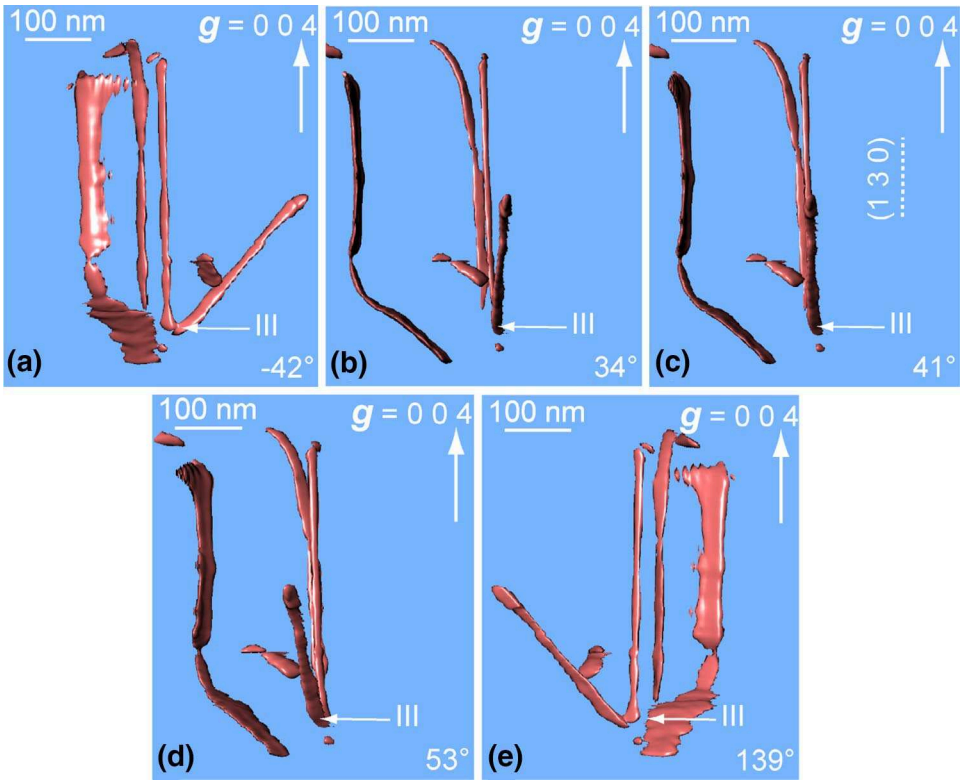

Fig. 4 [001] dislocation, from grain III, lying in (130). The [001] dislocation labelled "III" (indicated by a *white arrow*) is viewed along the [210] zone axis (**a**); the $[4\bar{1}0]$ zone axis (**b**); the $[3\bar{1}0]$ zone axis (**c**), the $[2\bar{1}0]$ zone axis (**d**), and the $[\bar{2}10]$ zone axis (**e**). This dislocation belongs to the (130) plane since it appears as a *straight line* parallel to this plane, in (**c**)

Table 2 Occurrence of each glide plane

Glide planes/grain	Grain I	Grain II	Grain III	Grain IV	Grain V	Grain VI	Total
(100)	3	2	2	0	0	0	7
(010)	2	1	2	2	1	2	10
{110}	7	6	13	4	2	0	32
{120}	0	1	2	0	2	0	5
{130}	0	1	2	1	1	0	5

Table 3 Observation of cross-slip events

Dislocations showing cross-slip	Dislocation segments		
	1	2	3
Dislocation 1 in grain II	(100)	(110)	$(1\bar{1}0)$
Dislocation 2 in grain II	(110)	(130)	
Dislocation in grain III	(110)	$(1\bar{1}0)$	

Discussion

Plastic deformation of olivine at 900 °C corresponds to a low-temperature regime where [001] glide is activated with a strong lattice friction on screw dislocations (Durinck et al. 2007; Demouchy et al. 2013a, b). Fast non-screw segments are thus less represented in the deformed grains. Their characterization is, however, critical to identify the slip planes of [001] dislocations. In this study, we have used the following approach: first, dislocation lines containing non-screw segments and exhibiting significant curvatures were chosen. Then, the reconstructed volumes were tilted until the dislocation line appears as a straight line. Finally, the normal to the straight line identifies the slip plane. Subsequently, the reconstructed volume allows to reach any orientation which expands significantly the number of lines defects that can be characterized. Indeed, about sixty glide planes have been characterized in the present study. As an example, Fig. 2c shows that a tilt angle of 71° is necessary to set the (110) plane edge-on. Under this orientation condition, the observed reconstructed volume is in the missing wedge of the tilted series.

Here, we present the technical justifications which validate our approach. We recall that dislocation transmission electron tomography has been performed using several techniques.

The WBDF technique gives a high dislocation signal-to-noise ratio, but generally the background contrast and the dislocation contrast are not homogeneous (Barnard et al. 2006a, b, 2010). In order to reconstruct dislocation tomographic volumes with a sufficiently high quality, the analysed region has to exhibit a relatively constant orientation and thickness.

The STEM technique gives a more homogeneous contrast for the background. Thanks to the principle of reciprocity, dislocations can be well imaged by diffraction contrast in this mode. Its principle consists in a correspondence between conventional TEM (CTEM) and STEM. To achieve conditions equivalent to CTEM, STEM conditions must involve a small collecting angle (close to a parallel beam). For that purpose, we have increased the camera length and decreased the size of the condenser aperture.

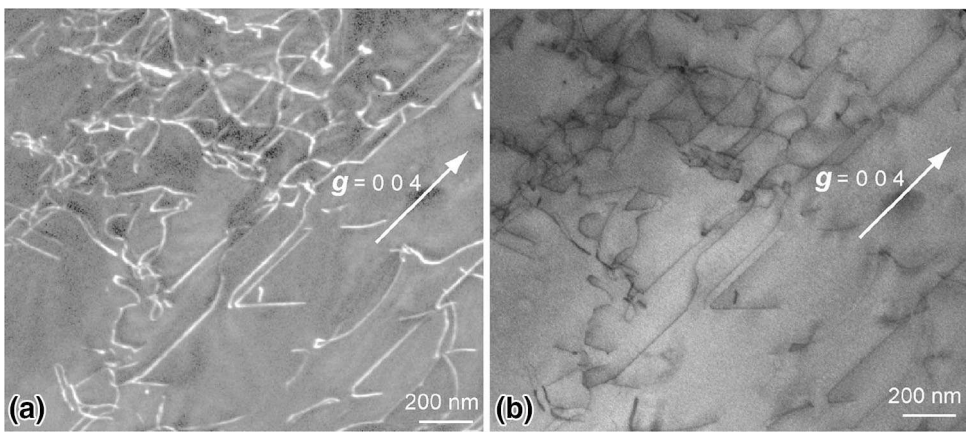

Fig. 5 Comparison between a WBDF micrograph and the STEM corresponding micrograph: **a** WBDF image obtained with the g:004 diffraction vector (the dislocation contrast width is 11.7 nm and the dislocation signal-to-noise ratio is 113 %); **b** corresponding weak-beam bright-field STEM image obtained with the g:004 diffraction vector, a camera length of 200 mm, a spot size of 2 nm and a condenser aperture of 20 μm (the dislocation contrast width is 9.5 nm but the dislocation signal-to-noise ratio is only 18 %)

Nevertheless, the diffraction disc has to be fully positioned on the dark-field detector without any overlapping with the bright-field detector. In our study, with a FEI® Tecnaï $G^2$20Twin LaB_6 200 kV S/TEM, the best conditions are obtained with a camera length of 200 mm and a condenser aperture of 20 μm (Fig. 5b). These conditions are not so far from the conditions of Phillips et al. (2011a, b). Indeed, the authors have obtained an optimal camera length of 163 mm, with a FEI® Tecnai F20 FEG 200 kV S/TEM. Figure 5 shows that using our best STEM conditions, the dislocation are observed with a comparable resolution (contrast width 11.7 nm in WBDF conditions and 9.5 nm in STEM conditions), but with a signal-to-noise ratio approximately 6 times lower than in WBDF (113 % in WBDF conditions and 18 % in STEM conditions). It is expected that the use of a FEG would improve this aspect.

In our study, the best compromise between contrast homogeneity and signal-to-noise ratio is obtained when precession is combined with the WBDF technique. Indeed, the WBDF technique provides a high signal-to-noise ratio for dislocations, and the precession decreases heterogeneities along the dislocations lines (oscillating contrast) and in the background (Rebled et al. 2011). This technique reduces and often eliminates bend contours. Precession modifies and integrates s_g, which removes or attenuates the thickness fringes as well as the oscillating contrast of

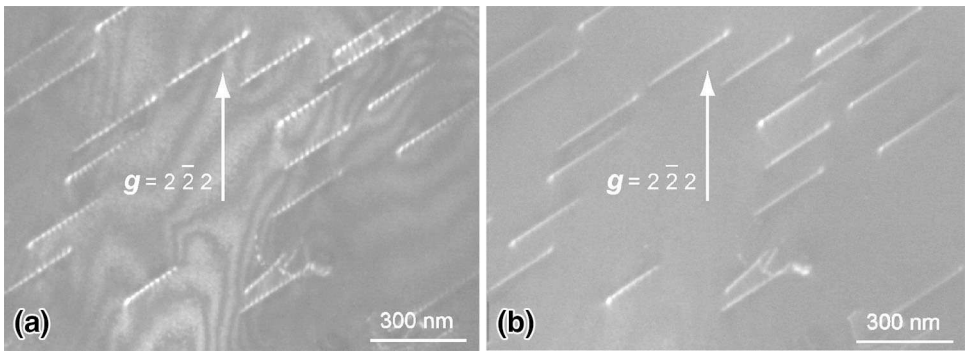

Fig. 6 Comparison between a WBDF micrograph and the corresponding WBDF micrograph associated with precession: **a** WBDF image obtained with the $2\bar{2}2$ diffraction vector (dislocation oscillating contrast and thickness fringes are marked); **b** corresponding WBDF micrograph associated with a 0.1° precession angle (dislocation oscillating contrast and thickness fringes have disappeared)

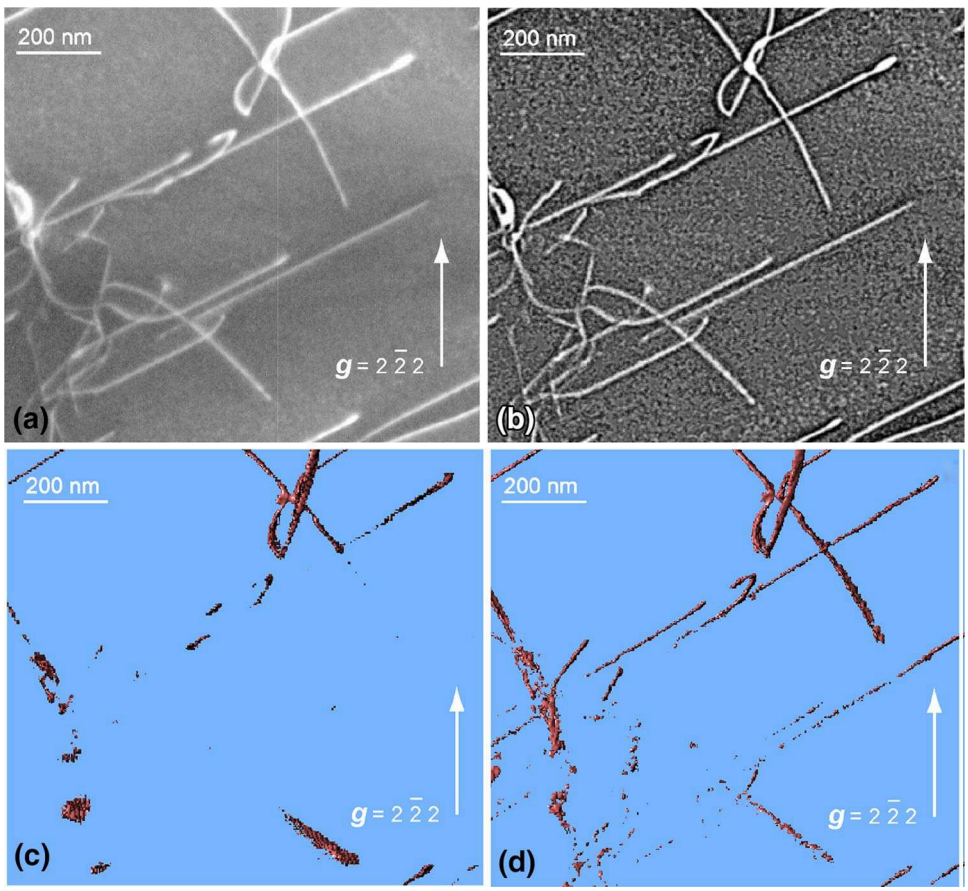

Fig. 7 Effect of a kernel filtering: **a** WBDF image obtained with the $2\bar{2}2$ diffraction vector associated with a 0.1° precession angle (reconstructed volume of a part of grain IV with the conditions specified in Table 1); **b** corresponding WBDF micrograph filtered with a kernel (the dislocation contrast is enhanced); **c** electron transmission tomographic volume resulting from **a**; **d** electron transmission tomographic volume resulting from **b** (the kernel filtering has kept most of the dislocation population details)

inclined dislocations. Figure 6 gives an example of the precession effect on the dislocation contrast and background homogeneity.

To enhance the dislocation contrast, each image of the tilted series has been convoluted with a kernel matrix (Barnard et al. 2010). Figure 7a is obtained in WBDF conditions, associated with a 0.1° precession angle, without a convolution with a kernel matrix. It is compared with Fig. 7b, for which a convolution with a kernel matrix has been applied. Thus, we can verify that the kernel highly increases the dislocation contrast. The resulting 3D reconstructions from the unfiltered images (Fig. 7c) and the filtered images (Fig. 7d) show that the kernel allows keeping most of the dislocation population details.

To the best of our knowledge, the present study represents the first investigation of the slip planes of [001] dislocations in a deformed olivine polycrystal. We have noted a majority of [001] dislocations gliding in {110}, whereas a dominant role of the (100) glide plane was expected (e.g. Gaboriaud et al. 1981). Our study highlights the contribution of glide of [001] dislocations in several other planes when olivine is deformed at 900 °C: (010), {120} and {130}. It is also shown that some [001] dislocation lines belong to several glide planes demonstrating an easy ability for cross-slip under these conditions. This mechanism originally suggested for [100] glide in olivine (Poirier and Vergobbi 1978; Li et al. 2006) has been recently suggested for [001] glide as well (Faul et al. 2011; Raterron et al. 2007, 2009). It had, however, never been characterized so far.

Conclusion and perspectives

Electron tomography gives access to a 3D characterization of dislocations microstructures. We show here that this technique is very efficient to characterize glide planes of dislocations with accuracy. In the present study, we show that in a polycrystal of olivine deformed in the low-temperature regime [i.e. below 1,000 °C and with a predominance of [001] screw dislocations], electron tomography allows to verify the activation of previously reported (100), (010) and {110} planes, and permits identification of new slip planes: {120} and {130}. Furthermore, the detailed analysis of the geometry of dislocation lines makes it possible to characterize in details complex mechanisms such as cross-slip. This information is very important as an input parameter for the visco-plastic self-consistent modelling of crystal preferred orientation evolution of olivine-rich aggregates (Tommasi et al. 2000; Mainprice et al. 2005; Durinck et al. 2007; Castelnau et al. 2009, 2010) and thus for a better understanding of deformation mechanism of the Earth's uppermost mantle.

Acknowledgments A Marie Curie fellowship awarded to S.D. (PoEM: Plasticity of Earth Mantle, FP7-PEOPLE-20074-3-IRG, N°230748-PoEM) supported this study. The TEM national facility in Lille is supported by the CNRS (INSU) and the Conseil Régional du Nord Pas de Calais, France. This work was supported by funding from the European Research Council under the Seventh Framework Programme (FP7), ERC grant N°290424—RheoMan.

References

Arslan I, Tong JR, Midgley PA (2006) Reducing the missing wedge: high-resolution dual axis tomography of inorganic materials. Ultramicroscopy 106:994–1000

Bai Q, Kohlstedt DL (1992) High-temperature creep of olivine single crystals, 2 dislocation structures. Tectonophysics 206:1–29

Barber D J, Wenk HR, Hirth G, Kohlstedt DL (2010) Dislocations in minerals. In: Hirth JP, Kubin L (eds) Dislocations in Solids. Elsevier, Oxford, United-Kingdoms, 19:171–232

Barnard JS, Sharp J, Tong JR, Midgley PA (2006a) High-resolution three-dimensional imaging of dislocations. Science 313:319

Barnard JS, Sharp J, Tong JR, Midgley PA (2006b) Three-dimensional analysis of dislocation networks in GaN using weak-beam dark-field electron tomography. Phil Mag 86:4901–4922

Barnard JS, Eggeman AS, Sharp J, White TA, Midgley PA (2010) Dislocation electron tomography and precession electron diffraction: minimising the effects of dynamical interactions in real and reciprocal space. Phil Mag 90:4711–4730

Buseck PR, Dunin-Borkowski RE, Devouard B, Frankel RB, McCartney MR, Midgley PA, Pósfai M, Weyland M (2001) Magnetite morphology and life on Mars. Proc Natl Acad Sci USA 98:13490–13495. doi:10.1073/pnas.241387898

Castelnau O, Blackman DK, Becker TW (2009) Numerical simulations of texture development and associated rheological anisotropy in regions of complex mantle flow. Geophys Res Lett 36:L12304. doi:10.1029/2009GL038027

Castelnau O, Cordier P, Lebensohn RA, Merkel S, Raterron P (2010) Microstructures and rheology of the Earth's upper mantle inferred from a multiscale approach. C R Physiques 11:304–315

Chen S, Hiraga T, Kohlstedt DL (2006) Water weakening of clinopyroxene in the dislocation creep regime. J Geophys Res 111:B08203

Darot M, Gueguen Y (1981) High-temperature creep of forsterite single crystals. J Geophys Res 86:6219–6234. doi:10.1029/JB086iB07p06219

Demouchy S (2010) Diffusion of hydrogen in olivine grain boundaries and implications for the survival of water-rich zones in the Earth's mantle. Earth Planet Sci Lett 295:305–313

Demouchy S, Schneider SE, Mackwell SJ, Zimmerman ME, Kohlstedt DL (2009) Experimental deformation of olivine single crystals at lithospheric temperatures. Geophys Res Lett 36:L04304. doi:10.1029/2008GL036611

Demouchy S, Tommasi A, Barou F, Mainprice D, Cordier P (2012) Deformation of olivine in torsion under hydrous conditions. Phys Earth Planet Int 202–203:56–70

Demouchy S, Mussi A, Barou F, Tommasi A, Cordier P (2013a) Visco-plasticity of polycrystalline olivine at high pressure and 900 °C: fresh outcomes from high resolution EBSD and electron tomography. AGU Fall meeting, session T012

Demouchy S, Tommasi A, Ballaran TB, Cordier P (2013b) Low strength of Earth's uppermost mantle inferred from tri-axial

deformation experiments on dry olivine crystals. Phys Earth Planet Inter 220:37–49
Demouchy S, Mussi A, Barou F, Tommasi A, Cordier P (2014) Viscoplasticity of polycrystalline olivine at high pressure and 900 °C: fresh outcomes from high resolution EBSD and electron tomography. Tectonophysics (in press)
Durham WB, Goetze C (1977) Plastic flow of oriented single crystals of olivine: 1 Mechanical data. J Geophys Res 82:5737–5753. doi:10.1029/JB082i036p05737
Durham WB, Goetze C, Blake B (1977) Plastic flow of oriented single crystals of olivine: 2. Observations and interpretations of the dislocation structures. J Geophys Res 82:5755–5770. doi:10.1029/JB082i036p05755
Durinck J, Devincre B, Kubin L, Cordier P (2007) Modeling the plastic deformation of olivine by dislocation dynamics simulations. Am Mineral 92:1346–1357
Evans B, Goetze C (1979) The temperature variation of hardness of olivine and its implication for polycrystalline yield stress. J Geophys Res 84:5505–5524. doi:10.1029/JB084iB10p05505
Faul UH, Fitz Gerald JD, Farla RJM, Ahlefeldt R, Jackson I (2011) Dislocation creep of fine-grained olivine. J Geophys Res 116:B01203
Gaboriaud RJ, Darot M, Gueguen Y, Woirgard J (1981) Dislocations in olivine indented at low-temperatures. Phys Chem Miner 7:100–104
Gueguen Y (1979) High temperature olivine creep: evidence for control by edge dislocations. Geophys Res Lett 6:357–360. doi:10.1029/GL006i005p00357
Gueguen Y, Darot M (1982) Dislocations in forsterite deformed at a high-temperature. Philos Mag A 45:419–442
Hazen RM (1976) Effects of temperature and pressure on the crystal structure of forsterite. Am Mineral 61:1280–1293
Head AK, Humble P, Clarebrough LM, Morton AJ, Forwood CT (1973) Computed electron micrographs and defect identification. North-Holland Publishing Company, Amsterdam London
Jaoul O, Michaut M, Gueguen Y, Ricoult D (1979) Decorated dislocations in forsterite. Phys Chem Miner 5:15–19
Kohlstedt DL, Goetze C (1974) Low-stress high-temperature creep in olivine single crystals. J Geophys Res 79:2045–2051. doi:10.1029/JB079i014p02045
Kohlstedt DL, Goetze C, Durham WB, Van der Sande J (1976) New technique for decorating dislocations in olivine. Sciences 191:1045–1046
Li L, Weidner D, Raterron P, Chen J, Vaughan M, Shenghua M, Durham B (2006) Deformation of olivine at mantle pressure using D-DIA. Eur J Mineral 18:7–19. doi:10.1127/0935-1221/2006/0018-0007
Mainprice D, Tommasi A, Couvy H, Cordier P, Frost DJ (2005) Pressure sensitivity of olivine slip systems and seismic anisotropy of earth's upper mantle. Nature 433:731–733
McCammon CA (2005) The paradox of mantle redox. Science 308:807–808
Midgley PA, Dunin-Borkowski RE (2009) Electron tomography and holography in materials science. Nature Mater 8:271–280
Miller WH (1839) A treatise on Crystallography. Cambridge, England, printed for J. and J.J. Deighton; London: J.w. Parker
Paterson MS (1970) A high pressure, high temperature apparatus for rock deformation. Int J Rock Mech Min Sci 7:512–517
Paterson MS (1990) Rock deformation experimentation. In: Duba AG, Durham WB, Handin JW, Wang HF (Editors), The brittle-ductile transition in rocks: the Head volume. Geophys. Monogr. Ser., AGU, Washington D.C., 59:187-194
Penczek P, Radermacher M, Frank J (1992) Three-dimensional reconstruction of single particles embedded in ice. Ultramicroscopy 40:33–53
Phakey P, Dollinger G, Christie J (1972) Transmission electron microscopy of experimentally deformed olivine crystals. In: H.C. Heard, I.Y. Borg and N.L. Carter (Editors), Flow and Fracture of rocks. Am Geophys Un Geophys Monogr Series. doi: 10.1029/GM016p0117
Phillips PJ, Brandes MC, Mills MJ, De Graef M (2011a) Diffraction contrast STEM of dislocations: imaging and simulations. Ultramicroscopy 111:1483–1487
Phillips PJ, Mills MJ, De Graef M (2011b) Systematic row and zone axis STEM defect image simulations. Phil Mag 91:2081–2101
Poirier JP, Vergobbi B (1978) Splitting of dislocations in olivine, cross-slip-controlled creep and mantle rheology. Phys Earth Planet Inter 16:370–378
Raleigh CB (1968) Mechanisms of plastic deformation of olivine. J Geophys Res 73:5391–5406. doi:10.1029/JB073i016p05391
Raterron P, Wu Y, Weidner DJ, Chen J (2004) Low-temperature olivine rheology at high pressure. Phys Earth Planet Inter 145:149–159. doi:10.1016/j.pepi.2004.03.007
Raterron P, Chen J, Li L, Weidner D, Cordier P (2007) Pressure-induced slip-system transition in forsterite: single-crystal rheological properties at mantle pressure and temperature. Am Mineral 92:1436–1445. doi:10.2138/am.2007.2474
Raterron P, Amiguet E, Chen J, Li L, Cordier P (2009) Experimental deformation of olivine single crystals at mantle pressures and temperatures. Phys Earth Planet Inter 172:74–83. doi:10.1016/j.pepi.2008.07.026
Rebled JM, Yedra L, Estrade S, Portillo J, Peiro F (2011) A new approach for 3D reconstruction from bright field TEM imaging: beam precession assisted electron tomography. Ultramicroscopy 111:1504–1511
Sharp JH, Barnard JS, Kaneko K, Higashida K, Midgley PA (2008) Dislocation tomography made easy: a reconstruction from ADF STEM images obtained using automated image shift correction. J Phys Conf Ser 126:012013
Tanaka M, Honda M, Mitsuhara M, Hata S, Kaneko K, Higashida K (2008a) Three-dimensional observation of dislocations by electron tomography in a silicon crystal. Mater Trans 49:1953–1956
Tanaka M, Higashida K, Kaneko K, Hata S, Mitsuhara M (2008b) Crack tip dislocations revealed by electron tomography in silicon single crystal. Scripta Mater 59:901–904
Tommasi A, Mainprice D, Canova G, Chastel Y (2000) Viscoplastic self-consistant and equilibrium-based modeling of olivine lattice preferred orientations: implications for the upper mantle seismic anisotropy. J Geophys Res 105:7893–7908

Characterization of dislocation interactions in olivine using electron tomography

Alexandre MUSSI[1*], Patrick CORDIER[1] and Sylvie DEMOUCHY[2]

[1]Unité Matériaux et Transformations, UMR 8207 CNRS-Université Lille1,
F-59655 Villeneuve d'Ascq, France
[2]*Géoscience Montpellier, UMR 5342 CNRS - Université Montpellier 2,*
F-34095 Montpellier, France

Cite as:
A. Mussi, P. Cordier & S. Demouchy (2015) Characterization of dislocation interactions in olivine using electron tomography. Philosophical Magazine, 95(4), 335-345, https://doi.org/10.1080/14786435.2014.1000996

Abstract

We have investigated by electron tomography, in a transmission electronic microscope, the interactions between dislocations in olivine single crystals and polycrystals deformed in axial compression at T<1000 °C (T<0.5T_m). Dislocations are mostly of the $[001]$ type, except in the polycrystal where $[100]$ and $[001]$ dislocations have been activated. A few $\langle 101 \rangle$ junctions have been found and characterized. Many collinear interactions have been identified either involving direct interactions between crossing dislocations of opposite Burgers vectors or indirect interactions between dislocations gliding in parallel planes and sessile dislocation loops. We suggest that collinear interaction, already identified as the primary source of strain hardening in FCC metals, is the main dislocation interaction mechanism in olivine deformed at temperatures below 1000 °C.

Keywords: Dislocation, junction, collinear interaction, TEM, electron tomography, olivine.

[*]Corresponding author: alexandre.mussi@univ-lille1.fr

1. Introduction

Mantle convection, which drives plate tectonics, is needed to dissipate the internal heat of the Earth. This convection process within a solid mantle involves plastic deformations of rocks at a large scale. Olivine $(Mg, Fe)_2SiO_4$ is the main constituent of Earth's upper mantle, which extends down to 410 km of depth. Understanding plasticity in olivine is thus essential for studying the rheology of the upper mantle. Olivine has an orthorhombic symmetry with a ≈ 4.752 Å, b ≈ 10.193 Å and c ≈ 5.977 Å when described within the *Pbnm* space group [1]. Studies on plastic deformation of olivine and forsterite (the pure magnesium end-member) single and polycrystals were mostly conducted at high temperatures (T>1000°C; $T>0.5T_m$) [2-9] and occasionally at lower temperatures [10-17]. Most studies focused on the slip system characterizations and have shown the occurrence of:

- dislocations with $[100]$ and $[001]$ Burgers vectors only (i.e., dislocations with $[010]$ Burgers do not contribute to plastic deformation in olivine [18]);
- the (001), $\{011\}$, $\{021\}$, $\{031\}$ and (010) glide planes, for $[100]$ dislocations, at high temperatures;
- the (100), (010) and $\{110\}$ glide planes, for $[001]$ dislocations, at high and low temperatures.

Until now, dislocation interactions have only been considered through numerical modelling [19]. As olivine has only two perpendicular slip directions ($[100]$ and $[001]$), the formation of junctions is not favourable and dislocation storage is not anticipated. This is consistent with common observations of olivine deformed at high temperature where only low-angle subgrain boundaries are observed. Nevertheless, recent experiments performed at low temperature have shown numerous dislocation entanglements [16, 20].

In this study, the dislocation interactions in olivine are experimentally characterized by transmission electron microscopy (TEM) from samples previously used for the olivine rheology studies conducted by Demouchy et al. at low temperatures [17, 20]. Electron tomography is used in this work to investigate three-dimensional dislocation microstructures in order to understand dislocation interaction mechanisms.

2. Experimental details

2.1. Sample and deformation experiment

Three specimens, all prepared from San Carlos olivine (Arizona, USA), were investigated:

- A polycrystal deformed at 900°C, at a strain rate of 1.1×10^{-5} s^{-1} (PoEM 22);
- A single crystal oriented to activate the $[001](010)$ slip system and deformed at 850°C, 7.06×10^{-6} s^{-1} (PoEM 11);
- A single crystal compressed at 806°C, 5.1×10^{-5} s^{-1}, and oriented to activate the $[001](100)$, the $[001](110)$ and the $[100](001)$ slip systems (PoEM 9).

All samples were deformed in compression under a confining pressure of 300 MPa of argon using a high-pressure high-temperature gas apparatus [17, 20, 21, 22] at Geosciences Montpellier (University of Montpellier 2). The olivine polycrystal has been produced from an olivine fine-grained powder sintered at a high temperature (1250°C) during 3 hours under the same confining pressure conditions. The specimens are cylindrical: 9.45 mm in diameter and 20.03 mm long for PoEM 22; 4.2 mm in diameter and 6.61 mm long for PoEM 11; and 4.19 mm in diameter and 6.32 mm long for PoEM 9.

2.2. Transmission electron tomography

Sections cut from the three samples have been mechanically polished down to a thickness of ca. 30 μm. The resulting foils were Ar-ion sputtered with a Gatan® DuoMill TM model 600, to reach electron transparency. Then, thin carbon films were spread on the thin foils to insure electron conduction. TEM analyses were performed with a FEI® Tecnaï $G^2$20Twin microscope, operating at 200 kV with a LaB_6 filament at the TEM facility at the University of Lille1. Dislocation microstructures were investigated in the weak-beam dark-field (WBDF) mode associated with a 0.1° precession angle to weaken thickness fringes [23]. Nineteen tilted series were acquired every 2° with an average tilt angle ranging from -54° to 50°. Most of them were acquired with WBDF conditions associated with precession (WBDF-P). The tilted series alignments were performed manually (a pixel precision could be achieved), as the contrasts of WBDF micrographs are too weak to allow automatic alignments. The contrast of the tilted series needed to be enhanced to optimize the quality of the reconstructed volume. Consequently, the micrographs have been filtered using a polynomial fit with the ImageJ software to improve contrast

homogeneity of the background and of dislocations. Two reconstruction algorithms have been employed to generate the 3D images:

- The weighted back projection algorithm [24] used with the TomoJ plugin [25] accessible in ImageJ;
- The simultaneous iterative reconstruction technique algorithm [26] used with the Gatan® 3D reconstruction software.

3. Results

A total of nineteen different areas have been analysed. Six of them come from PoEM 22, six from PoEM 11 and seven from PoEM 9. The analysed area sizes are ranging from 1.5 to 4.3 μm. The average dislocation density is approximately 1.7×10^{13} m^{-2}.

A typical microstructure observed in PoEM 11 is shown in Figure 1. All dislocations are in contrast with the 004 diffraction vector (***g***) and out of contrast with ***g***: $1\bar{3}0$ (figure 1). Consequently, PoEM 11 is exclusively composed of $[001]$ dislocations. Similarly, using ***g***: $22\bar{2}$ and ***g***: 062, we verified that PoEM 9 is also exclusively composed of $[001]$ dislocations. On the contrary, in PoEM 22, which is a polycrystal, both $[100]$ and $[001]$ dislocations are found with an approximate ratio 3:1 (see figure 8 in Demouchy et al. [20]).

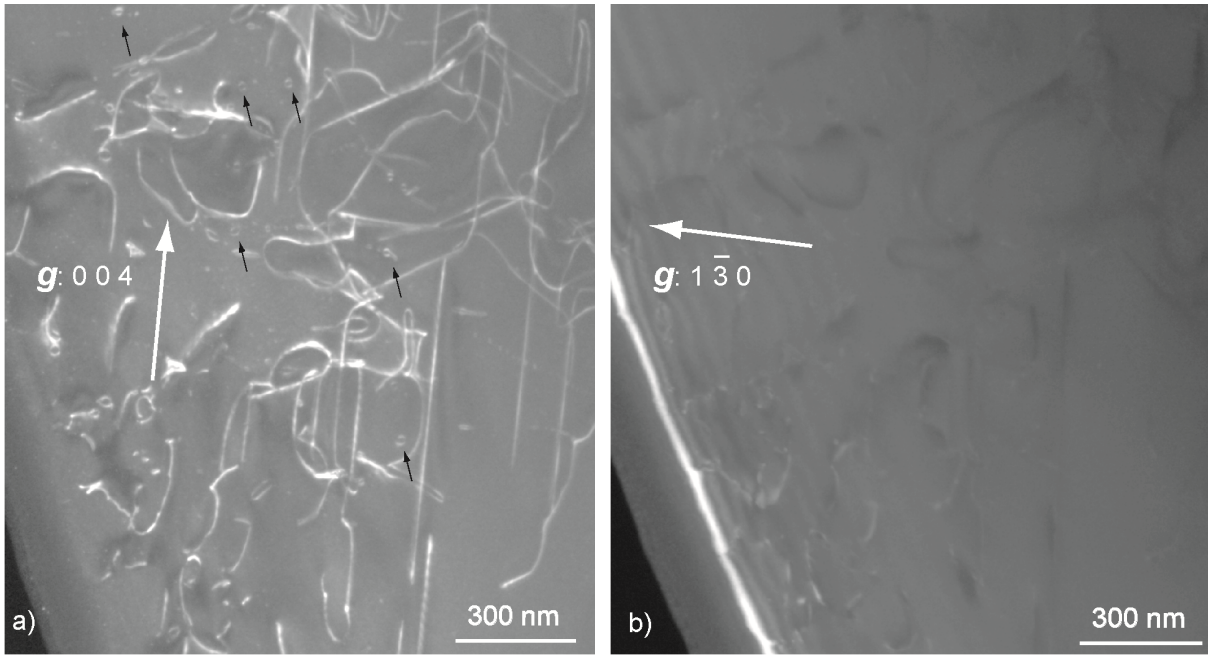

Figure 1: *WBDF-P micrographs of* $[001]$ *dislocations in PoEM 11. Viewing direction near the* $[310]$ *zone axis. (a) All the dislocations are in contrast with* ***g****:* 004 *(black arrows are pointing sessile dislocation loops). (b) All the dislocations are out of contrast with* ***g****:* $1\bar{3}0$.

As expected from previous studies, evidences for dislocation junctions are rare. However we have found some in PoEM 22. An example is shown on figure 2. Dislocations coloured in blue and the one in yellow are in contrast with ***g***: 004 (figure 2(a)). But, all dislocations (blue, red and yellow) are in contrast with ***g***: $2\bar{2}2$ (figure 2(b)). Consequently, blue dislocations are of the $[001]$ type and red dislocations are of the $[100]$ type. An electron tomography reconstruction volume (ETRV) of this zone, obtained with the ***g***: $2\bar{2}2$, shows that the dislocation coloured in yellow is not the result, for a given orientation, of a superimposition of a blue and a red dislocation, but a distinct line attached to them. From the intensity profiles extracted from figure 2(b), we also note that the contrast of the yellow dislocation is significantly higher than the blue and the red ones (figure 2(c)). Since the contrast is linked to the ***g***.***b*** product (with ***b*** the Burgers vector) [27-28], we conclude that the Burgers vector of the yellow dislocation is $[101]$. As a result, the junction reaction is: $[100]+[001]\rightarrow[101]$.

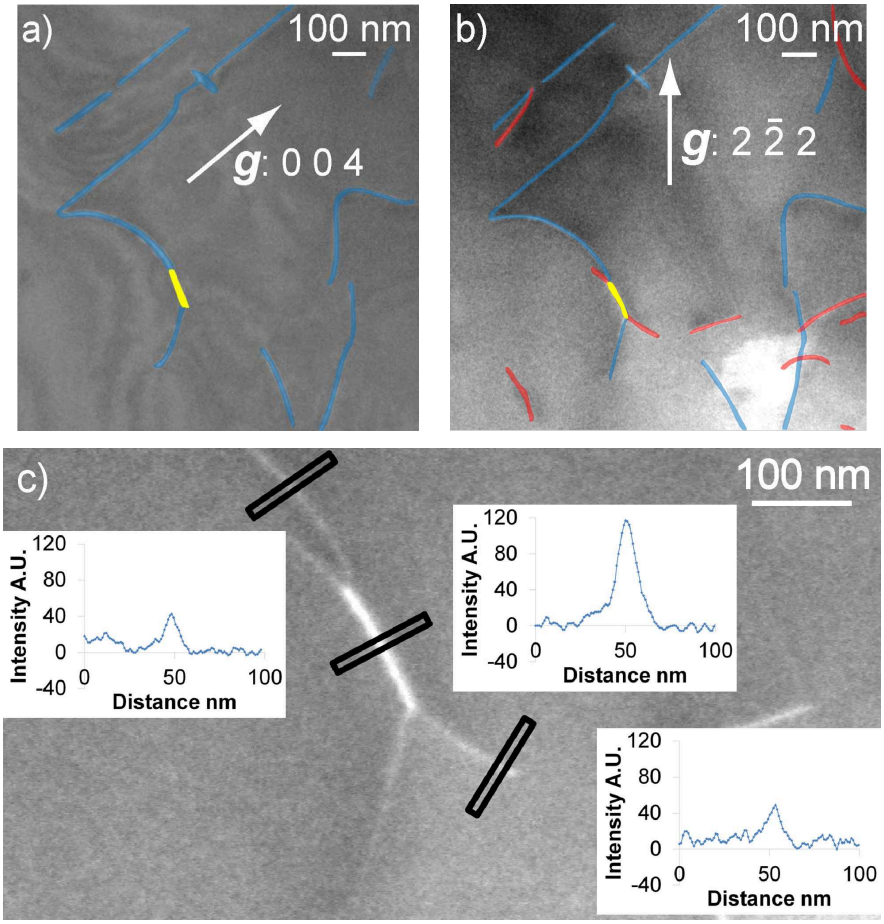

Figure 2: *Micrograph in WBDF-P conditions of a* $\langle 101\rangle$ *junction in PoEM 22. Viewing direction near the* $[110]$ *zone axis. (a) The dislocations coloured in blue and the one in yellow are in contrast with* ***g****:* 004*. (b) Blue, red and yellow dislocations are in contrast, with* ***g****:* $2\bar{2}2$*. (c) The intensity profiles, as inserts, across the blue, red and yellow dislocations with* ***g****:* $2\bar{2}2$*, show that the contrast of the yellow dislocation is significantly higher than the two other ones.*

A second zone from PoEM 22, where all dislocations are of $[001]$ type (as they are in contrast with ***g***: 004), is displayed in figure 3. We highlight three dislocations coloured in red, blue and green. The use of tomography enables us to find the glide planes of these dislocations by putting them edge on. The three long segments coloured in green glide in $(1\bar{1}0)$ (Figure 3(a)). The blue dislocation glides in (140) (Figure 3c). The dislocation coloured in red glides in (010). Figure 3 shows that interaction with the blue dislocation leads to an annihilation of the green dislocation with a missing segment aligned parallel to $[001]$. Similarly, the red dislocation interacts with the green dislocation generating an annihilation segment also parallel to $[001]$.

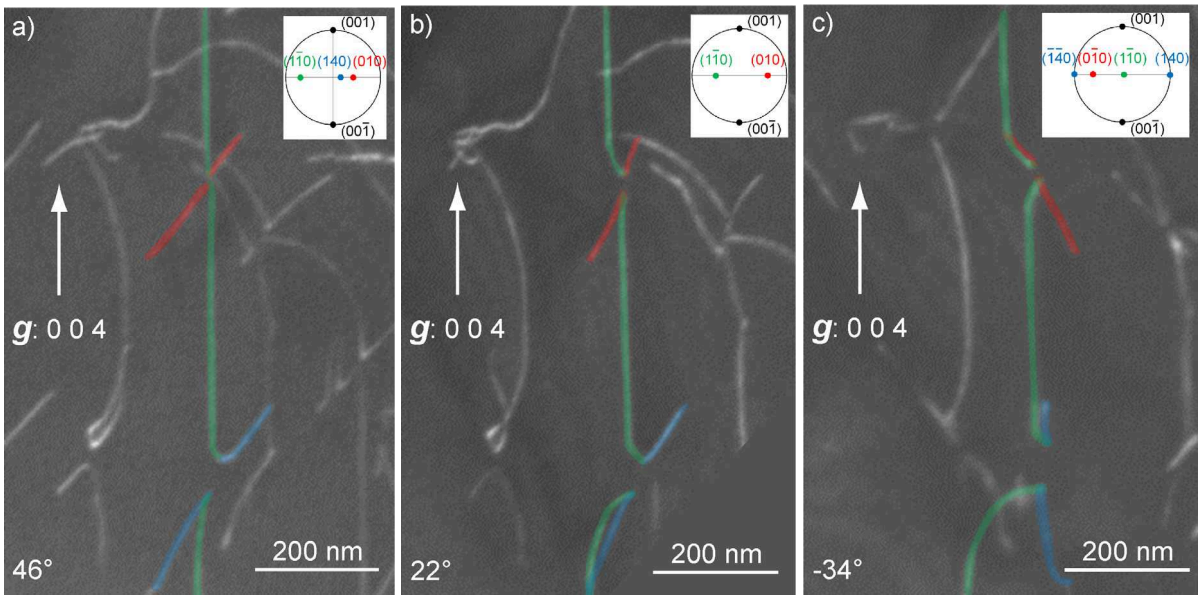

Figure 3: *Collinear interactions in PoEM 22. WBDF-P micrographs, with* ***g****:* 004*. Three orientations are presented corresponding to tilt angles of 46° (a), 22° (b) and -34° (c), with the corresponding stereographic projection on the top right hand corner. The ETRV, obtained with the* 004 *diffraction vector, enables us to find the glide planes of the dislocation coloured in green, in red and in blue. They are* $(1\bar{1}0)$*,* (010) *and* (140) *respectively. (a) The dislocation coloured in green is almost parallel to* $[001]$ *(the glide plane of this dislocation is nearly edge-on). (b) All the three glide planes are tilted. (c) The glide plane of the blue dislocation is practically edge-on, as this dislocation is seen almost vertical (i.e. along* $[001]$*) and as a straight line.*

Other configurations suggesting dislocation annihilations by collinear interactions have been found. The WBDF-P micrographs presented in figure 4 are from PoEM 9. They show two half loops facing each other, observed with ***g***: $22\bar{2}$, tilted at 40° (Figure 4a), at 4° (Figure 4(b)) and -34° (Figure 4(c)). All dislocations involved are of the $[001]$ type. The direction of the annihilated segment, which is indicated by a white dashed line, is not aligned with the screw direction: $[001]$. Electron tomography shows that those half loops are not glissile loops. They are each constituted of two

segments, which glide in two parallel (100) planes (Figure 5(f)). Hence, the singular point where they meet (i.e., highlighted in green on figure 5(d)) corresponds to the projection of a sessile segment connecting those two (100) planes (Figure 5(f)). This observation suggests that those two half loops correspond to an interaction process involving two $[001]$ dislocations gliding on two parallel (100) planes.

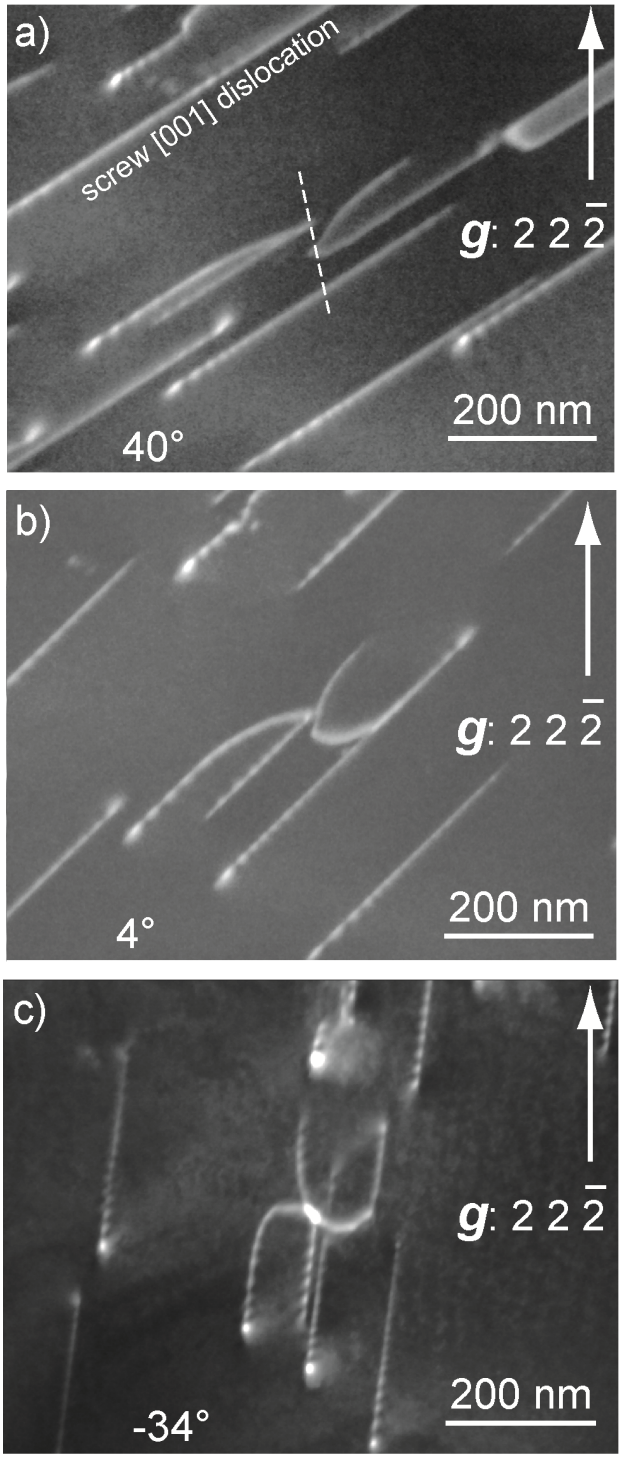

Figure 4: *Dislocation interaction observation in PoEM 9. (a) WBDF-P image, tilted at 40°, with* ***g****:* $22\bar{2}$*, where two half-loops are facing each other. Identical WBDF-P images but tilted at 4° (b) and identical WBDF-P images but -34° (c).*

4. Discussion

Electron tomography, which can reach angular resolution of 2°, is a powerful technique to characterize glide planes [20, 23, 29-37], cross-slip [23, 36], climb planes and dislocation interactions. In a previous study, we established that in olivine, $[001]$ dislocations could glide in $\{120\}$ and $\{130\}$ [23]. We show in figure 3(c) that $[001]$ dislocations can also glide in $\{140\}$.

We report here, to the best of our knowledge, the first unequivocal evidence of $\langle 101 \rangle$ junctions in olivine. Durinck et al. [19] have considered theoretically the possibility of dislocation junctions in olivine and shown that the formation of $\langle 101 \rangle$ junctions is very unlikely but not impossible. This is due to the fact that the $[100]$ and $[001]$ Burgers vectors are perpendicular. Under these conditions, the formation energy of a $\langle 101 \rangle$ junction is approximately the same as the sum of the energies of the initial $[100]$ and $[001]$ dislocation segments. We show here that in agreement with theoretical predictions, $\langle 101 \rangle$ junctions can form. However they are rare, which also confirms theoretical predictions that their formation is energetically unfavourable and that they correspond to weak junctions.

Moreover, Durinck et al. (2007) have shown that annihilation of dislocations with collinear Burgers vectors is statistically the main interaction mechanism in olivine. This interaction mechanism called collinear interaction was discovered eleven years ago [19, 38-41]. Two dislocations with opposite signs and gliding in two different glide planes cross and interact. They create an annihilation junction, the direction of which is the intersection of the two glide planes. The annihilation junction creates two pinning points which impede dislocations and favor dislocation storage.. The collinear interaction has been shown to represent the primary source of strain hardening in FCC metals [38-40]. However, experimental evidences of collinear interactions are still rare [38, 42]. In this study, we have observed many occurrence of collinear interaction. One example is shown on figure 3. In this particular case, a long $[001]$ dislocation segment (in green) gliding in $(1\bar{1}0)$ interacts with two $[00\bar{1}]$ dislocations which glide in (010) (red) and in (140) (blue). As expected, annihilation takes place where the dislocations meet and their lines are interrupted. The missing segment is indeed aligned along the intersections of the glide planes: $[001]$ (vertical on figure 3(b), 3(c)) as predicted.

The configuration described in figure 4 and 5 is quite common in our olivine samples. Several lines of evidence suggest that it results also from an interaction. First, the half loops are not glissile. They connect lines which glide on two parallel (100) planes. Also the dislocations involved in this interaction are of opposite signs as indicated by the asymmetry of the contrasts, where the dislocations intersect the thin foil surfaces (see arrows on figure 5(d)) as explained by the dynamical theory of diffraction [28]. These configurations cannot result from the standard collinear mechanism since they involve dislocations gliding on parallel planes. Indeed, the missing segment is not aligned along $[001]$ as highlighted on figure 4(a). To account for this configuration, we propose that the dislocations have interacted with a small dislocation loop contained in a $\{hkl\}$ type plane. Indeed, there are pervasive occurrences in our samples, of interactions between dislocations and loops as shown on figure 5(g). It can lead to a small annihilation as shown in figure 5(a). Since this interaction acts as a pinning point, it is possible that a second dislocation of opposite sign glides in the opposite direction on a parallel (100) plane and collides into this configuration. The possible result of the interaction is described on figure 5(b). The two lines of each half loop are connected by a short segment (in green) which is a remnant of the loop. However, when this short segment is viewed close to edge-on, it is almost invisible. Figure 5(c) presents a sketch of this dislocation configuration. This illustration corresponds to figure 5(d) (the small white arrows show that the two dislocations have opposite signs). The projection of the sketch along the $[011]$ zone axis (Figure 5(e)) shows that each dislocation segments of each half loop belong to two different (100) planes (edge-one with this orientation). The corresponding ETRV verifies this model (Figure 5(f)). It is only with a 92° rotation, made possible by the electron tomography, that it can be evidenced. Further confirmation can be found on many equivalent configurations in the same sample. Figure 5(g) shows one of them. It shows a $[001]$ screw dislocation interacting with a sessile loop, which corresponds to the schematic illustration of figure 5(a) (we can note another sessile loop on the upper right hand corner of the micrograph). Furthermore, figure 5(h) shows an interaction with a larger loop oriented in a different plane, which makes observation of the connecting segment easier.

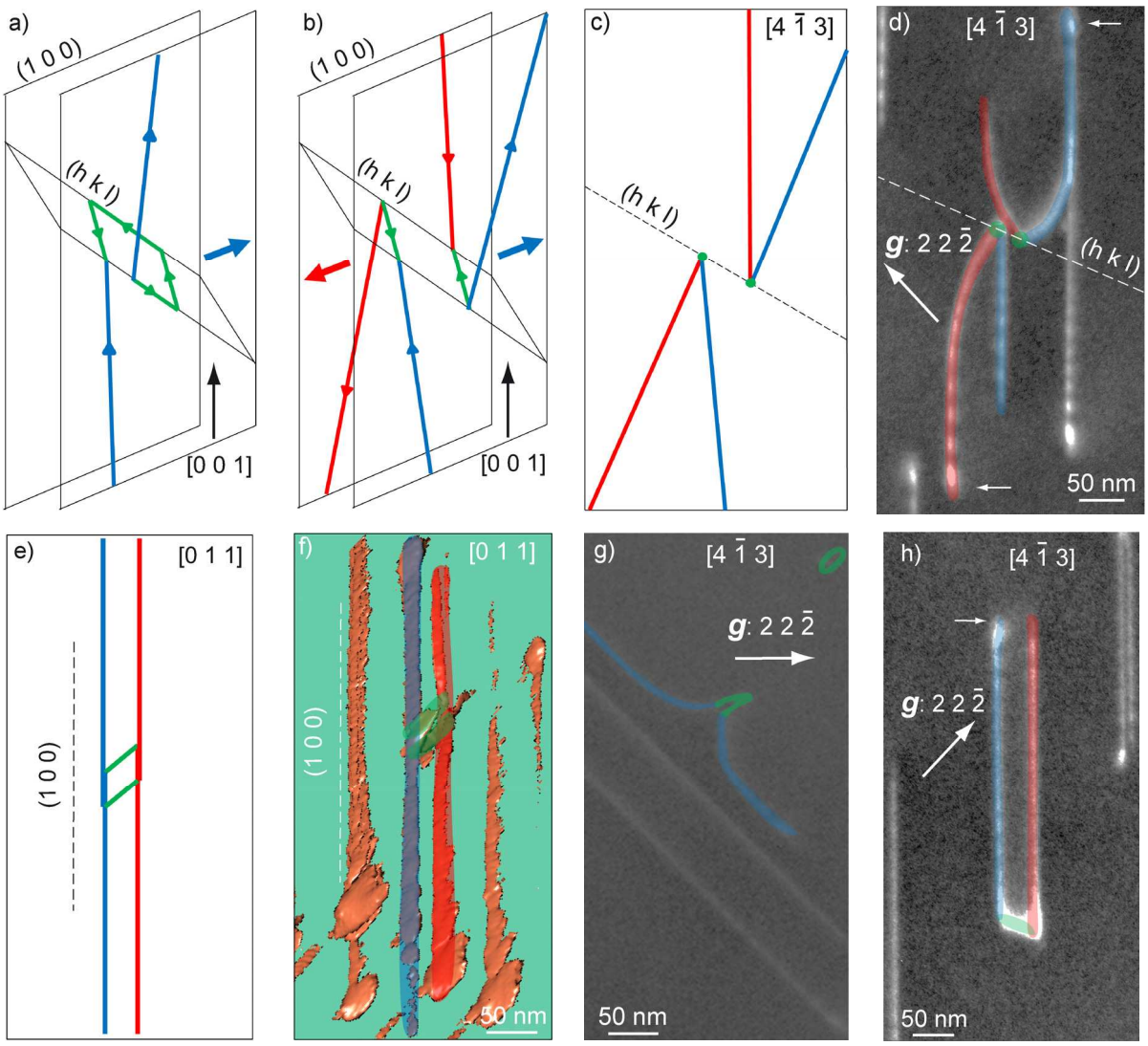

Figure 5: *Mechanism proposed for the dislocation interaction shown in figure 4. (a) A* $[001]$ *screw dislocation (in blue) glides on a* (100) *plane and interacts with a small sessile loop (in green), lying on a* (hkl) *plane, with an opposite Burgers vector, creating a small annihilation segment. (b) A* $[00\bar{1}]$ *screw dislocation (in red) glides in the opposite direction on a parallel* (100) *plane and interacts with the loop, creating another small annihilation segment. (c) Projection of the schematic illustration model along the* $[4\bar{1}3]$ *zone axis with the* (hkl) *plane edge-one. (d) Corresponding WBDF-P micrograph, obtained with* ***g****:* $2\bar{2}2$*. (e) Projection of the model along the* $[011]$ *zone axis. (f) Corresponding ETRV, verifying that the* (100) *planes are edge-one. (g) Micrograph in WBDF-P conditions of the same sample, showing a* $[001]$ *screw dislocation (in blue) interacting with a sessile loop (in green), corresponding to the schematic illustration of (a). (h) WBDF-P micrograph in the same sample, corresponding to the schematic illustrations of (e) and (f).*

5. Conclusion and perspectives

To summarize, we present here the dislocation interaction mechanisms observed in olivine single crystals and polycrystals deformed at temperature below 1000 °C.

When both $[100]$ and $[001]$ glides are activated simultaneously, reactions may take place leading to $\langle 101 \rangle$ junctions. We provide here a characterization of such junctions. However, our observations are compatible with theoretical predictions that such events are not common and do not lead to strong junctions.

Yet, our observations point at collinear annihilation as the main interaction process in olivine. As proposed on FCC metals, we find pervasive evidence for collinear annihilations between dislocations gliding in intersecting planes. The fact that $[001]$ dislocations tend to glide in many $\{hk0\}$ planes enhances the probabilities of such interactions. The presence in our samples of many debris in the form of sessile $[001]$ dislocation loops (see black arrows on figure 1(a)) is at the origin of another mechanism. This mechanism leads to collinear annihilation following the interaction with such loops of two dislocations gliding in parallel planes.

Altogether, our observations suggest that the collinear interaction, already identified as the main source for hardening in FCC metals, is also the main dislocation interaction mechanism in olivine deformed at temperature below 1000 °C. This mechanism was already proposed theoretically by Durinck et al. [19]. It is now verified experimentally.

Acknowledgements:

The TEM national facility in Lille is supported by the CNRS (INSU) and the Conseil Régional du Nord Pas de Calais, France.

References

[1] R.M. Hazen, Am. Mineral. 61 (1976) p.1280.

[2] Q. Bai and D.L. Kohlstedt, Philos. Mag. A. 66 (1992) p.1149.

[3] M. Darot and Y. Gueguen, J. Geophys. Res. 86 (1981) p.6219.

[4] W.B. Durham and C. Goetze, J. Geophys. Res. 82 (1977) p.5737.

[5] W.B. Durham, C. Goetze and B. Blake, J. Geophys. Res. 82 (1977) p.5755.

[6] Y. Gueguen, Geophys. Res. Lett. 6 (1979) p.357.

[7] Y Gueguen and M. Darot, Philos. Mag. A 45 (1982) p.419.

[8] O. Jaoul, M. Michaut, Y. Gueguen and D. Ricoult, Phys. Chem. Miner. 5 (1979) p.15.

[9] D.L. Kohlstedt and C. Goetze, J. Geophys. Res. 79 (1974) p.2045.

[10] C.B Raleigh, J. Geophys. Res. 73 (1968) p.5391.

[11] P. Phakey, G. Dollinger and J. Christie, *Transmission electron microscopy of experimentally deformed olivine crystals*, in *Flow and Fracture of rocks*, H.C. Heard, I.Y. Borg and N.L. Carter, eds., Am. Geophys. Un. Geophys. Monogr. Ser., AGU, Washington, 1972, p.117.

[12] B. Evans and C. Goetze, J. Geophys. Res. 84 (1979) p.5505.

[13] R.J. Gaboriaud, M. Darot, Y. Gueguen and J. Woirgard, Phys. Chem. Miner. 7 (1981) p.100.

[14] P. Raterron, Y. Wu, D.J. Weidner and J. Chen, Phys. Earth Planet. Inter. 145 (2004) p.149.

[15] S. Demouchy, S.E. Schneider, S.J. Mackwell, M.E. Zimmerman and D.L. Kohlstedt, Geophys. Res. Lett. 36 (2009) L04304.

[16] S. Demouchy, A. Mussi, F. Barou, A. Tommasi A and P. Cordier, AGU Fall meeting (2013) T43G-06.

[17] S. Demouchy, A. Tommasi, T.B. Ballaran and P. Cordier, Phys. Earth Planet. Inter. 220 (2013) p.37.

[18] K.Fujino, H. Nakazaki, H. Momoi, S.I. Karato, D.L. Kohlstedt, Phys. Earth Planet. Inter. 78 (1993) p.131.

[19] J. Durinck, B. Devincre, L. Kubin and P. Cordier, Am. Mineral. 92 (2007) p.1346.

[20] S. Demouchy, A. Mussi, F. Barou, A. Tommasi A and P. Cordier, Tectonophysics, 623 (2014) p.123.

[21] M.S. Paterson, Int. J. Rock Mech. Min. Sci. 7 (1970) p.512.

[22] M.S. Paterson, *Rock deformation experimentation*, in *The brittle-ductile transition in rocks*, A.G. Duba, W.B. Durham, J.W. Handin and H.F. Wang, eds., Geophys. Monogr. Ser., AGU, Washington, 1990, p.187.

[23] A. Mussi, P. Cordier, S. Demouchy and C. Vanmansart, Phys. Chem. Miner. 41 (2014) p.537.

[24] G.T. Herman, A.V. Lakshminarayanan and A. Naparstek, Comput. Biol. Med. (1976) p.259.

[25] C. Messaoudi, T. Boudier, C.O. Sanchez Sorzano and S. Marco, TomoJ (tomography software for three-dimensional reconstruction in transmission electron microscopy); software available at http://u759.curie.fr/fr/download/softwares/TomoJ

[26] P. Penczek, M. Radermacher and J. Frank, Ultramicroscopy 40 (1992) p.33.

[27] R. Gevers, Philos. Mag. 7 (1962) p.59.

[28] D. B. Williams and C. B. Carter, in *Transmission Electron Microscopy: A textbook for materials science* (Plenum Press, 2nd edition, 2009).

[29] J.H. Sharp, J.S. Barnard, K. Kaneko, K. Higashida and P.A. Midgley, J. Phys. Conf. Ser. 126 (2008) 012013.

[30] M. Tanaka, K. Higashida, K. Kaneko, S. Hata and M. Mitsuhara, Scripta Mater. 59 (2008) p.901.

[31] M. Tanaka, M. Honda, M. Mitsuhara, S. Hata, K. Kaneko and K. Higashida, Mater. Trans. 49 (2008) p.1953.

[32] S. Hata, H. Miyazaki, S. Miyazaki, M. Mitsuhara, M. Tanaka, K. Kaneko, K. Higashida, K. Ikeda, H. Nakashima, S. Matsumara, J.S. Barnard, J.H. Sharp and P.A. Midgley, Ultramicroscopy 111 (2011) p.1168.

[33] J. Kacher and I.M. Robertson, Acta Mater. (2012) p.6657.

[34] J. Kacher, B.P. Efting, B. Cui and I.M. Robertson Curr. Opin. Solid State Mater. Sci. 18 (2014) p.227.

[35] J. Kacher and I.M. Robertson, Philos. Mag. 94 (2014) p.814.

[36] G.S. Liu, S.D. House, J. Kacher, M. Tanaka, K. Higashida and I.M. Robertson, Mater. Charact. 87 (2014) p.1.

[37] K. Misumi, K. Kaneko, T. Nishiyama, T. Maeda, K. Yamada, K.i. Ikeda, M. Kikuchi, K. Takata, M. Saga and K. Ushioda, J. Alloys Compd. 600 (2014) p.29.

[38] R. Madec, B. Devincre, L. Kubin, T. Hoc and D. Rodney, Science 301 (2003) p. 1879.

[39] L. Kubin, R. Madec and B. Devincre, MRS proceedings 779 (2003) W1.6.

[40] B. Devincre, T. Hoc and L. Kubin, Mater. Sci. Eng. A (2005) p.182.

[41] A. Alankar, I.N. Mastorakos, D.P. Field and H.M. Zbib, J. Eng. Mater. Technol. 134 (2012) 021018.

[42] E.A. Stach, R. Hull, R.M. Tromp, F.M. Ross, M.C. Reuter and J.C. Bean, Philos. Mag. A 80 (2000) p.2159.

Eur. J. Mineral.
2015, **27**, 707–715
Published online 1 September 2015

On the deformation mechanism of olivine single crystals at lithospheric temperatures: an electron tomography study

ALEXANDRE MUSSI[1,*], MAULA NAFI[1], SYLVIE DEMOUCHY[2] and PATRICK CORDIER[1]

[1] Unité Matériaux et Transformations, UMR 8207 CNRS-Université Lille1, F-59655 Villeneuve d'Ascq, France
*Corresponding author, e-mail: alexandre.mussi@univ-lille1.fr
[2] Géoscience Montpellier, UMR 5342 CNRS - Université Montpellier, F-34095 Montpellier, France

Abstract: We present an electron tomography study of dislocations in deformed olivine single crystals, at *ca*. 0.5 T_m, along two distinct orientations. The easiest slip systems are [001](100) and [001]{110}. Disorientating a single crystal away from easy glide conditions leads to massive cross-slip, which generates three-dimensional dislocations, and thus contributes to hardening. Fast motion of curved non-screw dislocation in those planes leaves long straight screw dislocations which bear lattice friction and control plastic strain. We have identified several hardening mechanisms. Non-screw [001] dislocations interact elastically to form dipoles. Recovery mechanisms leading to dipole annihilation are observed, but they are slow at those temperatures and produce numerous sessile loops. These loops represent obstacles for gliding dislocations. Interactions between dislocations and sessile loops produce sessile segments (super jogs), which efficiently impede dislocation motions.

Key-words: olivine; dislocation; cross-slip; rheology; plasticity; electron tomography; hardening.

1. Introduction

The rheology of the lithosphere is of fundamental importance in geodynamics from both the point of view of plate tectonics and of mantle convection. The strength of the uppermost part of Earth's mantle, just below the discontinuity of Mohorovičić (Moho) which separates the crust and the mantle, is constrained by the rheology of olivine. However, the plasticity of olivine is still poorly understood under the relatively low temperatures (*i.e*. close to 0.5 T_m) relevant to the shallow mantle lithosphere. Constitutive equations obtained from laboratory experiments (Raterron *et al*., 2004, 2012; Mei *et al*., 2010; Demouchy *et al*., 2013a and b, 2014) yield a wide range of rheologies. In particular, it has been shown that the flow laws from Mei *et al*. (2010) predict a lithosphere that is too strong to match the flexures observed at Hawaii (Zhong & Watts, 2013). The flow laws recently proposed by Demouchy *et al*. (2013a and b, 2014) suggest lower stresses, 30 MPa (at 800°C, 10^{-14} s^{-1} and 300 MPa), to be compared with 300 MPa predicted by Mei *et al*. (2010) under similar conditions (at 800°C, 10^{-14} s^{-1} and 4–9 GPa). Understanding the deformation mechanisms appears to be essential to constrain extrapolation of laboratory-based flow laws to natural conditions; however, detailed studies of olivine under relatively low temperatures are scarce. Raleigh (1968) has characterized [001]{110} and [001](100) slip systems for temperatures below 1,000°C, analyzing the slip bands on the surfaces of single crystals of deformed olivine. Phakey *et al*. (1972) used transmission electron microscopy (TEM) to study the microstructures of single crystals deformed at low temperature; the authors observed the [001]{110} slip system as well as the occurrence of the [001](100) and [001](010) slip systems, at 800°C. Gaboriaud *et al*. (1981) have verified that, for deformation temperatures between 20°C and 600°C, deformed olivine exhibits mostly straight [001] screw dislocations suggesting a high lattice friction of this character at such low temperatures. For temperatures higher than 600°C, the authors have reported glide of [001] dislocations in the (100) planes and in few {110} planes. These observations raise fundamental questions which have not been solved in olivine yet. One is related to the extreme plastic anisotropy exhibited by olivine at low temperature, where the easy glide involves only one direction: [001]. Under such conditions, the origin of hardening observed at low temperature in deformed single crystals by Demouchy *et al*. (2013b) is not clear. Indeed, in most materials, strain hardening originates mostly from interactions between intersecting slip systems with distinct dislocations, which react and form junctions (Madec *et al*., 2002; Bulatov *et al*., 2006). This cannot be applied to olivine single crystals deformed at low temperature.

Recently, we have shown that electron tomography could be applied to dislocations in olivine to expand our analytical capabilities (Mussi *et al*., 2014, 2015). We have

0935-1221/15/0027-2481 $ 4.05
DOI: 10.1127/ejm/2015/0027-2481

emphasized the importance [001]{110} glide (Mussi *et al.*, 2014) and identified for the first time the collinear annihilation as a potential hardening mechanism in olivine (Mussi *et al.*, 2015). Here we take advantage of this new technique to further investigate the mechanisms leading to dislocation interactions in olivine at low temperature.

2. Experimental procedure

2.1. Description of samples and deformation experiments

In this study, we focus on two deformation experiments conducted by Demouchy *et al.* (2013b) on single crystals of olivine at *ca.* 0.5 T_m: PoEM 9 and PoEM 11. Sample PoEM 9 was orientated to activate the [001](100),[001](110) and [100](001) slip systems. PoEM 11 was orientated to activate [001](010), [001]{140}, [001]{130} and [001]{120} glides. The corresponding Schmid factors (providing the resolved shear stress for a given slip system) are reported in Table 1.

The single crystals were cored from San Carlos olivine (Arizona, USA) with cylindrical shapes (6.32 mm long and 4.19 mm diameter for PoEM 9, 6.61 mm long and 4.20 mm diameter for PoEM 11, see Demouchy *et al.*, 2013b). They have been deformed in compression, using a high-temperature, high-pressure gas–vessel apparatus (Paterson, 1970; Paterson, 1990) at Geosciences Montpellier (University of Montpellier), with an argon confining pressure of 300 MPa. The PoEM 9 and PoEM 11 specimens have been deformed in axial compression at 806°C (0.55 T_m) and 850°C (0.57 T_m), with strain rates of 5.1×10^{-5} s^{-1} and 7.1×10^{-6} s^{-1}, respectively.

2.2. Transmission electron microscopy

Slices from the deformed samples were mechanically thinned down to a thickness of 30 μm. To reach electron transparency, the foils were Ar-ion milled with a Gatan® DuoMill TM model 600. To ensure electron conduction, each thin foil was coated with a thin carbon layer. The TEM analyses were conducted with a FEI® Tecnaï G^2 20 twin microscope operating at a 200 kV accelerating voltage with a LaB_6 filament. Dislocations were analyzed using the weak-beam dark-field (WBDF) method. This technique enables us to obtain high spatial resolution micrographs (4 nm resolution), while keeping a high signal to noise ratio (Mussi *et al.*, 2014). The ''Electron Diffraction'' software (Morniroli & Steeds, 1982) enables us to calculate the simulated kinematical diffraction patterns. In this study, the orthorhombic (a = 4.752 Å, b = 10.193 Å, c = 5.977 Å; Hazen, 1976) crystal structure of olivine is described within the *Pbnm* space group. Precession (Vincent & Midgley, 1994) was performed with a ''Spinning Star'' precession module from the Nanomegas Company and was associated with the WBDF mode (WBDF-P) to homogenize the image contrast (Rebled *et al.*, 2011; Mussi *et al.*, 2014, 2015). A precession angle of 0.1° is sufficient to highly reduce the oscillating contrast of inclined dislocations and the thickness fringes, and this angle is small enough for the electron beam not to be masked by the objective aperture. Electron tomography was performed with a double-tilt sample holder with a maximal angular range of ± 60°. The obtained tilted series have been manually centred within one-pixel accuracy, and then filtered with the ImageJ software to enhance the dislocation contrast, and improve the background and dislocation contrast homogeneity. The 3D images have been generated with two reconstruction algorithms: the simultaneous iterative reconstruction technique algorithm (Penczek *et al.*, 1992) used with the Gatan® 3D reconstruction software, and the weighted back-projection algorithm (Herman *et al.*, 1976) used with the TomoJ plugin (Messaoudi *et al.*, 2007) accessible in ImageJ.

Table 1. Schmid factors for the [001]{*hk*0} slip systems corresponding to the PoEM 9 and PoEM 11 samples deformed in axial compression tests (Demouchy *et al.*, 2013b).

	Compression axis before compression		Compression axis before compression
PoEM 9	[1 0 1]	PoEM 11	[5 19 10]
(100)	0.49	(100)	0.03
(110)	0.44	(110)	0.15
(1$\bar{1}$0)	0.44	(1$\bar{1}$0)	0.09
(120)	0.36	(120)	0.21
(1$\bar{2}$0)	0.36	(1$\bar{2}$0)	0.16
(130)	0.28	(130)	0.25
(1$\bar{3}$0)	0.28	(1$\bar{3}$0)	0.21
(140)	0.23	(140)	0.26
(1$\bar{4}$0)	0.23	(1$\bar{4}$0)	0.23
(010)	Negligible	(010)	0.28

3. Results

Several areas have been analyzed in this study: seven from PoEM 9 and six from PoEM 11. On average, domain sizes are 2.4 ± 0.7 μm by 1.6 ± 0.4 μm for PoEM 9 and 2.0 ± 0.2 μm by 1.3 μm ± 0.1 μm for PoEM 11. The microstructures are composed of numerous [001] straight screw dislocations, entanglements and loops. Tomography reconstructions enable us to characterize the dislocation glide planes. A colour code linked to the glide planes is given in Table 2. Dislocations coloured in red and orange are both lying on sessile planes. We have measured dislocation densities of the order of 1.3×10^{13} m^{-2} for PoEM 9, for 10.1 % of strain and a higher dislocation density of 1.1×10^{14} m^{-2} for PoEM 11 for 21.5 % of strain. In PoEM 11, we have mostly focused on areas where entanglements of non-screw dislocations are observed, so the dislocation density reported here represents an upper bound of the overall microstructure.

3.1. Sample PoEM 9

A typical microstructure of PoEM 9 is presented on Fig. 1. The microstructure is dominated by straight segments of [001] screw dislocations (in yellow in Fig. 1b). It is not

Table 2. Colour code used to indicate the planes containing indexed dislocation segments.

Dislocation planes	(100)	(140)	(130)	(120)	(110)	$(1\bar{1}0)$
Dislocation colors	Black	Light purple	Light green	Light blue	White	Light grey
Dislocation planes	(010)	$(1\bar{4}0)$	$(1\bar{3}0)$	$(1\bar{2}0)$	Sessile ($l \neq 0$)	$\{hkl\}$ planes
Dislocation colors	Dark grey	Dark purple	Dark green	Dark blue	Red or orange	

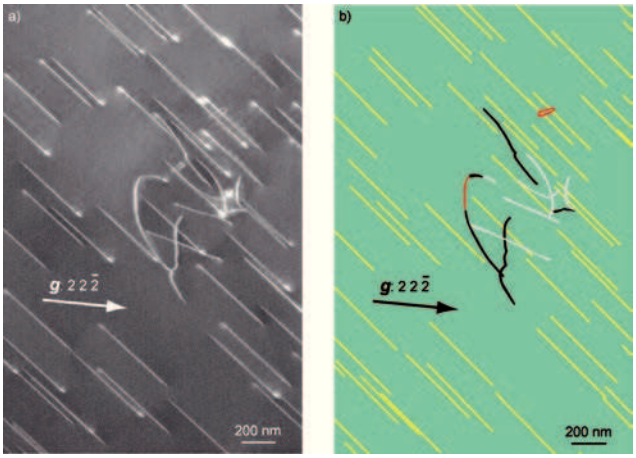

Fig. 1. Indexation of a tilted series of PoEM 9. (a) Micrograph in WBDF-P conditions, with **g**: 22$\bar{2}$, showing very few non-screw dislocation segments; (b) corresponding indexed micrograph (colours are linked to the dislocation glide and climb planes, as specified on Table 2), where (100), $(1\bar{1}0)$ glide planes and sessile planes are characterized (yellow dislocations could not be indexed due to their straight-lined configurations). (online version in colour)

possible to identify the glide plane of these yellow dislocations since only one orientation segment is available. However, with tomography we can obtain information on a sessile loop, a sessile dislocation segment and non-screw [001] dislocation segments gliding in (100) and $(1\bar{1}0)$ (see Table 2 and Fig. 1b). In PoEM 9, most [001] screw dislocations observed are perfectly rectilinear. We have noted very few cross-slip events and loops. Identified glide planes are mostly of the (100) and {110} type. Some zones more populated with non-screw dislocations (*i.e.*, generally lower than 1 μm in length) can be observed, however they are quite rare.

3.2. Sample PoEM 11

The microstructure of PoEM 11 is more complex. Numerous areas with concentrations of non-screw dislocations and entanglements are observed as illustrated in Fig. 2. Detailed characterizations using tomography show that many dislocations exhibit very intricate geometries. Their lines are composed of segments belonging to different planes (highlighted by different colours in Figs 2 and 3). We identify $[001](110)/[001](1\bar{1}0)$ cross-slip events and two $[001](110)/[001](1\bar{1}0)/[001](120)$ multiple cross-slip events in Fig. 3 (which is extracted from the lower

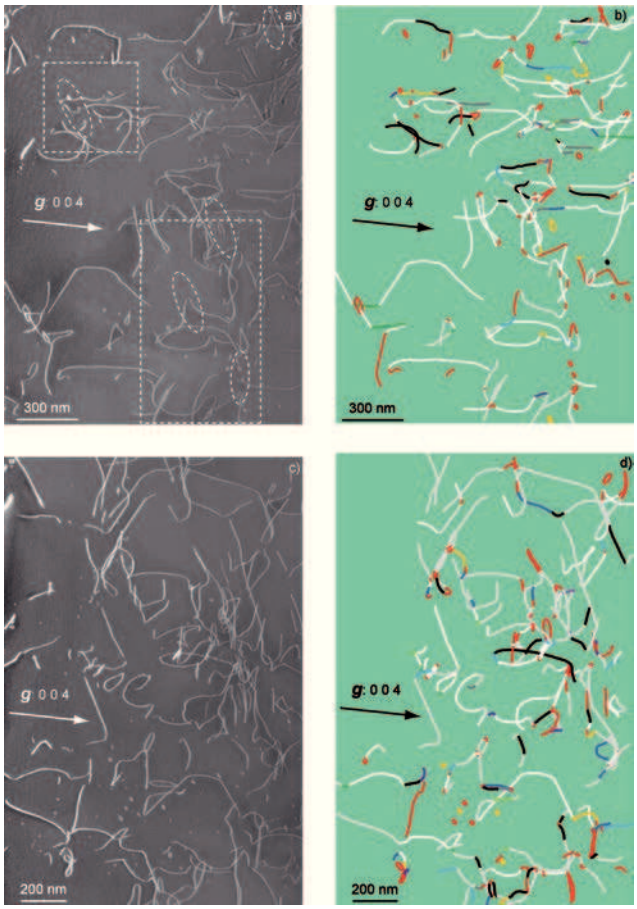

Fig. 2. Indexation of two tilted series of PoEM 11. (a) WBDF-P image observed with **g**: 004, the two dashed rectangles correspond to two regions magnified in Fig. 3c (bottom) and 7c (top), the five dashed ellipses point out sessile dislocation segments that are geometrically related to neighbouring sessile loops; (b) corresponding indexation where colours are linked to the dislocation glide and climb planes given in Table 2; one can notice a dominance of white (110) glide planes, and red and orange segments are sessile; (c) same WBDF-P conditions, but in another area; (d) corresponding indexation, colour code is given Table 2 (dominance of light grey $(1\bar{1}0)$ glide planes). (online version in colour)

right corner of Fig. 2a). Several glide planes have been characterized within these areas ((100), {110}, {120}, {130}, {140} and (010)), with a majority of {110} planes (Figs 2 and 3). Another important observation is linked to the dislocations coloured in red and orange, which are lying on sessile planes. It is worth noticing that numerous sessile dislocation segments can be geometrically related to neighbouring sessile loops.

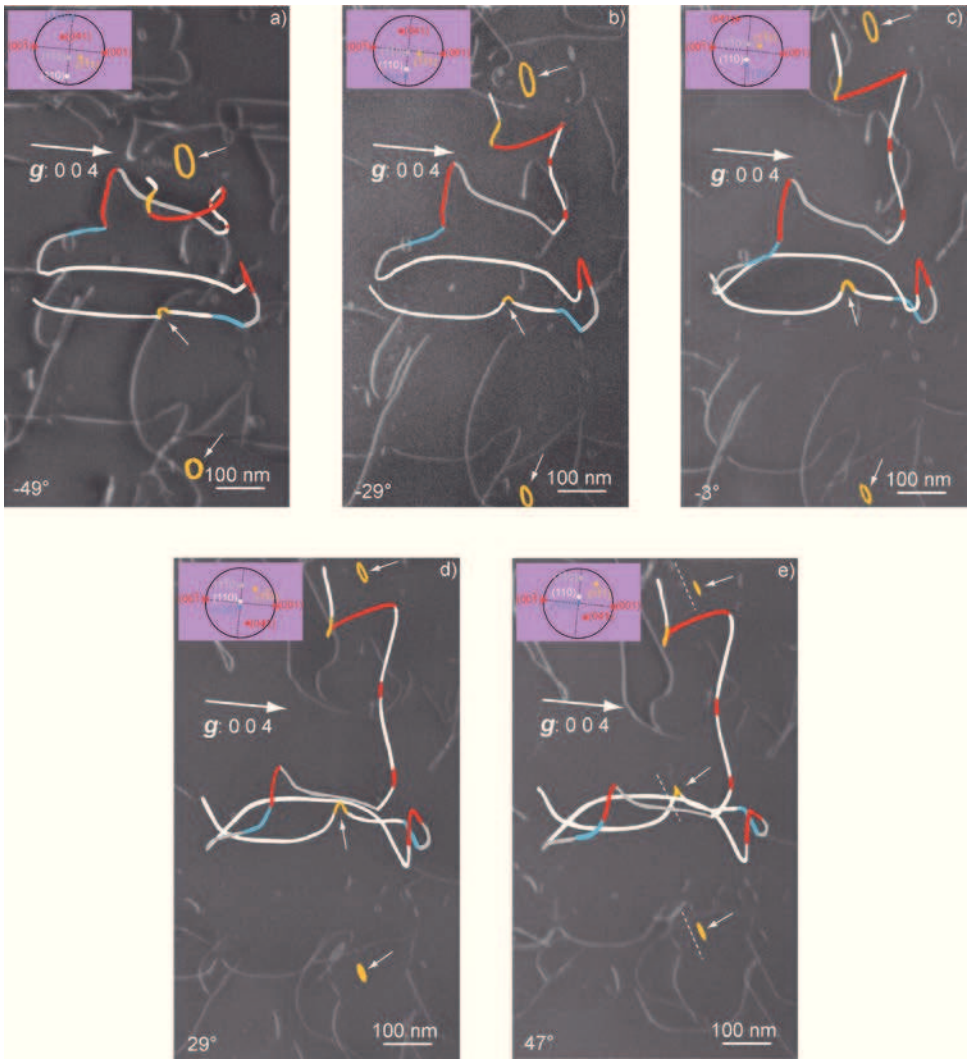

Fig. 3. Sample PoEM 11: detailed analysis of a portion of Fig. 2. Micrographs in WBDF-P conditions obtained with the 004 diffraction vector, with the corresponding stereographic projection on the top left corner: (a) the two coloured loops lie practically in the projection plane for a tilt angle of −49° (the colour code for the dislocation glide planes is given in Table 2) which is also the case for the orange dislocation segment in the middle of the micrograph (see white arrows); (b) micrograph tilted at −29°; (c) −3° (area extracted from Fig. 2a); (d) 29°; (e) with a projection angle of 47° the planes of the two dislocation loops are approximately edge-on. The traces of the lying planes are highlighted by white dashed lines. This is also the case for the dislocation segment coloured in orange in the middle of the micrograph, which likely results from the interaction of the white dislocation with a loop similar to the one noted by the white arrows. (online version in colour)

The occurrence of those sessile loops is pervasive and we can distinguish several families. Some small sessile loops form strings (Fig. 4a). They are clearly related to the collapse after pinching of very elongated, sometimes twisted (Fig. 4b), loops. However, all loops do not exhibit these characteristics. On the tilted series shown in Fig. 5, we observe four [001] sessile loops, which are approximately parallel and hence cannot result from the breakage described above. A third dislocation loops family, made of very small strings of debris (at the resolution limit of WBDF) is observed in association with a pinned dislocation in Fig. 6. The corresponding reconstructed volume tilted to 116° (Fig. 6c) shows that the pinned dislocation glides on the (110) plane.

All the glide, climb and cross-slip planes characterized in PoEM 9 and PoEM 11 are summarized in Table 3.

4. Discussion

The first striking observation is linked to the marked differences between the microstructures observed in the two samples investigated, which differ only by their loading axis. This raises the question on the importance of plastic anisotropy in olivine and will be discussed first. In this study, we focus on the mechanisms that may lead to dislocations interactions and strain hardening. We will then

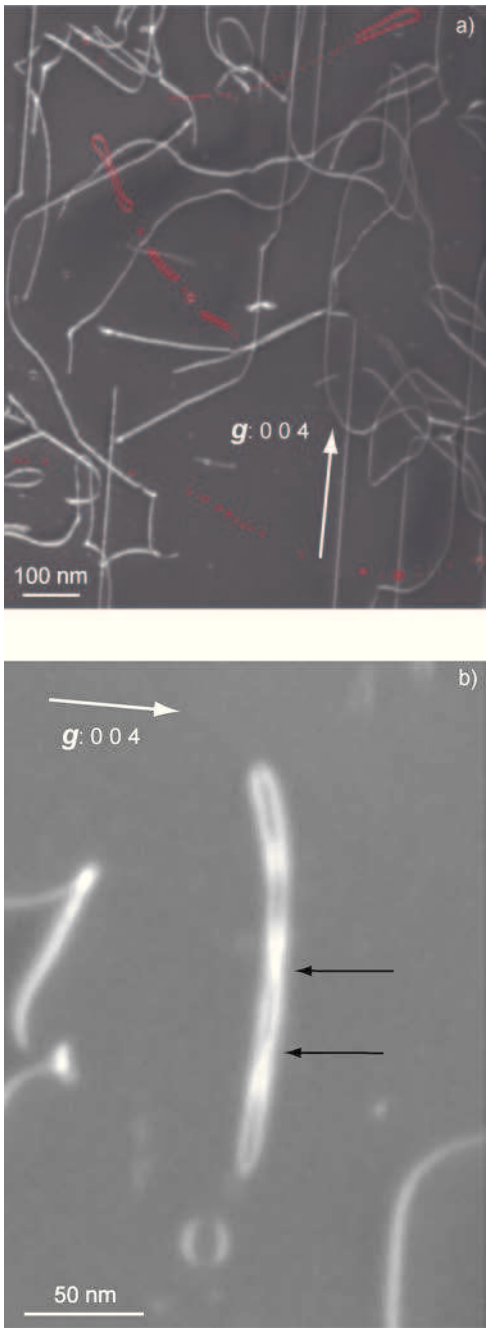

Fig. 4. Sample PoEM 11: break-up of dislocation dipoles into strings of dislocation loops. Micrograph in WBDF-P condition, with **g**: 004, where: (a) three dislocation dipoles (coloured in red) are annihilating by climb and two of them are practically totally annihilated; (b) magnification of a dipole loop in the process of pinching (arrows) just before the formation of strings of loops. (online version in colour)

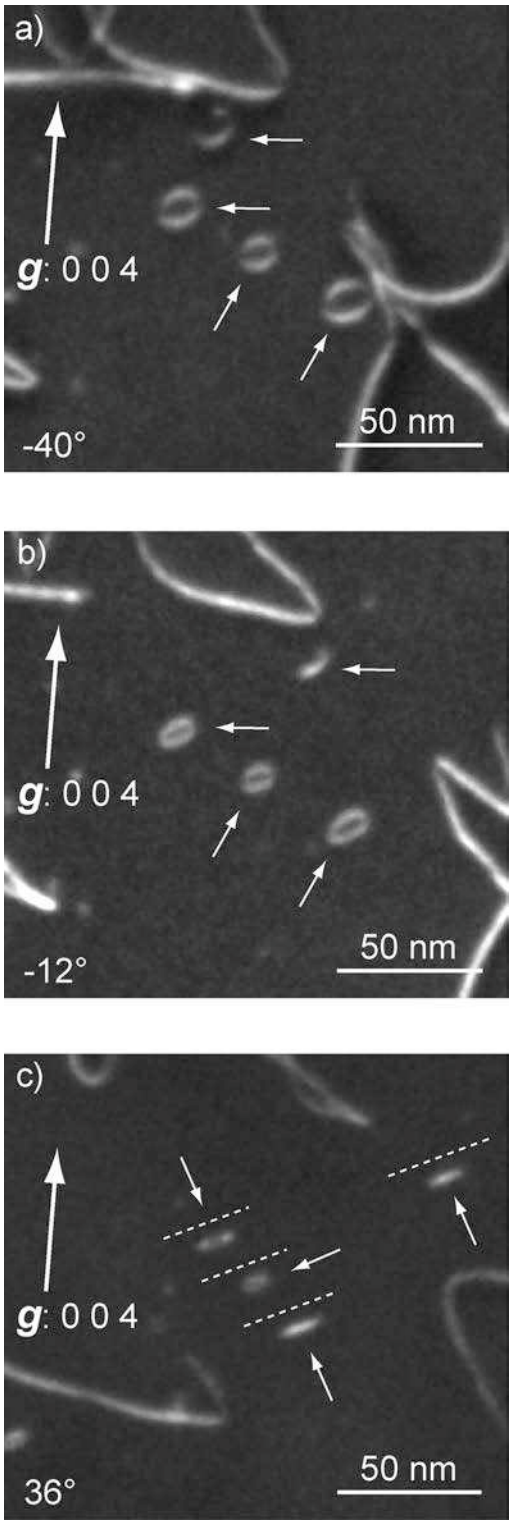

Fig. 5. Parallel dislocation loops in PoEM 11. WBDF-P images obtained with the 004 diffraction vector: (a) the four dislocation loops lie practically in the projection plane for a tilt angle of $-40°$ (indicated by white arrows); (b) projection angle of $-12°$; (c) the four loops are approximately edge-on and parallel (the traces of the lying planes are highlighted by white dashed lines), with a projection angle of 36° (as the Burgers vector [001], parallel to the **g** vector, is not contained in the plane of the loops, they are sessile).

discuss the significance of the pervasive occurrence of dislocations loops observed in these samples.

4.1. Comparison between PoEM 9 and PoEM 11

The PoEM 9 and PoEM 11 single crystals have been compressed at equivalent temperatures, similar strain

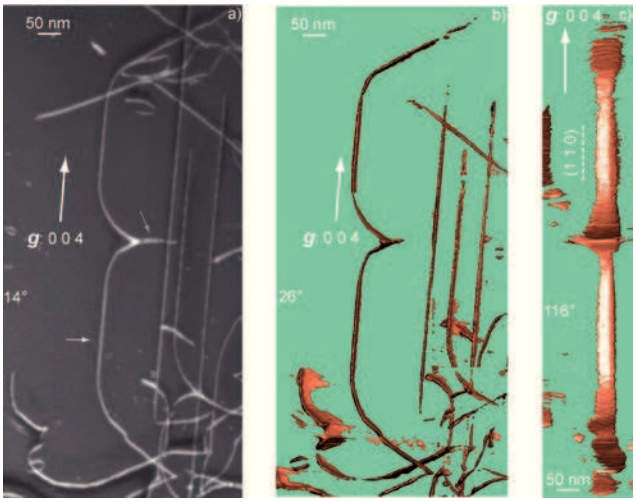

Fig. 6. Pinned dislocation in PoEM 11. (a) WBDF-P micrograph, tilted at 14°, diffraction vector: 004, showing a pinned [001] screw dislocation (indicated by a white arrow), leaving debris (at the resolution limit of WBDF) in its wake (indicated by a light grey arrow); (b) corresponding electron tomography reconstruction volume (tilted at 26°); (c) reconstructed volume tilted at 116°, where the glide plane of the pinned dislocation is edge-on. It corresponds to (110). (online version in colour)

Table 3. Summary of the number of the glide planes, climb planes and cross-slip planes characterized in PoEM 9 and PoEM 11.

PoEM 9	27.9 μm^2 total area	PoEM 11	16.6 μm^2 total area
(100)	20	(100)	57
(010)	0	(010)	17
{110}	40	{110}	335
{120}	0	{120}	46
{130}	2	{130}	20
{140}	1	{140}	26
Climb	6	Climb	175
Cross-slip	11	Cross-slip	306

rates, but along two distinct orientations (Table 1). From a purely geometrical point of view, Table 1 shows that PoEM 9 favours activation of [001](100) and [001]{110} followed by glide in {120}, {130} and {140}. The microstructure is very consistent with these constraints since glide appears to be essentially planar in PoEM 9, with the vast majority of dislocations gliding in (100) and {110} (Table 3). Some evidence for cross slip is however observed. The situation is more complex for PoEM 11 where several planes are solicited at a comparable level: (010), {140}, {130} or {120}, *i.e.* their Schmid factor is between 0.2 and 0.3. However, most dislocations (more than 60 % of the 500 characterized glide planes) are found to glide in {110}, which is only marginally solicited (*i.e.*, Schmid factor of about 0.1). This demonstrates that [001] glide in {110} is by far the easiest slip system under these experimental conditions. The (100) plane represents 10 % of the characterized glide planes in PoEM 11. Since this plane also corresponds to a very low resolved shear stress, we can conclude that [001](100) is the second easiest slip system. From this point of view, PoEM 9 and PoEM 11 demonstrate very consistently that [001]{110} represents the easiest slip system in olivine at *ca*. 0.5T_m, followed by [001](100). This is consistent with the conclusions of Phakey *et al*. (1972), describing deformation at 800°C of single crystals with orientations close to the one of PoEM 9. However, the implications of this strong plastic anisotropy are further illustrated.

Being solicited to activate easy slip, PoEM 9 exhibits mostly a planar dislocation microstructure (Fig. 1) dominated by straight screw segments and their mobility strongly controls the olivine plasticity. The microstructure of PoEM 11 is very different (compare Figs 1 and 2). Electron tomography shows that the main reason for this difference is that dislocations lines are not planar in PoEM 11. Along a given dislocation line, one finds segments belonging to different planes. Some of these segments are even sessile and their origin will be discussed in the next section. Let us focus here on glissile segments. Most of them correspond to planes that are not significantly solicited from the macroscopic point of view. This means that many dislocation segments escape by cross slip from the hard slip planes where, under external loading, they are expected to glide into easy {110} and (100) planes, probably under the influence of local stress heterogeneities. More than 60 % of the dislocations indexed in PoEM 11 involve cross slip. This results in a three-dimensional dislocation microstructure, which is intrinsically less glissile and also, as shown below, enhances further dislocation interaction mechanisms.

4.2. Sessile dislocation segment formation and sessile loop formation

The pervasive occurrence of sessile loops of various sizes represents the other characteristics of our samples. The formation of the strings of loops described in Fig. 4 is well known. It has been observed in ceramics deformed at high temperature (*e.g.*, Phillips *et al*., 1982a and b) and the formation mechanism has been discussed by Junqua & Grilhé (1984) and Lagerlöf *et al*. (1989). It is related to the dipole interaction between non-screw segments. Dipoles first evolve into very long closed loops as those observed in Fig. 4. Indeed, Fig. 4b illustrates very well the mechanism proposed by Junqua & Grilhé (1984) and Lagerlöf *et al*. (1989). By self-climb involving pipe diffusion, dipole fluctuations occur, which eventually leads by pinching to the formation of strings of loops. Further diffusion, in the bulk, leads to loop shrinking until they disappear. Collapse of loops has already been observed in olivine by Goetze & Kohlstedt (1973), who measured the shrinkage kinetics.

However, complete annealing of loops by diffusion requires time (especially at low temperature) and many interactions occur and are indeed observed between those remaining loops and gliding dislocations. The occurrence of the many sessile dislocation segments observed along

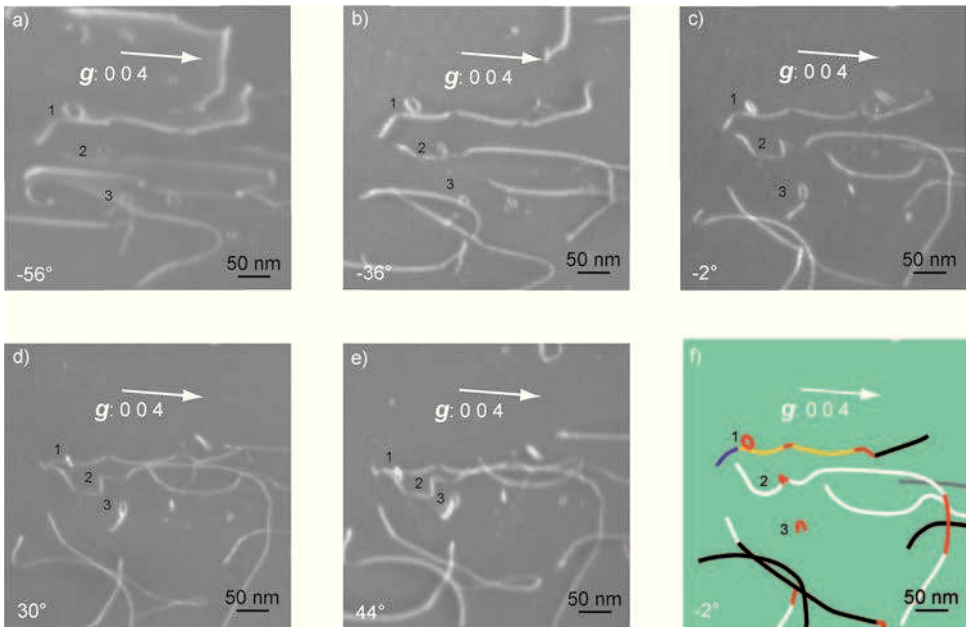

Fig. 7. Collinear interaction between a screw dislocation and a loop in PoEM 11. Micrographs obtained, with **g**: 004, where a family of three loops (labelled ''1'', ''2'' and ''3'') are in contrast (area extracted from Fig. 2a): projected angle of (a) −56°; (b) −36°; (c) −2°; (d) 30°; and (e) 44°. The indexed micrograph (f) which corresponds to (c) (colour code of dislocation glide and climb planes is given in Table 2) shows that the red sessile segment, labelled ''2'', comes from the collinear interaction of a screw dislocation and a sessile loop. (online version in colour)

the dislocation lines is interpreted as a result of these interactions involving collinear annihilations. This kind of interaction has been previously described by Mussi *et al*. (2015). The result is the so-called 'collinear interaction', involving annihilation, meaning the interaction of dislocations of opposite signs lying in different planes. An example of collinear interaction between a screw dislocation and a sessile loop is shown in Fig. 7. In this figure, which is extracted from the upper left corner of Fig. 2a, one can distinguish a family apparently composed of three sessile dislocation loops (labelled ''1'', ''2'' and ''3'') with diameters of around 30 nm. Electron tomography enables us to see that dislocation loops ''1'' and ''3'' are indeed the loops that are not in contact with the long screw dislocation in the middle of the micrographs. On the other hand, dislocation loop ''2'' has interacted with the long screw dislocation. Indeed, when rotating the tilted series around the [001] direction (Fig. 7b–e), it is visible that the dislocation loop ''2'' is not a closed loop any more. Having interacted with the screw dislocation, it has produced helicoidally shaped sessile segment. This interaction mechanism has already been observed using TEM analysis (*e.g.*, Fig. 5g in Mussi *et al*., 2015) and it has already been simulated by dislocation dynamics in zirconium (see Fig. 2 in Drouet *et al*., 2014). The interaction mechanism illustrated on Fig. 7f explains the occurrence of many sessile dislocation segments in the complex dislocations of Fig. 3 (in red and orange) and in Fig. 2. Indeed, collinear interactions with small and medium size dislocation loops (several nm to several tens of nm in diameter) can create sessile dislocation segments of different sizes.

The presence of sessile segments on a dislocation line impedes its motion. If the dislocation line has interacted with a very small loop, the sessile segment is small as well. It can be assimilated to a super jog and may be dragged under high stress. This sessile segment will act as a pinning which will leaves a string of small loops in its wake by dragging. This mechanism has been noted in Ti alloys (see Fig. 5b in Viswanathan *et al*., 2001) and is the origin of the microstructure shown in Fig. 6.

The occurrence of parallel sessile loops described in Fig. 5 can neither be explained by the break-up of dislocation dipoles by climb, nor by the debris dragging mechanism due to dislocation pinning. This mechanism cannot be explained up to now. Parallel sessile loops could be generated by a double cross-slip mechanism, but we found no intermediate configuration to support this assumption.

5. Conclusion

At 0.5 T_m, dislocation glide of [001] dislocations in {110} and (100) represents the easiest deformation mechanism in olivine. Dislocation mobility is very anisotropic in those planes as shown in Fig. 1. Screw segments are straight indicating a high lattice friction. Hence the mobility of them is much lower than that of non-screw dislocations. In the absence of further interaction, the mobility of [001] screw dislocations in those planes represents the strain-controlling mechanism. Disorientating the sample from the orientation that activates the easier slip systems induces

numerous cross-slip events which lead to complex, non-planar, dislocation line geometries. This represents a first source of strain hardening. However, the non-screw dislocations may play a role as well. They can interact elastically leading to the formation of dipoles, which represent another strain hardening mechanism. Even at low temperature (*ca.* 0.5 T_m), local diffusion is sufficient to activate recovery mechanisms involving dipole breakdown into strings of loops, which eventually shrink and disappear (Fig. 4). This process is slow however and, before they disappear, these sessile loops represent numerous obstacles to dislocation glide. Interaction with the smallest loops leads to the formation of super-jogs, which impede dislocation glide (Fig. 6). Interaction with larger loops contributes further (*i.e*. besides cross-slip) to produce complex three-dimensional dislocation lines (red and orange parts on Fig. 3). The formation of these super-jogs can be described by the collinear annihilation mechanism (Madec *et al*., 2003; Mussi *et al*., 2015).

To conclude, electron tomography allows us to clarify the complex geometry of dislocations activity in olivine samples deformed at 0.5 T_m. The present study confirms the strong plastic anisotropy of olivine at low temperature and highlights the implication of the loading conditions (parameterized here by the sample orientation) on the dislocation activity. The elementary mechanisms at the origin of strain hardening as well as the counteracting recovery mechanism are described.

Acknowledgements: A Marie Curie fellowship awarded to S.D. (PoEM: Plasticity of Earth Mantle, FP7-PEOPLE-20074-3-IRG, N°230748-PoEM) supported the experimental work on which this study is grounded. The TEM national facility in Lille is supported by the CNRS (INSU) and the Conseil Régional du Nord Pas de Calais, France. This work was supported by funding from the European Research Council under the Seventh Framework Program (FP7), ERC grant N°290424–RheoMan to P.C.

References

Bulatov, V.V., Hsiung, L.L., Tang, M., Arsenlis, A., Bartelt, M.C., Cai, W., Florando, J.N., Hiratani, M., Rhee, M., Hommes, G., Pierce, T.G., Diaz de la Rubia, T. (2006): Dislocation multi-junctions and strain hardening. *Nature*, **440**, 1174–1178.

Demouchy, S., Mussi, A., Barou, F., Tommasi, A., Cordier, P. (2013a): Visco-plasticity of polycrystalline olivine at high pressure and 900°C: fresh outcomes from high resolution EBSD and electron tomography. AGU Abstracts [Fall Meeting, 2013], session T012, T43G–06.

Demouchy, S., Tommasi, A., Ballaran, T.B., Cordier, P. (2013b): Low strength of Earth's uppermost mantle inferred from tri-axial deformation experiments on dry olivine crystals. *Phys. Earth Planet. Int.*, **220**, 37–49.

Demouchy, S., Mussi, A., Barou, F., Tommasi, A., Cordier, P. (2014): Viscoplasticity of polycrystalline olivine experimentally deformed at high pressure and 900°C. *Tectonophysics*, **623**, 123–135.

Drouet, J., Dupuy, L., Onimus, F., Mompiou, F., Perusin, S., Ambard, A. (2014): Dislocation dynamics simulations of interactions between gliding dislocations and radiation induced prismatic loops in zirconium. *J. Nucl. Mater.*, **449**, 252–262.

Gaboriaud, R.J., Darot, M., Gueguen, Y., Woirgard, J. (1981): Dislocations in olivine indented at low-temperatures. *Phys. Chem. Minerals*, **7**, 100–104.

Goetze, C. & Kohlstedt, D.L. (1973): Laboratory study of dislocation climb and diffusion in olivine. *J. Geophys. Res.*, **78**, 5961–5971.

Hazen, R.M. (1976): Effects of temperature and pressure on the crystal structure of forsterite. *Am. Mineral.*, **61**, 1280–1293.

Herman, G.T., Lakshminarayanan, A.V., Naparstek, A. (1976): Convolution reconstruction techniques for divergent beams. *Comput. Biol. Med.*, **6**, 259–262.

Junqua, N. & Grilhé, J. (1984): Apparitions d'instabilités sur des dipôles de dislocations coin. *Acta Metall. Mater.*, **32**, 2139–2147.

Lagerlöf, K.P.D., Mitchell, T.E., Heuer, A.H. (1989): Energetics of the break-up of dislocation dipoles into prismatic loops. *Acta Metall. Mater.*, **37**, 3315–3325.

Madec, R., Devincre, B., Kubin, L.P. (2002): From dislocation junctions to forest hardening. *Phys. Rev. Lett.*, **89**, 255508.

Madec, R., Devincre, B., Kubin, L., Hoc, T., Rodney, D. (2003): The role of collinear interaction in dislocation-induced hardening. *Science*, **301**, 1879–1882.

Mei, S., Suzuki, A.M., Kohlstedt, D.L., Dixon, N.A., Durham, W.B. (2010): Experimental constraints on the strength of the lithospheric mantle. *J. Geophys. Res.*, **115**, B08204.

Messaoudi, C., Boudier, T., Sanchez Sorzano, C.O., Marco, S. (2007): TomoJ: tomography software for three-dimensional reconstruction in transmission electron microscopy. *BMC Bioinform.*, **8**, 288.

Morniroli, J.P. & Steeds, J.W. (1982): Microdiffraction as a tool for crystal-structure identification and determination. *Ultramicroscopy*, **45**, 219–239.

Mussi, A., Cordier, P., Demouchy, S., Vanmansart, C. (2014): Characterization of the glide planes of the [001] screw dislocations in olivine using electron tomography. *Phys. Chem. Minerals*, **41**, 537–545.

Mussi, A., Cordier, P., Demouchy, S. (2015): Characterization of dislocation interactions in olivine using electron tomography. *Philos. Mag.*, **95**, 335–345.

Paterson, M.S. (1970): A high pressure, high temperature apparatus for rock deformation. *Int. J. Rock Mech. Min.*, **7**, 512–517.

— (1990): Rock deformation experimentation. *in* ''The Brittle-Ductile transition in rocks: the Heard volume'', A.G. Duba, W.B. Durham, J.W. Handin and H.F. Wang, eds. Geophysical Monograph Series. AGU, Washington, 187–194.

Penczek, P., Radermacher, M., Frank, J. (1992): Three-dimensional reconstruction of single particles embedded in ice. *Ultramicroscopy*, **40**, 33–53.

Phakey, P., Dollinger, G., Christie, J. (1972): Transmission electron microscopy of experimentally deformed olivine crystals. *in* ''Flow and fracture of rocks'', H.C. Heard, I.Y. Borg, N.L. Carter and C.B. Raleigh, eds. Geophysical Monograph Series. AGU, Washington, 117–138.

Phillips, D.S., Mitchell, T.E., Heuer, A.H. (1982a): Climb dissociation of dislocations in sapphire (α-Al_2O_3) revisited:

Crystallography of dislocation dipoles. *Philos. Mag. A*, **45**, 371–385.

Phillips, D.S., Pletka, B.J., Heuer, A.H., Mitchell, T.E. (1982b): An improved model of break-up of dislocation dipoles into loops: Application to sapphire (α-Al_2O_3). *Acta Metall. Mater.*, **30**, 491–498.

Raleigh, C.B. (1968): Mechanisms of plastic deformation of olivine. *J. Geophys. Res.*, **73**, 5391–5406.

Raterron, P., Wu, Y., Weidner, D.J., Chen, J. (2004): Low-temperature olivine rheology at high pressure. *Phys. Earth Planet. Int.*, **145**, 149–159.

Raterron, P., Girard, J., Chen, J. (2012): Activities of olivine slip systems in the upper mantle. *Phys. Earth Planet. Int.*, **200–201**, 105–112.

Rebled, J.M., Yedra, L., Estrade, S., Portillo, J., Peiro, F. (2011): A new approach for 3D reconstruction from bright field TEM imaging: beam precession assisted electron tomography. *Ultramicroscopy*, **111**, 1504–1511.

Vincent, R. & Midgley, P.A. (1994): Double conical beam-rocking system for measurement of integrated electron diffraction intensities. *Ultramicroscopy*, **53**, 271–282.

Viswanathan, G.B., Hayes, R.W., Mills, M.J. (2001): A study based on jogged-screw dislocations for high temperature creep in Ti alloys. *Mater. Sci. Eng. A-Struct.*, **319–321**, 706–710.

Zhong, S. & Watts, A.B. (2013): Lithospheric deformation induced by loading of the Hawaiian Islands and its implications for mantle rheology. *J. Geophys. Res.*, **118**, 6025–6048.

Received 3 March 2015
Modified version received 24 June 2015
Accepted 17 July 2015

PHILOSOPHICAL MAGAZINE, 2017
VOL. 97, NO. 33, 3172–3185
https://doi.org/10.1080/14786435.2017.1367858

Taylor & Francis
Taylor & Francis Group

Hardening mechanisms in olivine single crystal deformed at 1090 °C: an electron tomography study

Alexandre Mussi[a], Patrick Cordier[a], Sylvie Demouchy[b] and Benoit Hue[a]

[a]Unité Matériaux et Transformations, UMR 8207 CNRS – Université Lille1, Villeneuve d'Ascq, France; [b]Géoscience Montpellier, UMR 5342 CNRS – Université Montpellier, Montpellier, France

ABSTRACT

The dislocation microstructures in a single crystal of olivine deformed experimentally in uniaxial compression at 1090 °C and under a confining pressure of 300 MPa, have been investigated by transmission electron tomography in order to better understand deformation mechanisms at the microscale relevant for lithospheric mantle deformations. Investigation by electron tomography reveals microstructures, which are more complex than previously described, composed of [0 0 1] and [1 0 0] dislocations commonly exhibiting 3D configurations. Numerous mechanisms such as climb, cross-slip, double cross-slip as well as interactions like junction formations and collinear annihilations are the source of this complexity. The diversity observed advocates for microscale deformation of olivine significantly less simple than classic dislocation creep reported in metals or ice close to melting temperature. Deciphering mechanism of hardening in olivine at temperatures where ionic diffusion is slow and is then expected to play very little role is crucial to better understand and thus model deformation at larger scale and at temperatures (900–1100 °C) highly relevant for the lithospheric mantle.

ARTICLE HISTORY
Received 20 March 2017
Accepted 8 August 2017

KEYWORDS
Olivine; plastic deformation; dislocations; electron tomography; cross-slip; climb

1. Introduction

Cooling of the Earth is mediated by convection processes, which induces plastic deformation of mantle rocks at extremely slow strain rates. As the upper mantle is principally composed of olivine (>60% in volume), this mineral controls the mechanical properties of the Earth's upper mantle. In this study, we investigate the plastic behaviour of olivine at the temperature of 1090 °C (i.e. a temperature similar to those near the lithosphere/asthenosphere boundary). At this temperature and for grain size >1 mm, dislocation creep is expected to be the dominant mechanism of plastic deformation, with potentially contribution of dislocations with [1 0 0] and [0 0 1] Burgers vectors. Indeed, deformation in the [0 1 0] direction

CONTACT Alexandre Mussi alexandre.mussi@univ-lille1.fr

has never been reported for olivine (i.e. the so-called olivine paradox [1]). Below 1000 °C, olivine deforms by glide along [0 0 1] [2–6] while above 1200 °C [1 0 0] glide dominates [3,7–9]. A [0 0 1]/[1 0 0] transition temperature of approximately 1000 °C was reported by Raleigh [10], where the dislocation microstructures of deformed olivine seem to be complex. Indeed, Durham et al. [3] and Raterron et al. [8,9] have observed 3D shapes [1 0 0] and [0 0 1] dislocations in their samples. The behaviour of olivine single crystals deformed experimentally below 1000 °C has already been investigated yielding a mechanical data-set [11] together with transmission electron microscopy (TEM) observations [12,13]. Most of the deformed samples did not reach steady state, and deformation curves exhibit continuous hardening. Two samples were particularly interesting: specimen PoEM9 deformed at ~800 °C and specimen PoEM11, deformed at 850 °C. Only [0 0 1] dislocations have been reported in theses samples, but yet the dislocation microstructure, imaged by TEM was complex, as evidenced by several dislocation loop families and numerous 3D-dislocations. Furthermore, for polycrystalline olivine, deformed at higher temperature (900 °C, sample PoEM22 and 21), TEM analyses have demonstrated the occurrence of a majority of [0 0 1] dislocations with only few [1 0 0] [14]. A more recent study, also based on experimentally deformed olivine single crystals, but deformed in simple shear and at temperature ranging from 1000 and 1300 °C, has reported a transition temperature of approximately 1200 °C [15]. This mechanical study was completed by sample characterisation using electron backscatter diffraction (EBSD), but no TEM analyses were performed.

The aim of the present study is to further elucidate how dislocations interact to generate or not hardening during plastic deformation of olivine above 1000 °C, but below 1200 °C, where temperature is yet not high enough to induce significant ionic diffusion and recovery/annealing processes. We use the experimentally deformed samples from Demouchy et al. [11] and TEM for dislocation characterisations using up-to-date electron tomography to accurately understand how 3D-dislocations microstructures are produced. Electron tomography of dislocations allows overcoming the intrinsic limitations of observation of dislocation microstructures in the TEM (due to limitations in tilt amplitude) and ultimately provides a 3D numerical model of the dislocations geometries. These geometrical parameters (line directions, planes containing the lines in relation with the Burgers vectors) are very important to decipher the actual mechanisms operating in a deformed olivine.

2. Experimental methods

2.1. Description of the specimens and the deformation experiments

Olivine single crystals (from, San Carlos, AZ, USA) were deformed at 300 MPa in a confining medium of argon [16,17]. Prior to deformation, olivine cylinders were crystallographically oriented parallel to $[1\ 0\ 1]_c$ (i.e. the direction at 45° between [1 0 0] and [1 0 0] in the orthorhombic cell of olivine) to activate the

[0 0 1](1 0 0), [0 0 1](1 1 0), [1 0 0](0 0 1) and [1 0 0](0 1 1) slip systems [11]. Two samples are investigated here: PoEM8 and again PoEM9. The experimental conditions are summarised on Table 1. Technical details are fully reported in [11]. In brief, samples were deformed in axial compression at a constant displacement rate. Resulting deformation curves show large flow stresses (final stress of 754 and 498 MPa for PoEM9 and PoEM8, respectively), where steady state was not reached since a constant hardening was observed. At the end of the experiments, the deformation piston was maintained in place, and the temperature decreased (i.e. 'slow quench') at a rate of 150 °C/min. Recovered samples were cut parallel to the compression axis in two sections, two slabs located in the centre part of the section were prepared for EBSD and TEM characterisation, respectively. Sample preparation specific for electron tomography is detailed below.

2.2. Transmission electron tomography

Thin slabs were cut from the deformed specimen and mechanically polished down to a thickness of 30 µm. In order to reach electron transparency, the sample foils were Ar-ion milled with a Gatan® DuoMill TM model 600. Carbon films were deposited on the thin foils to ensure electron conduction. TEM investigations were performed with a FEI® Tecnaï G^{2}20Twin microscope, operating at 200 kV with a LaB_6 filament, using a double tilt sample-holder with a maximal angular range of ±60°. Olivine crystal structure is orthorhombic ($a \approx 4.75$Å, $b \approx 10.19$Å and $c \approx 5.98$Å). It is described here within a *Pbnm* space group [18]. The diffraction patterns were simulated with the Electron Diffraction software, in kinematic conditions [19]. Dislocations were characterised using the weak-beam dark-field (WBDF) technique. The use of a precessed electron beam [20] enabled us to: (1) facilitate indexing of the diffraction pattern (with a large precession angle (>1°), multiple diffraction paths are limited, which enables us to get closer to kinematic conditions); (2) homogenise the background and the dislocation contrasts [21,22]; a precession angle of 0.1° is high enough to drastically reduce the thickness fringe contrasts and the dislocation oscillating contrasts as well as low enough to avoid masking the precessed beam by the objective aperture.

Five and seven tilted series were acquired, every 2°, in WBDF conditions associated with precession, from approximately −60° to 56° and −56° to 48° for PoEM8 and PoEM9, respectively. As the contrast is weak in WBDF, the acquired tilted series have been manually centred within one-pixel accuracy [22] using the Gatan® image alignment software. Each micrograph has been numerically filtered with a kernel matrix [23] and/or a polynomial fit, using the ImageJ software, to

Table 1. Experimental conditions for deformation of the two olivine single crystals.

Specimen	Temperature	Final stresses (MPa)	$\dot{\varepsilon}$	$\varepsilon_{\text{Total (\%)}}$
PoEM9	806 °C	754	5.10^{-5} s^{-1}	10.1
PoEM8	1090 °C	498	10^{-5} s^{-1}	7.4

homogenise the background and the dislocation contrasts, and to increase the dislocation contrast. The weighted back projection algorithm [24] was used to reconstruct the dislocation volumes. This algorithm is accessible on the TomoJ plugin [25], which is available on ImageJ. Most dislocations have been redrawn using the UCSF Chimera software [26–28].

3. Results

3.1 Dislocation content

All the micrographs used for the tilted series of PoEM8 have been acquired in WBDF conditions with the $2\,2\,\bar{2}$ diffraction vector ($\boldsymbol{g}$). Five zones have been investigated, which represent an analysed volume of approximately 27 μm^3. A representative micrograph of PoEM8 is shown in Figure 1. Dislocations are curved; no straight dislocations (often taken as indicative of glide controlled by lattice friction) can be found. There are dislocations with $[1\,0\,0]$ and $[0\,0\,1]$ Burgers vectors which can be distinguished using $\boldsymbol{g} = 2\,2\,\bar{2}$ (Figure 1(a)) and $0\,6\,\bar{2}$ (Figure 1(b)). A few junctions are pointed out by yellow arrows (Figures 1, 2, 3 and 4). With

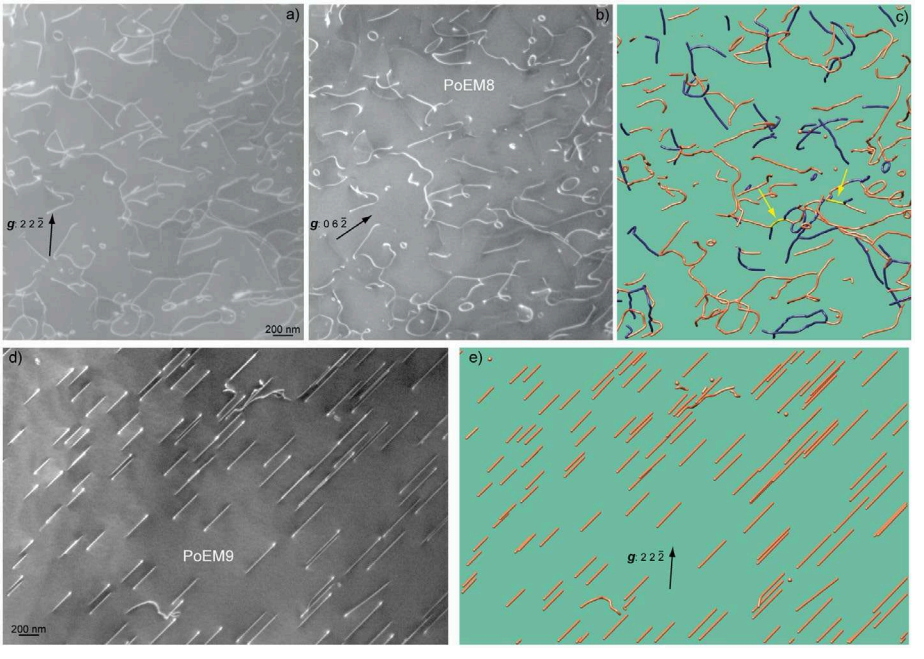

Figure 1. (Colour online) Typical PoEM8-PoEM9 microstructures: (a) WBDF micrograph obtained with the $2\,2\,\bar{2}$ diffraction vector ($[1\,0\,0]$ and $[0\,0\,1]$ dislocations are in contrast); (b) WBDF micrograph obtained with $\boldsymbol{g} = 0\,6\,\bar{2}$ on the same region as (a) (only $[0\,0\,1]$ dislocations are in contrast); (c) Corresponding 3D reconstruction ($[1\,0\,0]$, $[0\,0\,1]$ and $\left[1\,0\,\bar{1}\right]$ dislocations are shown in blue, orange and yellow colours, respectively), the two yellow arrows point out $\left[1\,0\,\bar{1}\right]$ junctions; (d) Characteristic microstructure of PoEM9 only composed of $[0\,0\,1]$ dislocations, with a large majority of straight lined screw segments, few non-screw segments and scarce dislocation loops [10]; (e) 3D reconstruction of (d) ($[0\,0\,1]$ dislocations are shown in orange).

$\boldsymbol{g} = 2\,2\,\bar{2}$, the $[1\,0\,\bar{1}]$ junctions exhibit contrasts twice as bright as [1 0 0] and [0 0 1] segments. Indeed, the $\boldsymbol{g}\cdot\boldsymbol{b}$ product is equal to 4 for $b = [1\,0\,\bar{1}]$, and 2 for $b = [1\,0\,0]$ and $b = [0\,0\,1]$. The [1 0 1] junctions are out of contrast as the $\boldsymbol{g}\cdot\boldsymbol{b}$ product is equal to 0 with $b = [1\,0\,1]$. In the reconstructed volume shown in Figure 1(c), orange, blue and yellow colours are used to differentiate dislocations with [1 0 0], [0 0 1] and $[1\,0\,\bar{1}]$ Burgers vectors, respectively. Small loops ($\varnothing \approx 30$ nm) and larger loops ($\varnothing_{max} \approx 250$ nm) of [1 0 0] and [0 0 1] dislocations are observed. Electron tomography has provided the possibility to index more than 1000 planes containing dislocation segments. They are reported in Table 2. The proportion of gliding[1] dislocations is close to 40% and approximately 70% of the whole indexed planes are composed of [0 0 1] dislocation segments. The total dislocation density, which is calculated from the total dislocation length digitised in Chimera, is 2.6×10^{13} m^{-2}.

3.2. Dislocation distribution and slip systems

Electron tomography allows, by indexing the planes containing dislocation segments, to discriminate those in glide configurations (so-called 'gliding') from the sessile ones, as shown in Figure 2, where numerous dislocations from the [0 0 1](1 1 0) and [1 0 0](0 0 1) slip systems can be characterised. Dislocations belonging to the [0 0 1](1 1 0) slip system are shown in white while those from [1 0 0](0 0 1) are drawn in black. Considering all the tilted series (Table 2), we find that 76% of gliding dislocation belong to [0 0 1]{1 1 0}, whilst 16% belong to [0 0 1](1 0 0). Over half of the gliding [1 0 0] segments are lying in (0 0 1). Moreover,

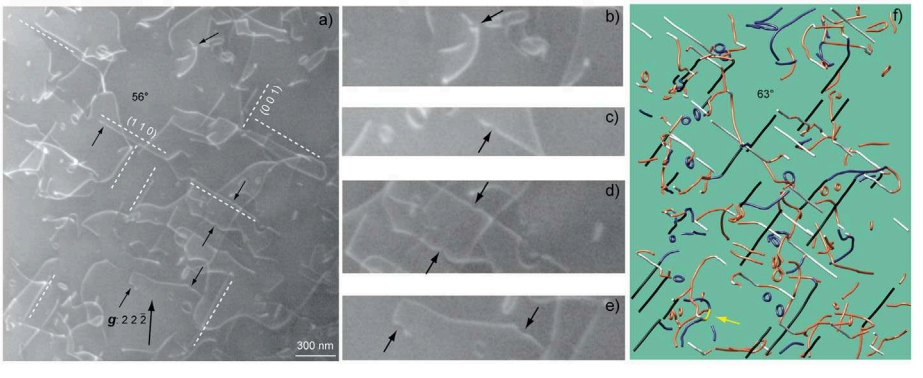

Figure 2. (Colour online) Main slip systems and cross-slip or/and collinear annihilations in PoEM8: (a) WBDF micrograph performed with $\boldsymbol{g} = 2\,2\,\bar{2}$, with a tilt angle of 56° where: the (1 1 0) and the (0 0 1) plane are indicated, black arrows point out probable specific configurations, which may be cross-slip or/and collinear interactions with small dislocation loops (some isolated loop, with approximately the same sizes, are in the vicinity); (b) Three Enlargement of (a), upper part; (c) Enlargement of (a), upper part of the image centre; (d) Enlargement of (a), lower part of the image centre; (e) Enlargement of (a), lower part; (f) Corresponding reconstruction volume, with a projected angle of 63° where: black dislocation segments designate the edge-on [1 0 0](0 0 1) slip systems, white dislocation segments designate the edge-on [0 0 1](1 1 0) slip systems, the yellow arrow points out a $[1\,0\,\bar{1}]$ junction.

a high proportion of dislocations from [1 0 0]{0 1 1} and [1 0 0]{0 2 3} slip systems are also observed. Since the angle between (0 1 1) and (0 2 3) is only of 9°, we have grouped them, and together they represent approximately one third of all the gliding [1 0 0] segments. We will now focus on the indexed planes, which cannot be related to gliding dislocations. Their role is important since they represent 60% of the indexed dislocations.

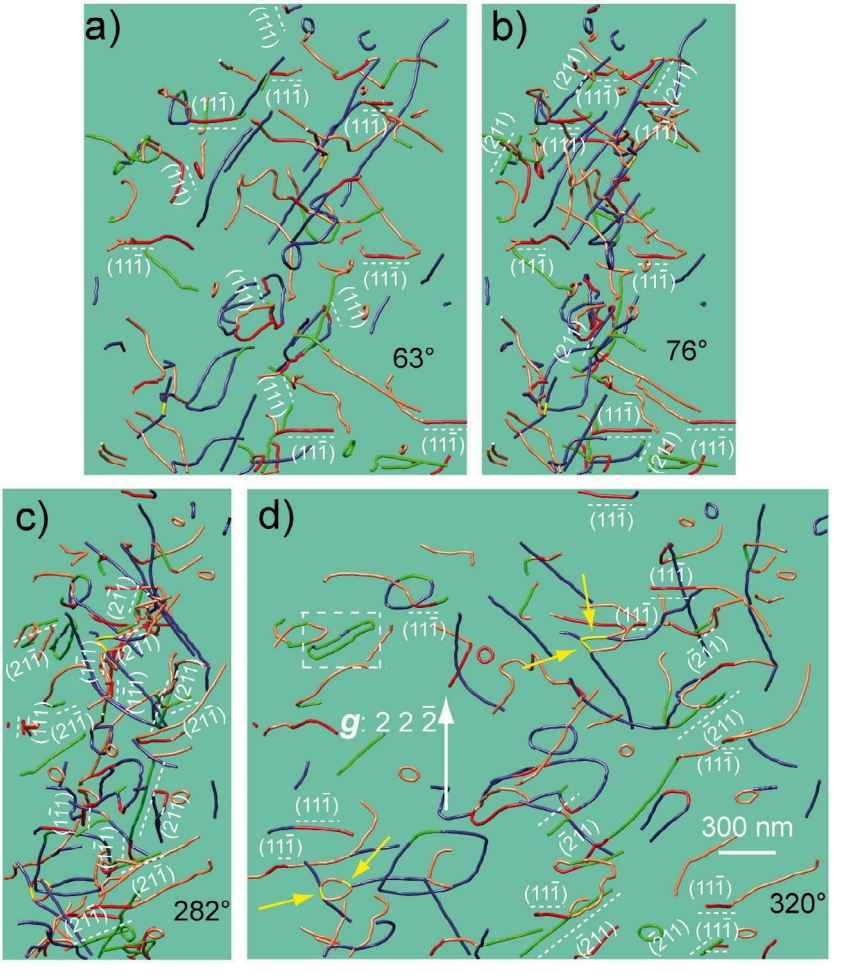

Figure 3. (Colour online) Dislocation climb planes (the dislocation segments which lie on the {1 1 1} planes are coloured in red and the dislocation segments are coloured in green for the {2 1 1} planes): (a) 3D reconstruction of a PoEM8 tilted series obtained with $\boldsymbol{g} = 2\,2\,\bar{2}$, with a projected angle of 63° (the $(1\,1\,\bar{1})$ and (1 1 1) planes are edge-on with this projection condition); (b) Projection angle of 76° (the $(1\,1\,\bar{1})$ and (2 1 1) planes are edge-on along this direction); (c) 282° tilt angle (the $(1\,1\,\bar{1})$, $(1\,\bar{1}\,1)$, $(2\,1\,\bar{1})$ and $(2\,\bar{1}\,1)$ planes are edge-on with this orientation); (d) Projection angle of 320° (the $(1\,1\,\bar{1})$ and $(\bar{2}\,1\,1)$ planes are edge-on with this projection condition), the white dashed square points out a break-up of a dislocation dipole by climb, the four yellow arrows point out $[1\,0\,\bar{1}]$ junctions; The numerous dislocation segments which lie on the {1 1 1} and the {2 1 1} planes (19 segments in {1 1 1} and 23 segments in {2 1 1}) show the occurrence of climb in PoEM8.

3.3. Sessile dislocation segments

There are a variety of indexed planes containing sessile dislocation segments, but several planes are more abundant (Table 2). A total of 25% of all planes containing sessile dislocation segments are members of the {1 1 1} family for both [1 0 0] and [0 0 1] Burgers vectors, 12% of [0 0 1] dislocations lie within (0 0 1). 9% of dislocations with [1 0 0] and [0 0 1] Burgers vectors lie within {2 1 1}. Consequently, approximately 50% of all the indexed planes of the sessile dislocations belong to {1 1 1}, (0 0 1) and {2 1 1}. The presence of numerous dislocation segments lying on {1 1 1} and {2 1 1} is clearly confirmed by Figure 3 (in red and green, respectively). The other indexed sessile dislocations are lying on odd {*hkl*} planes.

4. Discussion

4.1. Influence of temperature from 800 to 1090 °C (comparison between PoEM8 and PoEM9)

The compression axis of PoEM8 is along [10 4 19] and that of PoEM9 is along [1 0 1], i.e. at only 24° from each other. From a purely geometrical point of view, these two orientations are likely to activate the same slip systems, i.e. [0 0 1](1 0 0), [0 0 1](1 1 0), [1 0 0](0 0 1) and [1 0 0](0 1 1). The orientation alone is unlikely to be able to explain the marked differences between the dislocation microstructures observed in PoEM8 and in PoEM9 (Figure 1(d)–(e)). However, there is a difference of 300 °C between PoEM8 and PoEM9. Consequently, the comparison of these two experiments gives us the possibility to study the role of temperature in this range. The microstructure of PoEM9 is composed of [0 0 1] screw gliding dislocations only; while the microstructure of PoEM8 is mainly composed of non-screw, [1 0 0] and [0 0 1] dislocations, with 3D shapes and a large fraction of sessile components. The occurrence of [1 0 0] dislocations was expected in PoEM8, as the onset for [1 0 0] glide has already been reported in olivine above ca. 900–1000 °C in single crystals [2–4,8–10,15] and polycrystals [5,6,14,29,30]. Considering the Schmid factors associated with the slip systems in PoEM8, we find that [0 0 1]{1 1 0} and [1 0 0](0 0 1) are the most activated slip systems, followed by [0 0 1](1 0 0). As there are only [0 0 1] dislocations in PoEM9, the most activated slip systems are [0 0 1]{1 1 0}, followed by the [0 0 1](1 0 0) slip system [10].

The occurrence of large dislocation loops (several hundreds of nm), lying on undefined {*hkl*} planes, can be explained by the mechanism of double cross-slip [31]. Three configurations indicative of double cross-slip are found in PoEM8 as shown in Figure 4:

- the first configuration (Figure 4(a)) consists of a [0 0 1] dislocation, which double cross-slips on the (1 1 0) and $(1\ \bar{1}\ 0)$ planes;
- the second configuration (Figure 4(b)) consists of a [1 0 0] dislocation, which double cross-slips on the (0 1 0) and (0 0 1) planes;

- and the third one, more complex (Figure 4(c)), consists of a [0 0 1] dislocation, which double cross-slips on the (1 1 0) and $(1\,\bar{1}\,0)$ planes, with an interaction with a [1 0 0] dislocation, notice a $[1\,0\,\bar{1}]$ junction as well.

This mechanism has already been mentioned in a previous study on the dislocation population characterisation in deformed sample PoEM11 (see Figure 5 in [13]). From Table 1, approximately half of sessile dislocation segments lie on unexpected {*hkl*} planes. This seems to be the signature of a high occurrence of the double cross-slip mechanism in PoEM8.

The activation of [100] glide in PoEM8 may explain the difference of microstructure with PoEM9. [100] and [001] dislocations may interact and create sessile junctions which have already been predicted in olivine using Dislocation Dynamics simulations [32] and observed in TEM [12]. The observed 3D configurations may result from the need for entangled dislocations to find other degrees

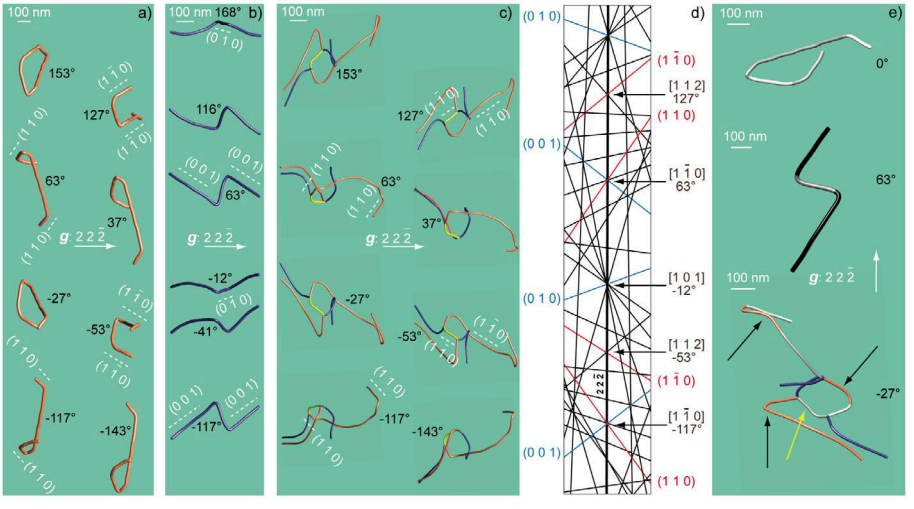

Figure 4. (Colour online) Double cross-slip mechanism: (a) Reconstructed volume of a [0 0 1] dislocation obtained with $\boldsymbol{g} = 2\,2\,\bar{2}$ (projected angle of −143°, −117°, −53°, −27°, 37°, 63°, 127° and 153°), the (1 1 0) planes are edge-on for the −117° and 63° tilt angles ($[1\,\bar{1}\,0]$ zone axis) and the $(1\,\bar{1}\,0)$ planes are edge-on for the −53° and 127° tilt angles ([1 1 2] zone axis); (b) Reconstructed volume of a [1 0 0] dislocation performed with the same diffraction vector as (a) (projected angle of −117°, −41°, −12°, 63°, 116° and 168°), the (0 0 1) planes are edge-on for the −117° and 63° tilt angles and the (0 1 0) planes are edge-on for the −12° and 168° tilt angles ([1 0 1] zone axis); (c) Complex dislocation configuration composed of a [1 0 0] and a [0 0 1] dislocation, a $[1\,0\,\bar{1}]$ junction (yellow segment) and an attractive [0 0 1]/[1 0 0] dislocation crossed state; moreover a double cross-slip configuration of the [0 0 1] dislocation is revealed (same description as (a)); (d) Simulation of the Kikuchi lines, between −165° and 180°, in kinematic conditions (Electron Diffraction Software [33]); the (0 1 0) and (0 0 1) Kikuchi lines are shown in blue colour (in reference with the [1 0 0] dislocation in blue colour) and the (1 1 0) and $(1\,\bar{1}\,0)$ Kikuchi lines are shown in red colour (in reference with the [0 0 1] dislocation in orange colour); (e) Summary of the three dislocation configurations in (a), (b) and (c) for tilt angles of 0°, 63° and −27°, respectively (the white dislocations segments designate the [0 0 1](1 1 0) slip systems, the light grey dislocations segments refer to the $[0\,0\,1](1\,\bar{1}\,0)$ slip systems and the black dislocation segments designate the [1 0 0](0 0 1) slip systems), the yellow arrow points out a $[1\,0\,\bar{1}]$ junction.

Table 2. Lying planes for the [1 0 0] and [0 0 1] dislocations in sample PoEM8.

Dislocation	Mechanisms	{*hkl*} planes	Total
[0 0 1]	Glide	(1 0 0)	41
		{1 1 0}	199
		{1 2 0}	9
		{1 3 0}	1
		{1 4 0}	3
		(0 1 0)	7
	Climb	(0 0 1)	81
		{1 1 1}	114
		{2 1 1}	38
		{1 1 2}	47
	Unknown	{*hkl*}	220
[1 0 0]	Glide	(0 0 1)	79
		{0 2 3}	32
		{0 1 1}	16
		{0 2 1}	11
		{0 4 1}	8
		(0 1 0)	7
	Climb	{1 1 1}	48
		{2 1 1}	20
	Unknown	{*hkl*}	91
[0 0 1] proportion			71%
[0 0 1] glide proportion			34%
[1 0 0] glide proportion			49%
Glide proportion			39%
Climb Proportion			32%
Unknown proportion			29%
		Total	1072

of freedom to move (cross-slip and/or climb). Climb is another possibility as at 1090 °C (i.e. approximately 70% of the melting temperature of olivine), ionic diffusion mechanisms are expected to still play a role. Approximately half of all the indexed sessile planes correspond to odd {*hkl*} planes (arising from double cross-slip mechanisms), and almost half of all the indexed sessile planes correspond to {1 1 1}, (0 0 1) and {2 1 1} (Table 2). As these three sessile plane families have frequently been indexed, there is a strong possibility that they come from a specific mechanism like climb. Consequently, we propose that {1 1 1}, (0 0 1) and {2 1 1} could be climb planes. Due to the low deformation temperature of PoEM9, few dislocation segments in climb configurations, had been observed in this specimen [13]. However, Durham and coworkers [2,3] had already draw attention on the importance of climb mechanisms in olivine single crystals deformed in the temperature range 1150–1600 °C.

Generally, climb and cross-slip are expected to induce strain softening during plastic deformation [34]. However, the PoEM8 stress/strain curve shows strain hardening (Figure 3 in Demouchy et al. [11]), which we discuss below.

4.2. Strain hardening during the deformation of an olivine single crystal at 1090 °C

Taking into account the previously mentioned aspects, a scenario for the different mechanisms activated during the plastic deformation of an olivine single crystal deformed at 1090 °C is now proposed.

As soon as the yield stress is reached, [0 0 1] and [1 0 0] dislocations multiply to reach a ratio of ⅔ of [0 0 1] and ⅓ for [1 0 0] (Table 2). Easy slip systems, i.e. [1 0 0](0 0 1), [0 0 1]{1 1 0} and [0 0 1](1 0 0), are then active. As [1 0 0] and [0 0 1] dislocations glide on different planes, they interact and generate [1 0 1] and $[1\,0\,\bar{1}]$ junctions (see Figures 1(c), 2(c), 3 and 4(c)–(e)), which impede dislocation glide. Dipoles of [0 0 1] and $[0\,0\,\bar{1}]$ dislocations, and of [1 0 0] and $[\bar{1}\,0\,0]$ dislocations also form, which is potentially another source of strain hardening. From Boioli et al. [35], we know that these dipoles progressively annihilate by climb, generating small sessile dislocation loops (Ø < 30 nm). As a result of diffusion, these small loops progressively disappear, increasing the proportion of the largest ones [36]. As an illustration, such an elongated dislocation loop can be noted in Figure 3(d) (framed area). This loop appears to be a closed-ended dipole (as shown in the Figure 6 in Lagerlöf et al. [37]). Gliding dislocations may interact with such remaining loops and create [1 0 1] and $[1\,0\,\bar{1}]$ junctions as well as collinear interactions. [1 0 0] and [0 0 1] dislocations are both affected by collinear annihilations. Junctions formed by collinear interactions are difficult to unzip [38]. Consequently, collinear interactions represent a third potential mechanism of strain hardening. Even if there are several strain hardening mechanisms, dislocations can overcome obstacles and move using mechanisms other than glide, including climb, cross-slip and multiple cross-slip. However, these mechanisms can also promote locking mechanisms, as they create 3D dislocation structures. Multiple cross-slip and more precisely double cross-slip generates large dislocation loops with a diameter of several hundreds of nm, lying in unprescribed {*hkl*} planes [31], for dislocations with [0 0 1] and [1 0 0] Burgers vectors. As mentioned previously, gliding dislocations can interact with these sessile loops, inducing a fourth strong strain hardening contribution. Consequently, we find that numerous strain hardening mechanisms are potentially involved during the plastic deformation of PoEM8, which is in agreement with the compression stress–strain curve evolution displayed in Figure 3 in Demouchy et al. [11].

It is worth mentioning that the picture presented here corresponds to deformation tests performed at laboratory strain rates (of the order 10^{-5} s^{-1}, Demouchy et al. [11]), which are considerably faster than mantle strain rates (of the order of 10^{-14} s^{-1}). The macroscopic hardening is obviously the result of a dynamic process, which involves a competition between formation of obstacles to dislocation glide and recovery processes, which overcome them. As for sessile loops for instance, their elimination being controlled by ion and vacancy diffusion, one can expect that more time being provided in nature, their hardening role should be reduced. A first assessment of this issue has been presented in Boioli et al. [35]. As a result, strain hardening near the lithosphere/asthenosphere boundary may be less significant than suggested by experimental data.

5. Conclusion

The dislocation microstructure of PoEM8 (1090 °C) is more complex than in PoEM9 (~800 °C) and several mechanisms could explain the generation of these microstructures (e.g. collinear interaction, climb, and cross-slip) but their de-convolution is difficult. Nevertheless, electron tomography enables us to characterise the double cross-slip mechanism and the comparison between the two experiments (PoEM8 and PoEM9) helps to identify different interaction mechanisms: (1) PoEM9 has been deformed well below 1000 °C (at 806 °C). Its microstructure is principally composed of straight screw [0 0 1] dislocations highlighting high lattice friction at 800 °C. The orientation of the compression axis of PoEM9 preferentially activates the [0 0 1]{1 1 0} and [0 0 1](1 0 0) slip systems. Few dipoles appear during plastic deformation. As the climb mechanism is weakly activated at such a temperature, the creation of sessile dislocation loops by progressive dipolar annihilations is consequently limited. The low occurrence of dislocation loops reduces collinear interactions, so the dislocation microstructure of PoEM9 is simple. (2) PoEM8 was deformed at 1090 °C. Its microstructure is composed of both [1 0 0] and [0 0 1] dislocations. The [1 0 0](0 0 1), [0 0 1]{1 1 0} and [0 0 1](1 0 0) slip systems dominate the microstructure, in agreement with the orientation of the compression axis. Moreover, both diffusion, and climb did occur due to the more elevated temperature. Consequently, planar glide controlled by lattice friction is not dominant and the dislocation shapes become 3-dimensional. With such a configuration, many junctions and collinear interactions form during the deformation. Dislocations can get away from their blocked configurations by cross-slip. The mechanism of double cross-slip produces large sessile dislocation loops, sources of new dislocation interactions. Consequently, the dislocation microstructure of PoEM8 is more diverse and intricate than the microstructure of PoEM9, and permits to revise the mechanisms of plastic deformation in the peridotitic mantle, where grain size is too large and temperature is too low to lead to only diffusion creep. Here, at 1090 °C, ionic diffusion is still at play, but only as a secondary process, unlocking locally dislocations. This result will allow to better model plastic deformation of the uppermost mantle at larger scale for temperatures (900–1100 °C) highly relevant for the lithospheric mantle.

Note

1. By 'gliding' dislocations, we mean dislocations which are in glide configuration, i.e. where the plane containing the dislocation line also contains the Burgers vector. This is to be opposed to sessile dislocations, for which the Burgers vector is not in the plane containing the dislocation line. Hence these sessile dislocations cannot glide in their plane. Sessile dislocations can be produced by mechanisms like climb or cross-slip.

Acknowledgements

A Marie Curie fellowship awarded to S.D. (PoEM: Plasticity of Earth Mantle, FP7-PEOPLE-20074-3-IRG, N°230748-PoEM) supported the experimental work used in this study. The TEM national facility in Lille is supported by the CNRS (INSU) and the Conseil Régional du Nord Pas de Calais, France. We thank D. Wallis for a careful review of the manuscript, which has contributed to improve clarity.

Disclosure statement

No potential conflict of interest was reported by the authors.

Funding

This work was supported by the Marie Curie fellowship awarded to Sylvie Demouchy (PoEM: Plasticity of Earth Mantle, FP7-PEOPLE-20074-3-IRG) [grant number N°230748-PoEM]; the European Research Council within the Seventh Framework Program (FP7) [grant number N°290424] – RheoMan to Patrick Cordier.

ORCID

Alexandre Mussi http://orcid.org/0000-0003-2093-0144
Patrick Cordier http://orcid.org/0000-0002-1883-2994

References

[1] P. Cordier, S. Demouchy, B. Beausir, V. Taupin, F. Barou, and C. Fressengeas, *Disclinations provide the missing mechanism for deforming olivine-rich rocks in the mantle*, Nature 507 (2014), pp. 51–56.
[2] W.B. Durham and C. Goetze, *Plastic flow of oriented single crystals of olivine: 1. Mechanical data*, J. Geophys. Res. 82 (1977), pp. 5737–5753.
[3] W.B. Durham, C. Goetze, and B. Blake, *Plastic flow of oriented single crystals of olivine: 2. Observations and interpretations of the dislocation structures*, J. Geophys. Res. 82 (1977), pp. 5755–5770.
[4] P. Phakey, G. Dollinger, and J. Christie, *Transmission electron microscopy of experimentally deformed olivine crystals*, in *Flow and Fracture of Rocks, Geophysical Monograph Series*, H.C. Heard, I.Y. Borg, N.L. Carter, and C.B. Raleigh, eds., AGU, Washington, 1972, pp. 117–138.
[5] Y. Gueguen, *High temperature olivine creep: Evidence for control by edge dislocations*, Geophys. Res. Lett. 6 (1979a), pp. 357–360.
[6] Y. Gueguen, *Les dislocations dans l'olivine des péridotites*, PhD thesis, Université Nantes, Nantes, 1979b.
[7] O. Jaoul, M. Michaut, Y. Gueguen, and D. Ricoult, *Decorated dislocations in forsterite*, Phys. Chem. Miner. 5 (1979), pp. 15–19.
[8] P. Raterron, J. Chen, L. Li, D. Weidner, and P. Cordier, *Pressure-induced slip-system transition in forsterite: Single-crystal rheological properties at mantle pressure and temperature*, Am. Mineral. 92 (2007), pp. 1436–1445.

[9] P. Raterron, E. Amiguet, J. Chen, L. Li, and P. Cordier, *Experimental deformation of olivine single crystals at mantle pressures and temperatures*, Phys. Earth Planet. Inter. 172 (2009), pp. 74–83.
[10] C.B. Raleigh, *Mechanisms of plastic deformation of olivine*, J. Geophys. Res. 73 (1968), pp. 5391–5406.
[11] S. Demouchy, A. Tommasi, T.B. Ballaran, and P. Cordier, *Low strength of Earth's uppermost mantle inferred from tri-axial deformation experiments on dry olivine crystals*, Phys. Earth Planet. In. 220 (2013), pp. 37–49.
[12] A. Mussi, P. Cordier, and S. Demouchy, *Characterization of dislocation interactions in olivine using electron tomography*, Philos. Mag. 95 (2015a), pp. 335–345.
[13] A. Mussi, M. Nafi, S. Demouchy, and P. Cordier, *On the deformation mechanism of olivine single crystals at lithospheric temperatures: An electron tomography study*, Eur. J. Mineral. 27 (2015b), pp. 707–715.
[14] S. Demouchy, A. Mussi, F. Barou, A. Tommasi, and P. Cordier, *Viscoplasticity of polycrystalline olivine experimentally deformed at high pressure and 900 °C*, Tectonophysics 623 (2014), pp. 123–135.
[15] J.A. Tielke, M.E. Zimmerman, and D.L. Kohlstedt, *Direct shear of olivine single crystals*, Earth Planet. Sci. Lett. 455 (2016), pp. 140–148.
[16] M.S. Paterson, *A high pressure, high temperature apparatus for rock deformation*, Int. J. Rock Mech. Min. 7 (1970), pp. 512–517.
[17] M.S. Paterson, *Rock deformation experimentation*, in *The Brittle-Ductile Transition in Rocks: The Head Volume, Geophysical Monograph Series*, A.G. Duba, W.B. Durham, J.W. Handin, and H.F. Wang, eds., AGU, Washington, DC, 1990, pp. 187–194.
[18] R.M. Hazen, *Effects of temperature and pressure on the crystal structure of forsterite*, Am. Mineral. 61 (1976), pp. 1280–1293.
[19] J.P. Morniroli and J.W. Steeds, *Microdiffraction as a tool for crystal-structure identification and determination*, Ultramicroscopy 45 (1982), pp. 219–239.
[20] R. Vincent and P.A. Midgley, *Double conical beam-rocking system for measurement of integrated electron diffraction intensities*, Ultramicroscopy 53 (1994), pp. 271–282.
[21] J.M. Rebled, L. Yedra, S. Estradé, J. Portillo, and F. Peiró, *A new approach for 3D reconstruction from bright field TEM imaging: Beam precession assisted electron tomography*, Ultramicroscopy 111 (2011), pp. 1504–1511.
[22] A. Mussi, P. Cordier, S. Demouchy, and C. Vanmansart, *Characterization of the glide planes of the [0 0 1] screw dislocations in olivine using electron tomography*, Phys. Chem. Miner. 41 (2014), pp. 537–545.
[23] J.S. Barnard, A.S. Eggeman, J. Sharp, T.A. White, and P.A. Midgley, *Dislocation electron tomography and precession electron diffraction – minimising the effects of dynamical interactions in real and reciprocal space*, Philos. Mag. 90 (2010), pp. 4711–4730.
[24] G.T. Herman, A.V. Lakshminarayanan, and A. Naparstek, *Convolution reconstruction techniques for divergent beams*, Comput. Biol. Med. 6 (1976), pp. 259–271.
[25] C. Messaoudi, T. Boudier, C.O. Sanchez Sorzano, and S. Marco, *TomoJ (tomography software for three-dimensional reconstruction in transmission electron microscopy)*, 2007; software available at https://u759.curie.fr/fr/download/softwares/TomoJ.
[26] E.F. Pettersen, T.D. Goddard, C.C. Huang, G.S. Couch, D.M. Greenblatt, E.C. Meng, and T.E. Ferrin, *UCSF Chimera: A visualization system for exploratory research and analysis*, J. Comput. Chem. 25 (2004), pp. 1605–1612.
[27] G.S. Liu, S.D. House, J. Kacher, M. Tanaka, K. Higashida, and I.M. Robertson, *Electron tomography of dislocation structures*, Mater. Charact. 87 (2014), pp. 1–11.

[28] A. Mussi, P. Cordier, S. Ghosh, N. Garvik, B.C. Nzogang, P. Carrez, and S. Garruchet, *Transmission electron microscopy of dislocations in cementite deformed at high pressure and high temperature*, Philos. Mag. 96 (2016), pp. 1773–1789.
[29] L. Li, D. Weidner, P. Raterron, J. Chen, M. Vaughan, M. Shenghua, and B. Durham, *Deformation of olivine at mantle pressure using D-DIA*, Eur. J. Mineral. 18 (2006), pp. 7–19.
[30] P. Raterron, J. Girard, and J. Chen, *Activities of olivine slip systems in the upper mantle*, Phys. Earth Planet. Int. 200–201 (2012), pp. 105–112.
[31] P.B. Hirsch, *The interpretation of the slip pattern in terms of dislocation movements*, J. Inst. Metals. 86 (1957), pp. 1957–1958.
[32] J. Durinck, B. Devincre, L. Kubin, and P. Cordier, *Modeling the plastic deformation of olivine by dislocation dynamics simulations*, Am. Mineral. 92 (2007), pp. 1346–1357.
[33] J.P. Morniroli, D. Vankieken, and L. Winter, *Electron Diffraction. Dedicated Software to Kinematicaly Simulate CBED Patterns*, USTL, Lille, 1994.
[34] J.P. Poirier, *Creep of Crystals. High-Temperature Deformation Processes in Metals, Ceramics and Minerals*, Cambridge University Press, Cambridge, 1985.
[35] F. Boioli, A. Tommasi, P. Cordier, S. Demouchy, and A. Mussi, *Low steady-state stresses in the cold lithospheric mantle inferred from dislocation dynamics models of dislocation creep in olivine*, Earth Planet. Sci. Lett. 432 (2015), pp. 232–242.
[36] B. Bakó, E. Clouet, L. Dupuy, and M. Blétry, *Dislocation dynamics simulations with climb: Kinetics of dislocation loop coarsening controlled by bulk diffusion*, Philos. Mag. 91 (2011), pp. 3173–3191.
[37] K.P.D. Lagerlöf, T.E. Mitchell, and A.H. Heuer, *Energetics of the break-up of dislocation dipoles into prismatic loops*, Acta Metall. Mater. 37 (1989), pp. 3315–3325.
[38] R. Madec, B. Devincre, L. Kubin, T. Hoc, and D. Rodney, *The role of collinear interaction in dislocation-induced hardening*, Science 301 (2003), pp. 1879–1882.

Chapitre III : Étude semi-quantitative de la plasticité par l'analyse de cartographies d'orientations au MET

Collaborateurs : Patrick Cordier (UMET), Jérémie Bouquerel (UMET), Shun-ichiro Karato (Geology and Geophysics Yale University)
Travaux réalisés depuis 2017 dans le cadre de la thèse de Billy Nzogang

Introduction :

Comme nous l'avons vu, la technique TETD permet de caractériser des microstructures complexes de dislocations, mais qu'en est-il des microstructures denses, surchargées de défauts ? Lorsque les densités de dislocations dépassent 10^{15} m^{-2}, les contrastes commencent à se superposer et se combiner, il est alors difficile voire impossible d'entreprendre des caractérisations. Néanmoins, l'empilement de dislocations crée des désorientations qui peuvent être mesurées par cartographie d'orientation cristalline automatique (ACOM). Le dispositif ASTAR (Rauch & Véron, 2014a) est d'un grand intérêt puisqu'il permet d'effectuer des ACOM avec une résolution spatiale à l'échelle du MET (ACOM-TEM).

I-3-1 ASTAR : son histoire

Les industries des transports prônent l'allègement des structures pour augmenter le nombre de passagers ou/et réduire les quantités de carburant. Avec une masse volumique de 2.7g/cm^3, l'aluminium fait partie des meilleurs candidats pour ces structures, mais ses propriétés mécaniques ne rivalisent pas avec celles des aciers. Une technique simple pour augmenter les limites d'élasticité d'alliages d'aluminium, est de réduire leurs tailles de grains (Hall, 1951 ; Petch 1953). L'extrusion coudée à aires égales (ECAE) est une technique efficace d'affinage de tailles de grains par recristallisation dynamique continue (Valiev & Langdon, 2007). Cependant, l'estimation de la taille des grains résultants est délicate : les grains sont soit trop petits pour parvenir à les caractériser au MEB par EBSD, soit les densités de dislocations sont trop importantes pour analyser la microstructure au MET (exemple du cuivre, partie gauche de la figure 16). Des études d'alliages d'aluminium, déformés par ECAE, ont été menées en parallèle par deux laboratoires français, le laboratoire LETAM (maintenant LE3M) à Metz et le laboratoire GPM2 (SIMAP à présent) à Grenoble. Etant dans l'impossibilité de caractériser la taille des grains de ces alliages hyper-déformés, ces deux laboratoires ont décidé, chacun de leur côté, de mettre au point un dispositif expérimental capable de faire des cartographies d'orientations cristallines automatiques à l'échelle du MET. Le LETAM a créé un dispositif ACOM-TEM sur le même principe que l'EBSD, par comparaisons de clichés Kikuchi expérimentaux à des clichés Kikuchi simulés (Fundenberger *et al.*, 2003). Le laboratoire GPM2, quant à lui, a créé un dispositif ACOM-TEM, par comparaison de clichés de taches de diffraction à une banque de clichés simulés en amont (Rauch & Dupuy, 2005). Les deux outils fonctionnent, mais, sur les domaines hyper-déformés, les lignes de Kikuchi ont tendance à s'épaissir (Guyot, 1974) alors que les clichés de points sont moins affectés par la déformation. L'outil simple et efficace, créé par Edgar Rauch, a finalement été commercialisé sous le nom d'ASTAR (Nanomegas®).

I-3-2 Les atouts d'ASTAR

En dix ans, ASTAR n'a de cesse d'évoluer. L'association de la précession a permis de rapprocher les clichés de diffraction expérimentaux au plus près des clichés simulés, et par conséquent d'augmenter considérablement la qualité des cartographies (Rauch & Véron, 2016 ; Valery *et al.*, 2016). Une interface graphique a récemment été mise au point pour recréer des images virtuelles en mode STEM micro-sonde (Rauch & Véron, 2014b) en sélectionnant, pour chaque cliché de diffraction, la tache transmise (virtual bright field en anglais), ou bien une tache diffractée (virtual dark field en anglais). Cet outil puissant permet à présent d'obtenir des cartographies d'orientation de grains de tailles nanométriques (voir figure 11 dans Rauch & Véron, 2014b) et des développements sont en cours pour parvenir à cartographier des grains superposés (Valery *et al.*, 2016).

Depuis les premières études sur l'EBSD (Venables & Harland, 1973), les avancées scientifiques sur les cartographies d'orientations en EBSD sont inévitablement plus importantes que celles d'ASTAR. C'est au travers des derniers développements effectués en EBSD que nous allons tenter d'obtenir des données semi-quantitatives sur la plasticité des minéraux, par MET, en les associant à ASTAR. Argon et Haasen (1993) ont montré que la désorientation moyenne d'un matériau est liée à son taux de déformation par la loi simple : $\theta_{mean} \propto \sqrt{\varepsilon}$. Dans cet état d'esprit, trois outils de cartographie ont été nouvellement mis en œuvre en EBSD, pour faire ressortir les variations de désorientation et donc de déformation (Wright *et al.*, 2011). Le GOS (Grain Orientation Spread) donne une couleur à chaque grain, couleur représentative de la moyenne des désorientations vis-à-vis de l'orientation moyenne du grain considéré (généralement du bleu pour les moyennes faibles au rouge pour les fortes). En d'autres termes, un grain bleu aura une très faible densité de dislocations (grains recristallisés ou orienté avec un faible facteur de Schmid, par exemple) alors qu'un grain rouge aura une forte densité de dislocations (grain brut, non restauré, orienté avec un facteur de Schmid élevé). Le GROD (Grain Reference Orientation Deviation) informe sur la désorientation d'un pixel par rapport à un pixel de référence du grain considéré. Le GROD est appelé « Mis2mean » lorsque le pixel de référence est l'orientation moyenne du grain. Cet outil ne permet pas de distinguer les grains mais tient compte des hétérogénéités intracristallines et des transmissions de contrainte entre grains. Le KAM (Kernel Average Misorientation) donne, à chaque pixel, la moyenne des désorientations entre le pixel considéré et les $n^{ièmes}$ voisins, en écartant les désorientations trop importantes caractéristiques de sous-joints (5 ° par exemple) ou de joints de grains (15 °). Ici aussi, le KAM, comme le GROD, ne permet pas de distinguer les grains (ou les sous-grains, suivant l'angle de désorientation limite choisi). Par ailleurs, il faut garder en tête que la déformation plastique d'un matériau peut résulter de trois contributions : les dislocations qui ont traversé le matériau, les dislocations qui sont stockées dans le matériau sans créer de désorientation (dislocations statistiquement stockées, SSD, comme les dipôles) et les dislocations stockées en créant des désorientations (dislocations géométriquement nécessaires, GND). Les densités de GND, sont révélées par les cartographies de KAM. Sans être absolue, la distribution de KAM donne un bon aperçu de la déformation plastique du matériau : la position du maximum informe sur le taux de déformation relatif moyen ; et la largeur à mi-hauteur, sur la répartition de cette déformation dans tout le matériau analysé.

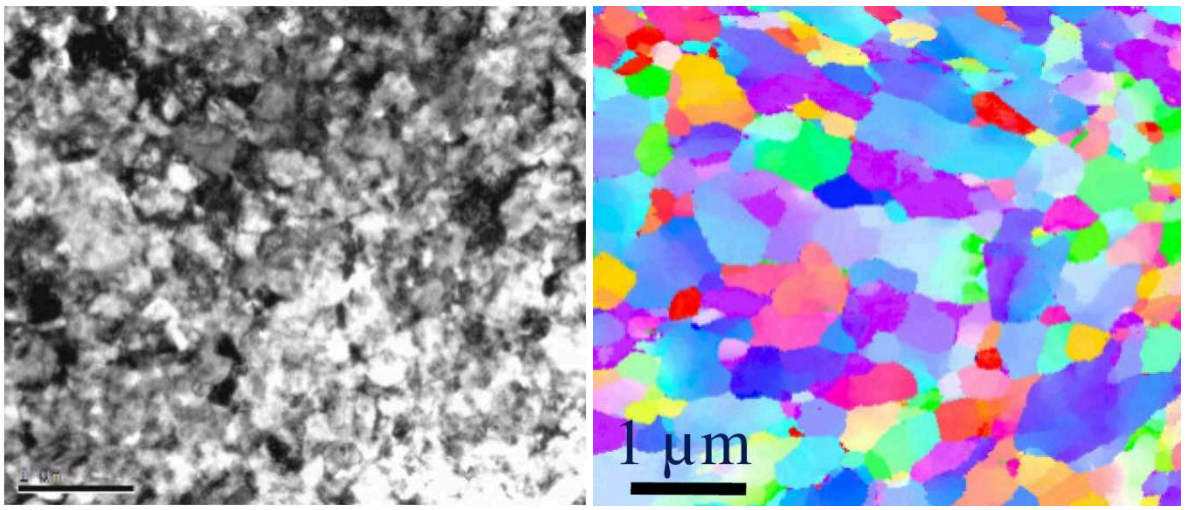

Figure 16 : *Micrographie MET du cuivre après traitement d'hyper-déformation (à gauche), cartographie ASTAR de la même zone (à droite). Images tirées de la présentation d'Edgar Rauch à l'école « Facets of electron cristallography » à Berlin du 7 au 9 juillet 2010.*

I-3-3 Des premiers résultats prometteurs

Trois articles ont d'ores et déjà été publiés sur le lien entre les cartographies d'orientations et la plasticité des minéraux. J'ai décidé de présenter l'article qui décrit le mieux l'apport et l'efficacité de cette méthodologie, à savoir le premier dans l'ordre chronologique (Nzogang *et al.*, 2018). Cette étude, détaillée dans l'article disponible à la fin de ce chapitre, est tirée des travaux de thèse de Billy Clitton Nzogang, thèse que je co-encadre avec Patrick Cordier.

Grace à une collaboration avec Shun-ichiro Karato et Jennifer Girard du laboratoire de Géologie et Géophysique de l'Université de Yale, nous avons obtenu un échantillon composé de bridgmanite et de ferropériclase, déformé par torsion, dans les conditions de pression et de température situées dans la partie supérieure du manteau inférieur. Suite à ce premier défi technique, un second défi se pose à nous : analyser la plasticité de ces deux phases par MET. Du fait des taux de déformation élevés, les analyses MET du ferropériclase ont révélé des densités de dislocations telles qu'aucune analyse individuelle de dislocation n'est possible. Ces fortes densités s'expliquent par l'activation des douze systèmes de glissement de la structure cubique à faces centrées du ferropériclase, associé à la création de nombreuses jonctions de dislocations. Par ailleurs, l'instabilité de la bridgmanite sous le faisceau d'électrons exclue également les caractérisations conventionnelles de dislocations par MET. Nous nous sommes donc dirigés vers ASTAR pour, simultanément obtenir des informations sur les taux de déformation des deux phases, et préserver la structure de la bridgmanite grâce au balayage rapide du faisceau en mode micro-sonde. Les cartographies GOS et GROD du ferropériclase ont montré des hétérogénéités de déformation marquées ainsi qu'une fragmentation progressive des grains avec le taux de déformation. Les distributions de KAM révèlent une augmentation continue de l'étendue des désorientations et de la désorientation moyenne, avec la déformation (voir figure 17). Ces résultats signent l'absence de recristallisation dans le ferropériclase malgré des taux de déformation compris entre 5 et 10. En ce qui concerne la bridgmanite (bien plus dure que le ferropériclase), les cartographies KAM révèlent la présence bandes de cisaillement amorphe au sein de zones très faiblement désorientées (voir figure 18). Cette forte hétérogénéité de désorientation montre que la bridgmanite semble se déformer, non pas par le mouvement de dislocations, mais par la

création de multiples bandes amorphes où se concentrent les cisaillements. Ces résultats auraient difficilement pu être obtenus sans l'apport d'ASTAR associé aux derniers outils tirés de l'EBSD.

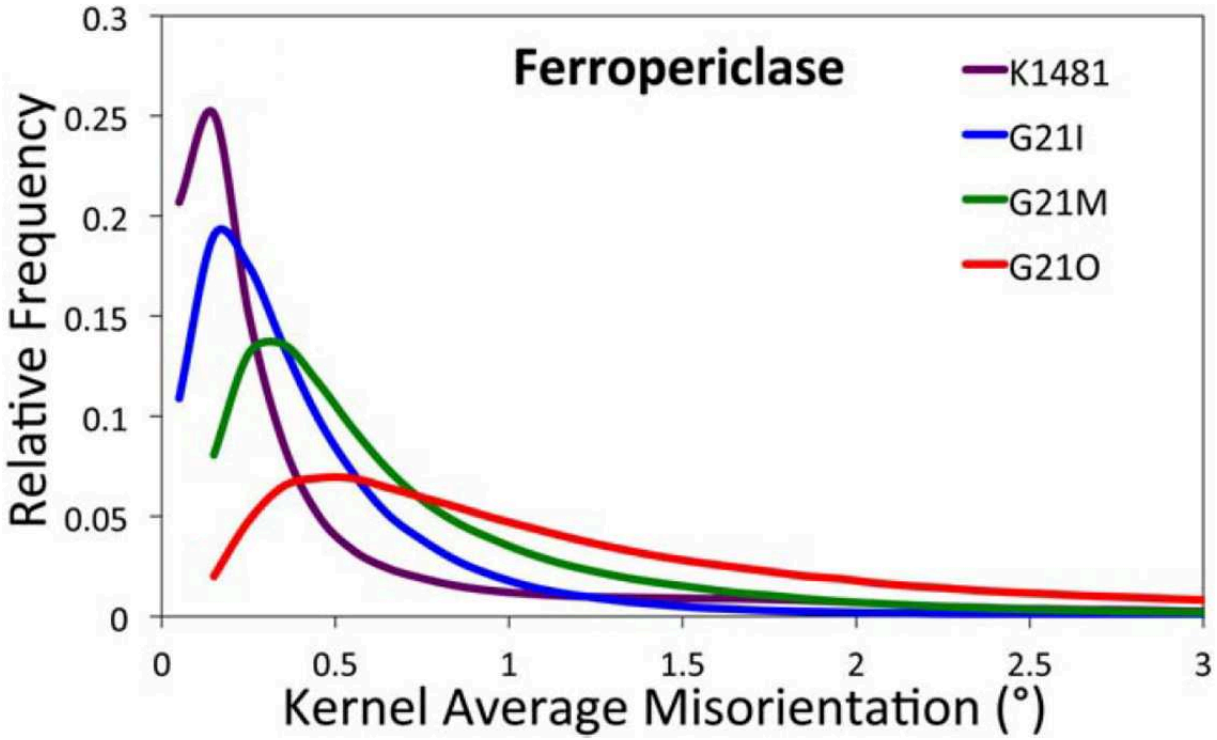

Figure 17 : *Distribution de KAM du ferropériclase, d'une lame FIB extraite du matériau non déformé (K1481), d'une lame FIB extraite de la zone interne de torsion (G21I, la moins déformée), d'une lame FIB extraite de la zone intermédiaire de torsion (G21M), et d'une lame FIB extraite de la zone externe de torsion (G21O, la plus déformée).*

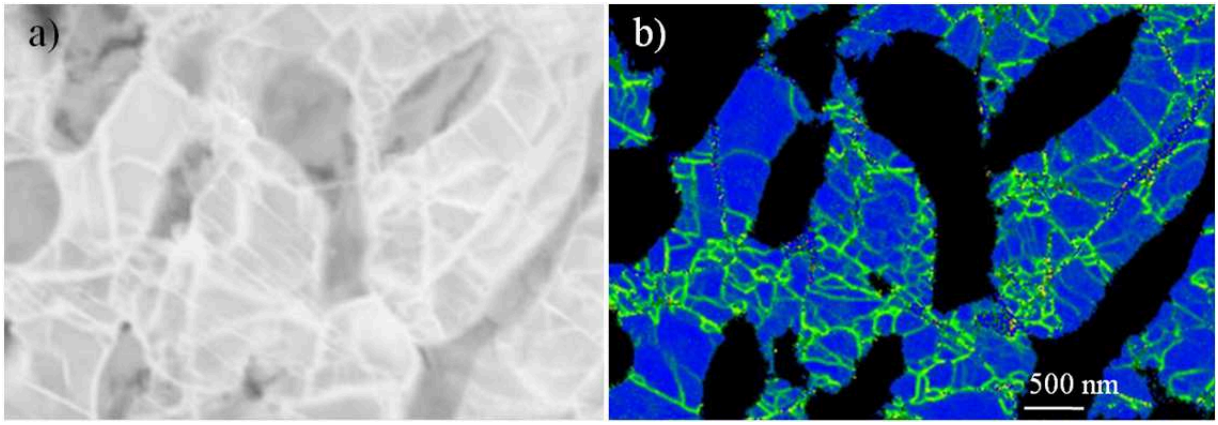

Figure 18 : *(a) Image virtuelle en champ clair du matériau biphasé bridgmanite (clair) / ferropériclase (sombre), où les bandes claires sont amorphes ; (b) cartographie KAM de la bridgmanite où l'essentielle de la désorientation s'effectue sur ces bandes amorphes (Nzogang et al., 2018).*

Références :

Argon, A. S. & Haasen, P. (1993): A new mechanism of work hardening in the late stages of large strain plastic flow in F.C.C. and diamond cubic crystals. *Acta Metall. Mater.*, **41**, 3289-3306.

Fundenberger, J.J., Morawiec, A., Bouzy, E., Lecomte, J.S. (2003): Polycrystal orientation maps from TEM. *Ultramicroscopy*, **96**, 127-137.

Guyot, P. (1974): Élargissement par les dislocations des pseudo-lignes de Kikuchi. *Rev. Phys. Appl.*, **9**, 393-397.

Hall, E.O. (1951): The Deformation and Ageing of Mild Steel: III Discussion of Results. *Proc. Phys. Soc. B* **64** 747-753.

Nzogang, B.C., Bouquerel, J., Cordier, P., Mussi, A., Girard, J., Karato, S. (2018): Characterization by Scanning Precession Electron Diffraction of an Aggregate of Bridgmanite and Ferropericlase Deformed at HP-HT, *Geochem. Geophys. Geosyst.*, **19**, 582-594.

Petch, N. J. (1953). The Cleavage Strength of Polycrystals. J. Iron Steel Inst., **174**, 25–28.

Rauch, E.F. & Dupuy, L. (2005): Rapid spot diffraction patterns identification through template matching. *Arch. Metall. Mater.*, **50**, 87-99.

Rauch, E.F., & Véron, M. (2014a): Automated crystal orientation and phase mapping in TEM. Materials Characterization, **98**, 1-9.

Rauch, E.F. & Véron, M. (2014b): Virtual dark-field images reconstructed from electron diffraction patterns. *Eur. Phys. J. Appl. Phys.*, **66**, 10701

Rauch, E.F., & Véron, M. (2016): Crystal Orientation Angular Resolution with Precession Electron Diffraction. *Microsc. Microanal.*, **22**, 500-501.

Valery, A., Rauch, E.F., Clément, L., Lorut, F. (2017): Retrieving overlapping crystals information from TEM nano-beam electron diffraction patterns. *J. Microsc.*, **268**, 208-218.

Valiev, R.Z. & Langdon, T.G. (2007): Principles of equal-channel angular pressing as a processing tool for grain refinement. *Prog. Mater. Sci.*, **51**, 881-981.

Venables, J.A. & Harland, C.J. (1973): Electron back-scattering patterns - A new technique for obtaining crystallographic information in the scanning electron microscope, *Philos. Mag.,* **2**, 1193-1200.

Wright, S.I., Nowell, M.M., Field, D.P. (2011): A Review of Strain Analysis Using Electron Backscatter Diffraction. *Microsc. microanal.*, **17**, 316-329.

Publications concernées par ces études (le travail précédé d'un astérisque sont reproduits à la fin de ce chapitre) :

Nzogang, B.C., Mussi, A., Cordier, P. (2018): Application of Scanning Electron Diffraction in the Transmission Electron Microscope for the characterization of dislocations in minerals, *Mineral. Mag.*, **83**, 71-79.

Nzogang, B.C., Thilliez, S., Mussi, A., Kawazoe, T,. Miyajima, N., Bouquerel, J., Cordier, P. (2018): Application of Scanning Precession Electron Diffraction in the Transmission Electron Microscope to the Characterization of Deformation in Wadsleyite and Ringwoodite, *Minerals*, **8**, 153.

*Nzogang, B.C., Bouquerel, J., Cordier, P., Mussi, A., Girard, J., Karato, S.I. (2018): Characterization by Scanning Precession Electron Diffraction of an aggregate of bridgmanite and ferropericlase deformed at HP-HT, *Geochem. Geophys. Geosyst.*, **19**, 582-594.

AGU PUBLICATIONS

Geochemistry, Geophysics, Geosystems

RESEARCH ARTICLE

10.1002/2017GC007244

Key Points:
- Microstructures of experimentally deformed bridgmanite and ferropericlase aggregates were studied orientation mapping in the TEM
- Bridgmanite deforms by localized shear deformation lamellae
- Most ferropericlase grains show strain much larger than the bulk strain of the sample without showing clear evidence for recrystallization

Supporting Information:
- Supporting Information S1
- Figure S1

Correspondence to:
P. Cordier,
patrick.cordier@univ-lille1.fr

Citation:
Nzogang, B. C., Bouquerel, J., Cordier, P., Mussi, A., Girard, J., & Karato, S. (2018). Characterization by scanning precession electron diffraction of an aggregate of bridgmanite and ferropericlase deformed at HP-HT. *Geochemistry, Geophysics, Geosystems*, *19*, 582–594. https://doi.org/10.1002/2017GC007244

Received 18 SEP 2017
Accepted 27 JAN 2018
Accepted article online 1 FEB 2018
Published online 2 MAR 2018

Characterization by Scanning Precession Electron Diffraction of an Aggregate of Bridgmanite and Ferropericlase Deformed at HP-HT

B. C. Nzogang[1], J. Bouquerel[1], P. Cordier[1], A. Mussi[1], J. Girard[2], and S. Karato[2]

[1]Univ. Lille, CNRS, INRA, ENSCL, UMR 8207-UMET-Unité Matériaux et Transformations, Lille, France, [2]Department of Geology and Geophysics, Yale University, New Haven, Connecticut, USA

Abstract Scanning precession electron diffraction is an emerging promising technique for mapping phases and crystal orientations with short acquisition times (10–20 ms/pixel) in a transmission electron microscope similarly to the Electron Backscattered Diffraction (EBSD) or Transmission Kikuchi Diffraction (TKD) techniques in a scanning electron microscope. In this study, we apply this technique to the characterization of deformation microstructures in an aggregate of bridgmanite and ferropericlase deformed at 27 GPa and 2,130 K. Such a sample is challenging for microstructural characterization for two reasons: (i) the bridgmanite is very unstable under electron irradiation, (ii) under high stress conditions, the dislocation density is so large that standard characterization by diffraction contrast are limited, or impossible. Here we show that detailed analysis of intracrystalline misorientations sheds some light on the deformation mechanisms of both phases. In bridgmanite, deformation is accommodated by localized, amorphous, shear deformation lamellae whereas ferropericlase undergoes large strains leading to grain elongation in response to intense dislocation activity with no evidence for recrystallization. Plastic strain in ferropericlase can be semiquantitatively assessed by following kernel average misorientation distributions.

Plain Language Summary We present a microstructural characterization of a mineralogical assemblage of the lower mantle deformed in the pressure-temperature conditions of the upper most lower mantle. We show that the magnesium silicate perovskite named bridgmanite is stiffer and deforms only along very localized shear bands. The magnesium oxide ferropericlase is much more ductile and takes most of the plastic strain.

1. Introduction

Deformation-induced microstructures carry critical information on the microscopic processes of deformation, hence on the relevance of deformation experiments for processes operating in the Earth's interior. Such characterizations are critical because the experimental conditions of deformation are vastly different from those in Earth's interior particularly in strain rate. For deformation under the shallow mantle conditions, experimental studies are straightforward (e.g., Karato et al., 1986; Mei & Kohlstedt, 2000), and a comparison of microstructures of experimentally deformed samples with those of naturally deformed rocks provides a guide to justify the extrapolation in strain rate (e.g., Karato & Wu, 1993).

The situation is very different for deformation in Earth's deep interior such as the lower mantle. Quantitative studies on deformation under the lower mantle pressure-temperature conditions and controlled strain rate became possible only recently (Girard et al., 2016). The experimental study by Girard et al. (2016) was conducted under the shallow lower mantle conditions (P = 27 GPa, T = 2,130 K) at a typical laboratory strain rate ($\sim 3 \times 10^{-5}$ s^{-1}). This provides the first opportunity to understand the processes of plastic deformation in the lower mantle. However, common to all experimental studies on plastic deformation, strain rates used are much higher (about 10 orders of magnitude, see, for instance, Paterson, 1987) than those expected in Earth, and stress needed to deform samples in these experiments (1–5 GPa) is substantially higher than those estimated for Earth's interior. Consequently, before applying these results, one needs to understand the microscopic processes of deformation.

Important microstructural observations include grains morphologies and the distribution of grain size, but also the intragranular defects contents: dislocations, their nature, and microstructures. Preliminary observations on grain morphology were reported by Girard et al. (2016) that provide evidence for stronger elongation of ferropericlase grains compared to bridgmanite. However, no characterization of defects microstructures has been performed to constrain active deformation mechanisms. Such a study is challenging because of technical difficulties including the high sensitivity of bridgmanite against electron beam radiation and the large strains involved in these experiments. Here we use a newly developed technique involving orientation and local misorientation mapping in transmission electron microscopy (TEM) to overcome these limitations.

Microstructures that develop as a result of plastic deformation are constituted of patterns of dislocation. Traditionally these features are studied by diffraction contrast in the TEM provided the dislocation density is not too high. For dislocations densities larger than ca. 10^{15} m^{-2}, individual dislocation contrasts overlap and cannot be resolved. Other parameters or proxies must then be found to follow the evolution of the plastic behavior. In 1993, Argon and Haasen (1993) have argued that a square root scaling law would describe the dependence of the mean, intragranular, misorientation angle θ_{mean} on plastic strain due to random fluctuations in the long-range strain field of dislocations:

$$\theta_{mean} \propto \sqrt{\varepsilon} \quad (1)$$

Some studies on microstructural evolution in deformed fcc metals and alloys have confirmed that plastic strain scales with misorientation (Hughes et al., 1997, 1998). Although, so far, these scaling laws have only been tested on metals, it is still interesting to note that they were found to be quite robust being independent of material properties such as stacking fault energy, solute content, etc., and process parameters such as temperature, strain, strain rate, strain paths, etc., suggesting a rather universal behavior. Intragranular misorientations can be detected in the reciprocal space through X-ray peak broadening which can be analyzed to provide average measurements of strain, including dislocation densities (Nyilas et al., 2006) and even information on Burgers vectors and slip systems (Cordier et al., 2004; Nisr et al., 2012). In the real space, scanning electron microscope (SEM)-based Electron Backscattered Electron Diffraction (EBSD) provides a very efficient and largely automated technique to sample long-range and short-range information on misorientations within deformed samples. Within the last decades, misorientations-based approaches have been used by metallurgists to follow the evolution of substructures during static and dynamic deformations (or loadings) (e.g., Schayes et al., 2016; Wright et al., 2011; Zhong et al., 2007).

In this paper, we present an alternative approach to SEM-based EBSD where orientation maps are obtained in the TEM from microbeam spot patterns. Compared to EBSD, this technique has several advantages. Being carried out in a TEM it benefits from the spatial resolution which results from the probe size, but also from the use of a thin foil. Also, TEM uses higher voltages which induce less damage in beam sensitive materials and spot patterns are less sensitive to the defect content and much more adapted to analyze highly deformed materials (see for instance, Figure 4 in Bollinger et al. (2015)). Of course, there are also some disadvantages, such as the need to prepare electron-transparent foils or the size of the sampled area which can be a strong limitation regarding the number of grains analyzed (especially if crystal preferred orientations were to be considered).

Here we apply scanning precession electron diffraction (SPED) to a high-pressure assemblage of bridgmanite and ferropericlase, shear deformed at large strains (of the order of 100%) in conditions of the uppermost lower mantle (Girard et al., 2016). Our goal is to study the defect distribution in bridgmanite and ferropericlase to better understand their deformation mechanisms at high-pressure and high-temperature. This is important to assess the scalability of the laboratory data to natural conditions.

Table 1
Samples Studied: Synthesis and Deformation Conditions

Run number	Pressure (GPa)	Temperature (K)	Strain (%)	Strain rate (s^{-1})
K1481	24	1,873	0	N.A.
Gamma 21 (G21)	27	2,130	100	5×10^{-5}

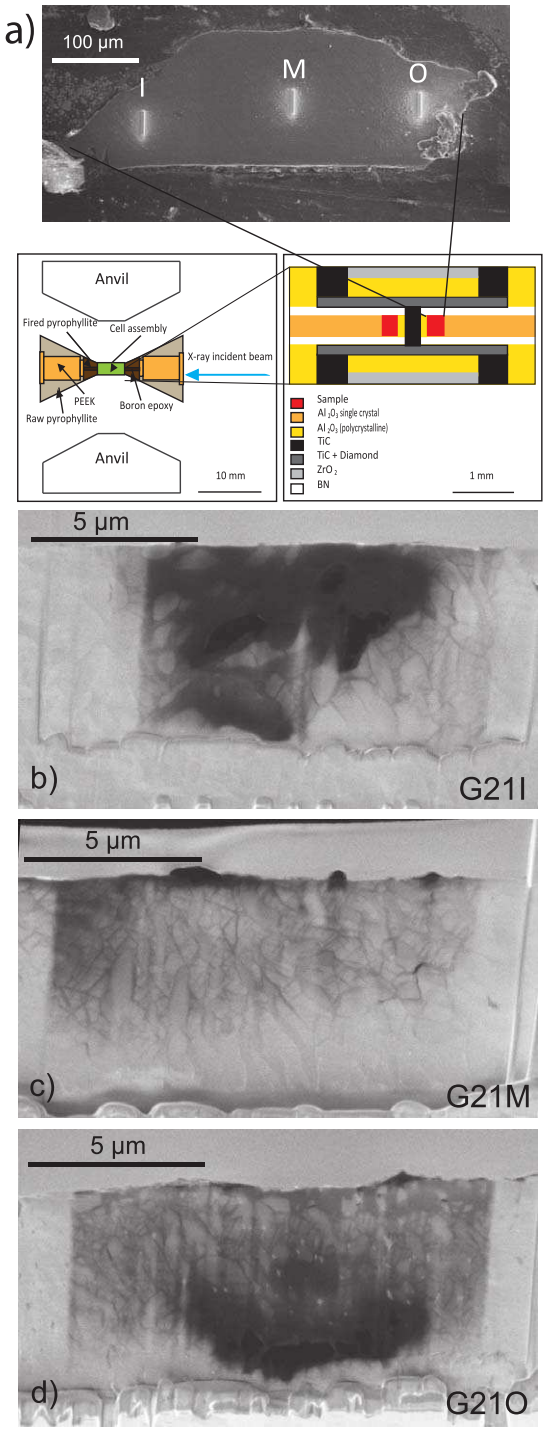

Figure 1. (a) Sketch of the deformation experimental setup with the locations where the three thin foils investigated in this study were extracted from Gamma 21. Their names are given according to their positions inner (I), middle (M), and outer (O): (b) FIB thin section G21I ("I" for inner position: lower strain), (c) FIB thin section G21M from the middle, and (d) FIB thin section G21O ("O" for outer position: higher strain).

2. Experimental Setup

2.1. Samples

Two samples have been investigated in this study. Their conditions of elaborations are summarized in Table 1.

The bridgmanite and ferropericlase assemblage have been synthesized under hydrostatic conditions during run K1481 using a Kawai type multi-anvil at Yale University (Table 1). The starting material, San Carlos olivine $(Mg_{0.9},Fe_{0.1})_2SiO_4$, was loaded in a molybdenum capsule, in an 8/3 cell assembly with a $LaCrO_3$ Furnace. The sample was annealed for 70 min at 24 GPa, 1,873 K. Pressure was estimated using pressure versus load calibration curve and temperature was estimated from power versus temperature calibration curve. The sample was then cut into 200 μm thick discs, and then cut into half ring (ID = 0.45 mm, OD = 1 mm) to be used in the Rotational Drickamer Apparatus (RDA) for deformation experiment (run Gamma 21).

Run Gamma 21 (Table 1) was performed using the RDA at the NSLS synchrotron beamline X17B2. A cross section of the cell assembly used at the beamline is shown in Figure 1. The sample was first compressed, then annealed for 60 min before starting the deformation. Pressure and temperature were estimated by in situ X-ray diffraction data obtained during annealing, using bridgmanite and ferropericlase equation of state (Komabayashi et al., 2010; MaO et al., 1991; Tange et al., 2012). Because the X-ray synchrotron beam has been lost at the beginning of the deformation, total strain was estimated from the angle of rotation of the anvil and the relationship between the angle of rotation and shear strain based on the previous results.

Electron-transparent foils (Figures 1b–1d) for TEM were extracted from the as-transformed (K1481) and HP-deformed (Gamma 21) samples using the focus ion beam technique with a FIB Dual Beam FEI Strata DB 235.

2.2. Transmission Electron Microscopy

TEM investigations were performed with a FEI® Tecnaï $G^2$20Twin microscope, operating at 200 kV and with a FEI CM30 microscope operating at 300 kV, both with a LaB_6 filament and using a double tilt sample-holder.

Orientation maps were acquired with a step size of 5 nm using SPED in the TEM with the ASTAR™ tool from NanoMEGAS (Rauch & Véron, 2014). The TEM is set in microbeam mode (spot size 4 nm) and the incident electron beam is scanned over the area thanks to a dedicated hardware control system of the TEM deflecting coils. The individual exposure time at each location is 10 or 20 ms. The spot patterns are collected with an external Stingray CCD camera that points on the TEM phosphorous screen and stored in the computer memory for further indexation and postprocessing. The diffraction patterns were collected as 144 × 144 pixels at a camera length of 89 mm. Electron diffraction spot patterns are indexed (providing the local crystal orientations) by comparing individually obtained patterns via cross-correlation matching techniques with precalculated electron diffraction templates generated every 1° (orientation resolution). For bridgmanite, templates have been generated from the crystallographic data of Tschauner et al. (2014). All crystallographic data for bridgmanite are presented within the *Pbnm* space

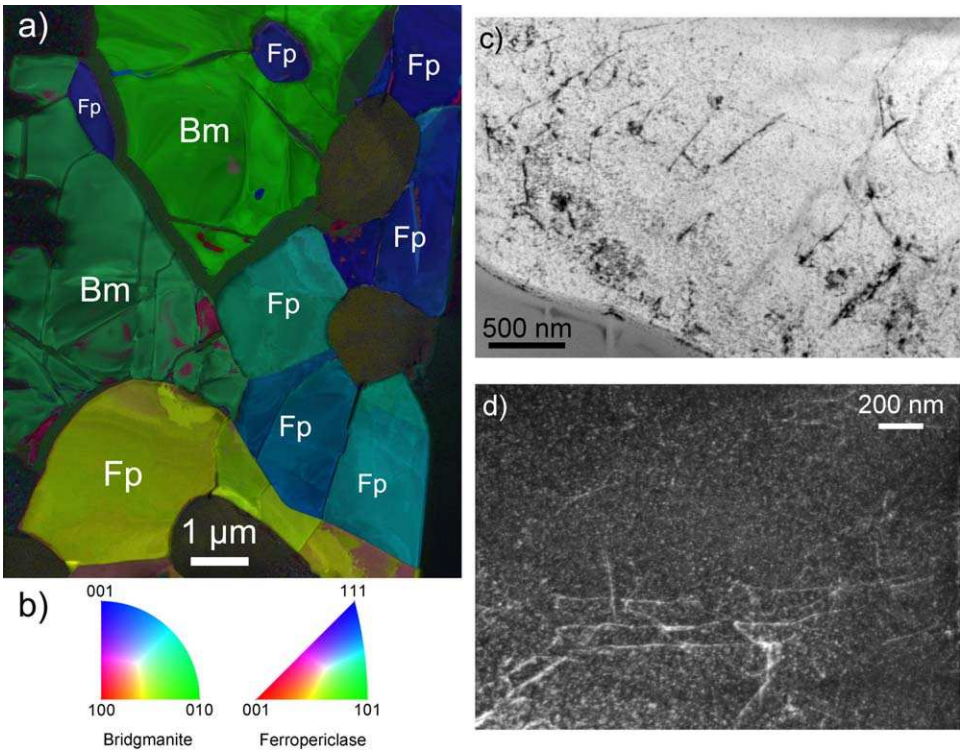

Figure 2. Starting material K1481. (a) Orientation map-spatial resolution 5 nm-1,600 × 2,000 data points—inverse pole figure (IPF). For each phase, the color indicates the crystallographic orientation of the vertical direction. Bm stands for bridgmanite and Fp for ferropericlase. (b) Color code for the crystallographic orientations of the IPF in Figure 2a. Ferropericlase is indexed within the *Fm3m* space group and bridgmanite within the *Pbnm* space group. (c) Ferropericlase: TEM bright field showing dislocations (dark lines) with a density of the order of 10^{12}–10^{13} m^{-2}. The spotty aspect in the background is due to damage induced by ion bombardment. (d) Ferropericlase: TEM dark field showing dislocations (white lines) with a density of the order of 10^{12}–10^{13} m^{-2}.

group (where a = 4.82 Å, b = 5.05 Å, and c = 6.92 Å). Ferropericlase templates were calculated from crystallographic data from Fei et al. (1992).

In this study, we used precession illumination in the TEM. When the precession mode is activated, a hollow-cone illumination is formed with the upper coils and equal and opposite signal is applied to the lower coils to bring the tilted beam back onto the optic axis. The net effect of the double-rocking is equivalent to having a stationary beam and a crystal which would precessed about the optic axis. The great advantage of this technique is that many more reflections are seen in the diffraction pattern and the intensity distribution gets closer to the kinematical diffracting conditions. We used precession angles in the range 0.5–1°. The orientations maps are presented as inverse pole-figures (IPF), where the color at each position represents the crystal orientation, that is, for the shear deformed sample, parallel either to the shear direction (SD), the radial direction (RD), or the compression direction (CD, i.e., parallel to the axis of the anvils). No cleaning procedure was applied to these maps. From the orientation maps, virtual bright field (VBF) maps can be generated which represents the fluctuation of the central beam intensity of the diffraction patterns. This builds up a STEM-like bright field contrast directly related to the orientation maps. The quality of indexation from template matching is quantified by the image correlation index, $Q(i)$, which is calculated for every template (Rauch & Dupuy, 2005):

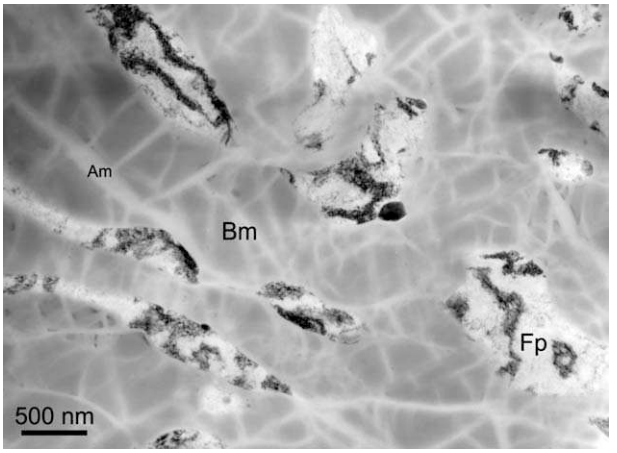

Figure 3. Overall microstructure of G21M (middle position). TEM bright field. Bm stands for bridgmanite, Fp for ferropericlase, and Am for amorphous material. In this sample, bridgmanite is well preserved although the grains contain pervasive amorphous lamellae.

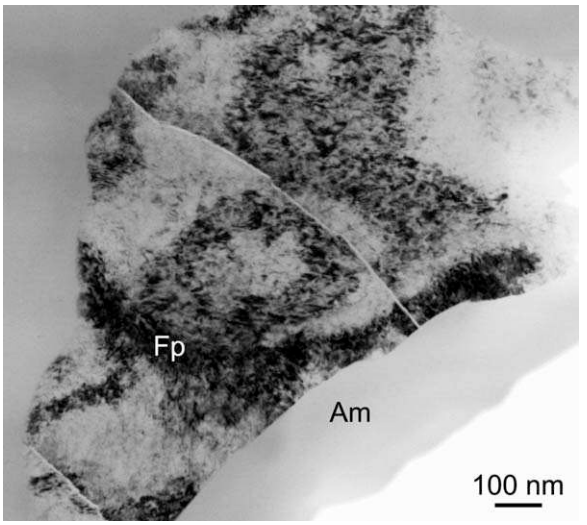

Figure 4. G21I (inner position). TEM bright field. Fp, ferropericlase and Am, amorphous material. All ferropericlase grains contain a very large density of dislocations, which precludes visualizing individual defects.

$$Q(i)=\frac{\sum_{j=1}^{m} P(x_j,y_j)T_i(x_j,y_j)}{\sqrt{\sum_{j=1}^{m} P^2(x_j,y_j)}\sqrt{\sum_{j=1}^{m} T_i^2(x_j,y_j)}} \quad (2)$$

In this expression, the diffraction pattern is represented by the intensity function $P(x,y)$ at each position (x,y) and each template i is described by the function $T_i(x,y)$. The highest Q value corresponds to the solution. The reliability of this solution can be quantified by the ratio of the matching indices for the two best solutions Q_1 and Q_2:

$$R=100\left(1-\frac{Q_1}{Q_2}\right) \quad (3)$$

In reliability maps, the brighter the pixel (i.e., the highest the reliability index) the more reliable is the indexation proposed. On the contrary, the darker is the pixel, the least reliable is the solution. This is typically the case at grain boundaries where two solutions of coexisting grains overlap or when for some reasons, the quality of the diffraction patterns is less. The presence of amorphous material represents an extreme case of that situation.

SPED can be compared with EBSD performed in transmission in an SEM (originally called t-EBSD for transmission EBSD or TKD for transmission Kikuchi diffraction). Both use electron-transparent thin foils and work in transmission. TKD is based on low-energy transmission Kikuchi diffraction in an SEM (Keller & Geiss, 2012; Suzuki, 2013; Trimby, 2012) whereas SPED involves high-energy microdiffraction in the TEM. It is important to highlight that the ASTAR™ algorithm saves all diffraction patterns and that no original data are lost. This is a huge advantage compared to commercial (standard) EBSD techniques which are usually not saving patterns and never perform image matching. Instead, in standard EBSD, indexing is based on Hough-transforms of the pattern for indexing and in most scenarios only the indexing is saved and the original data, namely the Kikuchi patterns, are discarded. From that perspective, SPED performed with ASTAR can be compared to the Dictionary Indexing approach for EBSD indexing, which also saves all patterns and performs image matching for indexing against a library of precomputed patterns (Marquardt et al., 2017; Ram et al., 2017; Singh & De Graef, 2016, 2017). If reliable results in terms of angular resolution (HR-EBSD or HR-KAM, cf. Britton et al., 2010) are needed, high-resolution patterns must be acquired (1,600 × 1,000 pixels). This results in an extremely large set of data to postprocess. In the most common TKD setups (except for Brucker), the EBSD camera is not in the most suitable condition for pattern acquisition and the patterns are generally deformed. This could

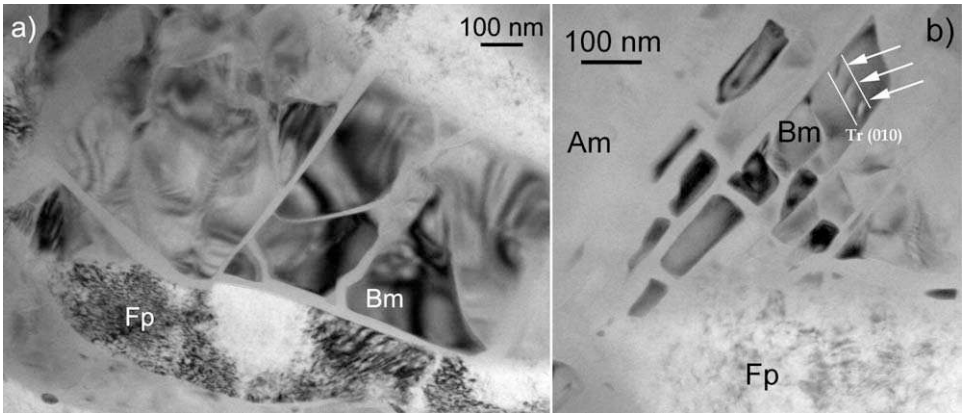

Figure 5. G21M (middle position). TEM bright field (Bm, bridgmanite; Fp, ferropericlase; and Am, amorphous material). The remaining crystalline bridgmanite parts are set in Bragg orientation to promote diffraction contrast. No evidence for defects is found in any grains besides the three dislocations arrowed in Figure 5b. See text for the analysis of the trace of the glide plane.

result in lower angular resolution that conventional EBSD. Still, TKD looks superior to SPED in term of angular resolution, but this advantage disappears with beam sensitive samples. The acquisition rate should be much higher with TKD to avoid beam damage and requires new technology which only becomes available.

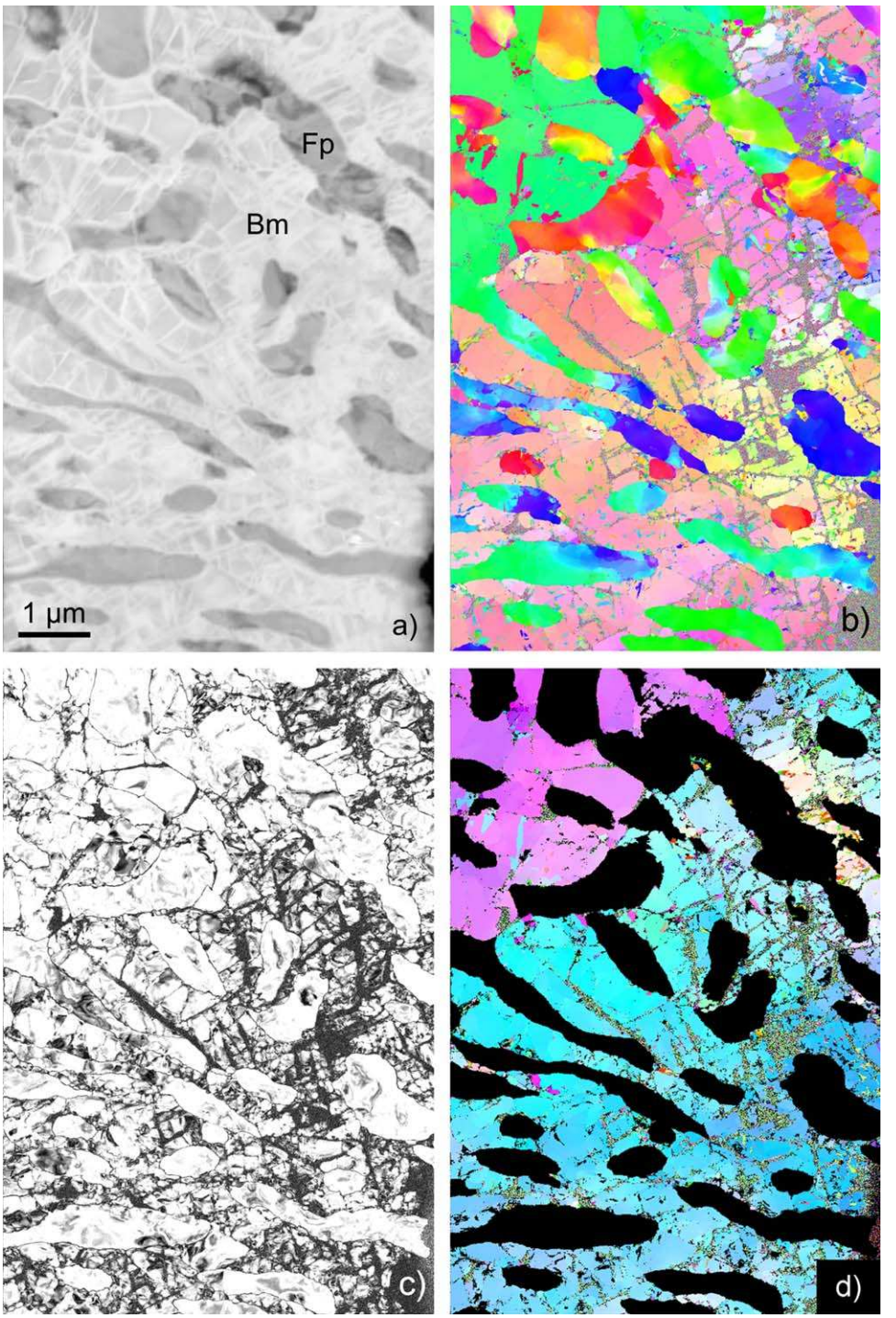

Figure 6. G21M (middle position). (a) SPED-virtual bright field. Spatial resolution 5 nm-1,200 × 1,800 data points. (b) SD-IPF: inverse pole figure map corresponding to the shear direction (horizontal). (c) Reliability map (plotted between 0 and 35). Less reliable places appear dark. (d) RD-IPF: inverse pole figure map of bridgmanite corresponding to the radial direction (perpendicular to the map plane). (e) CD-IPF: inverse pole figure map of ferropericlase corresponding to the compression direction (vertical). (f) IPF color legend. Ferropericlase is indexed within the *Fm3m* space group and bridgmanite within the *Pbnm* space group.

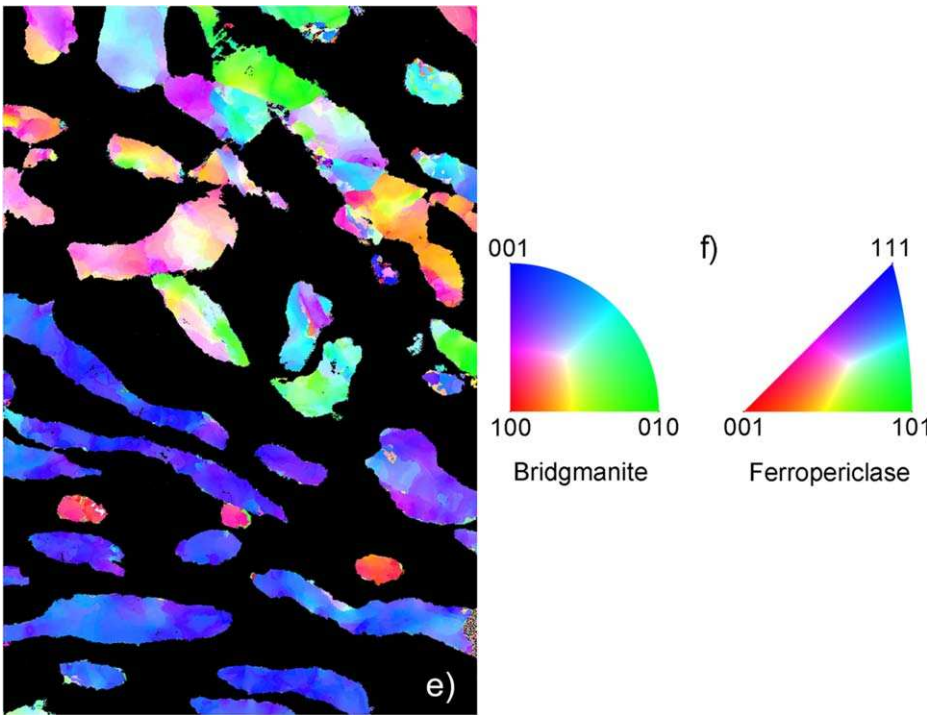

Figure 6. (Continued).

Although Q-maps have been proposed as a first approach to detect residual plastic strain, several parameters can affect this parameter as discussed above (Wright et al., 2011). In this study, we rather focus on the measurements of local misorientations as recently developed in the EBSD community (e.g., Wright et al., 2011). Postprocessing of the orientation maps was performed with the TSL OIM^{TM} Analysis 7 commercial software provided by EDAX. As commonly used in EBSD, several quantities are calculated from the orientation maps:

1. The *Kernel Average Misorientation* (KAM) calculates the average misorientation between a pixel and its neighbors provided that the misorientation does not exceed a predefined threshold value, e.g., 5°, thus the incorporation of well-defined grain boundaries is avoided. If plastic deformation results from dislocation glide and crystal lattice rotation, this approach allows quantitative evaluation of the local plastic strain gradients (Godfrey et al., 2005). A kernel is a set of points of prescribed size surrounding the scan point of interest. The size of the kernel is generally prescribed to the *n*th nearest-neighbors. Hence, this parameter is sensitive to the step size of the measurement grid.
2. The *Grain Orientation Spread* (GOS) is the average deviation in orientation between each point in a grain and the average orientation of the grain. This approach leads to assigning the same value of the GOS to every scan point contained within a grain.
3. The *Grain Reference Orientation Deviation* (GROD) is based on the misorientation between a reference point of that grain and the other points. The reference point can be the mean misorientation of the grain (in that case the GROD is also called *Mis2mean* in MTEX) or the point of the grain where the KAM is the lowest.

KAM, GROD, and GOS approaches appear to be complementary. GROD maps show the orientation field referenced to a fixed point whereas KAM approach shows the magnitude of the gradient, which can be seen as the first derivative of the orientation field.

3. Observations

3.1. Starting Material (K1481)

The microstructure of the starting material is illustrated in Figure 2. As already reported in Girard et al. (2016), it consists in a mixture of bridgmanite and ferropericlase grains which are mostly equiaxed. With

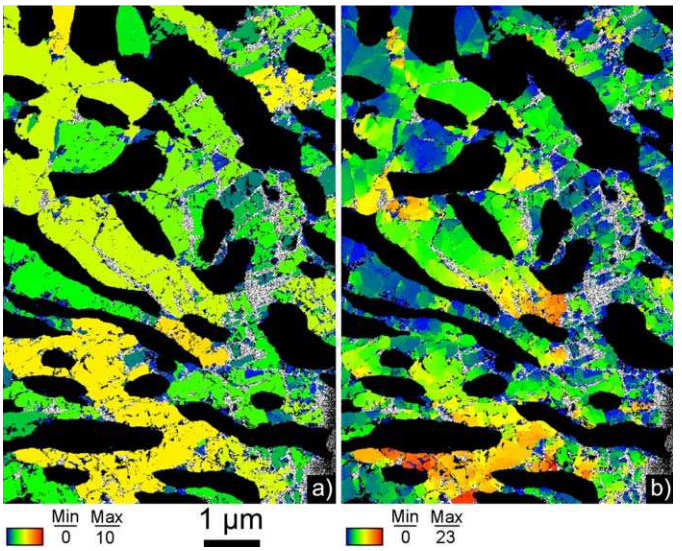

Figure 7. Bridgmanite in G21M (middle position). Same map area as Figure 6. (a) Grain Orientation Spread (GOS) map. Each grain displays a color corresponding to its average internal misorientation. (b) Grain Reference Orientation Deviation (GROD) or Mis2mean map since here, the reference is the mean misorientation in each grain. This representation highlights intragranular misorientations which would correspond to small color changes in Figures 6b, 6d, and 6e.

conventional bright-field TEM analyses, only ferropericlase shows some dislocations, with a density of the order of 10^{12}–10^{13} m^{-2} at the most (Figures 2c and 2d).

3.2. Conventional TEM Observation of Gamma 21

Although ferropericlase is found equally well in the three thin foils, the preservation of bridgmanite after FIB milling is very uneven. In G21M, crystalline bridgmanite has been well preserved everywhere in the thin section although this phase contains systematically numerous amorphous lamellae (Figure 3). In G21I, most bridgmanite has been amorphized in the central part of the thin section. Almost no bridgmanite is preserved in G21O.

The strong plastic strain of ferropericlase is suggested by the elongated shape of most grains (already observed at the SEM: Girard et al., 2016) as seen in Figure 3 (with clearer evidence in Figure 6e) in G21M, but also from the very large dislocation density which prevents further analysis with conventional techniques (Figure 4).

In bridgmanite, rapid amorphization under the electron beam prevents from having an exhaustive characterization of the microstructure. However, the only remaining crystalline areas are remarkably free of dislocations (Figure 5a). Only three dislocations have been observed, they are displayed in Figure 5b. Taking into account the orientation of the grain (close to the zone axis [746]) from the orientation map (see below), the orientation of the trace of the glide plane, and the thickness of the thin foil, one finds that the plane containing the dislocations is compatible with (010). One notes the pervasive occurrence of amorphous lamellae which preexisted observation (but broaden rapidly under the beam). It is worth mentioning that, because of the sensitivity of the samples to the beam, we took care to record the orientation maps described below before any exposure of the samples and that the conventional TEM investigation has been done only at the end of the study.

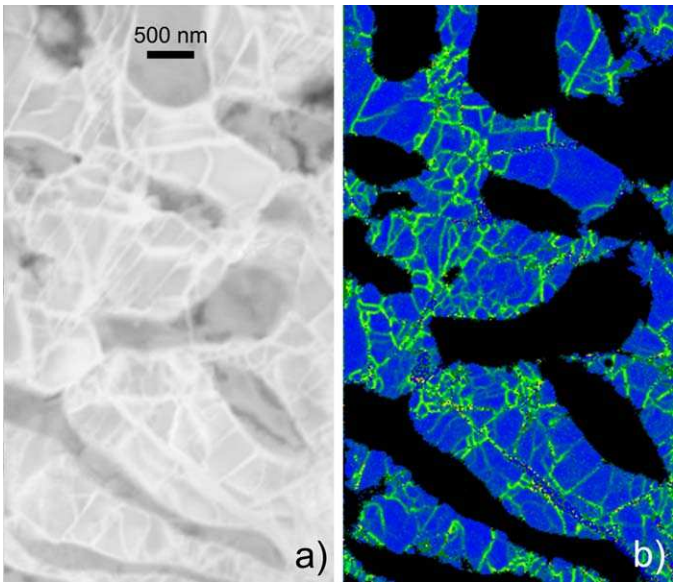

Figure 8. Origin of amorphous lamellae in bridgmanite from G21M (middle position). (a) SPED-virtual bright field where the amorphous lamellae in bridgmanite appear brighter than the crystalline parts (ferropericlase appear even darker). (b) Kernel Average Misorientation (KAM—third neighbor) in bridgmanite. This representation highlights local gradients of orientation. One can see that amorphous lamellae correlate with high KAM, demonstrating that they localize shear and thus have a mechanical origin and do not result from sample preparation.

3.3. Orientation Imaging Mapping on Gamma 21

To gain more information on the deformation, we have acquired orientation maps by SPED with the ASTAR™ system. Figure 6 shows the maps obtained on G21M (which is the sample for which both phases are best preserved). The virtual bright field shows the microstructure of the two phases, and also the amorphous lamellae later imaged in TEM bright field. From the indexation of the diffraction patterns, it is possible to plot the IPF maps either corresponding to the shear direction, to the compression direction or to the radial direction. In Figure 6b, we present the IPF of both phases corresponding to the shear direction (SD). It is possible to separate both phases as shown in Figures 6d and 6e. The indexation is usually very good. This can be assessed from the reliability map (Figure 6c). The reliability drops at the grain boundaries when the diffraction patterns consist in the superposition of those of the two grains. The reliability map thus offers a good visualization of the grain boundaries. The reliability is also poor in thicker areas or when crystallinity is less. Such is the case in some places in bridgmanite, for instance along the thickest amorphous lamellae (Figures 6c and 6d).

3.3.1. Bridgmanite

The orientation map of bridgmanite from Gamma 21 reveals rather large grains (several micrometers) which contain elongated ferropericlase grains. The colors are not perfectly uniform in the IPF suggesting

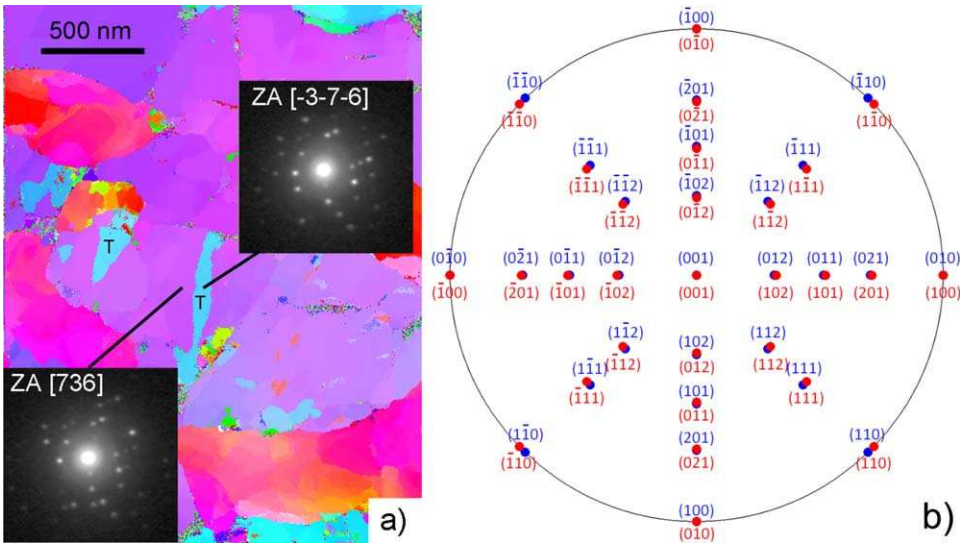

Figure 9. G21M (middle position). (a) CD-IPF (enlargement) showing twinned domains *T* (see text) with corresponding diffraction patterns (indices are given within the *Pbnm* space group). (b) Twin model resulting from the switch of the [100] and [010] axis (*Pbnm* space group) corresponding to an 87.3° rotation around [001].

some misorientation in the bridgmanite grains. The GOS (Figure 7a) is well suited to reveal these variations and quantify them. It shows that all bridgmanite grains (or domains within those grains) exhibit significant internal misorientation. The GROD (Figure 7b) shows that these misorientations are pervasive and rather heterogeneous. The GROD seems to be more pronounced when bridgmanite forms narrow channels between elongated ferropericlase grains suggesting strain resulting from the infiltration process of ferropericlase grains.

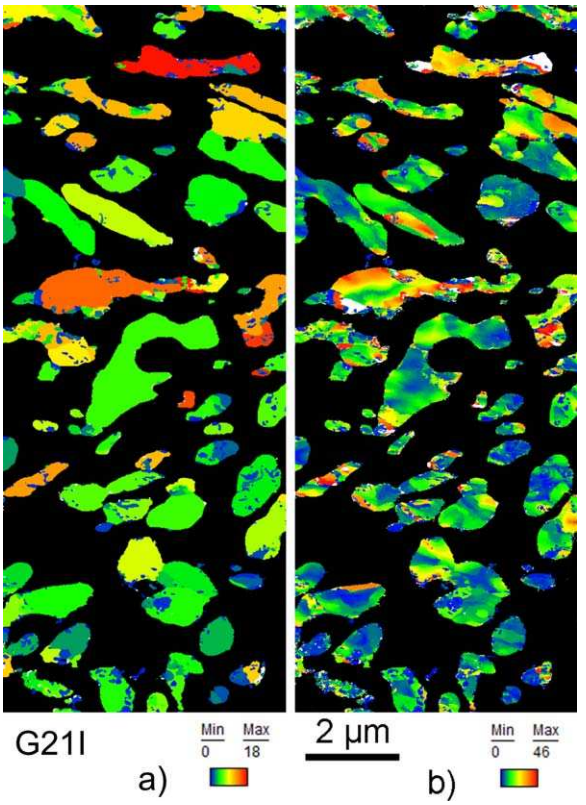

Figure 10. Ferropericlase in G21I (inner position see Figure 1). Total map acquired with a spatial resolution 5 nm-1,200 × 3,000 data points. (a) Grain Orientation Spread (GOS) and (b) Grain Reference Orientation Deviation (GROD) using the average orientation for each grain as the reference (Mis2mean).

Further understanding comes from plotting point to point misorientation profiles across the amorphous lamellae. This shows that these lamellae correspond to jumps of misorientation between largely undeformed regions (supporting information Figure S1). These features appear well on the KAM maps, which highlight places where strong misorientation localizes. Comparison of the KAM with the TEM bright field or the SPED-virtual bright field (Figure 8) demonstrates that misorientation gradients correlate very well with the amorphous lamellae. These lamellae thus appear to be the location where deformation localized in bridgmanite.

In bridgmanite, some domains attract attention (Figure 9a or Figures 6b and 6d (upper left corner)). They exhibit a remarkable misorientation with the surrounding matrix of 87.4 ± 0.1°. The analysis of the diffraction patterns of both domains shows that they correspond to switching the [100] and [010] axis, i.e., to the {110} pseudomerohedral twinning of the *Pbnm* orthorhombic structure already reported (e.g., Wang et al., 1992). Indeed, this model (Figure 9b) predicts a theoretical misorientation of 87.3° between the variants which is in excellent agreement with the value found experimentally.

3.3.2. Ferropericlase

As already mentioned above and in Girard et al. (2016), the morphology of the ferropericlase grains is already a strong indication of large strain in this phase. It seems that from the inner to the outer sample there is a gradient in the microstructure with more elongated (G21M) and then fragmented (G21O) ferropericlase grains as one goes

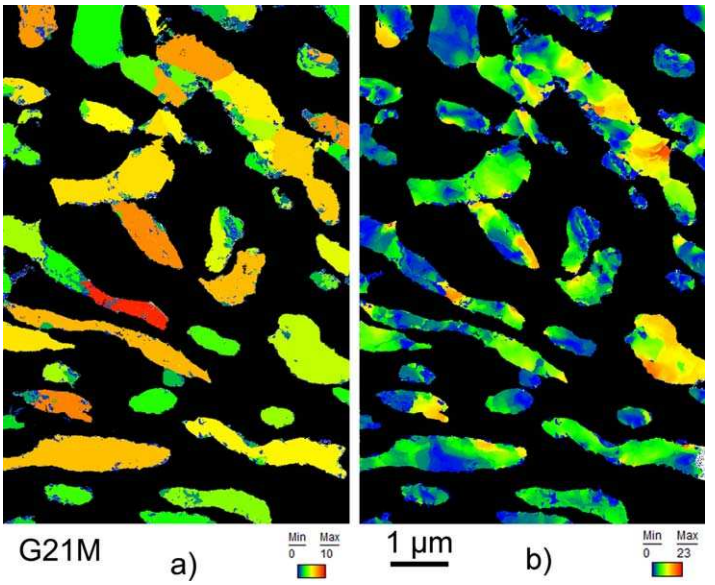

Figure 11. Ferropericlase in G21M (middle position). Same map area as Figure 6. Total map acquired with a spatial resolution 5 nm-1,200 × 1,800 data points. (a) Grain Orientation Spread (GOS) and (b) Grain Reference Orientation Deviation (GROD) using the average orientation for each grain as the reference (Mis2mean).

from inside to outside the deformation sample. The GOS maps (Figures 10a, 11a, and 12a) show that all grains are strongly internally disoriented (i.e., deformed). Comparison is, however, quite difficult since heterogeneities lead to use different scales. The GROD maps (Figures 10b, 11b, and 12b) show that the indistinct, large dislocation densities observed in the TEM bright-fields hide some complex, heterogeneous structures at a very fine scale. One can understand that such strong local heterogeneities can ultimately lead to fractures during foil thinning as seen in Figure 4.

4. Discussion

TEM-based SPED appears as a powerful complement to in situ X-ray diffraction to study the plastic behavior of high-pressure phases, especially in case of samples that include beam sensitive minerals and also aggregates of phases exhibiting a large viscosity contrast. In the present case, in situ X-ray diffraction acquired during deformation provided information on stress against shear strain. Where strain, obtained from a marker or (here) from the rotation of the anvils, could only be assessed on average, in situ X-ray diffraction provides information which can distinguish both phases. Using this technique, Girard et al. (2016) could demonstrate that ferropericlase is much softer than bridgmanite at 27 GPa and 2,130 K, with average flow stress 4–5 times smaller in ferropericlase than in bridgmanite. SEM, backscattering images of the recovered Gamma 21 already showed (Girard et al., 2016) that ferropericlase grains undergone strains much larger than the average value of the sample estimated to 100%.

Our microscopic investigation confirms these observations. Prior to deformation, ferropericlase in K1481 is often larger than 1 μm and rather equiaxed (Figure 2). After deformation (Figures 6 and 10−12), the grains of ferropericlase are strongly stretched, eventually leading to fragmentation into grains of a few hundreds of nanometers in size. These processes have been observed in monomineralic magnesiowüstite deformed in shear for ca. $\gamma = 5$ to ca. $\gamma = 10$ (Heidelbach et al., 2003; see also similar observations in halite deformed under large shear strains: Wenk et al., 2009). We can see in Figure 6e that most grains in the lower part of the map exhibit very close orientations. We can speculate that they result from the stretching and fragmentation of a single larger grain of ferropericlase. It is difficult from a cross section only to decide whether this also corresponds to a three-dimensional interconnectivity in G21M. Conventional TEM observations show further evidence of accumulated strain with very large dislocations densities. In the starting material, the dislocation density was found to be of the order of 10^{12}–10^{13} m^{-2}. In ferropericlase from Gamma 21, the dislocation densities are much larger. They are so large that no measurement of dislocation density is now possible. This illustrates the usual limitation of TEM studies on samples deformed at large strains. Here we show how SPED can overcome this limitation.

Beyond the shape of the grains and without directly imaging the dislocations, the IPF of ferropericlase (Figure 6e) show that grains do not exhibit a single orientation. Indeed misorientation profiles show extremely strong gradients inside every grains. To gain more information on these misorientations, we have applied the standard posttreatments used in EBSD. First, we used the grain-based method to better reveal the presence of intracrystalline misorientations. The GOS affects a single value (taken as the average) for the misorientation to a body identified as a grain.

Figures 10a, 11a, and 12a show that all ferropericlase grains, even the smallest, exhibit average misorientations of several degrees. The spatial distribution of those misorientations is better illustrated using the GROD, which represents at each measurement point the misorientation with a reference value. Here we choose the average misorientation as the reference. The GROD is then usually called the Mis2mean. The Mis2mean maps (Figures 10b, 11b, and 12b) show that deformation in ferropericlase is very heterogeneous at a very small scale. This information could not be withdrawn from standard diffraction contrast imaging (e.g., Figure 4). Being cubic, ferropericlase exhibits a large number of equivalent slip systems which involve dislocations which can interact

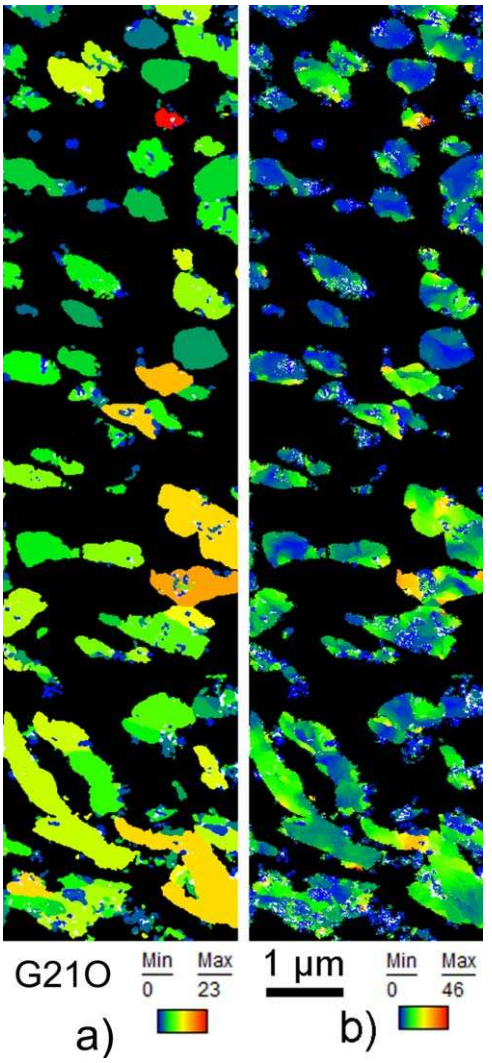

Figure 12. Ferropericlase in G21O (outer position). Total map acquired with a spatial resolution 5 nm-600 × 2,400 data points. (a) Grain Orientation Spread (GOS) and (b) Grain Reference Orientation Deviation (GROD) using the average orientation for each grain as the reference (Mis2mean).

and form various kinds of junctions. This is the origin of strong dislocation storage in this material which can lead to significant strain hardening (Amodeo et al., 2014). Usually, this dislocation storage leads to recrystallization, i.e., to the formation of new grains free of dislocations, even in single crystals (see, for instance, Mariani et al., 2009). Here we find no evidence of dislocation-free grains or domains. Further quantification is difficult. Indeed, the grain grouping algorithms (GOS and GROD) are by definition sensitive to the body considered as a grain. A usual criterion is to consider a limit of misorientation of 15° as a standard limit to discriminate subgrains and grain boundaries. In the present case, ferropericlase grains are strongly deformed and present strong misorientations which challenge the automatic detection of "grains." Hence, we consider that GOS and GROD are useful to highlight the strong strains undergone by the ferropericlase grains, but not well adapted to further quantification. We prefer here to rely on short-range misorientation parameters with a kernel-based algorithm like the KAM. In that case, to provide comparable results, one must compare maps acquired with the same spatial resolution, and the same kernel size must be used. Figure 13 corresponds to maps acquired with a step size of 5 nm and processed with third nearest-neighbor kernels. Figure 13b shows in the case of ferropericlase that KAM distributions can resolve more quantitative information. The KAM distribution in K1481 is clearly distinct from those in Gamma 21. Being much narrower, indicating much less intragranular misorientation, it is clearly consistent with what is expected from the undeformed state. More interestingly, one also observes a consistent evolution of the KAM distribution with the sample position in the experimental setup. From the inner position to the outer position in the sample ring, one finds that (i) the KAM distribution peak shifts to higher values of misorientation, (ii) the peak fractions decrease, and (iii) the distributions broaden. This evolution is characteristic of increasing strain. One can see here that our analysis is able to evidence the radial strain gradient which is expected in a torsion test.

Although preservation of bridgmanite remains a challenging issue, we have been able to gather enough diffraction patterns on this phase to gain information on its deformation mechanisms. From G21M (which is the sample where bridgmanite is best preserved), one can essentially see two large grains with a morphology which cannot be distinguished from those in K1481. The GOS and GROD maps of those grains (Figure 7) show evidence of intragranular misorientation which suggests some deformation. The KAM distributions (Figure 13a) also show that Gamma 21 is clearly distinct from the undeformed state. The difference in the distributions from G21I and G21M is also consistent with a radial strain gradient although it is less conclusive than in ferropericlase. Here we get more information from the KAM map. In Figure 8, one can see an excellent correlation between the KAM spatial distribution and the presence of amorphous lamellae observed in the virtual bright field or in the TEM bright-field images. We interpret that these amorphous lamellae are regions where strain was localized during HP-HT deformation. The only information that we have to further constrain deformation mechanisms that were active at HP-HT comes from the three dislocations observed. Their alignment allows to infer their glide plane which is compatible with (010). Considering the possible slip systems predicted in bridgmanite (Ferré et al., 2007; Hirel et al., 2014; Mainprice et al., 2008), this suggests that the observed dislocation would belong to the [100](010) slip system. Our (single) observation is not compatible with the [001](100) slip system inferred by Tsujino et al. (2016) from crystal preferred orientation developments. We have also observed a few pseudomerohedral twins in bridgmanite. Twinning occurs and can be observed, but it is not pervasive, showing that twinning does not represent a significant deformation mechanism for bridgmanite under those conditions.

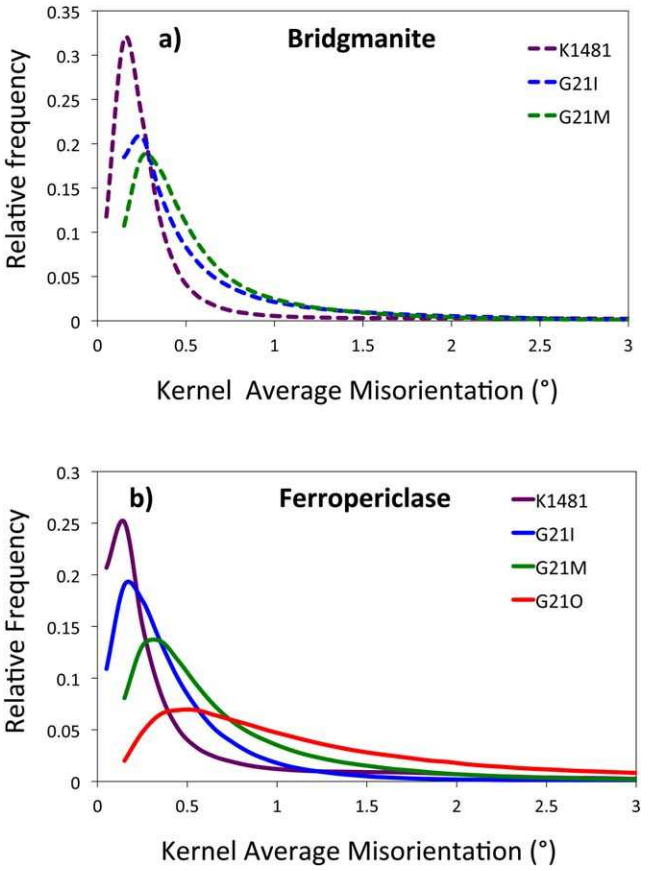

Figure 13. KAM distributions in undeformed and deformed bridgmanite and ferropericlase in each sample investigated here, i.e., for the deformed samples for increasing strains from the inner to the outer positions (see Figure 1). (a) Third nearest-neighbor KAM distributions in bridgmanite, where the starting material is compared with G21I and G21M. Since bridgmanite was completely amorphized in G21O, this sample is not represented here. (b) Third nearest-neighbor KAM distributions in ferropericlase for all samples including the starting material.

5. Conclusions

SPED represents a powerful new technique to analyze samples deformed at HP-HT. Applied to aggregates of bridgmanite and ferropericlase deformed in conditions of the uppermost lower mantle, it provides new information about the plastic behavior of those phases. We see only evidence form intracrystalline plasticity by dislocation motion although the deformed microstructure of bridgmanite and ferropericlase suggest very different mechanisms and plastic behavior. Ferropericlase shows strong evidence for large strains (much larger than the average 100% strain of the aggregate) with intense dislocation activity and storage leading to what we interpret as elongation leading to fragmentation of the grains. Despite these high strains, we observe no evidence for dynamic recrystallization. Evidence of deformation is demonstrated in bridgmanite although clearly less pronounced. It occurs essentially through localized, amorphous, shear deformation lamellae. An evidence for dislocations belonging to the [100](010) slip system is reported.

Acknowledgments
The work in Lille was supported by funding from the European Research Council under the Seventh Framework Programme (FP7), ERC grant 290424—RheoMan to P. Cordier. The TEM facility in Lille (France) is supported by the Conseil Regional du Nord-Pas de Calais, and the European Regional Development Fund (ERDF). We thank D. Troadec (IEMN-Lille) for sample preparation with the FIB. We are grateful to Dr. K. Marquardt and an anonymous reviewer for their comments which helped improving the manuscript. Data are available from https://figshare.com/s/4a19bbda734beef58be1.

References

Amodeo, J., Devincre, B., Carrez, P., & Cordier, P. (2014). Dislocation reactions, plastic anisotropy and forest strengthening in MgO at high temperature. *Mechanics of Materials*, *71*, 62–73.

Argon, A. S., & Haasen, P. (1993). A new mechanism of work hardening in the late stages of large strain plastic flow in F.C.C. and diamond cubic crystals. *Acta Metallurgica et Materialia*, *41*(11), 3289–3306. https://doi.org/10.1016/0956-7151(93)90058-Z

Bollinger, C., Merkel, S., Cordier, P., & Raterron, P. (2015). Deformation of forsterite polycrystals at mantle pressure: Comparison with Fe-bearing olivine and the effect of iron on its plasticity. *Physics of the Earth and Planetary Interiors*, *240*, 95–104. https://doi.org/10.1016/j.pepi.2014.12.002

Britton, T. B., Maurice, C., Fortunier, R., Driver, J. H., Day, A. P., Meaden, G., et al. (2010). Factors affecting the accuracy of high resolution electron backscatter diffraction when using simulated patterns. *Ultramicroscopy*, *110*(12), 1443–1453.

Cordier, P., Ungár, T., Zsoldos, L., & Tichy, G. (2004). Dislocation creep in $MgSiO_3$ perovskite at conditions of the Earth's uppermost lower mantle. *Nature*, *428*(6985), 837–840.
Fei, Y., Mao, H.-K., Shu, J., & Hu, J. (1992). P-V-T equation of state of magnesiowüstite $(Mg_{0.6}Fe_{0.4})O$. *Physics and Chemistry of Minerals*, *18*(7), 416–422.
Ferré, D., Carrez, P., & Cordier, P. (2007). First-principles determination of dislocations properties of $MgSiO_3$ perovskite at 30 GPa based on the Peierls-Nabarro model. *Physics of the Earth and Planetary Interiors*, *163*, 283–291.
Girard, J., Amulele, G., Farla, R., Mohiuddin, A., & Karato, S.-I. (2016). Shear deformation of bridgmanite and magnesiowüstite aggregates at lower mantle conditions. *Science*, *351*(6269), 144–147. https://doi.org/10.1126/science.aad3113
Godfrey, A., Cao, W. Q., Liu, Q., & Hansen, N. (2005). Stored energy, microstructure, and flow stress of deformed metals. *Metallurgical and Materials Transactions A*, *36*, 2371–2378.
Heidelbach, F., Stretton, I., Langenhorst, F., & Mackwell, S. (2003). Fabric evolution during high shear strain deformation of magnesiowüstite $(Mg_{0.8}Fe_{0.2}O)$. *Journal of Geophysical Research: Solid Earth*, *108*(B3), 2154. https://doi.org/10.1029/2001JB001632
Hirel, P., Kraych, A., Carrez, P., & Cordier, P. (2014). Atomic core structure and mobility of [100](010) and [010](100) dislocations in $MgSiO_3$ perovskite. *Acta Materialia*, *79*, 117–125.
Hughes, D. A., Chrzan, D. C., Liu, Q., & Hansen, N. (1998). Scaling of misorientation distributions. *Physical Review Letters*, *81*(21), 4664–4667.
Hughes, D. A., Liu, Q., Chrzan, D. C., & Hansen, N. (1997). Scaling of microstructural parameters: Misorientations of deformed induced boundaries. *Acta Materialia*, *45*(1), 105–112.
Karato, S., Paterson, M. S., & Fitz Gerald, J. D. (1986). Rheology of synthetic olivine aggregates: Influence of grain-size and water. *Journal of Geophysical Research: Solid Earth*, *91*(B8), 8151–8176. https://doi.org/10.1029/JB091iB08p08151
Karato, S., & Wu, P. (1993). Rheology of the upper mantle: A synthesis. *Science*, *260*(5109), 771–778.
Keller, R. R., & Geiss, R. H. (2012). Transmission EBSD from 10 nm domains in a scanning electron microscope. *Journal of Microscopy*, *245*, 245–251.
Komabayashi, T., Hirose, K., Nagaya, Y., Sugimura, E., & Ohishi, Y. (2010). High temperature compression of ferropericlase and the effect of temperature on iron spin transition. *Earth and Planetary Science Letters*, *297*(3–4), 691–699.
Mainprice, D., Tommasi, A., Ferré, D., Carrez, P., & Cordier, P. (2008). Predicted glide systems and crystal preferred orientation of polycrystalline silicate Mg-Perovskite at high pressure: Implications for the seismic anisotropy in the lower mantle. *Earth and Planetary Science Letters*, *271*(1–4), 135–144.
Mao, H. K., Hemley, R. J., Fei, Y., Shu, J. F., Chen, L. C., Jephcoat, A. P., et al. (1991). Effect of pressure, temperature and composition on lattice parameters and density of $(Fe,Mg)SiO_3$-perovskite to 30 GPa. *Journal of Geophysical Research: Solid Earth*, *96*(B5), 8069–8079. https://doi.org/10.1029/91JB00176
Mariani, E., Mecklenburgh, J., Wheeler, J., Prior, D. J., & Heidelbach, F. (2009). Microstructure evolution and recrystallization during creep of MgO single crystals. *Acta Materialia*, *57*, 1886–1898.
Marquardt, K., De Graef, M., Singh, S., Marquardt, H., Rosenthal, A., & Koizuimi, S. (2017). Quantitative electron backscatter diffraction (EBSD) data analyses using the dictionary indexing (DI) approach: Overcoming indexing difficulties on geological materials. *American Mineralogist*, *102*(9), 1843–1855.
Mei, S., & Kohlstedt, D. L. (2000). Influence of water on plastic deformation of olivine aggregates 2. Dislocation creep regime. *Journal of Geophysical Research: Solid Earth*, *105*(B9), 21471–21481. https://doi.org/10.1029/2000JB900180
Nisr, C., Ribárik, G., Ungár, T., Vaughan, G. B. M., Cordier, P., & Merkel, S. (2012). High resolution three-dimensional X-ray diffraction study of dislocations in grains of $MgGeO_3$ post-perovskite at 90 GPa. *Journal of Geophysical Research: Solid Earth*, *117*, B03201. https://doi.org/10.1029/2011JB008401
Nyilas, K., Couvy, H., Cordier, P., & Ungár, T. (2006). The dislocation structure and crystallite-size in forsterite (olivine) deformed at 1400°C by 11 GPa. *Zeitschrift für Kristallographie Supplements*, *2006*(Suppl_23_2006), 135–140.
Paterson, M. S. (1987). Problems in the extrapolation of laboratory rheological data. *Tectonophysics*, *133*(1–2), 33–43.
Ram, F., Wright, S., Singh, S., & De Graef, M. (2017). Error analysis of the crystal orientations obtained by the dictionary approach to EBSD indexing. *Ultramicroscopy*, *181*, 17–26.
Rauch, E. F., & Dupuy, L. (2005). Rapid spot diffraction patterns identification through template matching. *Archives of Metallurgy and Materials*, *50*, 87–99.
Rauch, E. F., & Véron, M. (2014). Automated crystal orientation and phase mapping in TEM. *Materials Characterization*, *98*, 1–9.
Schayes, C., Bouquerel, J., Vogt, J. B., Palleschi, F., & Zaefferer, S. (2016). A comparison of EBSD based strain indicators for the study of Fe-3Si steel subjected to cyclic loading. *Materials Characterization*, *115*, 61–70.
Singh, S., & De Graef, M. (2016). Orientation sampling for dictionary-based diffraction pattern indexing methods. *Modelling and Simulation in Materials Science and Engineering*, *159*, 81–94.
Singh, S., & De Graef, M. (2017). Dictionary indexing of electron channeling patterns. *Microscopy and Microanalysis*, *23*(1), 1–10. https://doi.org/10.1017/S1431927616012769
Suzuki, S. (2013). Features of transmission EBSD and its application. *JOM*, *65*(9), 1254–1263. https://doi.org/10.1007/s11837-013-0700-6
Tange, Y., Kuwayama, Y., Irifune, T., Funakoshi, K.-I., & Ohishi, Y. (2012). V-T equation of state of $MgSiO_3$ perovskite based on the MgO pressure scale: A comprehensive reference for mineralogy of the lower mantle. *Journal of Geophysical Research: Solid Earth*, *117*, B06201. https://doi.org/10.1029/2011JB008988
Trimby, P. W. (2012). Orientation mapping of nanostructured materials using transmission Kikuchi diffraction in the scanning electron microscope. *Ultramicroscopy*, *120*, 16–24.
Tschauner, O., Ma, C., Beckett, J. R., Prescher, C., Prakapenka, V. B., & Rossman, G. R. (2014). Discovery of bridgmanite, the most abundant mineral in Earth, in a shocked meteorite. *Science*, *346*(6213), 1100–1102.
Tsujino, N., Nishihara, Y., Yamazaki, D., Seto, Y., Higo, Y., & Takahashi, E. (2016). Mantle dynamics inferred from the crystallographic preferred orientation of bridgmanite. *Nature*, *539*(7627), 81–85.
Wang, Y., Guyot, F., & Liebermann, R. C. (1992). Electron microscopy of (Mg, Fe)SiO3 Perovskite: Evidence for structural phase transitions and implications for the lower mantle. *Journal of Geophysical Research: Solid Earth*, *97*(B9), 12327–12347. https://doi.org/10.1029/92JB00870
Wenk, H.-R., Armann, M., Burlini, L., Kunze, K., & Bortolotti, M. (2009). Large strain shearing of halite: Experimental and theoretical evidence for dynamic texture changes. *Earth and Planetary Science Letters*, *280*(1–4), 205–210. https://doi.org/10.1016/j.epsl.2009.01.0
Wright, S. I., Nowell, M. M., & Field, D. P. (2011). A review of strain analysis using electron backscatter diffraction. *Microscopy and Microanalysis*, *17*(3), 316–329.
Zhong, Y., Yin, F., Sakaguchi, T., Nagai, K., & Yang, K. (2007). Dislocation structure evolution and characterization in the compression deformed Mn–Cu alloy. *Acta Materialia*, *55*(8), 2747–2756.

Deuxième partie
Projets de recherche

Introduction :

Il faut admettre qu'actuellement les études expérimentales quantitatives en MET des mécanismes fondamentaux de la plasticité ne sont pas encore maitrisées. Pour l'instant, les études restent qualitatives. Généralement, les vecteurs de Burgers sont caractérisés et parfois leurs natures (vis, coin, mixtes). Suivant la qualité des analyses, quelques mécanismes peuvent être révélés, comme la montée, le glissement dévié, les interactions entre dislocations, mais ils proviennent, la plupart du temps, d'études poussées de moins d'une dizaine de dislocations. Dans ces conditions, il est impossible d'obtenir une statistique suffisante pour être capable d'affecter une pondération rigoureuse sur les différents mécanismes rencontrés.

Pour augmenter la statistique, il faudrait mettre de côté l'échelle microscopique (analyses fortement locales où le risque de passer à côté de l'information clef reste élevé) et se diriger vers l'échelle mésoscopique, c'est-à-dire celle du MEB. C'est suite à cette idée que l'imagerie par contraste de canalisation d'électrons (ECCI) a vu le jour (Gutierrez-Urrutia *et al.* (2009), Zaefferer & Elhami (2014), Yamasaki *et al.* (2015), Schayes *et al.* (2016), Kriaa *et al.* (2017)). Cet outil permet de caractériser des populations de dislocations à l'échelle du MEB. Nous sommes donc en droit de nous demander si la MEB n'est pas le meilleur outil pour caractériser les mécanismes fondamentaux de déformation plastique d'un point de vue quantitatif. Cette technique est prometteuse mais, en ce qui concerne les premières analyses ECCI de minéraux (Miyajima *et al.* (2018) pour l'olivine, Rogowitz *et al.* (2018) pour la pyrite FeS_2 et Miyajima *et al.* (2019) pour le grenat), les contrastes sont encore à ce jour de qualité insuffisante. Par ailleurs, les faibles tensions appliquées au MEB ont tendance à accentuer l'endommagement des minéraux par irradiation électroniques. L'ECCI, comme la MET, nécessite des conditions précises d'orientations pour mettre les dislocations en contraste ; les analyses se font donc grain par grain. La valeur ajoutée de cette technique se conçoit bien pour les monocristaux de dimensions millimétriques ou centimétriques, où l'analyse des dislocations se fait effectivement à l'échelle mésocopique, voire macroscopique. Mais les analyses quantitatives ont pour principal intérêt de s'approcher au plus près des conditions réelles, or les minéraux se présentent rarement sous formes monocristallines. Pour résumer, les analyses des dislocations au MET sont qualitatives et difficilement quantitatives alors que les analyses au MEB sont quantitatives, suivant certaines conditions (grains de tailles supérieures à 100 μm), et moins qualitatives qu'au MET.

Actuellement, nous sommes en passe de réaliser de la MET quantitative. Grâce à la TETD nous sommes parvenus, pour la première fois, à effectuer plus de 1000 indexations de plans qui contiennent des segments de dislocations, ce qui nous a permis d'attribuer un pourcentage d'occurrence pour différents mécanismes fondamentaux de déformation plastique (montée et glissement) dans l'olivine déformée à 1090°C (Mussi *et al.*, 2017). Bien évidemment, cette méthodologie pourrait être utilisée pour d'autres minéraux que l'olivine. Cependant, de nombreux minéraux de la croute, du manteau supérieur et inférieur (quartz, coesite, stishovite, DHMS, wadsleyite, ringwoodite, akimotoite, bridgmanite, etc.) sont sensibles aux irradiations électroniques. Il faudrait mettre au point une technique capable de conserver les structures cristallines des minéraux en cours d'acquisition tomographique ou bien parvenir à faire de la tomographie à faible nombre de projections (< 10), ou mieux encore, combiner ces deux approches. Il est impensable actuellement d'imaginer faire de l'ECCI sur de la bridgmanite. Sur ce sujet, la MET conserve une longueur d'avance manifeste sur la MEB. C'est pourquoi, je souhaite développer la TETD des minéraux sensibles aux faisceaux d'électrons.

Même si mes domaines d'études restent éloignés des simulations numériques de la déformation plastique, des collaborations pourraient être constructives pour compléter et parfaire les analyses quantitatives de la plasticité. L'association de la TETD avec la dynamique des dislocations (DD) me semble très prometteuse. Ce lien permettrait de redonner du mouvement aux dislocations dans des conditions rigoureuses puisqu'à partir de microstructures de dislocations tridimensionnelles initiales réelles. Des mécanismes fondamentaux de déformation plastique (connus ou inconnus) pourraient être révélés par cette nouvelle approche. Ces futurs travaux pourraient être enrichis et validés par des études atomistiques de dynamique moléculaire. Cette démarche scientifique pourrait être appliquée, au préalable, aux conditions de pressions, de températures et de vitesses de déformation accessibles au laboratoire, pour ensuite entreprendre des comparaisons modélisations / expériences (essais mécaniques). En second lieu, après validation, nous pourrions poursuivre cette méthodologie dans les conditions du manteau terrestre. Cette nouvelle approche me semble très encourageante, c'est pourquoi j'aimerais m'engager dans des collaborations avec des experts en simulations numériques de la déformation plastique, sur cette thématique.

En parallèle à mes travaux de recherches sur les DHMS et les mécanismes de plasticité de l'olivine, je souhaite développer, au travers de plusieurs collaborations, trois axes de recherche importants à mes yeux :

- l'étude quantitative de la plasticité par l'analyse poussée de cartographies d'orientations au MET ;
- la TETD pour les minéraux sensibles au faisceau d'électrons ;
- l'édification de ponts entre la DD et les caractérisations MET.

L'amélioration des résolutions spatiale et angulaire des cartographies d'orientations au MET, permettrait d'accéder à des informations mésoscopiques sur la plasticité, au travers des désorientations générées par les sollicitations collectives des dislocations, mais également à des informations microscopiques, par le biais des champs de déformation individuels des dislocations et des disclinaisons. Cette transition d'échelle donnerait la possibilité de révéler les GND, les SSD et les disclinaisons, mais aussi de distinguer leurs contributions respectives dans le processus de déformation.

Les DHMS (phase A, superhydrous B, phase D, phase H, etc.) et les phases profondes du manteau (ringwoodite, stishovite, bridgmanite, etc.) sont généralement peu stables sous le faisceau d'électrons. Les caractérisations MET de leurs microstructures de dislocations sont difficiles voire impossibles, ce qui exclue les étapes de validation par comparaisons modélisations/expériences. La TETD à faible nombre d'images projetées pourrait lever ce verrou scientifique.

Depuis le début des années 90 (Canova & Kubin, 1991), les modélisations numériques par DD sont en perpétuelle amélioration. La description discrète des dislocations a évolué d'une représentation purement vis/coin (Devincre 1993) à une représentation vis/mixte/coin (Madec *et al.*, 2001), puis nodale (Weygand *et al.*, 2002). Parallèlement à ces développements, les modèles DD se sont raffinés par la prise en compte de la montée, du glissement dévié, parmi d'autres mécanismes … Mais pourtant, les microstructures des dislocations initiales de DD sont souvent construites aléatoirement, loin des conditions réelles. L'incorporation des microstructures de dislocations 3D obtenues par TETD dans les codes DD permettrait de modéliser au mieux les déformations plastiques des minéraux à l'échelle mésoscopique.

Références :

Canova, G.R. & Kubin, L.P. (1991): Dislocation microstructures and plastic flow: a three dimensional simulation. In Maugin, G.A., Editor, Continuum models and discrete systems (Longman Scientific and technical), **2**, 93-101.

Devincre, B. (1993) : Simulations dynamiques des dislocations a une échelle mésoscopique : une étude de la déformation plastique. PhD thesis, Univ. Paris 11.

Devincre, B., Kubin, L.P., Lemarchand, C., Madec, R. (2001): Mesoscopic simulations of plastic deformation. *Mater. Sci. Eng., A*, **309-310**, 211-219.

Gutierrez-Urrutia, I., Zaefferer, S., Raabe D. (2009): Electron channeling contrast imaging of twins and dislocations in twinning-induced plasticity steels under controlled diffraction conditions in a scanning electron microscope. *Scripta Mater.*, **61**, 737-740.

Kriaa, H., Guitton, A., Maloufi, N. (2017): Fundamental and experimental aspects of diffraction for characterizing dislocations by electron channeling contrast imaging in scanning electron microscope. *Sci. Rep.*, **7**, 9742.

Miyajima, N., Li, Y., Abeykoon, S., Heidelbach, F. (2018): Electron channelling contrast imaging of individual dislocations in geological materials using a field emission scanning electron microscope equipped with an EBSD system. *Eur. J. Mineral.*, **30**, 5-15.

Miyajima, N., Mandolini, T., Heidelbach, F., Bollinger, C. (2019): Combining ECCI and FIB milling techniques to prepare site-specific TEM samples for crystal defect analysis of deformed minerals at high pressure. *C. R. Geosci.*, en ligne.

Mussi, A., Cordier, P., Demouchy, S., Hue, B. (2017): Hardening mechanisms in olivine single crystal deformed at 1090 °C: an electron tomography study, *Philos. Mag.*, **97**, 3172-3185.

Rogowitz, A., Zaefferer, S., Dubosq, R. (2018): Direct observation of dislocation nucleation in pyrite using combined electron channelling contrast imaging and electron backscatter diffraction. *Terra Nova*, **30**, 423-430.

Schayes, C., Vogt, J.B., Bouquerel, J., Palleschi, F., Zaefferer, S. (2016): Cyclic plasticity mechanism of the M330-35A steel. *Int. J. Fatigue*, **82**, 530–539.

Weygand, D., Friedman, L.H., Van der Giessen, E., Needleman, A. (2002): Aspects of boundary-value problem solutions with three-dimensional dislocation dynamics. *Modelling Simul. Mater. Sci. Eng.*, **10**, 437-468.

Yamasaki, S., Mitsuhara, M., Ikeda, K., Hata, S., Nakashima, H. (2015): 3D visualization of dislocation arrangement using scanning electron microscope serial sectioning method. *Scripta Mater.*, **101**, 80-83.

Zaefferer, S. & Elhami, N.N. (2014): Theory and application of electron channelling contrast imaging under controlled diffraction conditions. *Acta Mater.*, **75**, 20-50.

Chapitre I : Cartographies d'orientations ultimes au MET

Je souhaite m'engager dans l'amélioration des capacités qu'offrent l'ACOM-TEM pour l'étude quantitative de la plasticité dans les minéraux. Une meilleure résolution spatiale et angulaire permettrait de distinguer les GND des SSD, mais également, de caractériser des disclinaisons. Ces objectifs semblent tout à fait accessibles puisqu'une première caractérisation ACOM-TEM, associée à une analyse de déformation élastique locale, à l'aide du logiciel Topspin (logiciel d'analyse des positions relatives des taches de diffraction, Darbal *et al.*, 2014), a permis de caractériser le champ de déformation élastique d'une dislocation individuelle dans le Mg (voir figure 20, tirée de l'article de Rottmann & Hemker (2018)).

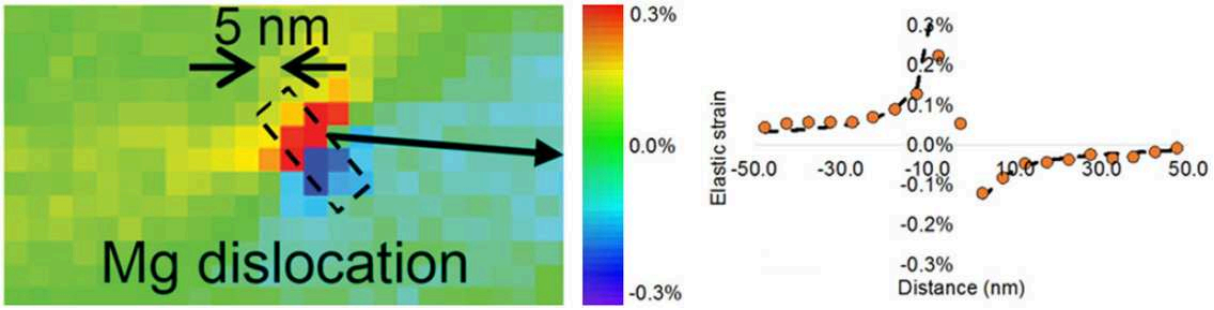

Figure 20 : *Champ de déformation élastique autour d'une dislocation dans un grain de Mg (à gauche) ; profil de déformation élastique à travers la dislocation (à droite) ; tirée de l'article de Rottmann et Hemker (2018).*

II-1-1 Amélioration de la résolution angulaire

L'amélioration de la résolution angulaire en ACOM-TEM pourrait être envisagée de la manière suivante : Après avoir effectué une première cartographie d'orientation du grain à analyser (cartographie précise à ±0.5 °), la gamme d'orientation de la zone pourrait être délimitée à l'orientation moyenne du grain considéré à ±15 ° (par exemple). Pour limiter la taille des données, une banque de clichés de diffraction simulés pourrait être recréée mais, cette fois-ci, tous les 0.05 °, dans cette gamme angulaire restreinte. Pour l'étape d'acquisition des clichés de diffraction, il faudrait augmenter la résolution numérique de la caméra. L'optimisation du positionnement automatique des taches de diffraction est assurément plus fine lorsque ces taches sont acquises avec un nombre conséquent de pixels. Par ailleurs, la qualité des cartographies pourrait être améliorée en augmentant la dynamique de la caméra. En effet, des traitements d'images pour faire ressortir les taches de diffraction aux indices de Miller élevés, et des traitements de débruitage, sont réalisables avec une caméra 16bit ($6{,}5.10^4$ niveaux de gris) et, mieux encore, avec une caméra 32bit ($4{,}3.10^9$ niveaux de gris). L'amélioration de la qualité des clichés et l'augmentation du nombre de taches de diffraction à comparer avec les clichés simulés, permettraient d'affiner la résolution angulaire des cartographies d'orientation. Bien sûr, dans ces conditions, la taille des données et les temps de calcul augmentent considérablement. Inévitablement, la taille des zones à analyser doit être réduite en conséquence.

II-1-2 Amélioration de la résolution spatiale

En collaboration avec Ahmed Addad du Centre Commun de Microscopie (CCM) de Lille, nous souhaitons faire l'acquisition de cubes de données (ou data cube en anglais) de clichés de diffraction quasi ponctuels avec une taille de faisceau sub-nanométrique. Le MET FEI® Titan Themis, inauguré à Lille le 9 novembre 2017, nous permet d'atteindre ces

conditions ultimes. Des clichés de diffractions ont pu être acquis avec une taille de sonde de seulement 5 Å associé à un angle de convergence d'à peine 0.83 mrad (nous conserver l'aspect ponctuel des clichés de diffraction dans ces conditions d'illumination). L'intensité exacerbée du filament X-FEG permet également de conserver un rapport signal sur bruit élevé.

Je suis intimement persuadé que l'obtention de cartographies d'orientation avec une résolution spatiale de 0.5 nm et une résolution angulaire de 0.05 °, et l'utilisation du logiciel Topspin, permettraient de quantifier et distinguer les GND des SSD, mais également de révéler la présence de disclinaisons.

Références :

Darbal, A.D., Narayan, R.D., Vartuli, C., Aoki, T., Mardinly, J., Nicolopoulos, S., Weiss, J.K. (2014): Applications of Automated High Resolution Strain Mapping in TEM on the Study of Strain Distribution in MOSFETs. *Microsc. Microanal.*, **20**, 1066-1067.

Rottmann P.F. & Hemker, K.J. (2018): Nanoscale elastic strain mapping of polycrystalline materials. *Mater. Res. Lett.*, **6-4**, 249-254.

Chapitre II : Tomographie électronique des dislocations des minéraux sensibles aux électrons

Bien plus que la troisième dimension, la TETD ajoute une dimension statistique à la MET. Avec jusqu'à 1000 indexations par échantillons, la statistique commence enfin à prendre du sens en MET. Démêler les microstructures les plus complexes devient possible et permet d'affecter un pourcentage de présence à chaque mécanisme mis en jeu (glissement, montée, glissement dévié, etc.). D'autre part, contrairement à l'EELS et au faisceau convergent, cette technique donne un accès direct aux épaisseurs de lames minces. Les densités de dislocations peuvent également être obtenues au plus près des densités réelles. Par ces différents aspects, la TETD permet d'accéder à une première approche MET quantitative de la plasticité. Mais ces bénéfices sont-ils adaptables aux minéraux sensibles aux irradiations électroniques ?

II-2-1 Optimisation de l'acquisition des séries tiltées

La TETD, grâce à la troisième dimension, maximise l'accès aux informations, c'est là son intérêt majeur. Les zones d'intérêt sont donc moins longtemps bombardées par le faisceau d'électrons. L'acquisition récente du PO HATA (Hata *et al.*, 2011) permet d'optimiser les étapes de positionnements des échantillons (rapides et précis) pour entreprendre de la TETD dans les meilleures conditions, et amoindrit ainsi le temps de maintien sous le faisceau. Le MET de dernière génération, FEI® Titan Themis, nouvellement acquis, est doté d'un module « low dose » et la présence d'un monochromateur (jamais totalement éteint) permet également de contrôler la dose. Par ailleurs, ce microscope possède une source cohérente et très intense (filament X-FEG). Les micrographies de dislocations peuvent donc être obtenues en mode STEM micro-sonde pour s'assurer d'avoir un contraste homogène et une dose moins forte qu'en WBDF, tout en conservant un bon rapport signal sur bruit. Nous allons voir par la suite que l'utilisation de séries tiltées à faible nombre d'images projetées (une dizaine) peut suffire pour obtenir des volumes reconstruits de qualité. Bien sûr, une gamme angulaire conséquente doit être conservée et les micrographies parasitées par des contrastes impropres (diffraction multiple près d'axes de zones, par exemple) doivent être éliminées.

II-2-2 Tomographie à faible nombre d'images projetées

De nouveaux algorithmes de reconstruction tomographique, à faible nombre d'images projetées, ont récemment vu le jour. A titre d'exemple, la technique de reconstruction algébrique discrète (DART) utilise l'algorithme ART où le volume reconstruit est binarisé à chaque itération (Batenburg & Sijbers, 2007). L'utilisation de cette technique pour la TETD est pertinente puisque les micrographies de dislocations sont par essence segmentables (dislocations blanches sur fond noir).

La collaboration de Laurent Dupuy et Fabien Onimus (CEA Saclay), avec Karine Gouriet et Patrick Cordier (équipe Plasticité du laboratoire UMET), soutenu par le post doctorat de Van-Tuan Dang commun au CEA et à l'UMET (depuis début février 2019), a, parmi ses objectifs, de mettre au point un algorithme d'optimisation des reconstructions 3D des dislocations. Cette méthode, décrite en détail dans la section II-3-1, a donné des premiers résultats prometteurs et permettrait de limiter le nombre de clichés des séries tiltées en gardant une qualité élevée des volumes reconstruits.

II-2-3 ASTAR associé à la TETD

Les atouts d'ASTAR ne se cantonnent pas à l'accès aux cartographies d'orientations, cet outil a également l'avantage de donner la possibilité d'imager les dislocations (Kiss *et al.*, 2016 et Nzogang *et al.* 2019).

Les champs sombres virtuels (VDF pour Virtual Dark Field) qui découlent des cartographies d'orientations, ressemblent trait pour trait aux clichés WBDF (Nzogang *et al.*, 2019). Or le mode d'obtention des VDF produit des conditions d'illumination à très faible dose. En effet, pour obtenir des clichés de diffraction quasi ponctuels, le plus petit diaphragme condenseur doit être utilisé ; pour garder une résolution spatiale suffisante pour imager les dislocations, il faut prendre la plus petite taille de spot (1 nm en l'occurrence) ; et enfin, pour ne pas saturer le contraste des clichés de diffraction, des temps de quelques dizaines de ms seulement sont nécessaires pour l'acquisition de chaque points d'analyse. Même si l'acquisition des cartographies peut durer plus de dix heures, la dose électronique envoyée sur chaque point d'analyse est très faible. Nous avons mesuré une dose de $3{,}5.10^{5}$ electron.nm^{-2}.s^{-1} par pixel (Nzogang *et al.*, 2019) alors qu'une dose minimale de $1{,}2.10^{8}$ electron.nm^{-2}.s^{-1} avait été mesurée pour les analyses des phases hydratées en WBDF. L'échantillon est donc approximativement 300 fois moins maltraité par cartographie ASTAR que par la technique conventionnelle WBDF.

L'association de l'imagerie des dislocations par ASTAR avec la TETD à faible nombre de clichés, permettrait de caractériser les mécanismes de déformation plastique de matériaux hautement sensibles aux électrons. D'un point de vue pratique, l'acquisition d'un cliché de diffraction en précession permettrait d'identifier les vecteurs diffractant les plus à même de mettre en contraste les dislocations du matériau (FS élevés et produits $\boldsymbol{g}.\boldsymbol{b}$ non nuls). Ensuite, grâce au PO HATA, le vecteur diffractant sélectionné serait orienté parfaitement suivant l'axe principal du PO. Enfin, entre 5 et 10 cartographies de dislocations pourraient être enregistrées pour entreprendre ensuite la reconstruction 3D. Une dernière cartographie proche d'un axe de zone à faibles indices de Miller permettrait enfin de caractériser les vecteurs de Burgers des dislocations reconstruites en 3D (Nzogang *et al.*, 2019).

Pour illustrer le potentiel de cette approche, nous pouvons évoquer le cas de la phase H ($MgSiO_4H_2$). Cette DHMS, fortement hydratée est susceptible d'être présente dans le manteau inférieur jusqu'à la frontière manteau/noyau lorsqu'elle est en solution solide avec la phase δ-AlO(OH) (Nishi *et al.*, 2014). Pour l'instant, aucune étude n'a été conduite sur la rhéologie de cette phase. A cet effet, une collaboration pourrait être envisagée, avec nos collègues expérimentateurs en hautes pression, pour élaborer et déformer un polycristal de phase H. Au cours de nos différentes analyses MET, nous nous sommes rendus compte que la phase A était bien plus sensible aux électrons que la superhydrous B. Nous avons déduit de cette observation que la proportion d'hydrogène présente dans les DHMS pourrait être liée à leur sensibilité aux électrons (respectivement 21 %at et 11 %at pour la phase A et la superhydrousB). La phase H, avec 25 %at d'hydrogène dans sa structure, devrait probablement être encore plus sensible aux électrons que la phase A. L'étude des microstructures de dislocations de la phase H pourrait donc être menée en associant ASTAR à la TETD. Grâce à la visualisation 3D, il ne serait plus nécessaire de multiplier les micrographies WBDF pour déterminer les systèmes de glissement de cette phase.

Bien évidemment la TETD des minéraux sensibles ne se destine pas uniquement aux DHMS. Nous pourrions également utiliser cette technique pour étudier les microstructures 3D

de dislocations du quartz, de l'akimotoite et de la phase la plus abondante de la Terre : la bridgmanite qui contrôle la rhéologie du manteau terrestre.

Références :

Batenburg, K.J. & Sijbers, J. (2007): Dart: A Fast Heuristic Algebraic Reconstruction Algorithm for Discrete Tomography. *IEEE Int. Conf. Image Processing*, **4**, 133-136.

Hata, S., Miyazaki, H., Miyazaki, S., Mitsuhara, M., Tanaka, M., Kaneko, K., Higashida, K., Ikeda, K., Nakashima, H., Matsumara, S., Barnard, J.S., Sharp, J.H., Midgley, P.A. (2011): High-angle triple-axis specimen holder for three-dimensional diffraction contrast imaging in transmission electron microscopy. *Ultramicroscopy*, **111**, 1168-1175.

Kiss, A.K., Rauch, E.F., Lábár, J.L. (2016): Highlighting material structure with transmission electron diffraction correlation coefficient maps. *Ultramicroscopy*, **163**, 31-37.

Nishi, M., Irifune, T., Tsuchiya, J., Tange, Y., Nishihara, Y., Fujino, K., Higo, Y. (2014): Stability of hydrous silicate at high pressures and water transport to the deep lower mantle. *Nat. Geosci.*, **7**, 224-227.

Nzogang, B.C., Mussi, A., Cordier, P. (2019): Application of Scanning Electron Diffraction in the Transmission Electron Microscope for the characterization of dislocations in minerals, *Mineral. Mag.*, **83**, 71-79.

Chapitre III : Etudes quantitatives par l'association de la DD aux données expérimentales

Le principe de la DD consiste à utiliser des segments rectilignes pour reconstruire des lignes de dislocation dans un milieu élastique, où l'espace, le temps et le caractère des lignes sont discrétisés. Les positions de chacun de ces segments (connectés entre eux) sont liées au réseau cristallin. Les propriétés élastiques des dislocations sont prises en compte au travers des propriétés de tension de ligne et d'interactions (jonctions, annihilation colinéaire, etc.) ; et leurs mobilités sont liées au choix du pas de temps. Le calcul de la force effective (force appliquée associée à la force exercée par l'ensemble des dislocations) et le calcul du déplacement élémentaire, sont effectués pour chaque segment et chaque pas de temps.

Depuis 2007, Laurent Dupuy et Marc Fivel ont créé le logiciel de DD nodal *Numerical Modeling of Dislocation* (NuMoDis). Ce logiciel, en perpétuelle évolution (Bako *et al.*, 2011; Drouet *et al.*, 2014), permet de modéliser le mouvement de dislocations parfaites et partielles ainsi que leurs multiples interactions.

II-3-1 Association de la DD avec la TETD

Nous envisageons d'incorporer des microstructures de dislocation 3D obtenues par TETD directement au sein du logiciel NuMoDis pour être au plus près des conditions réelles de déformation et d'ajouter la dimension temporelle à la 3D. L'étape de finalisation de la TETD (la plus chronophage) consiste à retracer les dislocations en 3D, à l'aide du logiciel Chimera (Pettersen *et al.*, 2004), pour leur restituer leur forme cylindrique et se rapprocher le plus possible des microstructures réelles de dislocations (voir section I-2-1-b). D'un point de vue pratique, les dislocations sont redessinées dans le volume reconstruit, comme des colliers de perles, en positionnant et en associant des marqueurs sur les zones les plus contrastées (vers les cœurs de dislocations). Cette étape permet d'affecter à chaque dislocation des positions et des liens de marqueurs qui pourront être introduits en tant que nœuds dans le logiciel NuMoDis. Nous avons débuté une collaboration sur l'optimisation des reconstructions 3D des dislocations avec Laurent Dupuy et Fabien Onimus, au service de recherches métallurgiques appliquées du CEA à Saclay, et avec Karine Gouriet et Patrick Cordier, de l'équipe Plasticité au laboratoire UMET à Lille. Le principe consiste à retracer les dislocations par le suivi des dislocations (ou tracking en anglais), pour chaque image projetée (voir le principe sur la figure 21), et de reconstruire l'image en 3D par la méthode des moindres carrés. Pour maximiser la qualité du retraçage des dislocations pour chaque angle de projection θ_i (c'est-à-dire combler les zones mal contrastées), une reconstruction 3D est effectuée à chaque étape (à partir des images projetées et retracées, de 1 à i), puis reprojetée sur l'image qui correspond à l'angle de projection suivant (i+1). Les objets reconstruits auront l'avantage d'être directement incorporables dans NuMoDis. Ce travail est soutenu par Van-Tuan Dang, post-doctorant depuis le 14 février 2019 au CEA Saclay.

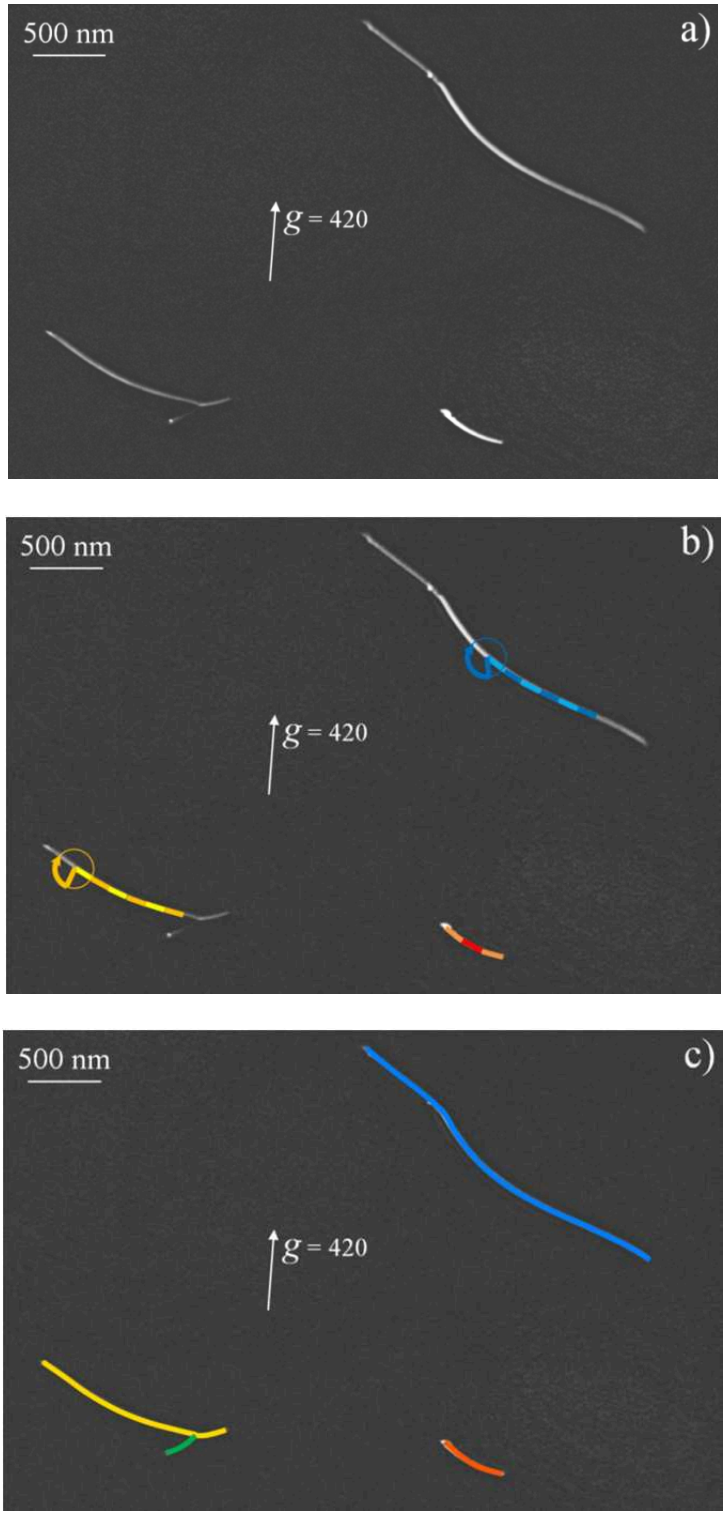

Figure 21 : *Suivi des dislocations dans le grenat (Koidu Pipe) : a) Micrographie WBDF obtenue avec le vecteur diffractant* 420 *associé à 0.1 ° de précession. b) Description d'un exemple de retraçage par suivi du contraste des dislocations : sur chaque dislocation, un segment, de longueur et de largeur prédéfinies, tourne sur lui-même pour déterminer l'orientation où le contraste est maximal (chaque dislocation a une couleur spécifique), le travail se poursuit pour un second segment sur chaque dislocation, et ainsi de suite … c) Finalisation du retraçage par suivi.*

A courts termes, nous devrions commencer par l'étude de configurations simples de microstructures 3D de dislocations dans l'olivine, obtenues par TETD. A titre d'exemple, nous pourrions débuter par l'étude de deux dislocations peu avant leurs interactions. La DD permettrait de « réanimer » ces dislocations et de les faire interagir. Ces mécanismes élémentaires vont nous permettre d'accéder à des mécanismes fondamentaux d'interactions de dislocation dans l'olivine. Même si, a priori, les interactions dans l'olivine sont connues (jonctions $\langle 101 \rangle$ et annihilations colinéaires, Durinck 2007 ; Mussi 2015b), en poursuivant nos études dans cette direction, il est fort probable que la DD mette à jour de nouvelles configurations d'interactions de dislocations.

Dans la lignée, nous allons étudier par DD, la mobilité d'un sous-joint de grain (SJG) dans l'olivine, tirée de la TETD. D'après le critère de Von-Mises, cinq systèmes de glissement indépendants sont nécessaires pour qu'un polycristal se déforme de manière homogène uniquement par glissement de dislocations. Ce critère peut se réduire à quatre systèmes indépendants dans le cas de déformations inhomogènes (Hutchinson, 1977). Bien que l'olivine polycristalline se déforme sans difficulté, l'absence de glissement suivant $[010]$ restreint le nombre de systèmes de glissement indépendants à trois ($[100](010)$, $[100](001)$ et $[001](010)$, ou encore $[100](010)$, $[001](100)$ et $[001](010)$). Pour expliquer ce paradoxe, un autre mécanisme doit nécessairement intervenir pour assurer la cohésion entre les grains au cours de la déformation plastique de l'olivine. D'après Cordier *et al.* (2014), il pourrait s'agir du mécanisme de mouvement des disclinaisons (DeWit, 1973). Les disclinaisons se concentrent sous forme de dipôles dans les joints de grains (JG) et SJG et participent à leurs mouvements au cours de la déformation plastique. C'est pour cette raison que nous désirons nous intéresser à la mobilité des JG et SJG. Nous avons tout à apprendre sur ce pan encore obscur de la physique des matériaux. Puisqu'il est possible, grâce à la TETD, de reconstruire les dislocations individuelles qui composent les SJG, nous allons associer la DD à la TETD pour analyser la mobilité de ce défaut plan.

Etudiés depuis pourtant plus de 50 ans (Raleigh 1968), les mécanismes de déformation plastique de l'olivine sont encore mal compris. Ce verrou scientifique s'explique par la grande complexité des mécanismes qui interviennent simultanément au cours de la déformation de l'olivine, comme :

- le glissement cristallographique $[100](001)$, $[001](100)$ et $[001]\{110\}$,
- le glissement non cristallographique $[001]\{hk0\}$ (Mahendran *et al.*, 2017),
- le glissement dévié (Poirier & Vergobbi, 1978 ; Li *et al.*, 2006 ; Mussi *et al.*, 2015a, 2017),
- la montée (Mussi *et al.*, 2015a-2017),
- les interactions par annihilations colinéaires (Durinck *et al.*, 2007 ; Mussi *et al.*, 2015b),
- les interactions par jonctions $\langle 101 \rangle$ (Durinck *et al.*, 2007 ; Mussi *et al.*, 2015b),
- le mouvement de disclinaisons (Cordier *et al.*, 2014), etc.

Par conséquent, dans les années à venir, des mécanismes plus complexes que le glissement simple, seront à ajouter à NuMoDis pour modéliser au mieux le comportement plastique de l'olivine. Une première étude de montée de dislocations a été entreprise avec NuMoDis mais uniquement sur l'aluminium (Bako *et al.*, 2011). La modélisation de la montée des dislocations dans des minéraux tels que l'olivine pose des problèmes complexes de charge. A titre d'exemple, Hirel et ses collaborateurs (2016) ont proposé, pour la bridgmanite $MgSiO_3$, le scénario de montée de dislocations suivant :

- Les dislocations absorbent des lacunes d'oxygène et forment autour d'elles des nuages ioniques de lacunes de charges négatives (atmosphères de Debye-Hückel).
- Les lacunes d'oxygène, présentes dans les cœurs de dislocations, vont ensuite diffuser lentement par le canal des dislocations (ou pipe-diffusion en anglais).
- Les cœurs de dislocations vont ensuite absorber les lacunes cationiques qui vont, comme précédemment, diffuser lentement par le canal des dislocations.
- Finalement, ces environnements appauvris en lacunes de charges positives et négatives, vont permettre à ces dislocations de cœurs neutres de monter (Hirel *et al.*, 2016).

Le mécanisme de montée de la bridgmanite est à rapprocher de celui de l'olivine. Il est bien plus compliqué que celui de l'aluminium et reste hypothétique. Je souhaite accompagner Karine Gouriet et Patrick Cordier (équipe Plasticité du laboratoire UMET), en collaboration avec Laurent Dupuy et Fabien Onimus (CEA Saclay), dans le développement de NuMoDis pour prendre en compte la montée dans l'olivine. Ce travail s'étendra certainement sur plusieurs années.

Le glissement dévié intervient également dans la déformation plastique de l'olivine (Poirier & Vergobbi, 1978 ; Li *et al.*, 2006 ; Mussi *et al.*, 2014, 2015a et 2017). Le CEA Saclay et le laboratoire CEMES de Toulouse se sont penchés pour l'instant sur le mécanisme de glissement dévié dans le Ti et le Zr par simulations *ab initio* et analyses MET *in situ* (Clouet *et al.*, 2015). Le glissement dévié est à l'origine d'une modification du cœur des dislocations du Ti et du Zr, modification déclenchée par la présence d'oxygène en éléments d'additions (Clouet *et al.*, 2015). L'initiation du glissement dévié est donc le principal obstacle pour entreprendre des modélisations par DD car les modifications chimiques locales sont difficiles à simuler. Une première étude du glissement dévié dans le fer-α pur, effectuée avec NuMoDis, vient d'être publiée (Li *et al.*, 2018). Dans cette étude prometteuse, les auteurs ont utilisé une « dislocation composite » constituée d'un segment glissile dans le plan de glissement primaire et d'un segment glissile dans le plan de glissement dévié, pour dépasser le problème d'initiation du glissement dévié. Mon ambition, dans un deuxième temps, serait de me joindre à Karine Gouriet, Patrick Cordier, Laurent Dupuy et Fabien Onimus dans le développement de NuMoDis pour prendre en compte le glissement dévié dans l'olivine. Comme pour l'étude de la montée par DD, il faudra bien prendre en compte que les éléments d'addition sont des défauts ponctuels chargés. Ce travail est également soutenu actuellement par le post-doctorat de Van-Tuan Dang et demandera dans l'avenir des moyens d'accompagnement.

Bien évidemment, cette démarche scientifique ne se destine pas uniquement à l'étude de la déformation plastique de l'olivine. D'autres minéraux, dont les mécanismes de déformation plastique restent abscons, sont en ligne de mire. Le grenat fait partie de ces candidats.

II-3-2 Association de la DD à l'ACOM-TEM

Comme pour la TETD, nous pouvons faire un lien entre la DD et l'ACOM-TEM. Etant donnée la constante progression des puissances de calcul, il est tout à fait envisageable d'atteindre, dans un avenir proche, des taux de déformation plastique de plusieurs dizaines de % en DD. Ces taux de déformation permettraient d'extraire des cartographies de désorientation théoriques (GOS, GROD et KAM) à partir de simulations de DD. Les allures de ces cartographies simulées pourraient être liées aux modèles utilisés (glissement, montée, glissement dévié, entres autres …, et toutes combinaisons avec différentes pondérations). Les

comparaisons des cartographies expérimentales et simulées permettraient de quantifier le poids des différents mécanismes mis en jeu au cours de la déformation plastique.

Références :

Bakó, B., Clouet, E., Dupuy, L.M., Blétry, M. (2011): Dislocation dynamics simulations with climb: kinetics of dislocation loop coarsening controlled by bulk diffusion. *Philos. Mag.*, **91**, 3173-3191.

Clouet, E., Caillard, D., Chaari, N., Onimus, F., Rodney D. (2015): Dislocation locking versus easy glide in titanium and zirconium. *Nature Mater.*, **14**, 931-936.

Cordier, P., Demouchy, S., Beausir, B., Taupin, V., Barou, F., Fressengeas, C. (2014): Disclinations provide the missing mechanism for deforming olivine-rich rocks in the mantle. *Nature*, **507**, 51-56.

DeWit, R. (1973) : Theory of Disclinations: IV. Straight Disclinations. *J. Res. Natl. Bur. Stand. Sect. A*, **77A**, 607-658.

Drouet, J., Dupuy, L., Onimus, F., Mompiou, F., Perusin, S., Ambard, A. (2014): Dislocation dynamics simulations of interactions between gliding dislocations and radiation induced prismatic loops in zirconium. *J. Nucl. Mater.*, **449**, 252-262.

Durinck, J., Devincre, B., Kubin, L., Cordier, P. (2007): Modeling the plastic deformation of olivine by dislocation dynamics simulations. *Am. Mineral.*, **92**, 1346-1357.

Hirel, P., Carrez, P., Clouet, E., Cordier, P. (2016): The electric charge and climb of edge dislocations in perovskite oxides: The case of high-pressure MgSiO3 bridgmanite. *Acta Mater.*, **106**, 313-321.

Hutchinson, J.W., (1977): Creep and as related plasticity to single of hexagonal crystal slip polycrystals. *Met. Trans. A.*, **8A**, 1465-1469.

Li, L., Weidner, D., Raterron, P., Chen, J., Vaughan, M., Mei, S., Durham, B. (2006): Deformation of olivine at mantle pressure using the D-DIA. *Eur. J. Mineral.*, **18**, 7-19.

Li, Y., Robertson, C., Shukeir M., Dupuy, L. (2018): Screw dislocation interaction with irradiation defect-loops in α-iron: evaluation of cross-slip effect using dislocation dynamics simulations. *Model. Simul. Mater. Sci. Eng.*, **26**, 055009.

Mahendran, S., Carrez, P., Groh, S., Cordier, P. (2017): Dislocation modelling in Mg2SiO4 forsterite: an atomic-scale study based on the THB1 potential. *Model. Simul. Mater. Sci. Eng.*, **25**, 054002.

Mussi, A., Cordier, P., Demouchy, S. (2015a): Characterization of dislocation interactions in olivine using electron tomography, *Philos. Mag.*, **95**, 335-345.

Mussi, A., Cordier, P., Demouchy, S., Hue, B. (2017): Hardening mechanisms in olivine single crystal deformed at 1090 °C: an electron tomography study. *Philos. Mag.*, **97**, 3172-3185.

Mussi, A., Cordier, P., Demouchy, S., Vanmansart C. (2014): Characterization of the glide planes of the [001] screw dislocations in olivine using electron tomography. *Phys. Chem. Miner.*, **41**, 537-545.

Mussi, A., Nafi, M., Demouchy, S., Cordier, P. (2015b): On the deformation mechanism of olivine single crystals at lithospheric temperatures: an electron tomography study. *Eur. J. Mineral.*, **27**, 707-715.

Pettersen, E.F., Goddard, T.D., Huang, C.C., Couch, G.S., Greenblatt, D.M., Meng, E.C., Ferrin, T.E. (2004): UCSF Chimera: A visualization system for exploratory research and analysis. *J. Comput. Chem.*, **25**, 1605–1612.

Poirier, J.P. & Vergobbi, B. (1978): Splitting of dislocations in olivine, cross-slip-controlled creep and mantle rheology. *Phys. Earth Planet. Inter.*, **16**, 370-378.
Raleigh, C.B. (1968): Mechanisms of plastic deformation of olivine. *J. Geophys. Res.*, **73**, 5391-5406.

Troisième partie
Informations personnelles

I Curriculum Vitæ

MUSSI Alexandre
Né le 28 Octobre 1977
Adresse : 9 Rue François Villon - 59160 Lomme (France)
Tel: +333 20 40 66 39
Professional tel: +333 20 43 49 60
E-mail: alexandre.mussi@univ-lille.fr

Formation et diplômes

- Thèse de Doctorat en Science et Génie des Matériaux – 2003 – Université de Grenoble
- DEA en Science et Génie des Matériaux (Ingénieur E.N.S.E.E.G.) – 2000 – Université de Grenoble

Profession actuelle

- Maître de Conférences au département Mesures Physiques à l'IUT a de Lille 1 – Depuis Septembre 2007

Expérience Académique

- Post-doctorat à l'Université de Poitiers (Institut P') au département de Physiques et Propriétés des Nanostructures (dans l'équipe filmes oxydes fonctionnels sous la direction de R. J. Gaboriaud) – 2007
- Post-doctorat à l'Université de Poitiers (Institut P') au département de Physiques et Mécanique des Matériaux (dans l'équipe Physique de la Plasticité et des défauts sous la direction de J. Rabier) – 2005-2006
- Demi-ATER à l'Université de Grenoble au laboratoire Science et Ingénierie des Matériaux et Procédés (dans l'équipe de Physique des Métaux sous la direction de P. Donnadieu) – 2004

Membre de Société Professionnelle

- Société Française de Minéralogie et de Cristallographie (Membre du conseil scientifique)

Activité de Recherche

Microscopie électronique en transmission (MET)
Spécialisé en caractérisation de défauts cristallins créés par déformation plastique (dislocations) en utilisant :

- Le contraste de diffraction en MET conventionnelle,
- L'optimisation de la caractérisation des dislocations en utilisant la diffraction électronique en précession (DEP),
- L'imagerie en faisceau-faible champ-sombre (WBDF),
- La caractérisation des dislocations par diffraction électronique par faisceau convergent à grand angle (LACBED),
- La tomographie électronique des dislocations en mode STEM (scanning transmission electron microscopy),
- La tomographie électronique des dislocations en mode WBDF, associé à la précession électronique.
- La cartographie d'orientation cristalline automatique (ACOM–TEM) pour étudier la plasticité à l'échelle mésoscopique.

Déformation plastique des minéraux du manteau et des zones de subduction
Etude des minéraux déformés sous pression atmosphérique et sous haute pression, en analysant :

- Les microstructures de dislocations,
- Les interactions de dislocations,
- Les mécanismes de déformation plastique.

Production Scientifique

- Articles dans des revues internationales à comité de lecture : 27
  - 14 en premier auteur
  - 3 en deuxième auteur dont 1 derrière un étudiant en thèse co-encadrée
- Chapitre d'ouvrage : 1
- Actes publiés dans des conférences internationales : 5
- Actes publiés dans des conférences nationales : 1
- Présentation orale invitée dans une conférence internationale : 1
- Séminaire invité national : 2 (2 en tant qu'orateur)
- Conférence internationale, présentation orale avec acte : 3 (1 en tant qu'orateur)
- Conférence internationale, présentation orale sans acte : 16 (6 en tant qu'orateur)
- Conférence internationale, poster sans acte : 10 (3 en tant qu'orateur)
- Conférence nationale, présentation orale sans acte : 8 (6 en tant qu'orateur)
- Conférence nationale, poster sans acte : 11 (8 en tant qu'orateur)

La liste des publications et des conférences (en incluant les présentations orales invitées) est donnée ci-dessous.

Encadrement

- Stage IUT : 1 (Simon Thilliez 2017)
- Stage ingénieurs : 2 (Loïc Habran 2017 + Raiquen Alvarez 2015)
- Stage de M2 : 1 (Maula Nafi 2014 + Julien Gallet 2019)
- Thèse (co-encadrement 50%) : 1 (Billy Clitton Nzogang 2015-2018)

Service pour la communauté :

Enseignement

- Responsable des enseignements de Matériaux pour les premières années au département Mesures Physiques (2009-2018)

Administration

- Responsable des stages et des relations département Mesures Physiques -Industries – Depuis Septembre 2015
- Comité d'achat d'un MET de dernière génération (2009-2014): TITAN Themis (installé en Février 2016)

Organisation de conférences

- "Colloque Plasticité 2011" - Villeneuve d'Ascq 2011 – Membre du comité d'organisation
- "Colloque Plasticité 2019" - Villeneuve d'Ascq 2019 – Membre du comité d'organisation

Organisation d'écoles

- "Ecole de tomographie Gatan" - Villeneuve d'Ascq 2009 – Membre du comité d'organisation

Enseignant dans des écoles internationales

- "MinTEM 2014" - Villeneuve d'Ascq 2014
- "MinTEM 2012" - Villeneuve d'Ascq 2012

• "MinTEM 2011" - Villeneuve d'Ascq 2011

Referee d'articles

• *European Journal of Mineralogy*
• *Philosophical Magazine*

Comités de sélections

Local : Membre de 3 comités de sélection pour des postes de Maître de Conférences à l'Université de Lille:

- 2017 (laboratoire UMET rattaché à l'UFR de physique de l'Université de Lille);
- 2017 (laboratoire UMET rattaché au département Mesures Physiques l'IUT A de Lille);
- Vice-president 2016 (laboratoire UMET rattaché à l'UFR de physique de l'Université de Lille).

National : Membre de 4 comités de sélection pour des postes de Maître de Conférences:

- École des Mines de Nancy 2015;
- IUT de Maubeuge 2014;
- IUT de Strasbourg 2013;
- Université de Poitiers 2012.

Investissements

• Projets d'investissements à l'Université de Lille1:
- Participation à la rédaction d'un dossier BQR (porte objet High Angle Triple Axis pour la tomographie électronique) = 40k€, 2015

• Projets d'investissements au département Mesures Physiques à l'IUT A de Lille1:
- DSC 131 Evo Setaram = 18k€, 2008
- Four Fisher Scientific = 1k€, 2010
- Dilatomètre Dil 402 PC Netzsch = 28k€, 2010
- MEB de table (24k€, 2014) avec un détecteur d'électrons rétrodiffusés (15k€, 2015)
- Microscope optique Zeiss = 19k€, 2017
- Classé premier pour un diffractomètre de Rayons X de paillasse = 55 k€, 2019

II Production scientifique

ARTICLES

ARTICLES DANS DES REVUES INTERNATIONALES À COMITÉ DE LECTURE

27 - B.C. Nzogang, M. Thieme, **A. Mussi**, S. Demouchy, P. Cordier, Characterization of recovery by sub-grain and grain boundary migration in experimentally deformed polycrystalline olivine, European Journal of Mineralogy (2019). Révisions soumises.

26 - B.C. Nzogang, **A. Mussi**, P. Cordier, Application of Scanning Electron Diffraction in the Transmission Electron Microscope for the characterization of dislocations in minerals, Mineralogical Magazine 83 71-79 (2019) [doi: 10.1180/mgm.2018.144].

25 - C. Bollinger, B.C. Nzogang, **A. Mussi**, J. Bouquerel, D. Molodov, P. Cordier, Microstructural Evidence for Grain Boundary Migration and Dynamic Recrystallization in Experimentally Deformed Forsterite Aggregates, Minerals 9 17 (2019) [doi: 10.3390/min9010017].

24 - B. Malfait, N.T. Correia, **A. Mussi**, L. Paccou, Y. Guinet, A. Hédoux, Solid-state loading of organic molecular materials within mesoporous silica matrix: Application to ibuprofen, Microporous and Mesoporous Materials 277 203-207 (2019) [doi: 10.1016/j.micromeso.2018.10.022]

23 - A. Zaki, M. Wastiaux, S. Casale, **A. Mussi**, J. F. Dhenin, C. Lancelot, J.P. Dacquin, P. Granger, Nano-engineered hierarchical porous silicas for enhanced catalytic efficiency in the liquid phase, Catalysis Science & Technology 8 4604-4608 (2018) [doi: 10.1039/C8CY00726H]

22 - B.C. Nzogang, S. Thilliez, **A. Mussi**, T. Kawazoe, N. Miyajima, J. Bouquerel, P. Cordier, Application of Scanning Precession Electron Diffraction in the Transmission Electron Microscope to the Characterization of Deformation in Wadsleyite and Ringwoodite, Minerals 8 153 (2018) [doi: 10.3390/min8040153].

21 - B.C. Nzogang, J. Bouquerel, P. Cordier, **A. Mussi**, J. Girard, S-I Karato, Characterization by Scanning Precession Electron Diffraction of an aggregate of bridgmanite and ferropericlase deformed at HP-HT, Geochemistry, Geophysics, Geosystems 19 582-594 (2018) [doi: 10.1002/2017GC007244].

20 - **A. Mussi**, P. Cordier, S. Demouchy, B. Hue, Hardening mechanisms in olivine single crystal deformed at 1090 °C: an electron tomography study, Philosophical Magazine 33 3172-3185 (2017) [doi: 10.1080/14786435.2017.1367858].

19 - **A. Mussi**, P. Cordier, S. Ghosh, N. Garvik, B.C. Nzogang, P. Carrez, S. Garruchet, Transmission electron microscopy of dislocations in cementite deformed at high pressure and high temperature, Philosophical Magazine 96 1773-1789 (2016) [doi: 10.1080/14786435.2016.1177670].

18 - **A. Mussi**, M. Nafi, S. Demouchy, P. Cordier, On the deformation mechanism of olivine single crystals at lithospheric temperatures: an electron tomography study, European Journal of Mineralogy 27 707-715 (2015) [doi: 10.1127/ejm/2015/0027-2481].

17 - F. Boioli, A. Tommasi, P. Cordier, S. Demouchy, **A. Mussi**, Low steady-state stresses in the cold lithospheric mantle inferred from dislocation dynamics models of dislocation creep in olivine, Earth and Planetary Science Letters 432 232-242 (2015) [doi: 10.1016/j.epsl.2015.10.012].

16 - **A. Mussi**, P. Cordier, S. Demouchy, Characterization of dislocation interactions in olivine using electron tomography, Philosophical Magazine 95 335-345 (2015) [doi: 10.1080/14786435.2014.1000996].
15 - **A. Mussi**, P. Cordier, S. Demouchy, C. Vanmansart, Characterization of the glide planes of the [001] screw dislocations in olivine using electron tomography, Physics and Chemistry of Minerals 41 537-545 (2014) [doi: 10.1007/s00269-014-0665-1].
14 - S. Demouchy, **A. Mussi**, F. Barou, A. Tommasi, P. Cordier, Viscoplasticity of polycrystalline olivine experimentally deformed at high pressure and 900°C, Tectonophysics 623 123-135 (2014) [doi: 10.1016/j.tecto.2014.03.022].
13 - **A. Mussi**, P. Cordier, D. J. Frost, Transmission electron microscopy characterization of the dislocations and slip systems of the dense hydrous magnesium silicate superhydrous B, European Journal of Mineralogy 25 561-568 (2013) [doi: 10.1127/0935-1221/2013/0025-2308].
12 - **A. Mussi**, D. Eyidi, A. Shiryaev, J. Rabier, TEM observations of dislocations in plastically deformed diamond, physica status solidi (a) 210 191-194 (2013) [doi: 10.1002/pssa.201200483].
11 - K. Deboudt, A. Gloter, **A. Mussi**, P. Flament, Red-ox speciation and mixing state of iron in individual African dust particle, Journal of Geophysical Research 117 D12307 (2012) [doi: 10.1029/2011JD017298].
10 - **A. Mussi**, P. Cordier, D. J. Frost, Crystal defects in dense hydrous magnesium silicate phase A deformed at high pressure: characterization by transmission electron microscopy, European Journal of Mineralogy 24 429-438 (2012) [doi: 10.1127/0935-1221/2011/0024-2126].
9 - C. Rollion-bard, D. Blamart, J. Trebosc, G. Tricot, **A. Mussi**, J. P. Cuif, Boron isotopes as pH proxy: A new look at boron speciation in deep-sea corals using 11B MAS NMR and EELS, Geochimica et Cosmochimica Acta 75 1003-1012 (2011) [doi: 10.1016/j.gca.2010.11.023].
8 - **A. Mussi**, P. Cordier, D. Mainprice, D. J. Frost, Transmission electron microscopy characterization of dislocations and slip systems in K-lingunite: Implications for the seismic anisotropy of subducted crust, Physics of the Earth and Planetary Interiors 182 50-58 (2010) [doi: 10.1016/j.pepi.2010.06.013].
7 - **A. Mussi**, G. Bernard granger, A. Addad, N. Benameur, F. Beclin, A. Bataille, Inversion defects in MgAl2O4 elaborated by pressureless sintering, pressureless sintering plus hot isostatic pressing, and spark plasma sintering, Scripta Materialia 61 516-519 (2009) [doi: 10.1016/j.scriptamat.2009.05.011].
6 - **A. Mussi**, L. Thilly, J. Rabier, J.L. Demenet, Determination of mechanical properties of parallelepiped materials embedded in solid medium and deformed under confining pressure, Materials Science and Engineering A 478 140-146 (2008) [doi: 10.1016/j.msea.2007.05.119].
5 - **A. Mussi**, J. Rabier, L. Thilly, J.L. Demenet, Plasticity and deformation microstructure of 4H-SiC below the brittle-to-ductile transition, physica status solidi (c) 4 2929-2933 (2007) [doi: 10.1002/pssc.200675438].
4 - S. Gravier, L. Charleux, **A. Mussi**, J.J. Blandin, P. Donnadieu, M. Verdier, Mechanical behaviour of nanocomposites derived from zirconium based bulk amorphous alloys, Journal of Alloys and Compounds 434 79-83 (2007) [doi: 10.1016/j.jallcom.2006.08.113].

3 - **A. Mussi**, J.L. Demenet, J. Rabier, TEM study of defects generated in 4H-SiC by micro indentations on the prismatic plane, Philosophical Magazine Letters 86 561-568 (2006) [doi: 10.1080/09500830600930198].

2 - **A. Mussi**, J.J. Blandin, L. Salvo, E.F. Rauch, Resistance to strain-induced damage of an ultra-fine grained magnesium alloy deformed in superplastic conditions, Acta Materialia 54 3801-3809 (2006) [doi: 10.1016/j.actamat.2006.04.011].

1 - K. Mathis, **A. Mussi**, Z. Trojanova, P. Lukac, E.F. Rauch, Effect of equal channel angular pressing on mechanical properties of AZ91 alloy, Kovové materiály - Metallic Materials 41 293 - 299 (2003).

CHAPITRE D'OUVRAGE

1' - F. Boioli, P. Carrez, P. Cordier, A.M. Goryaeva, K. Gouriet, P. Hirel, A. Kraych, S. Mahendran, **A. Mussi**, B.C. Nzogang, R. Reali, S. Ritterbex, and X.Y. Sun, Multiscale Modeling of the Mantle Rheology: The RheoMan Project, Cordier & Goryaeva, France, 2018.

ACTES PUBLIÉS DE CONFÉRENCES INTERNATIONALES

5'' - J.L. Demenet, M. Amer, **A. Mussi**, J. Rabier, Effect of electronic doping on the plasticity of homoepitaxial 4H-SiC single crystals, Journal of Physics: Conference Series 281 012003 (2011) [doi: 10.1088/1742-6596/281/1/012003].

4'' - J.L. Demenet, M. Amer, **A. Mussi**, J. Rabier, Dislocation activity in 4H-SiC in the brittle domain, Materials Science Forum 645-648 335-338 (2010) [doi: 10.4028/www.scientific.net/MSF.645-648.335].

3'' - **A. Mussi**, J.J. Blandin, E.F. Rauch, Microstructure Refinement and Improvement of Mechanical Properties of a Magnesium Alloy by Severe Plastic Deformation, Proc. 2nd International Conference on Nanomaterials by Severe Plastic Deformation: Fundamentals – Processing – Applications 740-745 (2005) [doi: 10.1002/3527602461.ch13g].

2'' - K. Máthis, **A. Mussi**, Z. Trojanová, P. Lukác, E.F. Rauch, J. Lendvai, Mechanical Properties of AZ91 Alloy after Equal Channel Angular Pressing, Proc. 2nd International Conference on Nanomaterials by Severe Plastic Deformation: Fundamentals – Processing – Applications 190-193 (2005) [doi: 10.1002/3527602461.ch3m].

1'' - **A. Mussi**, J.J. Blandin, N.V. Ravi Kumar, L. Dupuy, L. Salvo, E.F. Rauch, Superplastic Forming of Al and Mg Alloys : Only a Question of Weight Reduction ?, Euro-SPF 04 (2004).

ACTES PUBLIÉS DE CONFÉRENCES NATIONALES

1''' - **A. Mussi**, N. Ravi Kumar, J.J. Blandin, M. Suery, E.F. Rauch, Optimisation des propriétés d'usage et de la capacité de mise en forme d'un alliage de magnésium par contrôle de la taille des grains, Matériaux 2002, CM-011 (2002).

COMMUNICATIONS

Présentation orale invitée dans une conférence internationale

1 - P. Cordier, S. Demouchy, A. Mussi, A. Tommasi, New Insights on the Rheology of Olivine Deformed under Lithospheric Temperature Conditions, AGU Fall Meeting 2014, San Francisco, United States, December 2014.

Séminaire invité national

2 - A. Mussi, P. Cordier, S. Demouchy, Etude des mécanismes de déformation plastique de l'olivine par tomographie électronique en transmission, CEA Saclay, France, Février 2016.

1 - A. Mussi, J.L. Demenet, J. Rabier, L. Thilly, Plasticité et microstructures de déformation de 4H-SiC dans le domaine fragile, Laboratoire TECSEN à Marseille, France, Octobre 2006.

Conférence internationale, présentation orale avec acte

3 - J.L. Demenet, M. Amer, A. Mussi, J. Rabier, Effect of electronic doping on the plasticity of homoepitaxied 4H-SiC single crystals, Extended Defects in Semiconductors, Brighton, United Kingdom, September 2010.

2 - A. Mussi, J.L. Demenet, T. Rouxel, J. Rabier, Effect of doping on the plasticity of homoepitaxied 4H-SiC single crystals: a microindentation study, Material Research Society, Spring Meeting, San Francisco, United States, April 2010.

1 - A. Mussi, J. Rabier, L. Thilly, J.L. Demenet, Plasticity mechanisms in 4H-silicon carbide near and below the brittle-to-ductile transition, Extended Defects in Semiconductors, Halle, United Germany, September 2006.

Conférence internationale, présentation orale sans acte

16 - B. Malfait, N.T. Correia, A. Mussi, L. Paccou, Y. Guinet, A. Hédoux, Solid-state loading of pharmaceutical materials within mesoporous silica matrices , 1st International Conference on Contemporary Pharmacy Challenges: 1st International Conference on Contemporary Pharmacy Challenges:, Wisla, Pologne, Septembre 2018.

15 - P. Cordier, B.C. Nzogang, J. Bouquerel, A. Mussi, J. Girard, S.i. Karato, Characterization by Scanning Precession Electron Diffraction of bridgmanite and ferropericlase aggregates deformed at HP-HT, AGU Fall Meeting 2017, La Nouvelle Orleans, États-Unis, Décembre 2017.

14 - P. Cordier, F. Boioli, C. Bollinger, H. Idrissi, A. Mussi, B.C. Nzogang, D. Schryvers, Dislocations: do you want them moving or in 3D ?, EGU General Assembly 2016, Vienna, Austria, April 2016.

13 - A. Mussi, P. Cordier, S. Demouchy, Dislocation characterization using electron tomography with the WBDF technique, GUMP days, Lausanne, Switzerland, November 2015.

12 - A. Mussi, P. Cordier, S. Demouchy, Characterization of the olivine plasticity using electron tomography, European Material Research Society Fall Meeting, Warsaw, Poland, September 2015.

11 - K. Gouriet, P. Cordier, A. Mussi, Understanding deformation mechanisms of a dense hydrous magnesium silicate (Phase A), 7th International Conference on Multiscale Materials Modeling, Berkeley, California, United States, October 2014.

10 - K. Gouriet, P. Cordier, P. Carrez, A. Mussi, R. Caracas, Modeling of dislocation core structures in $Mg_7Si_2O_8(OH)_6$ phase A., AGU Fall Meeting 2013, San Francisco, United States, December 2013.

9 - S. Demouchy, A. Mussi, F. Barou, A. Tommasi, P. Cordier, Visco-plasticity of polycrystalline olivine at high pressure and 900°C: fresh outcomes from high resolution EBSD and electron tomography, AGU Fall Meeting 2013, San Francisco, United States, December 2013.

8 - J.L. Demenet, M. Amer, A. Mussi, J. Rabier, Effect of electronic doping on the plasticity of homoepitaxied 4H-SiC single crystals, Extended Defects in Semiconductors 2012, Thessaloniki, Greece, June 2012.

7 - J.L. Demenet, M. Amer, A. Mussi, J. Rabier, Effect of electronic doping on the plasticity of homoepitaxied 4H-SiC single crystals, Extended Defects in Semiconductors 2010, Brighton, United-Kingdom, September 2010.

6 - P. Cordier, A. Mussi, D. Mainprice, D. J. Frost, Transmission electron microscopy characterization of dislocations and slip systems in $KAlSi_3O_8$ Lingunite: implications for seismic anisotropy in subducting slabs, EGU General Assembly 2010, Vienne, Austria, May 2010.

5 - A. Mussi, J.L. Demenet, T. Rouxel, J. Rabier, Effect of doping on the plasticity of homoepitaxied 4H-SiC single crystals: a microindentation study, MRS 2010, Spring Meeting, San Fransisco, United States, April 2010.

4 - A. Mussi, J.L. Demenet, J. Rabier, L. Thilly, Plasticité de α SiC proche de la transition fragile ductile, French Ceramic Group Conference GFC 2007, Cherbourg, France, March 2007.

3 - A. Mussi, J.L. Demenet, J. Rabier, L. Thilly,Plasticity mechanisms in 4H-silicon carbide near and below the brittle-to-ductile transition, Extended Defects in Semiconductors 2006, Halle, Deutschland, September 2006.

2 - A. Mussi, J.L. Demenet, J. Rabier, L. Thilly, Mécanisme de plasticité dans SiC au voisinage de la transition fragile – ductile, Plasticité 2006, Poitiers, France, March 2006.

1 - A. Mussi, J.J. Blandin, E.F. Rauch, Microstructure refinement and improvement of mechanical properties of a magnesium alloy by severe plastic deformations, Hétérogénéités de deformations, 8th French and Polish conference at the LPMTM laboratory, Villetaneuse, France, October 2001.

Conférence internationale, poster sans acte

10 - C. Bollinger, K. Marquardt, F. Ferreira, B.C. Nzogang, A. Mussi, P. Cordier, On the Role of Grain Boundary Processes and Mobility on the Rheology of Forsterite: Microstructural Evidence, AGU Fall Meeting 2018, Washington, DC, États-Unis, December 2018.

9 - B.C. Nzogang, J. Bouquerel, P. Cordier, A. Mussi, J. Girard, S.i. Karato, Characterization by Scanning Precession Electron Diffraction of bridgmanite and ferropericlase aggregates deformed at HP-HT , EGU General Assembly 2018, Vienna, Autriche, April 2018.

8 - B. Malfait, N.T. Correia, A. Mussi, Y. Guinet, A. Hédoux, Confinement of APIs inside porous silicate matrices by milling: analysis of the physical state and stability of confined APIs - 11th World Meeting on Pharmaceutics, Biopharmaceutics and Pharmaceutical Technology, Granada, Spain, March 2018.

7 - A. Mussi, P. Cordier, B.C. Nzogang, S. Demouchy, Electron tomography study of dislocations in olivine single crystals, 2nd Europeam Mineralogical Conference - EMC2016, Rimini, Italia, September 2016.

6 - A. Mussi, P. Cordier, D. Frost, Transmission electron microscopy characterization of the dislocation populations in the dense hydrous magnesium silicate "superhydrous B", EMC2012, Francfort, Deutschland, EMC2012-138, September 2012.

5 - C. Rollion-Bard, D. Blamart, J. Trebosc, G. Tricot, A. Mussi, J.P. Cuif, Boron Isotopes as pH Proxy: Combination of Boron Speciation and Isotope Composition Data, Goldschmidt 2011, Prague, Czech republic, April 2011.

4 - P. Cordier, A. Mussi, D.J. Frost, Transmission electron microscopy characterization of the dislocations of phase A deformed at 11 GPa, 400°C in the multianvil apparatus, AGU Fall Meeting , San Francisco, United States, December 2011.

3 - K. Deboudt, A. Gloter, A. Mussi, P. Flament, C. Colliex, Red-ox speciation and mixing state of iron in African dust by analytical microscopy, Past, present and future of (S)TEM and its applications, Past, present and future of (S)TEM and its applications, A tribute to the work of Christian Colliex, Paris, France, June 2010.

2 - J.L. Demenet, M. Amer, A. Mussi, J. Rabier, Dislocations activity under high stress in 4H-SiC_Activity in non-basal planes, International Conference on Silicon Carbide and Related Materials 2009, Nürnberg, Deutschland, October 2009.

1 - A. Mussi, J.J. Blandin, E.F. Rauch, Microstructure refinement and improvement of mechanical properties of a magnesium alloy by severe plastic deformation, NanoSPD2 Vienna, Austria, December 2002.

Conférence nationale, présentation orale sans acte

8 - B.C. Nzogang, A. Mussi, P. Cordier, Characterization of dislocations in minerals by Scanning Electron Diffraction in the Transmission Electron Microscope, Plasticité 2018, Nancy, France, Avril 2018.

7 - B.C. Nzogang, J. Bouquerel, A. Mussi, P. Cordier, J. Girard, S.i. Karato, Application des cartes d'orientation en Microscopie Electronique en Transmission à l'étude de la plasticité des phases du manteau inférieur de la Terre, Journées Annuelles de la SF2M, Lyon, France, Octobre 2017.

6 - A. Mussi, P. Cordier, La tomographie électronique des dislocations, 15th Société Française de microscopie, Bordeaux, France, July 2017.

5 - A. Mussi, S. Demouchy, P. Cordier, Caractérisation de la plasticité dans l'olivine par tomographie électronique, 23rd General congres of the Société Française de Physique, Strasbourg, France, August 2015.

4 - A. Mussi, P. Cordier, S. Demouchy, Caractérisation de la plasticité de l'olivine par tomographie électronique, Plasticité 2015, Autrans, France, April 2015.

3 - A. Mussi, P. Cordier, S. Demouchy, A. Tommasi, Détermination des plans de glissement des dislocations [001] vis dans l'olivine par tomographie électronique, Plasticité 2013, Paris, France, April 2013.

2 - A. Mussi, P. Cordier, D. Mainprice, D J. Frost, Caractérisations des dislocations et des systèmes de glissement dans la lingunite en MET, Plasticité 2010, Marseille, France, March 2010.

1 - A. Mussi, J.L. Demenet, J. Rabier, L. Thilly, Mécanismes de plasticité dans SiC au voisinage de la transition fragile ductile, Plasticité 2006, Annecy, France, March 2006.

Conférence nationale, poster sans acte

11 - A. Mussi, P. Cordier, J. Gasc, S. Demouchy, S. Koizumi, Microstructural evidence of grain boundary sliding in iron-free forsterite aggregates deformed 900-1200 °C, Plasticité 2019, Villeneuve d'Ascq, France, Avril 2019.

10 - B.C. Nzogang, J. Bouquerel, P. Cordier, A. Mussi, J. Girard, S.i. Karato, Characterization by Scanning Precession Electron Diffraction of bridgmanite and ferropericlase aggregates deformed at HP-HT, Plasticité 2018, Nancy, France, Avril 2018.

9 - B.C. Nzogang, A. Mussi, P. Cordier, S. Ghosh, N. Garvik, P. Carrez, S. Garruchet, Etude des dislocations dans la cémentite par tomographie électronique, Plasticité 2016, Poitiers, France, April 2016.

8 - A. Mussi, P. Cordier, S. Demouchy, Caractérisation des dislocations [001] dans l'olivine déformée à basse température, par tomographie électronique, Plasticité 2014, Lyon, France, April 2014.

7 - A. Mussi, D. Eyidi, A. Shiryaev, J. Rabier, Caractérisation des dislocations obtenues après déformation plastique de monocristaux de diamant, Plasticité, Paris, France, Avril 2013.

6 - A. Mussi, P. Cordier, D.J. Frost, Caractérisations par microscopie électronique en transmission des populations de dislocations dans le silicate de haute pression hydraté « superhydrous B », Plasticité 2012, Metz, France, April 2012.

5 - M. Amer, A. Mussi, J.L. Demenet, J. Rabier, Plasticité et dopage électronique dans le carbure de silicium, Plasticité 2010, Troyes, France, August 2010.

4 - A. Mussi, S. Rossignol, F. Pailloux, D. Kpogbemabou, R.J. Gaboriaud, Etude de Pt/CeO_2 par haute résolution, EELS et Z- Contraste, JEELS 2008, Poitiers, France, May 2008.

3 - A. Mussi, J.L. Demenet, L. Thilly, J. Rabier, J.L. Santailler, Plasticité et microstructures de déformation de 4H-SiC dans le domaine fragile, Plasticité 2007, Poitiers - Futuroscope, France, March 2007.

2 - A. Mussi, J.L. Demenet, J. Rabier, L. Thilly, J.L. Santailler, Etude de la plasticité autour de la transition fragile ductile en fonction du taux d'impuretés dans α-SiC, Plasticité 2005, La Rochelle, France, April 2005.

1 - A. Mussi, J.J. Blandin, E.F. Rauch, Affinage de la structure et amélioration des propriétés mécaniques d'un alliage de magnésium par hyper-déformations, Plasticité 2001, Aspet, France, March 2001.

Résumé

La convection des roches du manteau terrestre est le moteur du refroidissement de notre planète. Cette dynamique interne produit une activité géologique intense en surface : la dérive des continents. Pour maitriser la tectonique des plaques, il est nécessaire d'étudier la plasticité des minéraux qui constituent le manteau. Les déformations plastiques sont essentiellement régies par le mouvement de dislocations. Le microscope électronique en transmission (MET) est l'outil le plus adapté pour l'étude fondamentale de ces défauts linéaires nanométriques. Mes travaux de recherche sont principalement axés sur l'étude de la plasticité des minéraux du manteau par caractérisations MET des microstructures de dislocations. Des analyses poussées permettent d'obtenir des informations semi-quantitatives, voire quantitatives, sur les mécanismes de déformation plastique.

L'activité de la tectonique des plaques se concentre principalement dans les zones de subduction. Certaines plaques ont tendance à s'enfoncer rapidement dans le manteau, entrainant avec elles des phases hydratées qui, avec la pression et la température, se transforment en silicates magnésiens hydratés denses (DHMS). L'étude de ces phases a un double intérêt : nous informer sur le devenir de l'eau dans le manteau, et vérifier si les propriétés d'accommodation de déformation, comme les tremblements de terre silencieux, sont conservées en profondeur. Etant donnée la grande sensibilité de ces phases au faisceau d'électrons, nous avons développé une méthodologie pour caractériser les DHMS au MET.

Malgré plus de 50 ans d'étude, les mécanismes de déformation plastique de l'olivine, phase minérale majeure du manteau supérieur, restent confus. Dans la partie haute de la lithosphère, la forte friction de réseau entraine des configurations de dislocations rectilignes rendant difficiles l'accès aux systèmes de glissement, tandis que dans la partie basse du manteau supérieur, les interactions multiples et les aspects tridimensionnels des dislocations limitent considérablement l'interprétation des mécanismes de déformation plastique. Nous avons donc décidé de développer la tomographie électronique en transmission des dislocations (TETD) pour voir ces microstructures de dislocations sous un angle nouveau. Cette technique a clairement dépassé nos attentes : en plus d'apporter un aspect statistique et donc quantitatif à la plasticité au MET, au travers des systèmes de glissement, la TETD nous a permis de caractériser des mécanismes d'interactions complexe de dislocations et de quantifier la part de glissement, de montée et de glissement dévié, au cours de la déformation.

Les presses haute température / haute pression permettent actuellement de synthétiser et de déformer, aux conditions du manteau supérieur, des échantillons massifs (nous entendons par massif des échantillons dont le volume représente une fraction de mm^3). Les dispositifs où la déformation plastique est contrôlée (Déformation-DIA, presse rotative Drickamer) produisent généralement des taux de déformation élevés, entrainant des densités de dislocations supérieures à 10^{15} m^{-2}. Compte tenu de la superposition du contraste des dislocations, leurs analyses sont difficiles voire impossibles pour de telles densités de dislocations. En gardant à l'esprit que les déformations plastiques sont intimement liées aux désorientations cristallines, nous avons entrepris l'analyse de cartographies de désorientation pour sortir de cette impasse.

Ces activités de recherches sont présentées dans la première partie de ce mémoire. La seconde section porte sur mes futurs projets de recherche à courts, moyens et longs termes. Enfin, la dernière partie de ce manuscrit décrit mon parcours scientifique et la liste détaillée de mes responsabilités collectives, articles et communications.